Resolution improvement methods applied to digital holography

Daniel Claus

Dipl.-Ing.

This report is submitted as partial fulfilment

of the requirements for the PhD Programme of the

School of Engineering

University of Warwick

2010

www.warwick.ac.uk

Abstract

This thesis discusses the creation, acquisition and processing of digital holograms. Several techniques to improve the optical resolution have been investigated and developed. The optical resolution of numerically reconstructed digital holograms is restricted by both the sampling frequency and the overall sensor-size of the digital camera chip used. This thesis explores the limitations on the optical resolution of the holograms obtained. A typical sensor-size and sampling frequency for digital holograms is 10 mm and 100 lp/mm, respectively, whereas holographic plates used for optical holography can be more than a meter in size and have a sampling frequency of 3000 lp/mm. In order to take full advantage of the benefits digital holography offers, such as fast image acquisition and direct phase accessibility, the problem of reduced resolution needs to be overcome. Three resolution improvement methods have been developed in the scope of this PhD thesis. Prior to implementing the resolution improvement methods, different holographic setups have been analyzed, using the Space-bandwidth product (SBP) to calculate the information distribution both in the recording and reconstruction process.

The first resolution improvement method is based on the synthetic aperture method. In this manner an increased sensor area can be obtained resulting in a larger numerical aperture (NA). A larger NA enables a more detailed reconstruction. The problem encountered in doing this is that an increased optical

resolution results in a smaller depth of field. This has been overcome in this thesis by applying the extended depth of field method. As a result a high resolution in focus reconstruction of all longitudinal object regions is obtained. Moreover, the extended depth of field method allows a topological mapping of the object.

The second resolution improvement method is based on sampling the interference pattern with sub-pixel accuracy. This was carried out on a CMOS-sensor and implemented by moving the light sensitive pixel-area into the dead zone in a 4x4 grid to cover whole the pixel-area. As a result the sensor's sampling frequency is doubled. The increased sampling frequency permits a reduction of the recording distance which results in an increased optical resolution of the reconstructed hologram.

The third and novel approach described in this thesis has been to increase the optical resolution stored in a digital hologram by the combination of the synthetic aperture and the sub-pixel sampling methodBy analogy with the Fresnel-. The resolution improvement methods have been demonstrated both for lens-less digital holography and digital holographic microscopy.

iv

List of Publications

Posters

○ Daniel Claus, Dr. Brenda Timmerman, Prof. Peter Bryanston-Cross (2008). *Digital Holographic Interferometry*. Poster Competition. University of Warwick: May 2008.

Presentations

○ D. Claus, P. Bryanston-Cross, B. Timmerman (2007). *Digital Double Exposure Holography by means of Polarization Optics*. Digital Holography. Vancouver, OSA: June 2007.

○ D. Claus, P. Bryanston-Cross, B. Timmerman (2007). *Digital holography*. Colloquium School of Engineering, University of Warwick: December 2007.

○ D. Claus, P. Bryanston-Cross, B. Timmerman (2008) *Digitale Holografie*. Research Visit, Technische Universität Ilmenau: June 2008.

○ D. Claus, P. Bryanston-Cross, B. Timmerman (2008) *Digital Holography*. Research Visit, Universidad de Vigo: October 2008.

○ D. Claus, P. Bryanston-Cross, B. Timmerman (2008) *Improvement of resolution for digital holograms.* Research Visit, Institute für technische Optik Universität Stuttgart: December 2008.

○ D. Claus, B. Timmerman, and P. Bryanston-Cross (2009). *Resolution Improvement in Digital Holography.* Colloquium Warwick Innovative Manufacturing Research Centre, University of Warwick: April 2009.

○ D. Claus, Marco Fritzsche, B. Timmerman, and P. Bryanston-Cross (2009).*Resolution improvement in lensless digital holographic interferometry.* Stuttgart, Fringe 2009: September 2009.

Scientific publications

○ D. Claus, P. Bryanston-Cross,B. Timmerman (2007). *Digital Double Exposure Holography by means of Polarization Optics.* Digital Holography. Vancouver, OSA: June 2007.

○ D. Claus, Marco Fritzsche, B. Timmerman, and P. Bryanston-Cross (2009). *Resolution improvement in lensless digital holographic interferometry.* Stuttgart, Fringe 2009: September 2009.

○ D. Claus (2010). *High resolution digital holographic synthetic aperture applied to deformation measurement and extended depth of field method.* Appl. Opt., 49(16):3187-3198, 2010

Declaration of Originality

The author wishes to declare that apart from commonly understood and accepted ideas, or where reference is made to the work of others, the work in this thesis is his own. It has not been submitted in part, or in whole, to any other university for a degree, diploma or other qualification.

Daniel Claus

Coventry, 6th of October 2010

Acknowledgements

I would like to offer my sincere thanks to those people whose assistance and support was vital to the development and success of this project.

I would like firstly to give my special thanks to my family, especially my wife and my daughter, who gave me the necessary distance to my research project in order to remain focused and open minded to new ideas.

Furthermore, I would like to thank my supervisors Prof. Peter Bryanston-Cross and Dr. Brenda Timmerman, for making this project possible in conjunction with the Warwick Innovative Manufacturing Research Centre (WIMRC), for their trust, professional advice and assistance during this research.

I would also like to thank Dr. Daciana Udrea from the University of Warwick, Mr. Thomas Meinecke from the Technische Universitát Ilmenau, Dr. Ángel F. Doval from the Universidad de Vigo, Dr. Giancarlo Pedrini from the Universitát Stuttgart, Prof. Ferenc Gyímesi from the Budapest University of Technology and Economics, Dr. Héctor H. Cerecedo Núñez and Patrica Padilla Sosa from the Universidad de Veracruzana and Dr. Ulf Schnars from Airbus Deutschland GmbH for their valuable discussions.

Moreover, I would like to express my gratitude to the School of Engineering technicians. At this point I would especially like to thank Mr. Charles Joyce,

Contents

List of Tables

List of Figures

xvii

xix

xxiii

xxiv

List of Symbols

Symbol	Name	Definition
A_s	orthogonal amplitude	—
A_p	parallel amplitude	—
A_x	vertical amplitude	—
A_y	horizontal amplitude	—
α	interference angle	—
α'	auxiliary variable	$\alpha' = \frac{\pi X' x''}{\lambda r}$
b	distance between first and zeroth order	—
β'	auxiliary variable	$\beta' = \frac{\pi Y' y''}{\lambda r}$
β	solid angle between z-y plane and $\vec{k}$;	—
	solid angle between refracted ray of light and	—
	normal vector	
c	speed of light in medium	$\frac{1}{\sqrt{\mu\epsilon}} = \frac{c_0}{n}$
c_0	speed of light in vacuum;	$\frac{1}{\sqrt{\mu_0\epsilon_0}}$
CCD	charge coupled device	—
CMOS	complementary metal-oxide semiconductor	—
d	recording distance	—
d'	reconstruction distance	—

d_1	object-lens distance	$\frac{fd_2}{d_2-f}$
d_2	lens-image distance	$\frac{fd_1}{d_1-f}$
$\tilde{d_2}$	lens-hologram distance	—
d_{fb}	fibre-lens distance	—
d_{image}	distance between hologram and image	$\tilde{d_2} - d_2$
d_o	object distance	—
d_r	virtual reference source point distance to lens	—
d_{ref}	reference source point distance to hologram	—
d_{R2}	distance first lens surface to centre of curvature	—
d_{sp_lat}	lateral speckle size	$\frac{\lambda}{\zeta}$
d_{sp_axial}	axial speckle size	$\frac{4\lambda}{\zeta^2}$
D	lens-diameter	—
DHM	digital holographic microscope	—
DOF	depth of field	see l_{df}
δ	smallest resolvable object detail	—
$\delta x'$, $\delta y'$	size of intensity pattern in hologram-plane	—
$\Delta\nu_c$	spectral width	$\frac{1}{\tau_c}$
$\Delta\varphi$	phase difference, phase delay	$\varphi_2 - \varphi_1$
$\Delta\varphi_{max}$	maximum phase resolution	$\frac{\pi}{2} - \arccos\frac{2}{l_{grey}}$
$\Delta\varphi_{min}$	minimum phase resolution	$\arccos\left(1 - \frac{2}{l_{grey}}\right)$
$\Delta x'$	pixel-size in x' direction	—
$\Delta y'$	pixel-size in y' direction or lateral image offset for DHM	—
$\Delta x''$	pixel-size in x" direction	$\frac{\lambda d}{N\Delta x'}$ (for Fresnel)
$\Delta y''$	pixel-size in y" direction	$\Delta y'$ (for Rayleigh-Sommerfeld)
E	energy	

$\vec{E}$	electric field strength	$\frac{\vec{F}}{q}$
ϵ	absolute permittivity	$\epsilon_o \epsilon_r$
ϵ_0	electric constant;	$8.85418 \cdot 10^{-12}\,As/Vm$
ϵ_r	relative permittivity	$\frac{\epsilon}{\epsilon_0}$
ε	diffraction angle	—
η	diffraction efficiency	—
η_{fill}	fill-factor	—
η_{SBP}	setup efficiency parameter	$\frac{SBP}{SBP_{optimum}}$
f, f'	focal length in object and image plane	$\left[(n-1)\left(\frac{1}{R_1} + \frac{1}{R_2} + \frac{z_{Lens}(n-1)}{R_1 R_2 n}\right)\right]$
F	focal point	—
$\mathcal{F}$	Fourier Transform	—
$\mathcal{F}^{-1}$	inverse Fourier Transform	—
$\vec{F}$	force	—
FFT	Fast Fourier Transform	—
$\varphi,\ \phi$	phase angle	—
g	period of sinusoidal interference pattern	—
γ	solid angle between z-x plane and $\vec{k}$	—
γ_{12}	complex degree of coherence	$\frac{\Gamma_{12}(r_1,r_2,\tau)}{\sqrt{\Gamma_{11}(r_1,0)\Gamma_{22}(r_2,\tau)}}$
Γ'	magnification	$\frac{y'}{y}$
Γ''	magnification in reconstruction plane	—
Γ_{12}	mutual coherence function	$\left\langle \sqrt{I_1(r_1, t+\tau)}\sqrt{I_2(r_2,t)^*}\right\rangle$
Γ_{11}	intensity first pinhole	$I_1(r,t)$
Γ_{22}	intensity second pinhole	$I_2(r, t+\tau)$
h	Planck's constant;	$6.626068 \cdot 10^{-34} \mathrm{m^2\,kg/s}$
h_d	impulse-response of free space propagation	—
H_d	transfer-function of free space propagation	—

$\vec{H}$	magnetic field strength	—
HH'	principle planes of a lens	—
I	intensity	—
$\mathfrak{I}$	imaginary part of complex number	—
IFTA	fast fourier transform algorithm	—
Im	imaginary part	—
$\vec{j}$	Jones Vector	—
J	Jones Matrix	—
k	wave number	—
$\vec{K}$	sensitivity vector	$\frac{4\pi}{\lambda}\sin\alpha$
κ	incident lens internal angle for second lens surface	—
κ_T	angle of refracted light after passage through lens	—
l	counter	—
l_c	coherence length	—
l_ν	counter in Fourier domain	—
L	cavity length	—
L_c	cantilever length	—
laser	light amplification by stimulated emission of radiation	—
λ	wavelength	—
m	counter	—
m_ν	counter in Fourier domain	—
M	pixel-number in y'-direction	—
M'	pixel-number in y'-direction after zero-padding for DHM	—

MTF	modulation transfer function	—
μ	absolute permeability	$\mu_0 \mu_r$
μ_0	permeability constant	$4\pi \cdot 10^{-7} \mathrm{NA}^{-2}$
μ_r	relative permeability	$\frac{mu}{\mu_0}$
n	refractive index	$\sqrt{\mu_r \epsilon_r}$
N	pixel number in x'-direction	—
NA	numerical aperture	$n \sin \sigma_m ax$
N_F	Fresnel-number	$N_F = \frac{X'^2}{\lambda d}$
Nh	number of holograms	—
N_{zero}	pixel number required to display δ	$N_{zero} = 2N$
ν	frequency of light	$\frac{c}{\lambda}$
ν_{sa}	sampling frequency	$\frac{1}{\Delta x'}; \frac{1}{\Delta y'}$
ν_x	spatial frequency in x-direction	—
ν_{x_max}	maximum spatial frequency in x-direction	—
ν'_x	spatial frequency in x'-direction	—
ν_y	spatial frequency in y-direction	—
ν'_y	spatial frequency in y'-direction	—
∇	Nabla operator;	$\frac{\partial}{\partial x} i + \frac{\partial}{\partial y} j + \frac{\partial}{\partial z} k$
o_{21}	auxiliary variable	—
o_{32}	auxiliary variable	—
o_{31}	auxiliary variable	—
PBC	polarization beam splitter cube	
PSF	point spread function	—
PSI	phase stepping interferometry	—
q	electric charge	—
QWP	quarter wave plate	—
r	(curvature) radius	—

R	power reflectance	$\frac{R_s+R_p}{2}$
$\Re$	real part of complex number	—
R^2	squared correlation coefficient	—
R_s	power reflectance of s-component	$\frac{sin^2(\vartheta_T-\vartheta)}{sin^2(\vartheta_T+\vartheta)}$
R_p	power reflectance of p-component	$\frac{tan^2(\vartheta_T-\vartheta)}{tan^2(\vartheta_T+\vartheta)}$
RE	real part	
RMS	root mean square value	—
s	modulation depth	—
$\vec{S}$	poyntingvector	$\vec{E} \times \vec{H}$
SBP	space bandwidth product	—
SLM	spatial light modulator	
SNR	signal to noise ratio	$20\log\frac{\bar{X}}{\sigma}$
σ	standard deviation	—
t	time	—
T	period	—
TE	transfers electric component	—
TM	transfers magnetic component	—
TIFF	tag image file format	—
τ_c	coherence time	$\frac{l_c}{c}$
ϑ	incident surface angle	—
ϑ_{Br}	Brewster angle	$atan\frac{n_2}{n_1}$
ϑ_R	reflection angle	—
ϑ_T	transmission or refraction angle	—
θ	rotation angle of polarization optical element	—
u(x), u(x,y)	object-plane	—

u'(x'), u'(x',y')	hologram-plane	—
u"(x"), u"(x",y")	reconstruction-plane	—
v	auxiliary variable	—
V	contrast	$\frac{I_{max} - I_{min}}{I_{max} + I_{min}}$
ω	angular frequency	$2\pi\nu$
x, y	coordinates in the object-plane	—
y_1	maximum height at which fibre emitted light strikes the lens	—
x', y'	coordinates in the hologram-plane or lens image-plane	—
x", y"	coordinates in the reconstruction-plane	—
X	object-size	—
X'	sensor-size	$N\Delta x'$
X"	image-size	—
$\bar{X}$	mean value of population	—
z_{lens}	lens thickness	—
z_{max}	displacement applied to cantilever at L_c	—

CHAPTER 1

Introduction

1.1   Historic Context

<div align="center">(a)   (b)</div>

Figure 1.1:   (a) Dennis Gabor taken from Nobel − prize. (2010), (b) Joseph W. Goodman taken from Stanford University. (2010)

In 1948 the Hungarian born British scientist Dennis Gabor shown in Fig. 1.1(a) developed the theoretical concept of holography [Gabor (1948) and Gabor (1949)]. He coined the word holography from the Greek word 'holos'- whole and 'graphein' to write. Holography is based on a light source of sufficient coherence. It consists of two stages, the *recording* of the hologram and *reconstruction* of the image.
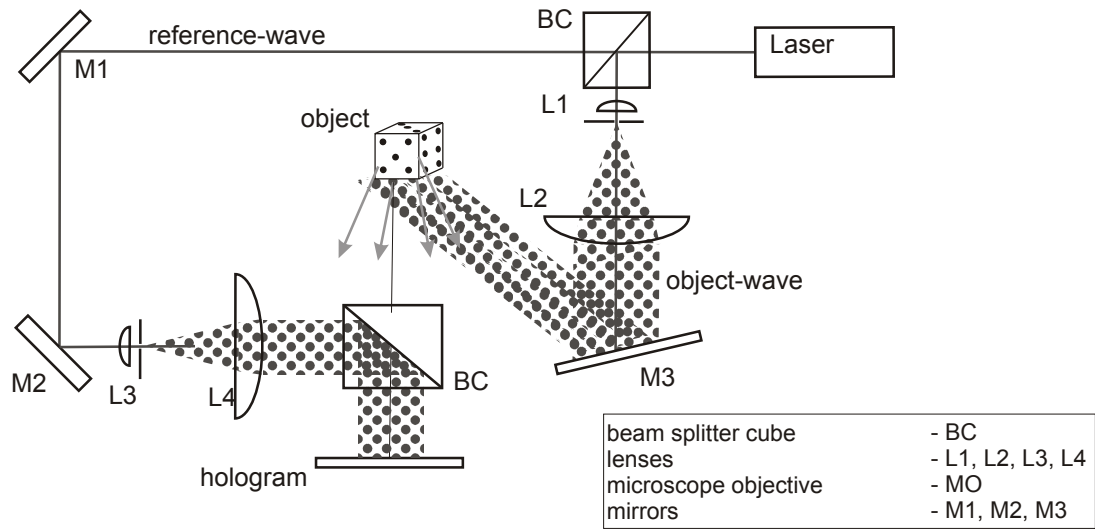
(a)
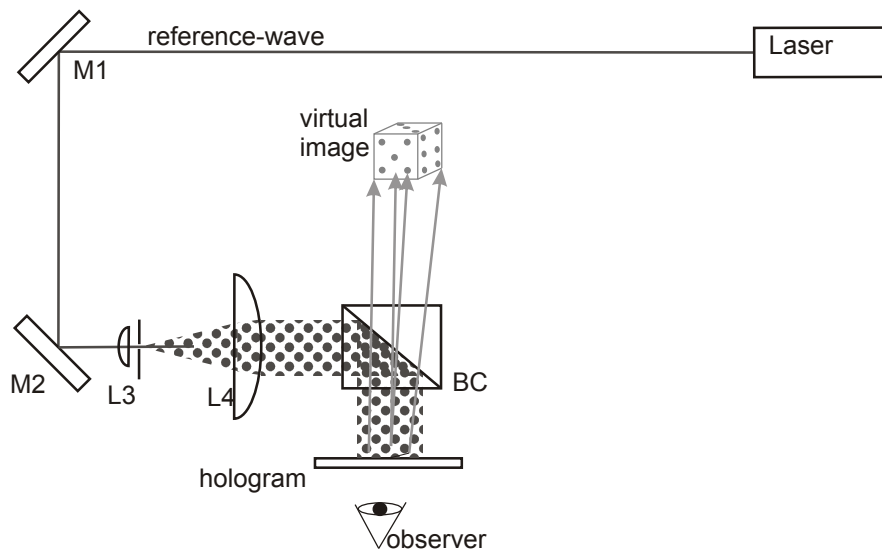
(b)

Figure 1.2: (a) Recording and , (b) reconstruction of a hologram

The recording process is schematically shown in Fig. 1.2(a). The light is split into an object and a reference-wave. The object scattered light overlaps with the reference-wave in the hologram plane, where it is recorded on a light sensitive media such as a photographic plate. The object's amplitude and phase is encoded in the recorded interference pattern. The hologram acts as a diffrac-

tion grating, which when illuminated with the reference-wave reproduces the object-wave, see Fig. 1.2(b). The validity of Gabor's idea could be confirmed by a number of scientists Rogers (1952), El-Sum and Kirkpatrick (1952) and Lohmann (1956). However, the interest in optical holography declined after a few years due to poor image quality. The low image quality was caused by two effects. Firstly, the lack of a sufficient coherent light source and secondly, the overlap of the desired image with the twin-image and the undiffracted light resulting in the DC-term in the reconstruction. The invention of the pulsed Ruby-laser by Maiman (1960) and the separation of the reconstructed image-terms by an off-line setup developed by Leith and Upatnieks (1962) gave holography the necessary tools to emerge as one of the most promising optical techniques of the 20th century. This can be confirmed by various publications made there-after such as Thompson (1978), Hariharan (1984) and Ostrovsky et al. (1991). Different holographic applications could be established such as holographic particle image velocimetry by Trolinger et al. (1969), holographic tomography by Sweeney and Vest (1973) and its most important application in interferometry by Powell and Stetson (1965). In holographic interferometry two or more object states are compared interferometrically. Whereas at least one object state must be holographically recorded and reconstructed according to Collier et al. (1965). Various applications of holographic interferometry were developed such as vibration analysis [Powell and Stetson (1965)], deformation measurement [Haines and Hildebrand (1966)] or determination of refractive index changes caused by a change of pressure or temperature [Horman (1965)]. The fringe counting, initially performed manually, could soon be replaced by computer algorithms Osten et al. (1987). This algorithm included digitizing and quantizing the photographed optical reconstruction, calculating the phase distribution by utilizing the geometric setup arrangement, determining the desired physical property distribution and

displaying the result. The introduction of phase shifting by Kreis et al. (1981) was a significant step forward in the computer aided fringe analysis. It was now possible to measure and not to estimate the interference phase. Moreover, the phase sign ambiguity could be resolved utilizing phase shifting algorithms. Although the fringe analysis was left to the computer, one still needed to wet chemically process the holographic plate. The focus was now set on replacing the holographic plate by digital means. Two solutions for the digital recording of interferograms could be developed namely Electron-Speckle-Pattern-Interferometry (ESPI) and digital holography. The first is based on in-focus recording of the object under investigation by a digital camera. Diffusely scattering object were investigated which resulted in the recording of the in-focus image covered with speckle. The grainy speckle pattern could easily be recorded by existing analog cameras. Adding the intensity of two recorded speckle pattern under different object states results in the creation of correlation fringes similar to the one observed with holographic interferometry. This technique became known as Electronic-Speckle-Pattern-Interferometry (ESPI) and enabled the computerised recording and processing of interferograms. ESPI today is a well established measurement tool for metrology and used in many applications. The major drawback of ESPI is the phase ambiguity which could just be resolved by the introduction of phase stepping by Creath (1985) and Stetson and Brohinsky (1985). Another disadvantages of ESPI is the quality demand on the optics involved in order to avoid the introduction of any kind of aberrations to the recorded speckle field, which otherwise will decrease the accuracy of the interferometric measurement. Contrary to ESPI, digital holography enables lens-less recording, which reduces the cost of the optical setup. Moreover, it permits phase determination by recording a single off-line hologram. This results in less experimental effort and offers the analysis of high speed events. The first digital hologram was recorded and

reconstructed utilizing computer aided methods by J. W. Goodman, shown in Fig. 1.1(b), and R.W. Lawrence Goodman and Lawrence (1967). Hence digital holography is older than ESPI. A lens-less Fourier-hologram was recorded on a vidicon-detector, consisting of a photoconductive surface scanned by an electron-beam. The output of the vidicon was sampled in a 256x256 array with a quantization of eight grey levels. This was the starting point of digital holography, but it still took some decades until results of sufficient resolution became available. Only in the last two decades digital holography has received more and more importance which is strongly linked with the rapid development of digital recording devices such as Charge-Coupled-Devices (CCD) and Complementary−OxideSemiconductor (CMOS) cameras.

1.2   Benefits of Digital Holography

Digital holography offers a higher degree of freedom for data acquisition and processing than optical holography does. Moreover, it enables the direct reconstruction of the phase without the need to apply phase stepping. This property is beneficial for the investigation of dynamic events. It was first demonstrated by Schnars (1994). Moreover, due to the numerical focusing a lens-less setup is enabled, which reduces the cost and accuracy demand for an optical system. On the contrary, in digital interferometry an optical system is needed, which focuses on the object in order to record the phase correctly. A comparison of digital holographic interferometry with various techniques applied in optical metrology is shown in Table 1.1. Digital holographic interferometry can cover a larger measurement range in the lateral dimension and likewise in the longitudinal dimension. If one wanted to cover the same range a combination of several measurement techniques needed to be applied. A high lateral resolution

Table 1.1: Measurement techniques for optical metrology (λ=632.8 nm), adapted from Braunecker et al. (2008)

Method	Range lateral resolution	RMS height resolution
Interferometry	1 μm - 1000 mm	0.2 nm - 200 nm
Macroscopic fringe projection	10 μm -2 m	10 μm - 1 mm
Microscopic fringe projection	1 μm - 30 mm	0.1 μm - 10 μm
Confocal micro-scope	0.5 μm - 30 mm	10 nm - 10 μm
White light inter-ferometry	0.7 μm - 5 mm	1 nm - 10 μm
Stylus instrument	100 nm - 100 mm	0.5 nm - 10 μm
Scattering	100 μm - 100 mm	0.5 nm - 10 nm
Digital holographic interferometry	500 nm - 1 m	1 nm - 50 mm

can be obtained by combing digital holography with microscopy demonstrated in Osten (2006a). Kuehn et al. (2008) demonstrated a height resolution in the sub-nanometer regime utilizing digital holography. A large range of measured object height can be obtained applying holographic multi-wavelength contouring demonstrated by Wagner et al. (2000). Moreover, the numerical reconstruction in digital holography enables one to reduce wave-aberration effects as demonstrated in Colomb et al. (2006). Additional benefits of digital holography are discussed in Section 4.7.

Nevertheless, digital holography still suffers from low spatial resolution typically (100 lp/mm) in comparison to a photographic film (3000 lp/mm) used in optical holography. This restricts the angle between object and reference-wave and hence the object-size and resolution obtained.

1.3 Outline of Thesis

This thesis focuses on the image quality and resolution improvement of digital holograms. The lateral resolution improvement will be demonstrated on the USAF 1951 test-target, whereas the phase resolution improvement will be demonstrated utilizing the standard deviation, which corresponds to the phase measurement uncertainty. Double exposure phase maps will be used to prove the phase improvement. The image quality improvement will be demonstrated by a reduced Signal to Noise Ratio (SNR) applied to intensity reconstruction.

In **Chapter 2** the optical foundation in order understand the concept of digital holography is represented. The relevant optical terminologies to describe the recording and reconstruction process of digital holograms are explained. Terms which refer to the recording process such as coherence, interference, intensity and the working principle of digital recording devices are explained. The most commonly applied diffraction models used for the numerical reconstruction of digitally recorded holograms are discussed.

Chapter 3 represents the digitized numerical reconstruction methods. Approaches to suppress the DC-term and the twin-image are introduced and illustratively demonstrated by examples. Novel numerical methods developed by the author, which improve the accuracy and the performance are represented.

In **Chapter 4** optical parameters of the reconstructed hologram are discussed. Rayleigh's and Abbe's resolution criteria including their valid application is represented. The derivation of optical parameters is presented, which is intended to improve the readers understanding. Moreover, properties of digital holography are represented, which in comparison to optical holography and other optical techniques outline the benefits of digital holography.

Chapter 5 is devoted to the Space-bandwidth-product (SBP), which represents an important parameter for the evaluation of optical systems. The required SBP in the recording process and the SBP obtained in the reconstruction process in respect to the hologram type is calculated. The work conducted by Lohmann (1967) and Xu et al. (2005) was extended to cover in-line and off-line configurations of Fresnel-hologram, Fourier-hologram and Image-plane hologram. A comparison of the performance of the three hologram types is conducted, which reveals important information for the correct choice of hologram-type in respect to the requirement.

Chapter 6 represents the main work conducted during the PhD period. Resolution improvement methods are represented and applied to digital holography. The first resolution improvement approach is based on the synthetic aperture method. Difficulties in conjunction with the recording of the object's phase is pointed out and possible solutions to overcome these difficulties are given. Moreover, the extended depth of field method is applied to the synthetic aperture method, which to the author's knowledge is novel. In addition to the synthetic aperture approach, the novel sub-pixel sampling method in combination with phase stepping is represented. The sub-pixel sampling method is based on sub-pixel movement of the camera sensor to result in a smaller pixel-size. Last but

not least, both resolution improvement methods, synthetic-aperture and sub-pixel sampling method, are combined.

In previous chapters all holograms described are recorded by a lens-less setup. The holograms in **Chapter 7** are recorded in combination with a microscope-objective to improve the resolution in order to investigate object details in the sub-micrometer region. Important steps for the recording process are highlighted and the optical parameters obtained in the reconstruction are represented. Furthermore, the resolution improvement methods discussed in Chapter 6 are applied to prove their validity in conjunction with a lens system. Moreover, a proof of principle to obtain the two dimensional refractive index contribution of the object in conjunction with the extended depth of field method is shown.

Chapter 8 concludes this thesis and discusses the implication of this work for future research.

Each chapter consists of an introduction, main body and conclusion. This offers the reader the option to read them separately.

CHAPTER 2

Fundamentals of Optics and Interferometry

Presented in this chapter are the physical principles to understand the recording and reconstruction process in holography. The recording process, in which coherent light beams are superimposed, is presented. Requirements will be demonstrated and terms like coherence and laser will be explained. The reconstruction process based on different diffraction models and their validity will be discussed in the second part of this chapter. The fundamental knowledge presented is in close correspondence with Goodman (1996), Saleh and Teich (1991) and Kreis (2005).

2.1 Light Waves

Light is a transverse, electromagnetic wave characterized by a time-varying electric and magnetic field. The nature of light can be mathematically described by Maxwell's equations. Maxwell's equation for a homogenous, isotropic, non
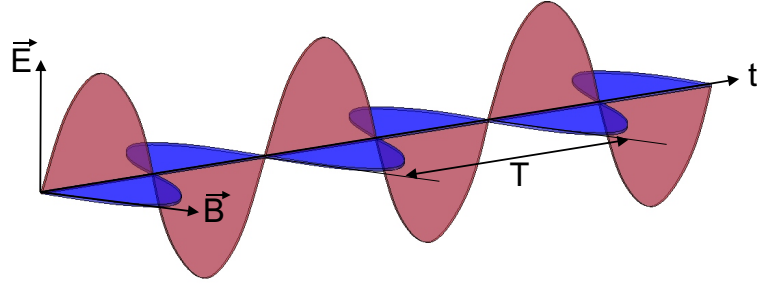
Figure 2.1: Propagation of electromagnetic light wave

conducting medium is:

$$\nabla \times \vec{E} = -\mu \frac{\partial \vec{H}}{\partial t}$$
$$\nabla \times \vec{H} = \epsilon \frac{\partial \vec{E}}{\partial t}$$
$$\nabla \cdot \epsilon \vec{E} = 0 \tag{2.1}$$
$$\nabla \cdot \mu \vec{H} = 0$$

Where $\vec{E}$ is the electric field strength and $\vec{H}$ the magnetic field strength. t indicates time and ∇ is the Nabla-operator which can be described according to Goodman (1996) by:

$$\nabla = \frac{\partial}{\partial x}\hat{i} + \frac{\partial}{\partial y}\hat{j} + \frac{\partial}{\partial z}\hat{k} \tag{2.2}$$

ϵ and μ denote the permittivity and the permeability of the medium in which the light wave propagates. The permittivity can be described by the product of the relative permittivity and the permittivity in a vacuum ($\epsilon = \epsilon_0 \epsilon_r$). The permeability can be calculated in an analogous manner ($\mu = \mu_0 \mu_r$). Both, electric and magnetic field, are perpendicularly orientated to each other, as shown in Fig. 2.1. A detailed derivation from Maxwell's equation to the wave equation can be found in Goodman (1996). The wave equation obtained is:

$$\nabla^2 \vec{u} - \frac{1}{c^2}\frac{\partial^2 \vec{u}}{\partial t^2} = 0 \tag{2.3}$$

The wave-equation for the electric field strength $\vec{E}$ and the magnetic field strength $\vec{H}$ are identical. Both, $\vec{E}$ and $\vec{H}$, have therefore been replaced by the symbolic vector $\vec{u}$, as shown in Eq. 2.3. c is the speed of light in the medium. c can be calculated using:

$$c = \frac{c_0}{n} \tag{2.4}$$

Where the refractive index n can be expressed by a combination of relative permittivity ϵ_r and relative permeability μ_r. For most materials μ_r at optical frequencies is close to one.

$$n = \sqrt{\mu_r \epsilon_r} \approx \sqrt{\epsilon_r} \tag{2.5}$$

Therefore, the electrical field can be considered to be the predominant interaction component of the electro-magnetic wave with the material. Thus $\vec{u}$ can be treated as a replacement for the electric field strength $\vec{E}$. Light waves are *transverse waves* oscillating perpendicular to the direction of propagation and are therefore described in vector notation. For most applications it is not necessary to use the full vector description of the field. A light wave oscillating in a single plane, namely a linearly polarized light wave, which propagates in the z-direction can be described in scalar notation as:

$$u(z,t) = A_0 \cos(kz - \omega t + \varphi_0) \tag{2.6}$$

Eq. 2.6 is also known as the *harmonic wave* equation. k is the wave number, which depends on the wavelength of light λ.

$$k = \frac{2\pi}{\lambda} \tag{2.7}$$

ω is the *angular frequency*, which is related to the frequency of light ν by

$$\omega = 2\pi\nu = \frac{2\pi}{T} \tag{2.8}$$

with

$$\nu = \frac{c}{\lambda} \tag{2.9}$$

The time for a whole 2π cycle is called the period T. Taking into account the substitutions made in Eq. 2.7 and Eq. 2.8 results in a harmonic wave-equation:

$$u(z,t) = u_0 \cos\left(\frac{2\pi}{\lambda}z - \frac{2\pi}{T}t + \varphi_0\right) \tag{2.10}$$

The harmonic wave equation can be expressed in complex notation by applying Euler's formula.

$$\exp(i\alpha) = \cos\alpha + i\sin\alpha \tag{2.11}$$

It is important to consider that only the real or imaginary part matches with Eq. 2.6 and hence makes physically sense.

$$u(z,t) = Re\{A_0 \exp[i(kz - \omega t + \varphi_0)]\} \tag{2.12}$$

This complex notation offers some advantages in terms of expressing the phase or to modulate the phase as we will see in Chapter 3. An alternative waveform often used to describe the nature of light is the *spherical wave*. In mathematical terms the coordinates are changed to polar coordinates $x = r\sin\beta$, $y = r\cos\beta\sin\gamma$ and $z = r\cos\beta\cos\gamma$ as shown in Fig. 2.2.
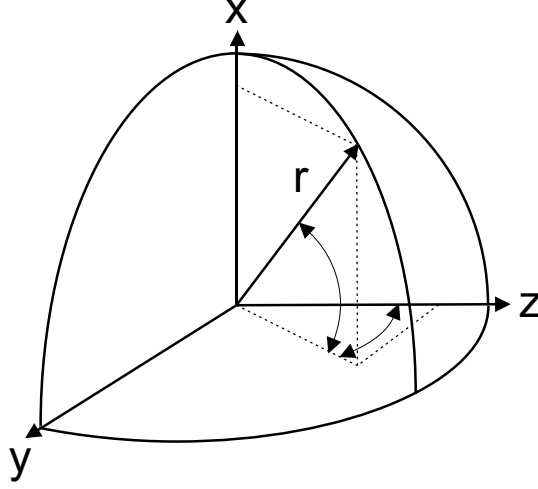
Figure 2.2: Transformation of cartesian coordinates in polar coordinates

Due to its geometry a spherical wave does not dependent on β and γ. Thus the scalar wave equation becomes

$$\frac{1}{r}\frac{\partial^2}{\partial r^2}ru - \frac{1}{c^2}\frac{\partial^2 u}{\partial t^2} = 0 \tag{2.13}$$

2.2 Intensity

The phase φ of the wave described in Eq. 2.12:

$$\varphi = \frac{2\pi}{\lambda}z - \omega t + \varphi_0 \tag{2.14}$$

is proportional to the wavelength of light $\lambda = \frac{c}{\nu}$. The wavelength of visible light ranges from 400 nm to 800 nm. The corresponding frequency ranges from $7.5 \cdot 10^{14}$ Hz to $3.7 \cdot 10^{14}$ Hz. Light sensor such as the eye, photodiode, CCD or CMOS are not able to detect such high frequencies. The only quantity which can be measured is the intensity. The intensity observed correlates to the sum of the energy per unit volume (ρ_E) namely energy density of electric (ρ_{el}) and magnetic

field (ρ_{mag}) *:

$$\rho_E = \rho_{el} + \rho_{mag} = \frac{1}{2}\epsilon E^2 + \frac{1}{2}\mu H^2 \tag{2.15}$$

With $H = \frac{E}{c\mu}$ and $c^2 = \frac{1}{\mu\epsilon}$ follows:

$$\rho_E = \frac{1}{2}\epsilon E^2 + \frac{1}{2}\epsilon E^2 = \epsilon E^2 \tag{2.16}$$

The electromagnetic energy is recorded in energy packets called photons. The photon energy E_{pho} is converted by the photoelectric effect into free electrons with a certain kinetic energy E_{kin}.

$$E_{pho} = W_A + E_{kin} \tag{2.17}$$

Where W_A is the material dependent energy gap which needs to be exceeded in order to generate free electrons. The intensity recorded is hence proportional to E^2. The frequency of visible light is of such large magnitude (10^{14}) that even the fastest high speed cameras ($\approx 10^5$ Hz) are too slow to resolve a time period of light. Hence the recorded intensity represents the integration of E^2 quantities.

2.3 Polarization Optics

The light wave is a transversal wave, which can have different planes of oscillation. In each plane perpendicular to the direction of propagation the vector of the electric field strength $\vec{E}$ and in analogue manner the magnetic field strength $\vec{H}$ follows a specific path Haferkorn (2003). The path may be describe a straight line, a circle or an ellipse. These different states of wave propagation can be described as linearly, circularly or elliptically polarized light. They can be produced by two

---

*taken from Lohmann and Sinzinger (2006)

Table 2.1: Different types of polarization

phase difference $\Delta\varphi$	$A_x \neq A_y$	$A_x = A_y$
0 °	linearly polarized light	diagonal linearly polarized
0 ° $< \varphi <$ 90 °	left elliptically polarized	left elliptically polarized
$\varphi =$ 90 °	left elliptically polarized	left circularly polarized
90 ° $< \varphi <$ 180 °	left elliptically polarized	left elliptically polarized
$\varphi =$ 180 °	linearly polarized	diagonal linearly polarized
180 ° $< \varphi <$ 270 °	right elliptically polarized	right elliptically polarized
270°	right elliptically polarized	right circularly polarized
270 ° $< \varphi <$ 360 °	right elliptically polarized	right elliptically polarized

linearly polarized wave-trains, which are orientated perpendicular to each other. The resulting states of polarization for various combinations of two perpendicular wave-trains with amplitude A_x and A_y and phase difference $\Delta\varphi$ between both wave-trains are shown Table 2.1.

There are different possibilities to obtain linearly polarized light. One way is to generate linearly polarized light within a laser cavity utilizing the Brewster window. Fig. 2.3(a) shows the light path starting from the incident wave on a dielectric medium, which is then split into a reflected wave, indicated by subscript R, and a refracted wave, indicated by subscript T.

If the sum of the reflection angle ϑ_R and the refraction angle ϑ_T is 90 ° only the s-component is reflected. The abbreviation 's' arises from the German word 'senkrecht', which means orthogonal. It is also referred to as the transverse electric (TE) or orthogonal component. The p-component, parallel component, also known as the transverse magnetic (TM) passes through the glass without experiencing any reflection loss. The power reflectance for the s-component R_s, p-component R_p, and the sum of both R according to Haferkorn (2003) is defined

(a)

(b)
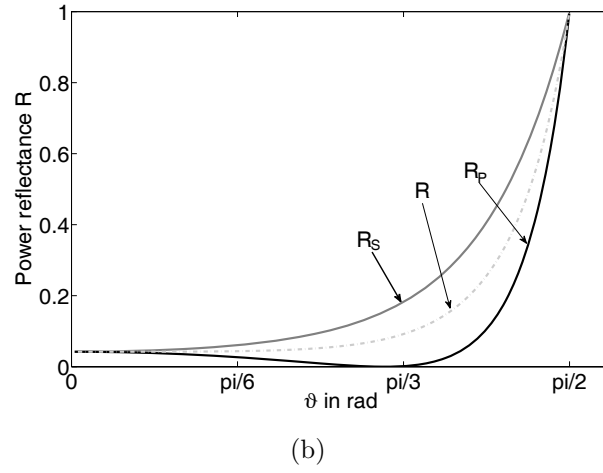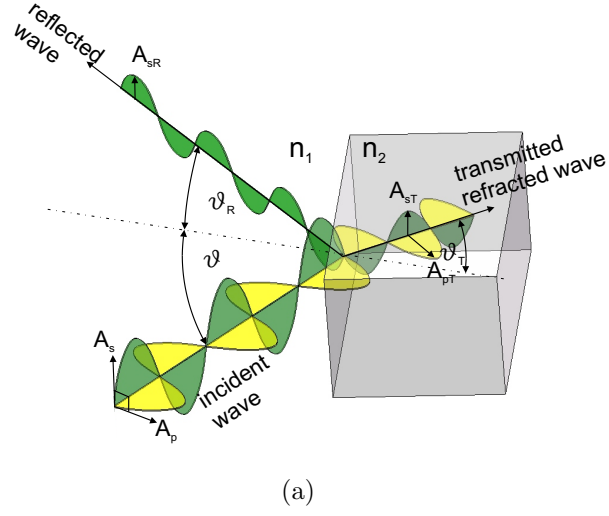
Figure 2.3: (a) Reflection and refraction between two media of refractive index n_1 and n_2 , (b) Power reflectance R versus incident angle ϑ for $n_1 = 1$ and $n_2(BK7) = 1.517$

as:

$$
\begin{aligned}
R_s &= \frac{\sin^2 (\vartheta_T - \vartheta)}{\sin^2 (\vartheta_T + \vartheta)} \\
R_p &= \frac{\tan^2 (\vartheta_T - \vartheta)}{\tan^2 (\vartheta_T + \vartheta)} \\
R &= \frac{R_s + R_p}{2}
\end{aligned}
\tag{2.18}
$$

The power reflectance as a function of the incident angle ϑ for BK7-glass is shown in Fig. 2.3(b). The incident angle at which only the s-component is reflected is referred to as the **Brewster-angle**. The Brewster-angle (ϑ_{Br}) can be directly

calculated as follows:

$$n_1 \sin \vartheta_{Br} n_1 = n_2 \sin \left(90° - \vartheta_{Br}\right) \quad \implies \quad \vartheta_{Br} = \mathrm{atan} \frac{n_2}{n_1} \qquad (2.19)$$

This relationship can be used to obtain polarized laser light. The vector normal to the surface of the polarising glass (also known as the Brewster window) is orientated at the Brewster-angle to the optical axis of the resonator. The s-component is thus reflected orthogonally outside the laser cavity. Light within the laser cavity is reflected back and forth. Therefore it passes through the Brewster window several times, which results in laser light containing only the p-component. Working with linearly-polarized light in interferometry offers a high degree of freedom by adapting either intensity and/or polarization to different situations. Moreover, the contrast of the interference pattern can be increased, which results in an improved resolution for the reconstructed hologram, which will be discussed in Section 4.4.3.

Sometimes the polarization state of one of the two interfering beams needs to be changed in order to obtain matched polarization state of both beams. Moreover, changing the polarization state enables the acquisition of more object information, as shown in Whittaker et al. (1994). A change of polarization state can be accomplished by the introduction of wave-retarder plates, which possess a certain phase delay $\Delta\varphi$ between optically slow and optically fast axis. The incident wave, shown in red in Fig. 2.4, oscillates on a plane at an angle θ_1 to the x-z plane. The amplitude of the incident wave can be split into its vertical A_x (green) and horizontal A_y (yellow) component. We assume that the optically fast axis is vertically aligned as shown in Fig. 2.4. The horizontal component in Fig. 2.4 is phase delayed by π (half-wave retarder) to the vertical component. This results in a changed angle θ_2 of the polarization plane.
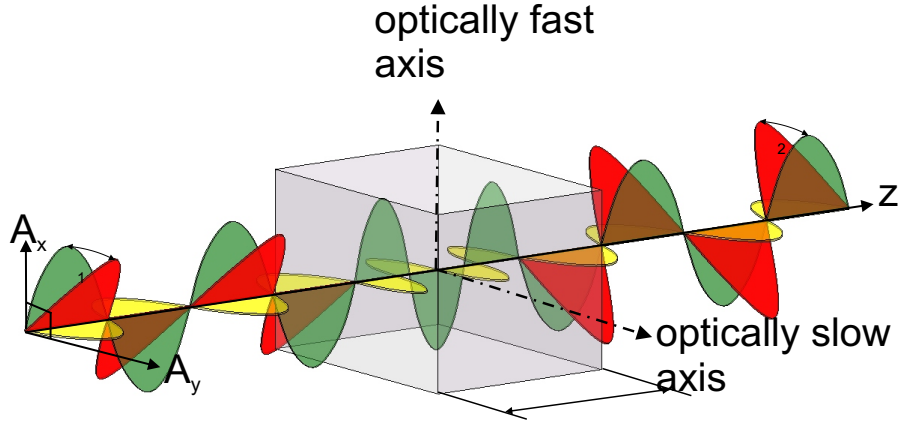
Figure 2.4: Passage of linearly polarized light trough a half-wave retarder

The influence of wave-retarders on the incident beam can be predicted utilizing **Jones-Calculus**. A wave-retarder with the phase delay $\Delta\varphi$ can be described by the following Jones-Matrix.

$$\mathbf{J} = \begin{pmatrix} 1 & 0 \\ 0 & \exp\left(-i\Delta\varphi\right) \end{pmatrix} \tag{2.20}$$

The incident light maintains a certain angle θ_1 to the x-z plane. Its Jones-vector is therefore obtained by its vertical and horizontal projection.

$$\begin{pmatrix} \cos\theta_1 \\ \sin\theta_1 \end{pmatrix} \tag{2.21}$$

A possible rotation angle θ between wave-retarder and the x-z-plane is accounted for by applying the rotation-matrix $\mathbf{R}(\theta)$ to $\mathbf{J}$.

$$\mathbf{R}\left(\theta\right) = \begin{pmatrix} \cos\theta & \sin\theta \\ -\sin\theta & \cos\theta \end{pmatrix} \tag{2.22}$$

The rotated wave-retarder becomes:

$$J_R(\theta) = R(\theta)^{-1} JR(\theta)$$

$$= \begin{pmatrix} \cos\theta & -\sin\theta \\ \sin\theta & \cos\theta \end{pmatrix} \begin{pmatrix} 1 & 0 \\ 0 & \exp(-i\Delta\varphi) \end{pmatrix} \begin{pmatrix} \cos\theta & \sin\theta \\ -\sin\theta & \cos\theta \end{pmatrix} \quad (2.23)$$

$$= \begin{pmatrix} \cos^2\theta + \sin^2\theta\exp(-i\Delta\varphi) & \frac{1}{2}\sin 2\theta\left[1-\exp(-i\Delta\varphi)\right] \\ \frac{1}{2}\sin 2\theta\left[1-\exp(-i\Delta\varphi)\right] & \sin^2\theta + \cos^2\theta\exp(-i\Delta\varphi) \end{pmatrix}$$

The rotated Jones-matrices of the most commonly applied polarization optical elements are shown in Table 2.2. It needs to be emphasized that θ of each individual element does not necessarily need to be the same. The influence of the polarization-optical element on the incident wave can be calculated using:

$$\vec{j}_{out} = J_R\vec{j}_{in} \quad (2.24)$$

Polarization optical elements in conjunction with digital holography will be used at a later stage of this thesis in Section 3.3.4 and Section 6.2.1.

Table 2.2: Jones-Matrix of polarization optical elements

Polarization element	Jones-Matrix	Rotated Jones Matrix	Application
Rotated polarizer	$\begin{pmatrix} 0 & 0 \\ 0 & 1 \end{pmatrix}$	$\begin{pmatrix} \cos^2 \theta & \frac{1}{2}\sin 2\theta \\ \frac{1}{2}\sin 2\theta & \sin 2\theta \end{pmatrix}$	Generate linearly polarized light, polariscope, photography
Rotated half-wave retarder	$\begin{pmatrix} 1 & 0 \\ 0 & -1 \end{pmatrix}$	$\begin{pmatrix} \cos 2\theta_1 & \sin 2\theta_1 \\ \sin 2\theta_1 & -\cos^2 \theta_1 \end{pmatrix}$	Phase stepping, polarization alignment in interferometry
Rotated quarter-wave retarder	$\begin{pmatrix} 1 & 0 \\ 0 & -i \end{pmatrix}$	$\begin{pmatrix} \cos^2 \theta_1 - i\sin^2 \theta_1 & \frac{1}{2}(1+i)\sin 2\theta_1 \\ \frac{1}{2}(1+i)\sin 2\theta_1 & \sin^2 \theta_1 - i\cos^2 \theta_1 \end{pmatrix}$	Phase stepping, polarization alignment in Michelson-interferometer, polariscope, optical isolator in conjunction with a polarizer
Dielectric mirror	$\begin{pmatrix} 1 & 0 \\ 0 & -1 \end{pmatrix}$	$\begin{pmatrix} \cos 2\theta_1 & \sin 2\theta_1 \\ \sin 2\theta_1 & -\cos 2\theta_1 \end{pmatrix}$	Polarization alignment

2.4   Interference of Light

This section is focused on the explanation of the principles of interferometry. The effect of interference occurs when two or more coherent light waves are superimposed. Let us consider two waves with amplitudes A_{01} and A_{02}. The angular frequency ω and the polarization plane is assumed to be the same for both waves. The different directions of propagation of both waves is accounted for by the corresponding k-vector.

$$
\begin{aligned}
u_1\left(r,t\right) &= A_{01} \exp\left[i\left(\vec{k_1}r - \omega t + \varphi_1\right)\right] \\
u_2\left(r,t\right) &= A_{02} \exp\left[i\left(\vec{k_2}r - \omega t + \varphi_2\right)\right]
\end{aligned}
\tag{2.25}
$$
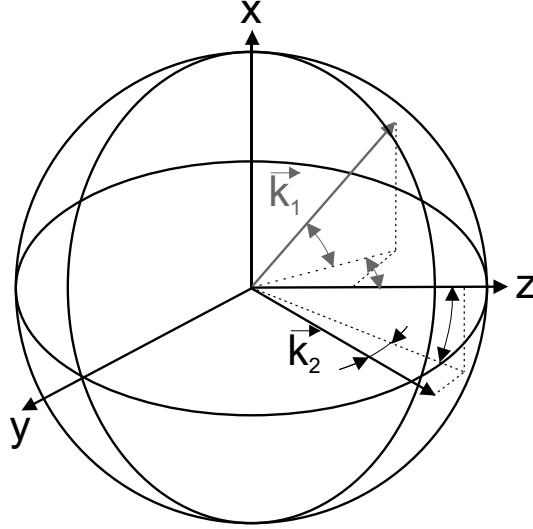
Figure 2.5: Decomposition of wave vectors

The interference can be described as:

$$
\begin{aligned}
(u_1(r,t) + u_2(r,t)) &= A_{01} \exp\left[i\left(\vec{k}_1 r - \omega t + \varphi_1\right)\right] \\
&\quad + A_{02} \exp\left[i\left(\vec{k}_2 r - \omega t + \varphi_2\right)\right] \\
&= \exp(-i\omega t)\left[A_{01}\exp\left\{i\left(\vec{k}_1 r + \varphi_1\right)\right\}\right. \\
&\quad \left. + A_{02}\exp\left\{i\left(\vec{k}_2 r + \varphi_2\right)\right\}\right] \\
&= \exp(-i\omega t)\left[A_{01}\exp(i\phi_1) + A_{02}\exp(i\phi_2)\right]
\end{aligned}
\tag{2.26}
$$

A possible combination of two different k-vectors is shown in Fig. 2.5. $\vec{k}_1$ and $\vec{k}_2$ can be described as:

$$
\vec{k}_1 = \frac{\vec{k}_z}{\cos\beta_1 \cos\gamma_1} \quad \vec{k}_2 = \frac{\vec{k}_z}{\cos\beta_2 \cos\gamma_2}
\tag{2.27}
$$

The recording media detects the intensity of both interfering waves, which is defined as:

$$
\begin{aligned}
I(r) &= |u_1(r,t) + u_2(r,t)|^2 \\
&= (u_1(r,t) + u_2(r,t))(u_1(r,t) + u_2(r,t))^* \\
&= A_{01}^2 + A_{02}^2 + A_{01}A_{02}\exp(i(\phi_1 - \phi_2)) \\
&\quad + A_{01}A_{02}\exp(-i(\phi_1 - \phi_2)) \\
&= A_{01}^2 + A_{02}^2 + 2A_{01}A_{02}\cos(\phi_1 - \phi_2) \\
&= A_{01}^2 + A_{02}^2 + 2A_{01}A_{02}\cos(\Delta\phi)
\end{aligned}
\tag{2.28}
$$

$$
\begin{aligned}
I(r) = A_{01}^2 + A_{02}^2 + 2A_{01}A_{02}\cos\left[k_z r\left(\frac{1}{\cos\beta_1\cos\gamma_1}\right.\right. \\
\left.\left. - \frac{1}{\cos\beta_2\cos\gamma_2}\right) + \Delta\varphi\right]
\end{aligned}
\tag{2.29}
$$

One can distinguish between *constructive* and *destructive* interference. Constructive interference occurs when the phase difference between the two waves is

a multiple of 2π.

$$|\Delta\phi| = 2n\pi \qquad \text{with } n = 0, 1, 2, ...$$

In that case, wave peaks overlap with one another. This happens when the cosine term becomes:

$$\cos\left[k_z r\left(\frac{1}{\cos\alpha_1 \cos\gamma_1} - \frac{1}{\cos\alpha_2 \cos\gamma_2}\right) + \Delta\varphi\right] = 1$$

Destructive interference is obtained when the cosine-term becomes 0. The phase difference between the two waves is:

$$|\Delta\phi| = (2n + 1)\frac{\pi}{2} \qquad \text{with } n = 0, 1, 2, ...$$

The resulting amplitude of two waves becomes smaller and in case of $A_{01} = A_{02}$ nullify each other. In order to obtain the maximum contrast of the recorded interference pattern the following conditions need to be fulfilled:

· The polarization-states of both interfering waves need to be matched.

· The same path-length is required for both waves.

· The intensity of both waves should be the same.

· Both waves need to be spatially filtered to obtain a Gaussian beam profile, which results in noise reduction.

· Only light from the object should contribute to the recorded object-wave. The recording of light scattered or reflected by other objects needs to be avoided.

· The dynamic range of the camera should be fully used in conjunction with subtraction of dark-measurement and avoiding over-exposure.

Having taken all these parameters into account should then enable the recording of an interferogram with the best possible contrast.

2.5 Coherence

In order to detect interference a light source of sufficient coherence needs to be used. Coherence is defined as the stability of the phase of a wave in space and time. Laser light consists of waves of finite length. An external energy source, such as Xenon flashlamp used for the Ruby laser, pumps energy into the laser medium. This results in electrons being moved from a ground energy level E_1 to a higher energy level E_2. We assume a very simplified case of a two-energy band model, as shown in Fig. 2.6. The electrons remain at that higher energy level, namely the meta-stable energy-level due to its long lifetime, for a few microseconds. This results in a higher number of atoms being in the excited state than in the ground state. An impinging wave causes all the electrons to fall back to the ground state. The energy released is transformed into light waves which have the same phase and the same propagation direction as the impinging
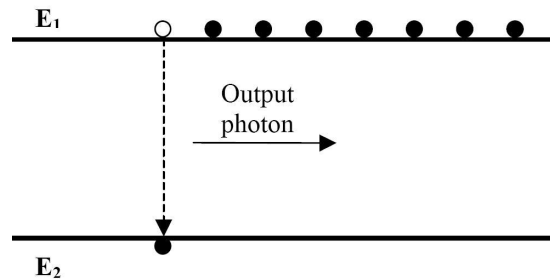
Figure 2.6: Creation of a photon by electron-jump from energy-level E_1 to E_2

wave. The wavelength λ of the emitted light is given by:

$$E_1 - E_2 = h\nu = h\frac{c}{\lambda} \quad \Rightarrow \quad \lambda = \frac{hc}{E_1 - E_2} \qquad (2.30)$$

Where h is Planck's constant. Inside the laser cavity, the waves which are perpendicularly orientated to the two cavity mirrors are then reflected back and forth. One of the mirrors is semi-transparent to permit light to leave the laser cavity. The reflected light is phase-matched-amplified by induced emission within the cavity. This amplification approaches a limit at which a standing wave is created. The nodes of the standing wave are located on the mirror surfaces. The relationship which relates the laser cavity length L and the wavelength λ, can be expressed by:

$$\lambda_n = \frac{2L}{n} \quad \text{(where n=1,2,3...)} \qquad (2.31)$$

As a result the emitted light consists of a spectrum with equidistant sharp lines, which are also known as longitudinal laser modes. These laser modes correspond to wavelengths of the standing wave, which are amplified by constructive interference within the laser-cavity. Other wavelengths are suppressed by destructive interference. These longitudinal laser modes are within the spectral-profile that would result without having a laser-cavity. In that manner the back and forth reflection in the laser cavity is the cause of temporal and spatial coherence. *Temporal coherence* describes the phase correlation between different points of a single wave in time. It can be measured by using a Michelson-interferometer as shown in Fig. 2.7(a). In Section 2.1 the harmonic wave equation was presented, see Eq. 2.10. Considering two such waves of matched amplitude and wavelength superimposing each other, results in the creation of a fringe pattern. If the path length of one of the beams is changed with respect to the other a lower contrast

V is obtained.

$$V = \frac{I_{max} - I_{min}}{I_{max} + I_{min}} \tag{2.32}$$

Increasing the path-length difference results in no contrast being recorded, see Fig. 2.7(b). The coherence length l_c is defined by the point at which V drops to e^{-1}.
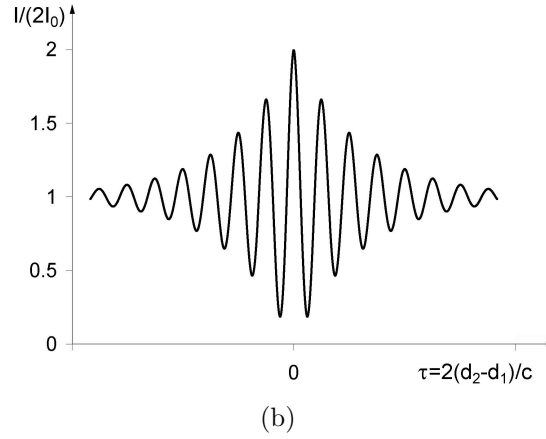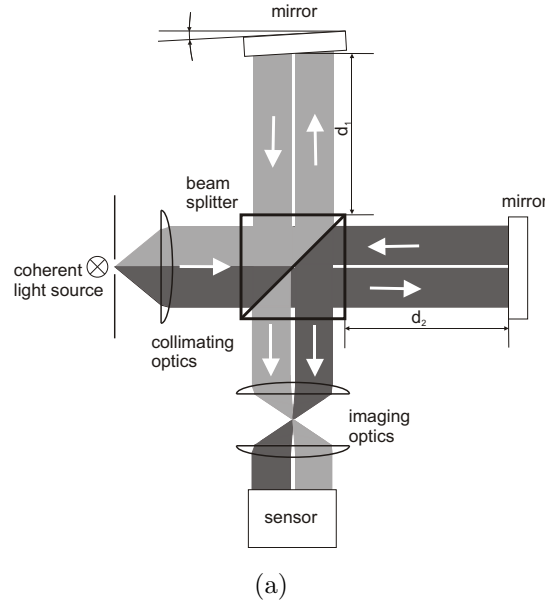
Figure 2.7: (a) Interferometric setup for measuring the coherence length l_c, (b) reduced contrast for increasing differences between the path lengths of the two interfering beams

It corresponds to twice the path-length difference, since the light travels the same way twice. l_c can be related to the coherence time τ_c by:

$$l_c = \tau_c c \tag{2.33}$$

For the Helium Neon laser used in this thesis a coherence length l_c of 23 cm has been measured. Another important measure of temporal coherence is the spectral width $\Delta\nu_c$, which can be calculated according to Saleh and Teich (1991) by:

$$\Delta\nu_c = \frac{1}{\tau_c} \tag{2.34}$$

The counterpart to the temporal coherence is the *spatial coherence* in space. This refers to the ability of laterally separated light point sources to interfere. The spatial coherence can be measured with the *Young's double slit experiment*. A wave emitted at the source S_0 travels to the small aperture A_1, see Fig. 2.8. At the aperture A_1 the incident wave generates a spherical wave in accordance with *Huygens' principle*. After traveling a long distance to the second aperture A_2 the generated wave at A_1 appears as an almost plane wave. The distance at which this approximation is valid will be discussed in Section 2.7.3. Two new waves are generated at the apertures S_1 and S_2, separated by the distance g . At a distance d from the plane A_2 the interference pattern is recorded on a screen.
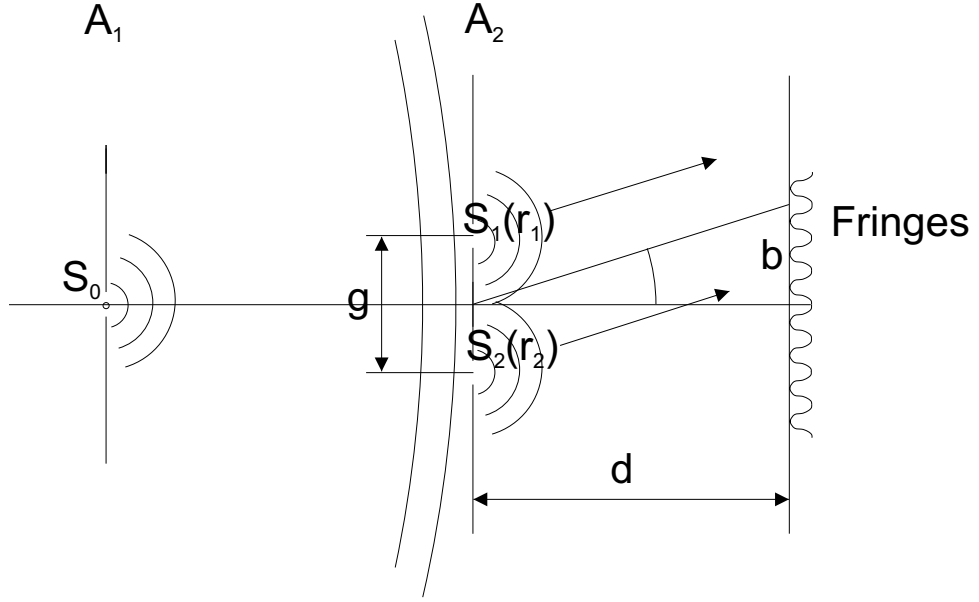
Figure 2.8: Young's double slit experiment

The intensity profile on the screen is described by the formula, taken from Hecht (2005):

$$I(b) = 4I_0 \cos^2\left(\frac{\pi g b}{\lambda d}\right) \tag{2.35}$$

The interference images shown in Fig. 2.9, were calculated with λ=632.8 nm, d=1 m and g=0.4 mm, 0.6 mm and 1 mm, respectively. A measure for the degree of spatial coherence is the *complex degree of coherence* $\gamma_{12}(r_1, r_2, \tau)$. It is linked
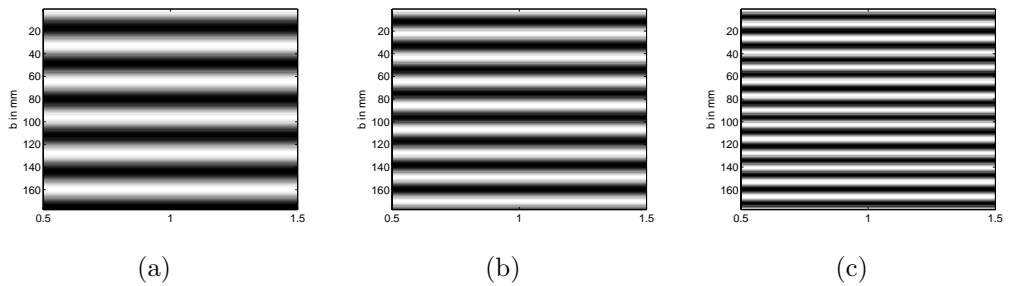
Figure 2.9: Intensity profiles for, (a) g=0.4 mm, (b) g=0.6 mm, and (c) g=1 mm

Table 2.3: Different light sources used in interferometry and their coherence properties

Source	l_c in mm	$\Delta\nu_c$ in Hz	output power in W
White light (400-800 nm)	$\approx 1 \cdot 10^{-3}$	$3.75 \cdot 10^{14}$	≈ 10
Low pressure sodium lamp	0.6	$5 \cdot 10^{11}$	10...180
Light emitting diode (LED)	0.05	$1.5 \cdot 10^{13}$	cw: ≤ 5 pulse: ≤ 10
Diode laser unstabilized	≈ 1	$21 \cdot 10^9$	$> 3 \cdot 10^3$
Diode laser stabilized	$\geq 1 \cdot 10^3$	$2 \cdot 10^7$	≈ 0.08
HeNe (632.8 nm) unstabilized	≈ 200	$1.5 \cdot 10^9$	$10^{-4}... 0.1$
HeNe stabilized (632.99 nm)	$\approx 3 \cdot 10^5$	$1.0 \cdot 10^6$	$2 \cdot 10^{-3}$
Pulsed ruby laser	$\geq 1 \cdot 10^3$	$3.3 \cdot 10^{11}$	10^{11}
Pulsed Nd:YAG	$\geq 1 \cdot 10^3$	$1.2 \cdot 10^{11}$	10^{10}

to the contrast of the recorded interference pattern.

$$\gamma_{12}\left(r_1, r_2, \tau\right) = \frac{\Gamma_{12}\left(r_1, r_2, \tau\right)}{\sqrt{\Gamma_{11}\left(r_1, 0\right) \Gamma_{22}\left(r_2, 0\right)}} \tag{2.36}$$

$\Gamma_{12}\left(r_1, r_2, \tau\right)$ is called the *mutual coherence function*.

$$\Gamma_{12}\left(r_1, r_2, \tau\right) = \left\langle \sqrt{I_1\left(r_1, t+\tau\right)}\sqrt{I_2\left(r_2, t\right)^*} \right\rangle \tag{2.37}$$

$$\Gamma_{11}\left(r_1, \tau\right) = \left\langle \sqrt{I_1\left(r_1, t+\tau\right)}\sqrt{I_1\left(r_1, t\right)^*} \right\rangle \tag{2.38}$$

$$\Gamma_{22}\left(r_2, \tau\right) = \left\langle \sqrt{I_2\left(r_2, t+\tau\right)}\sqrt{I_2\left(r_2, t\right)^*} \right\rangle \tag{2.39}$$

Where $\langle . . .\rangle$ denotes the cross-correlation function. The coherence length, spectral width, output power and wavelength of some selected light sources are shown in Table 2.3. The information shown in Table 2.3 has been collected from Saleh and Teich (1991), Schröder and Treiber (2007) and various supplier web-pages in order to update the information, e.g. SIOS GmbH. (2010)

[†], Apollo Instrument Inc. (2010)[‡] and Ondax Inc. (2010) [§]. In conclusion, the temporal coherence determines the axial extension of the object under investigation. The spatial coherence determines the lateral extension of the object under investigation. Hence macroscopic objects need to be investigated with a light source of increased temporal and spatial coherence. In addition to temporal and spatial coherence, other properties of a coherent light source are:

- narrow $\Delta\nu_c$

- light emitted from a laser is almost one directional

- the power density is higher than for incoherent light

- more stable amplitude

- ultra-short light pulses of 10^{-15}s can be generated

- it can be focused to a smaller spot than incoherent light

These benefits support the introduction of laser light in many different fields such as laser cutting Charles Day Ltd. (2010), laser welding TWI Ltd. (2010), optical trapping Dholakia and Lee (2008) and interferometry. However, there are also drawbacks to application of coherent light. For example a rough surface illuminated by laser light results in the occurrence of speckle pattern, which reduces the resolution of the recorded interferogram. Moreover, particles which might be floating in the optical path generate diffraction pattern which disturbs the recorded interferogram. Hence, arrangements need to be made to reduce this kind of environmental influences, e.g. optical table enclosure system as shown in Appendix C.2, introduction of optical fibres.

[†]reference for stabilized HeNe
[‡]reference for laser diode
[§]reference for stabilized laser-diode

2.6 Digital Recording Devices

(a)

(b)
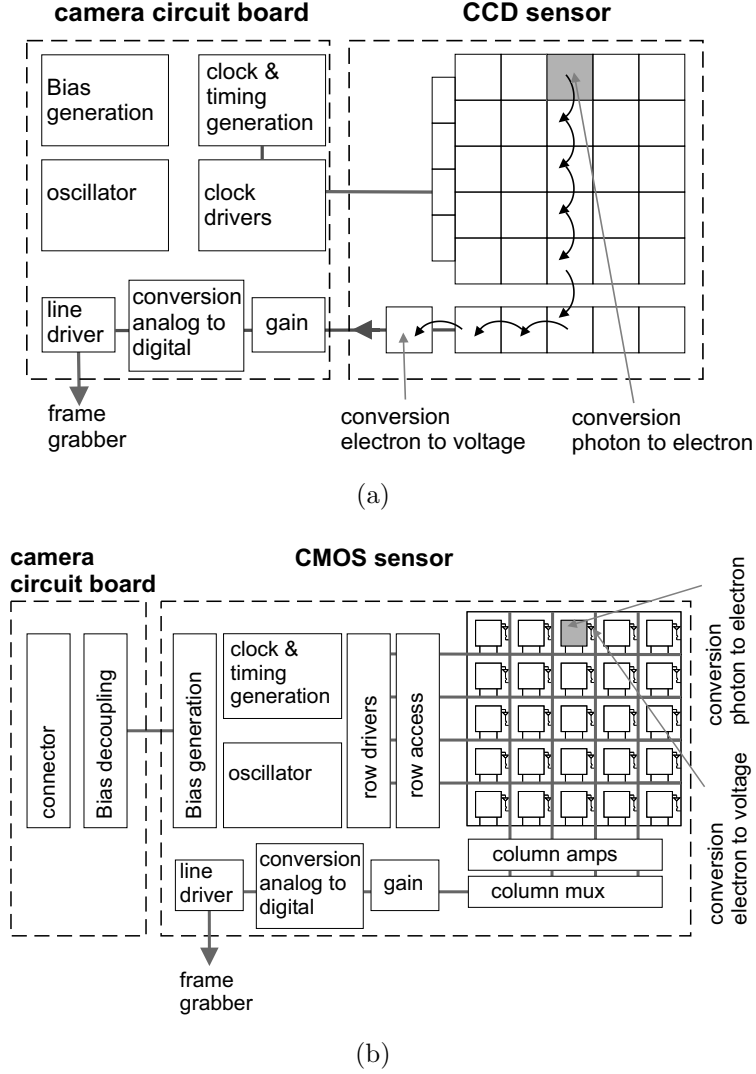
Figure 2.10: Sketch of working principle of, (a) a CCD sensor, and (b) a CMOS sensor

In optical holography the hologram is recorded on a holographic plate. Digital holograms are recorded on digital receivers which enable a faster and simplified image acquisition and processing. Generally CCD cameras and CMOS cameras are used for the recording of digital holograms. With a CCD camera the photon energy is converted into an electrical charge, which is then read out by transferring the charge down the pixel-column to a common output register, see Fig.

Table 2.4: Comparison CCD vs. CMOS

Parameter	CCD	CMOS
Costs	expensive	comparably less expensive
Electronics noise	low	moderate
Fill factor	$\leq100\%$	typically $\leq60\%$
Light sensitivity	high sensitivity	lower than CCD
Power consumption	10 times higher than CMOS	low
Recording speed	≤100 Hz	high speed kHz
Resolution	≥143 lp/mm (Sony ICX625 with 3.5 μm pixel-size)	≥ 357 lp/mm (Aptina MT9E013 with 1.4 μm pixel-size)
Smearing	line transfer smearing	no smearing
Uniformity of pixel-response	homogenous	less homogenous

2.10(a). Here the electrical charge is converted into voltage and is then sent to the camera-circuit board. A CMOS camera instead performs the charge to voltage conversion at each individual pixel by an attached transistor, see Fig. 2.10(b). These differences in sensor architecture have significant consequences for the sensor capabilities and limitations. A comparison of both methods has been conducted partly based on Litwiller (2001). The results of this comparison are shown in Table 2.4. It is based on the current state of the art technology available (March 2010). It is not easy to judge which of the two sensors is best. The best suited sensor technology depends on the particular application.

2.7 Approximation of Light Propagation

Different models are used to describe the propagation of light from the object-plane u(x,y) to the hologram-plane u'(x',y'). These propagation models are based on approximations made with respect to the wave-front curvature. They are applicable at different distances between object-plane and the hologram-plane. One can distinguish between the Rayleigh-Sommerfeld diffraction formula, the Fresnel-approximation, which is also known as the Near-field diffraction, and the Fraunhofer-approximation, known as Far-field diffraction.

2.7.1 Rayleigh-Sommerfeld Diffraction Formula
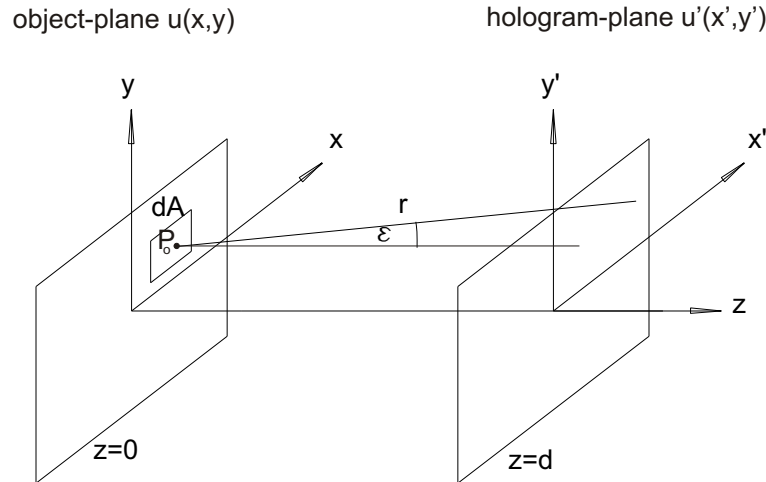
Figure 2.11: Propagation of light from the object-plane to the hologram-plane

At each object point an incident light waves generates a propagating elementary spherical wave according to Huygens' principle. A single spherical wave can be considered to originate from an area element dA, which represents a small surrounding of an object point x_o as shown in Fig. 2.11. The spherical waves originating from all object points overlap with another to unify to a common complex wave field in the hologram-plane. Hence an integration of the light

propagating from the area segments needs to be performed.

$$u(x', y') \propto \frac{1}{i\lambda} \int\limits_{-\infty}^{\infty} \int\limits_{-\infty}^{\infty} u(x, y) \frac{\exp{(ikr)}}{r} \cos\varepsilon \, \mathrm{d}A \qquad (2.40)$$

Where ε denotes the angle defined by the distance (d) and radius (r):

$$\cos\varepsilon = \frac{d}{r} \qquad (2.41)$$

The angle ε is reproduced by the intersection of the hologram plane with the tangential plane of the elementary spherical wave. For a large recording distance $d \cos\varepsilon$ can be dropped in Eq. 2.40. The term $\frac{\exp(ikr)}{r}$ indicates the *impulse response of free space propagation* of light (h_d). It represents the free space propagated spherical wave, which needs to be divided by its radius (r) due to conservation of energy. Hence the intensity recorded on a unit area decreases with increasing distance by $1/(\lambda^2 r^2)$, but the integrated intensity over the entire spherical wave remains constant. The factor ik is responsible for a phase shift of $\frac{\pi}{2}$ in all points of the object plane and can therefore be neglected. The radius can be substituted with the coordinates in the object-plane and hologram-plane.

$$r = \sqrt{(x' - x)^2 + (y' - y)^2 + d^2} \qquad (2.42)$$

Hence the impulse-response becomes:

$$h_d(x', y', x, y) = \frac{\exp\left[ik\sqrt{(x' - x)^2 + (y' - y)^2 + d^2}\right]}{\sqrt{(x' - x)^2 + (y' - y)^2 + d^2}} \qquad (2.43)$$

$$= h_d(x' - x, y' - y)$$

Eq. 2.43 indicates that the Rayleigh-Sommerfeld diffraction integral is shift-invariant and can hence be simplified by a convolution of the initial light distribution in the object-plane $u(x, y)$ with the impulse response h_d.

$$u(x', y') = u(x, y) \otimes h_d(x', y') = \mathcal{F}^{-1} \left[\mathcal{F} \{u(x', y')\} \cdot \mathcal{F} \{h_d(x', y')\} \right] \qquad (2.44)$$

The symbol $\otimes$ denotes the convolution operator. Eq. 2.44 can be simplified numerically by inserting the transfer-function H_d, which represents the Fourier-transformation of the impulse response ($H_d = \mathcal{F} \{h_d\}$). The transfer-function according to Goodman (1996) is:

$$H_d(\nu_x, \nu_y) = \begin{cases} \exp\left[i2\pi \frac{d}{\lambda} \sqrt{1 - (\lambda\nu_x)^2 - (\lambda\nu_y)^2} \right] & , \quad \sqrt{\nu_x^2 + \nu_y^2} < \frac{1}{\lambda} \\ 0 & , \quad \text{otherwise} \end{cases} \qquad (2.45)$$

H_d is a circular symmetric complex function and can be regarded as a linear spatial filter with a certain bandwidth. The filter blocks spatial frequencies larger than the circular region defined by the radius $\frac{1}{\lambda}$.

2.7.2 Fresnel-Approximation or Near-Field Diffraction

In the Fresnel-approximation the spherical wavefront described by the Rayleigh-Sommerfeld diffraction integral is replaced by a parabolic wavefront, as shown in Fig. 2.12(a). For the Fresnel-approximation the assumption $(x' - x)^2 + (y' - y)^2 \ll d^2$ is made. r in Eq. 2.42 is rewritten by taking d outside the square root:

$$r = d\sqrt{1 + \left[\frac{(x' - x)}{d} \right]^2 + \left[\frac{(y' - y)}{d} \right]^2} \qquad (2.46)$$

For r appearing in the denominator of Eq. 2.40 all terms apart from d can be dropped without introducing an error:

$$r \approx d \tag{2.47}$$

Whereas changes of a fraction of a wavelength can produce significant errors in the exponential term. The phase term within the square root is multiplied with the wave-number (k). The wave-number for visible light (λ=350-700 nm) ranges between $1.8 \cdot 10^7$ m^{-1} and $0.8 \cdot 10^7$ m^{-1}. Thus a more precise approximation must be found for the exponential term. The root expression in Eq. 2.46 can be expressed by a binomial series.

$$\sqrt{1+a} = 1 + \frac{1}{2}a - \frac{1}{8}a^2 + \frac{1}{16}a^3 - \ldots \tag{2.48}$$

Only the first two terms in Eq. 2.48 are taken into account and the parameter a is replaced by $\left(\left[\frac{(x'-x)}{d} \right]^2 + \left[\frac{(y'-y)}{d} \right]^2 \right)$. This results in:

$$r = d \left[1 + \frac{1}{2} \left(\frac{x'-x}{d} \right)^2 + \frac{1}{2} \left(\frac{y'-y}{d} \right)^2 \right] \tag{2.49}$$

With

$$\frac{\cos(\varepsilon)}{r} \approx \frac{1}{d}$$

$u(x', y')$ can be calculated as:

$$u(x', y') \approx \frac{\exp{(ikd)}}{i\lambda d} \int\limits_{-\infty}^{\infty} \int\limits_{-\infty}^{\infty} u(x, y) \exp\left[\frac{i\pi}{\lambda d}\left\{(x' - x)^2 + (y' - y)^2\right\}\right] dx\, dy$$

$$\approx \frac{\exp{(ikd)}}{i\lambda d} \exp\left[\frac{i\pi}{\lambda d}\left(x'^2 + y'^2\right)\right] \int\limits_{-\infty}^{\infty} \int\limits_{-\infty}^{\infty} u(x, y) \exp\left[\frac{i\pi}{\lambda d}\left(x^2 + y^2\right)\right]$$

$$\cdot \exp\left[\frac{-i2\pi}{\lambda d}\left(x'x + y'y\right)\right] dx\, dy$$

$$(2.50)$$

From Eq. 2.50 it follows that the light distribution in the object plane is multiplied with the impulse response of the Fresnel-approximation, which is represented by the chirp-function $\exp\left[\frac{i\pi}{\lambda d}\left(x^2 + y^2\right)\right]$. Aside from multiplicative amplitude and phase factors that are independent of x and y the light distribution in the hologram-plane u'(x',y') is obtained by a Fourier transformation of $u(x,\ y) \exp\left[\frac{i\pi}{\lambda d}\left(x^2 + y^2\right)\right]$. Eq. 2.50 describes a parabolic-wavefront approximation of the previously spherical-wavefronts described by Eq. 2.40. This imposes some restrictions with respect to the validity of the Fresnel-method. The Fresnel approximation is valid if the phase difference arising from the higher orders of the binomial series are a lot smaller than one radian and therefore negligible. This conditions results in:

$$kd\frac{a^2}{8} = \frac{\pi}{4\lambda}d\left[\left(\frac{x' - x}{d}\right)^2 + \left(\frac{y' - y}{d}\right)^2\right]^2 \gg 1rad \qquad (2.51)$$

This results in a minimum recording distance d:

$$d \gg \sqrt[3]{\frac{\pi}{4\lambda}\left[(x' - x)^2 + (y' - y)^2\right]^2} \qquad (2.52)$$

For an assumed object of 12 mm x 12 mm (x=y=-6 mm), a camera pixel size of 6.45 μm^2, pixel-number $N = 1392$ and $M = 1024$ (x'=1392·6.45/2 μm;

y'=1024·6.45/2 μm), and a HeNe-Laser (632.8 nm) the minimum recording distance at which the Fresnel-method is valid is 363 mm.

2.7.3 Fraunhofer Approximation or Far Field Approximation

The Fraunhofer model represents a stronger simplification by replacing the parabolic wavefront of the Fresnel-approximation with a plane-wavefront, see Fig. 2.12(a). The wavefront can be considered to be plane when the parabolic phase term $\frac{\pi}{\lambda d}\left(x^2 + y^2\right)$ in Eq. 2.50 becomes a lot smaller than one radian. This condition results in a minimum recording distance :

$$d >> k\frac{x^2 + y^2}{2} \tag{2.53}$$

The light distribution in the hologram-plane u'(x',y') is calculated by applying the Fourier transformation to the object's light distribution only.

$$u(x', y') \propto \frac{\exp\left(ikd\right)}{i\lambda d} \exp\left[\frac{i\pi}{\lambda d}\left(x'^2 + y'^2\right)\right] \int\limits_{-\infty}^{\infty} \int\limits_{-\infty}^{\infty} u(x, y) \exp\left[\frac{i2\pi}{\lambda d}\left(x'x + y'y\right)\right] \mathrm{d}x\,\mathrm{d}y \tag{2.54}$$

 For the Fraunhofer propagation model a minimum distance of 357.45 m is required, taking into account the same setup parameters as previously used for the Fresnel propagation-model in Section 2.7.2. Fig. 2.12 shows the different propagation models and the assumptions made in respect to the shape of the wavefront for each model. Different applications and setup geometries for each model are the consequences of this consideration.

(a)

(b)
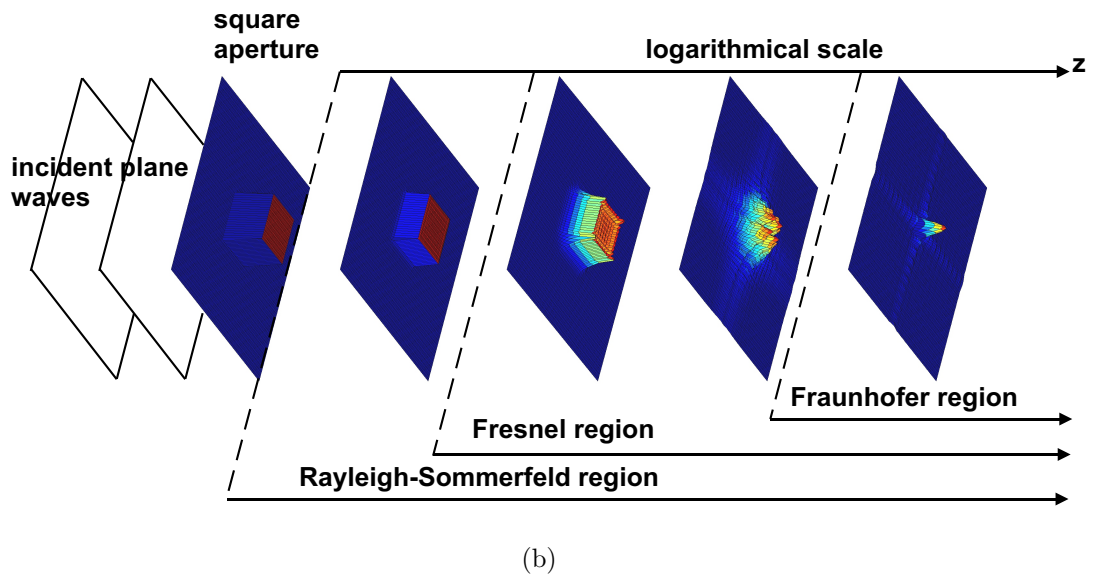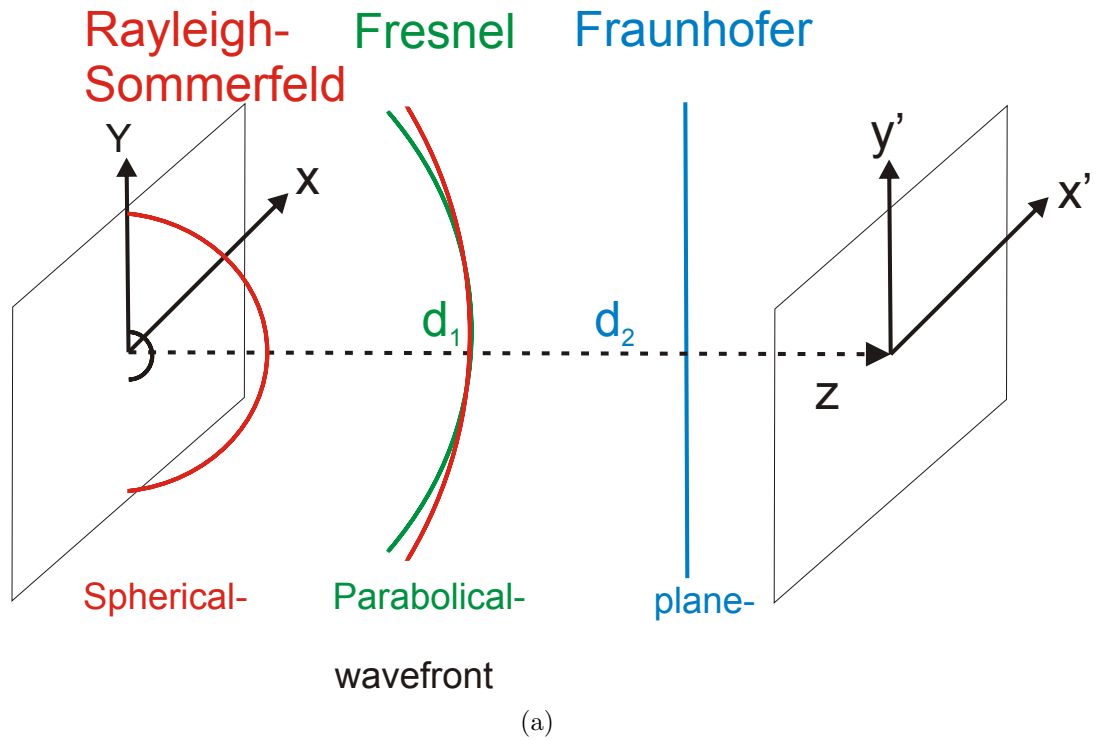
Figure 2.12: (a) Distances and corresponding wave-front for different propagation methods, (b) diffraction pattern of a rectangular aperture at different distances

2.7.4 Definition of Sign of Phase

A converging spherical wave which propagates in the z-direction has a positive phase. Each consecutive phase envelope is obtained by a forward propagation in time. A plane wave is set to have a positive phase if the wave-vector $\vec{k}$ points away from the optical axis.

The contrary case accounts for the definition of a negative phase. A converging spherical wave can be treated as a light-wave which back-propagates in time. A negative or reversing phase in holography refers to the reconstruction of the virtual image and a positive phase to the reconstruction of the real image. Fig. 2.13 shows the wavefront shape (spherical-wave) and geometry (plane-wave) for positive and negative phase.
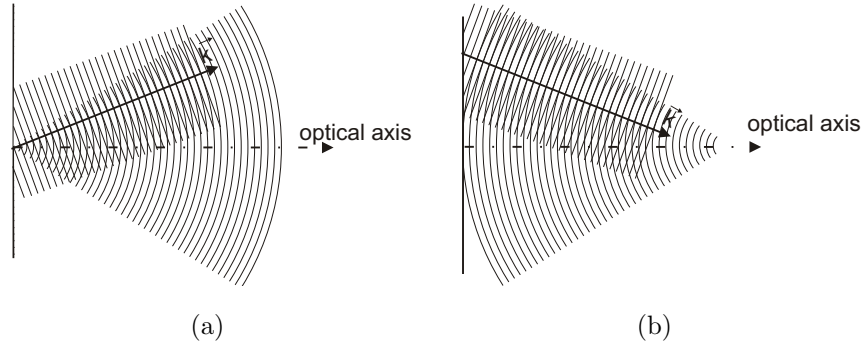
Figure 2.13: Spherical-wave and plane-wave with (a) positive phase and (b) negative phase

2.8 Conclusion

Basic terms required to understand holography were explained in this chapter. The terms coherence, interference, intensity and digital recording devices have been explained to support the understanding of the recording process. The recorded hologram is numerically reconstructed by applying the diffraction integral described in this chapter. Diffraction occurs when light strikes an obstacle

whose dimension is in the range of the wavelength. The observed light distribution forms a pattern of dark and bright regions. Diffraction is explained using Huygens' principle: *"Every point on a propagating wavefront serves as the source of spherical secondary wave, such that the wavefront at some later time is the envelope of these secondary wavefronts"*. Huygens' principle can mathematically be described by the propagation models, which were explained in this chapter. In that manner the fundamental knowledge was presented. This knowledge will be used to obtain the best possible setup in terms of fringe contrast and to reduce the impact of environmental influences. Moreover, the digitized numerical calculations for the reconstruction of digital holograms, which will be presented in Chapter 3, is based on the diffraction models discussed in Section 2.7.

CHAPTER 3

Reconstruction Methods

3.1 Introduction

In optical holography, reconstruction is performed by illuminating the developed holographic plate with the reference-wave as previously discussed in Section 1.1. This approach is not applicable for holograms which have been recorded utilizing digital receivers such as CCD or CMOS cameras. For simplification purposes only the CCD camera will be considered in subsequent explanations. Different options exist for the reconstruction of digitally recorded holograms using current technology:

    i displaying the hologram on a spatial light modulator (SLM) or similar means and illuminating it with the reference beam,

    ii simulating the reconstruction process numerically.

The first approach possesses the drawback of limited spatial resolution and disturbing diffraction effects which are caused by the SLM's pixelization. Furthermore it is not possible to reconstruct the phase in an unambiguous manner.

Therefore this chapter focuses on the study of the most commonly applied numerical reconstruction techniques in digital holography. Fig. 3.1 shows dif-

ferent planes which are involved in the optical and numerical wave-propagation process. In the x-y object plane, light impinges on the object, which results in the generation of spherical waves according to Huygens' principle. The interference pattern of the overlapping spherical object waves and the reference-wave is stored in the hologram plane on a CCD. Numerical methods are applied in order to perform the reconstruction of the digitally recorded holograms. Different numerical reconstruction techniques exist with respect to the object size and recording distance used in the experiment. One can distinguish between the **Rayleigh-Sommerfeld Diffraction Integral**, the **Fresnel-method** and the **Fourier-method**. Their corresponding diffraction equations have been described in Section 2.7. The digitization of the reconstruction algorithms were performed utilizing MATLAB and its implemented functions.
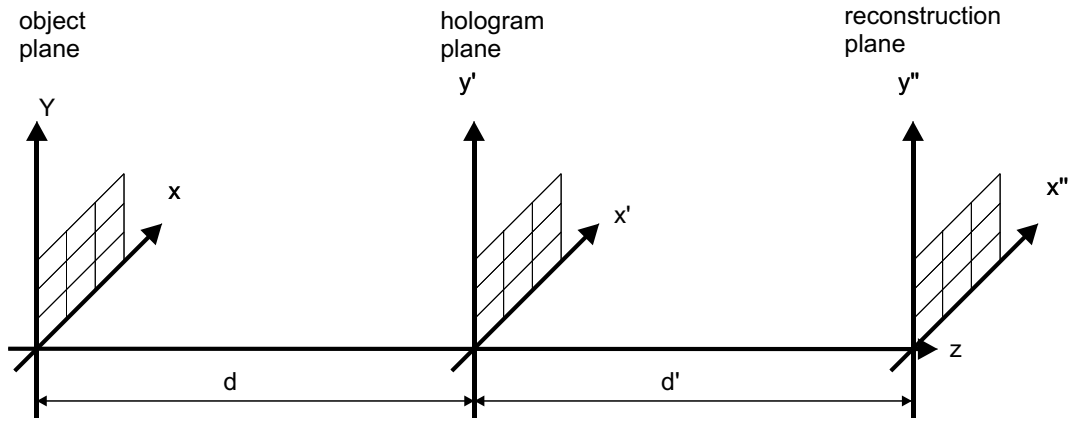
Figure 3.1: Nomenclature of coordinates used for the holographic recording and reconstruction process

3.2   Rayleigh-Sommerfeld Diffraction Integral

The Rayleigh-Sommerfeld Diffraction integral was already presented in Section 2.7. Its notation for the reconstruction including the reference-wave u_r is.

$$u(x'', y'') \propto \frac{1}{i\lambda} \int\limits_{-\infty}^{\infty} \int\limits_{-\infty}^{\infty} u(x', y') \cdot u_r^*(x', y') \frac{\exp\left[ik\sqrt{(x'' - x')^2 + (y'' - y')^2 + d'^2}\right]}{\sqrt{(x'' - x')^2 + (y'' - y')^2 + d'^2}} \mathrm{d}x' \mathrm{d}y'$$

$$(3.1)$$

Where $u_r^*(x', y')$ indicates the complex conjugated reference-wave. A constant phase for u_r is obtained when a plane reference-wave is used. For this special case, u_r does not need to be taken into account for the calculation of the numerical reconstruction. The numerical effort required to implement the Rayleigh-Sommerfeld diffraction integral using discrete values can be minimized by utilizing a digitized transfer-function, as shown in Eq. 3.2.

$$u''(l, m) = \mathcal{F}^{-1}[\mathcal{F}\left\{u'(l, m) \cdot u_r^*(l, m)\right\} \cdot H_d(\nu_{x'}, \nu_{y'})] \tag{3.2}$$

Where l and m are the counters in x and y directions, respectively, and $\mathcal{F}$ and $\mathcal{F}^{-1}$ denote the two dimensional Fourier transformation and inverse Fourier transformation, which can be implemented using a Fast Fourier Transform (FFT) algorithm. $H_d(\nu_{x'}, \nu_{y'})$ indicates the transfer-function, which was represented in Eq. 2.45. $H_d(\nu_{x'}, \nu_{y'})$ needs to be evaluated at its discrete spatial frequencies:

$$\nu_{x'} = \frac{l_\nu - 1}{N\Delta x'} \qquad \text{and} \qquad \nu_{y'} = \frac{m_\nu - 1}{M\Delta x'} \tag{3.3}$$

Where N x M denotes the number of pixels, $\Delta x'$ the pixel-size and l_ν and m_ν are the counters in the Fourier domain, which range from $l_\nu = 1...N$ and $m_\nu = 1...M$. The digitized transfer-function is shown in Eq. 3.4.
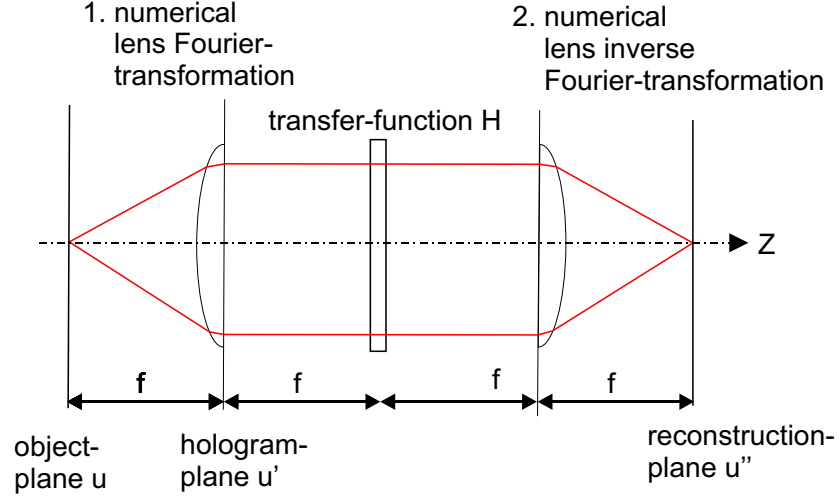
Figure 3.2: Optical model for Rayleigh-Sommerfeld Convolution integral

$$H_d(l_\nu, m_\nu) = \exp\left[i\frac{2\pi d}{\lambda}\left\{1 - \left(\lambda\frac{l_\nu - N/2 - 1}{N\Delta x'}\right)^2 \right.\right.$$
$$\left.\left. - \left(\lambda\frac{m_\nu - M/2 - 1}{M\Delta x'}\right)^2\right\}^{\frac{1}{2}}\right] \tag{3.4}$$

A problem encountered with the implementation of the numerical code in MAT-
LAB is that its initial matrix starting point is the upper left corner instead of the
center. Therefore, the initially defined spatial frequencies, see Eq. 3.3, had to
be shifted by half the sensor width for both directions $(l - N/2 - 1)$. Fig. 3.2
shows an optical model for the optical recording process and numerical recon-
struction process. Light from the object passes through a 4-f system by which it
is convolved with the transfer-function to result in a sharp image-point. Due to
applying a convolution integral the pixel size in the reconstruction plane $\Delta x''$ and
the hologram plane $\Delta x'$ are matched. Therefore care needs to be taken that the
object dimensions do not exceed the camera-sensor dimensions. Otherwise parts
of the object exceeding the sensor's dimension are convolved in the reconstructed
hologram, which results in a disturbed reconstruction. There are ways which
allow the recording of objects larger than the sensor dimensions of the camera.
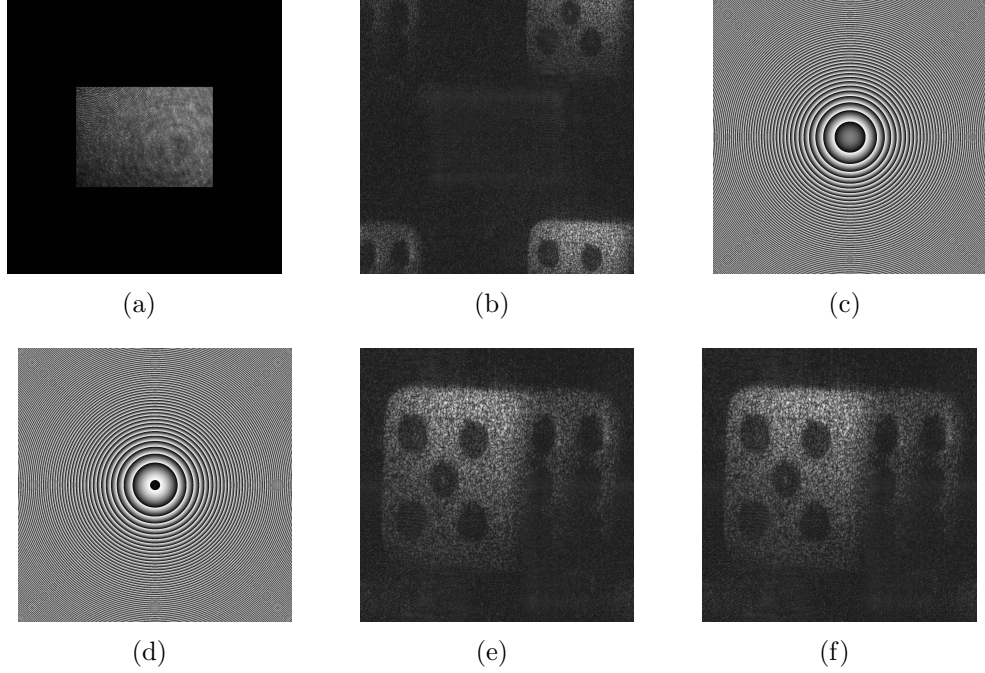
Figure 3.3: (a) Recorded 2800x2800 zero-padded intensity hologram (b) reconstruction with phase 2800x2800 pixels, (c) phase for a parabolic lens, (d) phase for a spherical lens, (e) corresponding reconstruction of (c) by applying a shifted transfer-function and $\Gamma = 0.7$ (1392x1392), (f) corresponding reconstruction of (d) with analogue parameters

3.2.1 Zero-padding

One approach is based on *zero-padding*. The recorded hologram is numerically extended by adding pixels of zero intensity to it as shown in Fig. 3.3(a). In case the object was not centered on the optical axis in the recording process, the reconstruction displays the image information split into different parts, which appear at the edge of the reconstruction, see Fig. 3.3(b). This effect is due to the nature of the convolution process and can be avoided by applying a shift in the reconstruction process so that the reconstructed image becomes centered. Schnars and Jueptner (2005) and Kreis (2005) applied a shift to the impulse response, which then needs to be two dimensionally Fourier-transformed in order to obtain the transfer-function. Alternatively, the shift can directly be applied to the transfer-function, which is less time consuming than applying it to the

impulse response. Hence, the shift needs to be converted into a corresponding shift in the frequency domain. From the Fourier-relationship follows that a pixel-size in the Fourier-domain is described as:

$$\Delta x'' = \frac{\lambda d'}{N\Delta x'} \tag{3.5}$$

In order to obtain the magnitude of the shift s_x Eq. 3.5 is differentiated in respect to $\Delta x'$:

$$\frac{\partial \Delta x''}{\partial \Delta x'} = -\frac{\lambda d}{N\Delta x''^2} \tag{3.6}$$

In $\nu_{x'}$-direction a shift s_x is applied which represents a multiplicative phase factor $-\frac{N\Delta x'^2}{d\lambda}$. In a similar manner the shift s_y is applied in the $\nu_{y'}$ direction. Taking into account the shifts s_x and s_y results in a rewritten Eq. 3.4:

$$H_d(l_\nu, m_\nu) = \exp\left[i\frac{2\pi d}{\lambda}\left\{1 - \left(\lambda\frac{l_\nu - N/2 - 1 - s_x\frac{N\Delta x'^2}{d\lambda}}{N\Delta x'}\right)^2\right.\right.$$
$$\left.\left. - \left(\lambda\frac{m_\nu - M/2 - 1 - s_y\frac{M\Delta x'^2}{d\lambda}}{M\Delta x'}\right)^2\right\}^{\frac{1}{2}}\right] \tag{3.7}$$

Results for the reconstructed intensity of a phase hologram, with and without shifting the transfer-function, are shown in Fig. 3.3.

3.2.2 Numerical Lens

Another method, which enables the recording of objects exceeding the camera's sensor dimension is the introduction of a *numerical lens* of a certain magnification Γ' between zero and one. The reconstruction distance d' needs to be adjusted with respect to Γ', which results in:

$$d' = d \cdot \Gamma' \tag{3.8}$$

Where d indicates the recording distance. The numerical formulation of the lens equation for a plano-convex lens with spherical and parabolic lens-surface have been derived in Appendix A.2. Its digitized notation for a spherical lens surface is:

$$L(l,m) = \exp\left[\frac{i2\pi f\,(n_{Lens}-1)^2}{\lambda} \cdot \sqrt{1 - \frac{\Delta x'^2\,(l-N/2-1)^2 + (m-M/2-1)^2}{f^2\,(n_{Lens}-1)}}\right] \tag{3.9}$$

And for a parabolic approximation is:

$$L(l,m) = \exp\left[\frac{-i\pi\Delta x'^2}{\lambda f}\left\{(l-N/2-1)^2 + (m-M/2-1)^2\right\}\right] \tag{3.10}$$

With

$$f = \frac{d\cdot d'}{d+d'} \tag{3.11}$$

It needs to be pointed out that Eq. 3.10 refers to the Fresnel region. Hence the focal length f needs to have a certain value in order to be valid, see Eq. 2.52. Otherwise the image quality of the numerical reconstruction could be degraded due to introduction of phase errors. The final equation for the convolution integral with a numerical lens L is:

$$u''(l,m) = \mathcal{F}^{-1}[\mathcal{F}\{u'(l,m)\cdot u_r(l,m)^\star \cdot L(l,m)\}\cdot H_{d'}(\nu_{x'},\nu_{y'})] \tag{3.12}$$

The intensity representation of the transfer function is shown in Fig. 3.4(a). Only a finite rectangular area with values different from zero contributes to the reconstruction. The same rectangular area restricts the phase data. The phase data outside the rectangle correspond to numerical noise and hence does not contribute to the transfer of high spatial frequencies according to Kreis (2005). In that manner the transfer-functions acts like a low-pass filter.
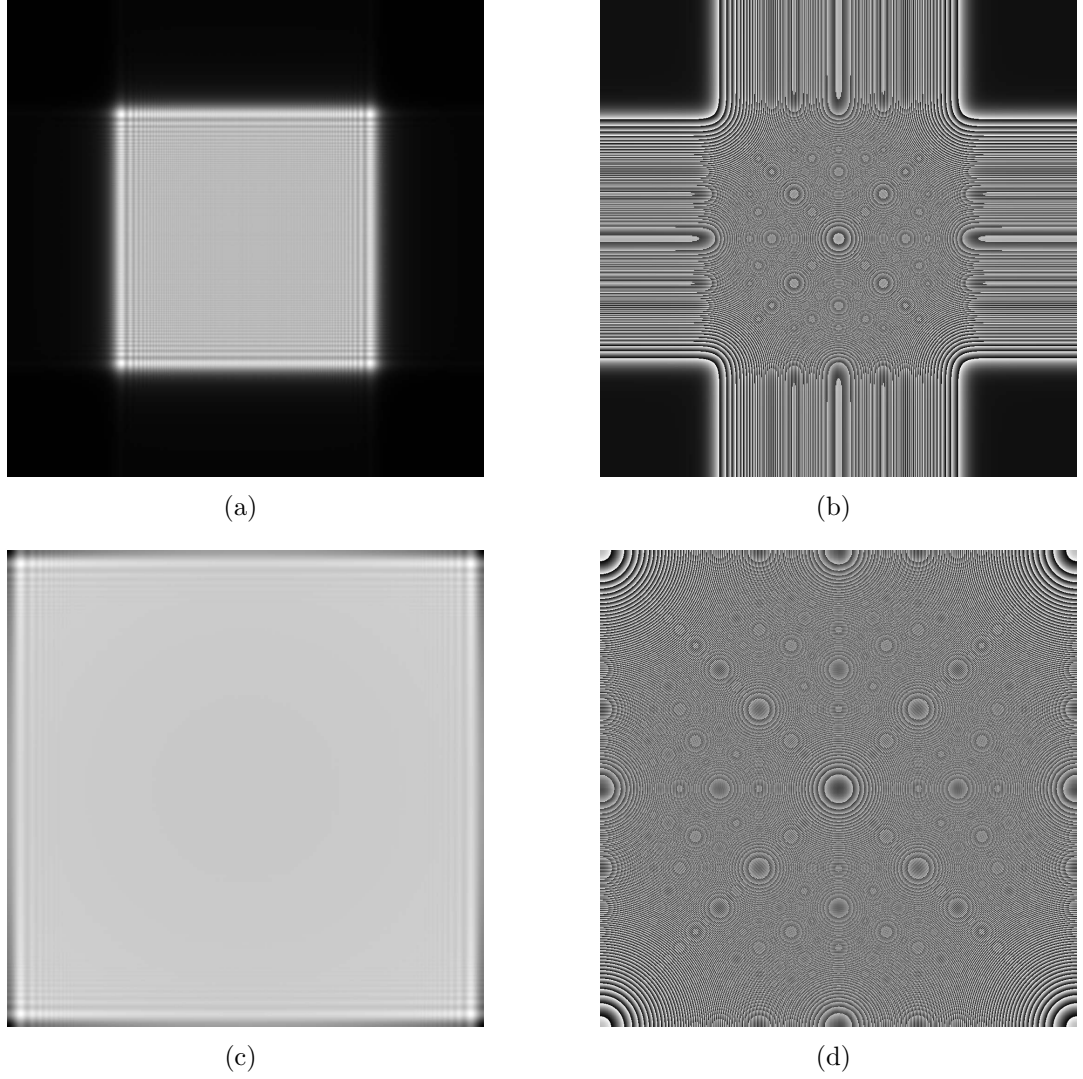
Figure 3.4: Transfer-function: (a) modulus and (b) phase for at d'=120 mm; (c) modulus and (d) phase for d'=67.3 mm

The larger the recording distance the stronger the filtering effect on high spatial frequencies is. Thus high spatial frequencies might be lost in the reconstruction process.

Therefore, a cascaded reconstruction algorithm has been proposed by Kreis (2005). The hologram is propagated in different propagation stages of a higher frequent impulse response to the final reconstruction plane, see Fig. 3.5. The distance between each propagation is calculated to maintain the highest possible
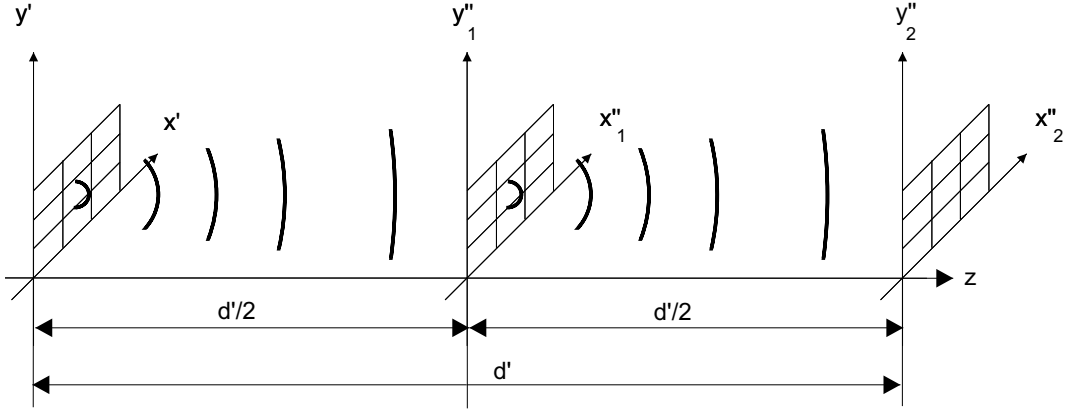
Figure 3.5: Cascaded reconstruction in two steps

spatial frequency, without violating the Nyquist criterion. Assuming that the impulse response is centered, highest spatial frequencies occur in the corners of the impulse response $l = 1$. The maximum phase difference $\Delta\phi$ between two pixels should not be larger than π according to the Nyquist criterion. The phase (in digitized notation) of the impulse response can be described by:

$$\phi = \frac{2\pi}{\lambda}\sqrt{(l - \frac{N}{2} - 1)^2\Delta x'^2 + (m - \frac{M}{2} - 1)^2\Delta x'^2 + d'^2} \qquad (3.13)$$

The phase needs to be differentiated with respect to l, whereas only the x'-direction is taken into account.

$$\frac{\Delta\phi}{\Delta l} \approx \frac{\partial\phi}{\partial l} = \frac{\pi}{\lambda}\frac{2\Delta x'^2(l - \frac{N}{2} - 1)}{\sqrt{d'^2 + \Delta x'^2(l - \frac{N}{2} - 1)^2}} \qquad (3.14)$$

Rearranging Eq. 3.14 to be solved for d' and inserting the corresponding values for l, $\Delta\phi$ and Δl results in:

$$\begin{aligned} d' &\geq \Delta x'\frac{N}{2}\sqrt{\frac{4\Delta x'^2}{\lambda^2} - 1} \\ &\approx \frac{N\Delta x'^2}{\lambda} \end{aligned} \qquad (3.15)$$

Figs. 3.4(c) and (d) show the intensity and phase at an optimum reconstruction distance, respectively. The calculation was based on the pixelfly qe camera with 1024x1024 pixels and 6.45 μm pixel-size, as shown in Appendix D.1. This camera was initially used to carry out the experiments. When the transfer-function covers the whole frequency range (as in Fig. 3.4(c) and (d)), the high spatial frequencies are maintained when applying the Rayleigh-Sommerfeld convolution integral. A more detailed discussion of the low-pass filtering effect of the transfer-function can be found in Kreis (2005).

3.3   DC-term and Twin Image Suppression

Before turning to the numerical realization of other reconstruction models the suppression of the DC-term and twin image, which was applied to obtain the reconstructions shown in Fig. 3.3(b) and succeeding sub-figures, is discussed. Some theoretical ideas in this section are based on Schnars and Jueptner (2005) and Kreis (2005). According to Eq. 2.28 the hologram can be considered to be a sinusoidal amplitude grating. The recorded intensity can hence be described by:

$$I = A_r^2 + A_o^2 + 2A_r A_o \cos \varphi \tag{3.16}$$

According to Goodman (1996) the amplitude transmission function of a sinusoidal amplitude grating, as shown in Fig. 3.6(a), is:

$$t_A = \frac{1}{2} + \frac{s}{2} \cos \left(2\pi \nu_0 x'\right) \tag{3.17}$$

Where s represents the modulation depth of the sinusoidal grating and ν_0 the spatial grating frequency.
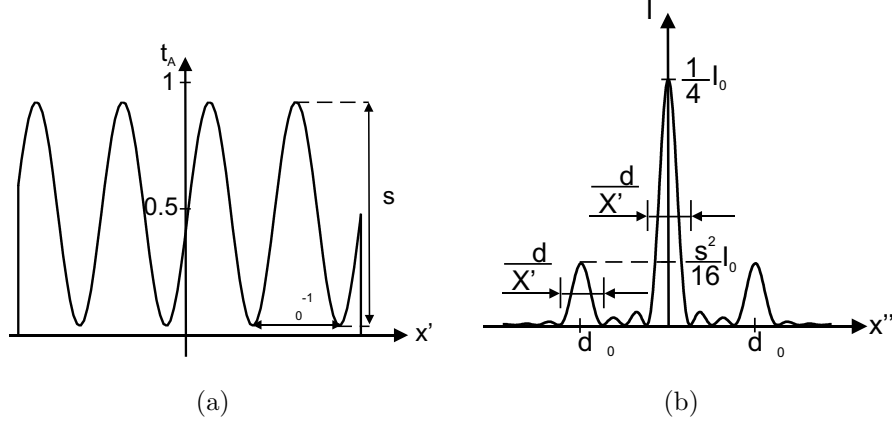
Figure 3.6: (a) Amplitude transmission-function for sinusoidal amplitude grating, (b) Fraunhofer diffraction pattern

The resulting Far-field diffraction pattern can be calculated by applying a Fourier-transformation.

$$\mathcal{F}\{t_A\} = \frac{1}{2}\delta(\nu_x) + \frac{s}{4}\delta(\nu_x + \nu_0) + \frac{s}{4}\delta(\nu_x - \nu_0) \qquad (3.18)$$

Three diffraction patterns are obtained namely a plus and minus first order, which correspond to the reconstructed image and twin-image, and a zero order also known as the DC-term. The diffraction efficiency η is introduced in order to evaluate the obtained intensity of the desired reconstructed image. The diffraction efficiency takes into accounts the initial intensity I_0, which corresponds to the reference-wave intensity if optical reconstruction was applied and the obtained intensity of the reconstructed hologram I. The result obtained needs to be squared in order to obtain the diffraction efficiency η for each corresponding diffraction order. The diffraction efficiency for the DC-term η_0, the image η_{+1}

Table 3.1: DC-term and twin-image suppression

Suppression method	DC-term suppression	Twin-image suppression
Averaged intensity subtraction	possible	not possible
Subtraction of reference-wave intensity A_r^2 and object-wave intensity A_o^2	possible	not possible
Filtering in Fourier domain (only applicable for off-line arrangement)	possible	possible
Phase stepping	possible	possible

and the twin-image η_{-1} for an amplitude grating are as follows:

$$\eta_0 = \frac{1}{4}$$
$$\eta_{+1} = \frac{s^2}{16}$$
$$\eta_{-1} = \frac{s^2}{16}$$

These values show that the intensity of the plus and minus first diffraction order is overexposed by the strong DC-term, which is shown in Fig. 3.6(b). Moreover, one needs to take care that intensity values are evenly distributed to cover the whole dynamic range of the sensor in order to obtain the optimum diffraction efficiency η for the reconstructed image. Methods which enable the suppression of the DC-term and in some cases the twin-image are shown in Table 3.1 and discussed in more detail hereafter.

3.3.1 Averaged Intensity Subtraction

One can suppress the DC-term by *subtracting the averaged hologram intensity* from the hologram.

$$I(l,m)^* = I(l,m) - \frac{\sum\limits_{l=1}^{N}\sum\limits_{m=1}^{M} I(l,m)}{NM} \tag{3.19}$$

Subtracting the averaged intensity value from the hologram results in an amplitude-transmission-function:

$$t_A = \frac{s}{2}\cos(2\pi\nu_0 x') \tag{3.20}$$

Its Fourier-transform results in the plus and minus first order only.

$$\mathcal{F}\{t_A\} = \frac{s}{4}\delta(\nu_x + \nu_0) + \frac{s}{4}\delta(\nu_x - \nu_0) \tag{3.21}$$

Both, amplitude transmission function and its Fraunhofer diffraction, are shown in Fig. 3.7(a) and (b), respectively. The diffraction efficiency of plus and minus first order matches with the one obtained by a sinusoidal amplitude grating, see Fig. 3.7(b).
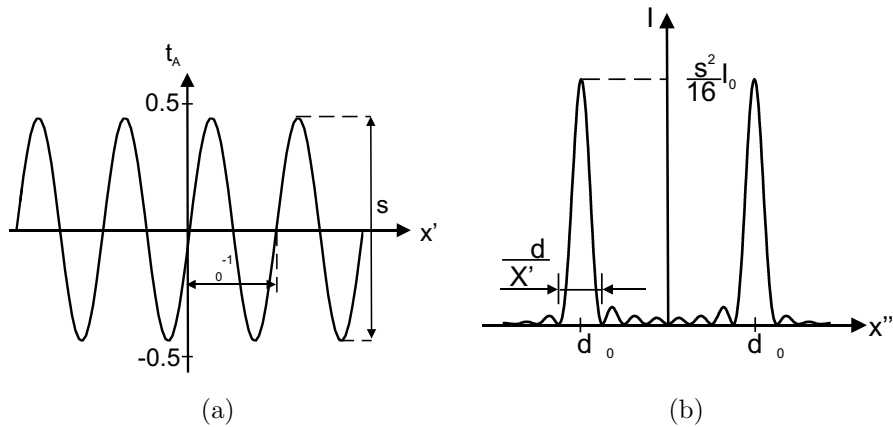
Figure 3.7: (a) Amplitude transmission-function for averaged intensity subtracted sinusoidal amplitude grating, (b) corresponding Fraunhofer diffraction pattern
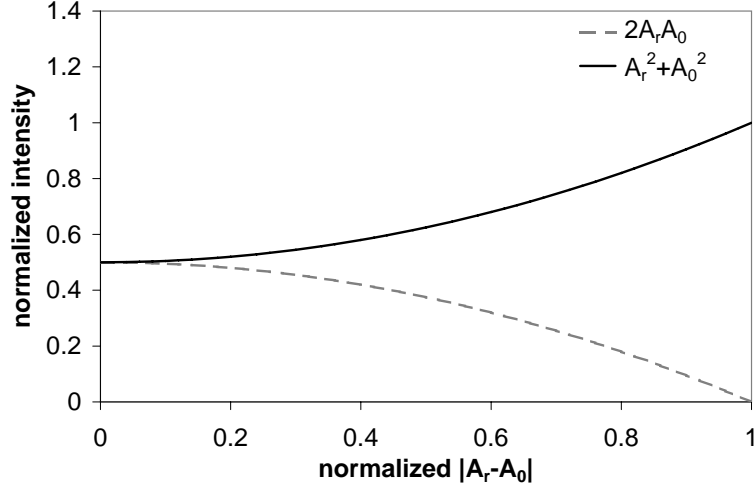
Figure 3.8: Influence of different ratios between reference- and object-wave amplitude

Care needs to be taken that the **intensity of the reference and object beams are matched** otherwise both terms in Eq. 3.16, $2A_oA_r$ and $A_o^2 + A_r^2$, differ in magnitude, which is shown Fig. 3.8. This would offset the sinusoidal intensity profile even further from the zero-line, which decreases the modulation depth and consequently decreases the diffraction efficiency. Furthermore, the reconstruction will not result in a successful DC-term suppression. This problem can be overcome by subtracting the minimum recorded intensity value and adjusting the grey values to cover the whole dynamic range. Having fulfilled this condition does not automatically guarantee a total DC-term suppression since this approach assumes a *homogenous intensity distribution*. Two numerical approaches have been carried out to overcome the problem of an inhomogeneous intensity distribution. The first method is based on adding a strong **inverted median filtered** image of the hologram's intensity distribution to the hologram itself. The median filter is used in order to obtain the shape of the intensity distribution without fringes. Therefore a very strong median filter needs to be applied. The median filter used in this particular case is 60x60 pixels. Once the inverse of the median filtered hologram is added to the hologram the averaged

Table 3.2: Comparison of termination speed

Suppression method	time in s	maximum value	minimum value
Inverted median filter	179.50	206.89	-97.10
Sliding window	40.18	178.21	-150.68

intensity is subtracted.

The second method is based on the assumption that the intensity distribution within a small region can be considered to be homogeneous. This region needs to be at least as large as the width covered by an interference fringe. A **sliding window** moved over the entire hologram is used to calculate the averaged intensity value within this region. Prior to the sliding window operation the image is padded with its average value on each side by half the width of the window-size. This step is necessary to avoid an abrupt cutoff for the values which are located at the sides of the hologram. The resulting sliding window averaged intensity map is then subtracted from the hologram. The reconstruction is DC-term free. In our case the width used was 10x10 pixels. The improved performance of both approaches is demonstrated in Figs. 3.10(b) and 3.10(c) compared to solely subtracting the averaged intensity as shown in Fig. 3.10(a), which does not fully suppress the DC-term. The sliding window operation terminates faster and possesses a larger degree of homogeneity for negative and positive values, see Table 3.2. Hence it is superior to the 'inverted median filter' method, which is confirmed by a stronger DC-term suppression.

Both, the 'inverted median filter' and the 'sliding window' method, benefit from requiring a single hologram only in order to perform the DC-term suppression. They could also be applied to an in-line configuration for which a plane reference-wave and a long recording distance in respect to the wavelength and the numerical aperture NA were used (see Eq. 4.33). In this case the reconstruction

consists of an in-focus image overlapped by a strongly blurred twin-image, which does not significantly affect the image quality according to Martinez-León and Javidi (2007).

3.3.2 Subtraction of Reference-wave and Object-wave Intensity

Another way of suppressing the DC-term is to record and subtract the object- and reference-wave intensity. This approach is associated with additional experimental effort, since one needs to block one of the beams whilst recording the other beam. The performance of the previously discussed DC-term suppression algorithms such as 'average intensity subtraction', 'inverted median filter' , 'sliding window operation' and 'subtraction of reference and object-beam' was investigated on a recorded interference pattern shown in Fig. 3.9(a), which possesses a Gaussian intensity distribution shown in Fig. 3.9(b). The results obtained utilizing the various DC-term suppression methods are presented in Figs. 3.9(c), (d), (e) and (f), respectively. The intensity profile obtained applying the 'subtraction of reference and object-beam' method possesses more evenly distributed positive and negative intensity values than when applying the initial 'average intensity subtraction' method. This results in a better DC-term suppression as demonstrated in Fig. 3.10(d).
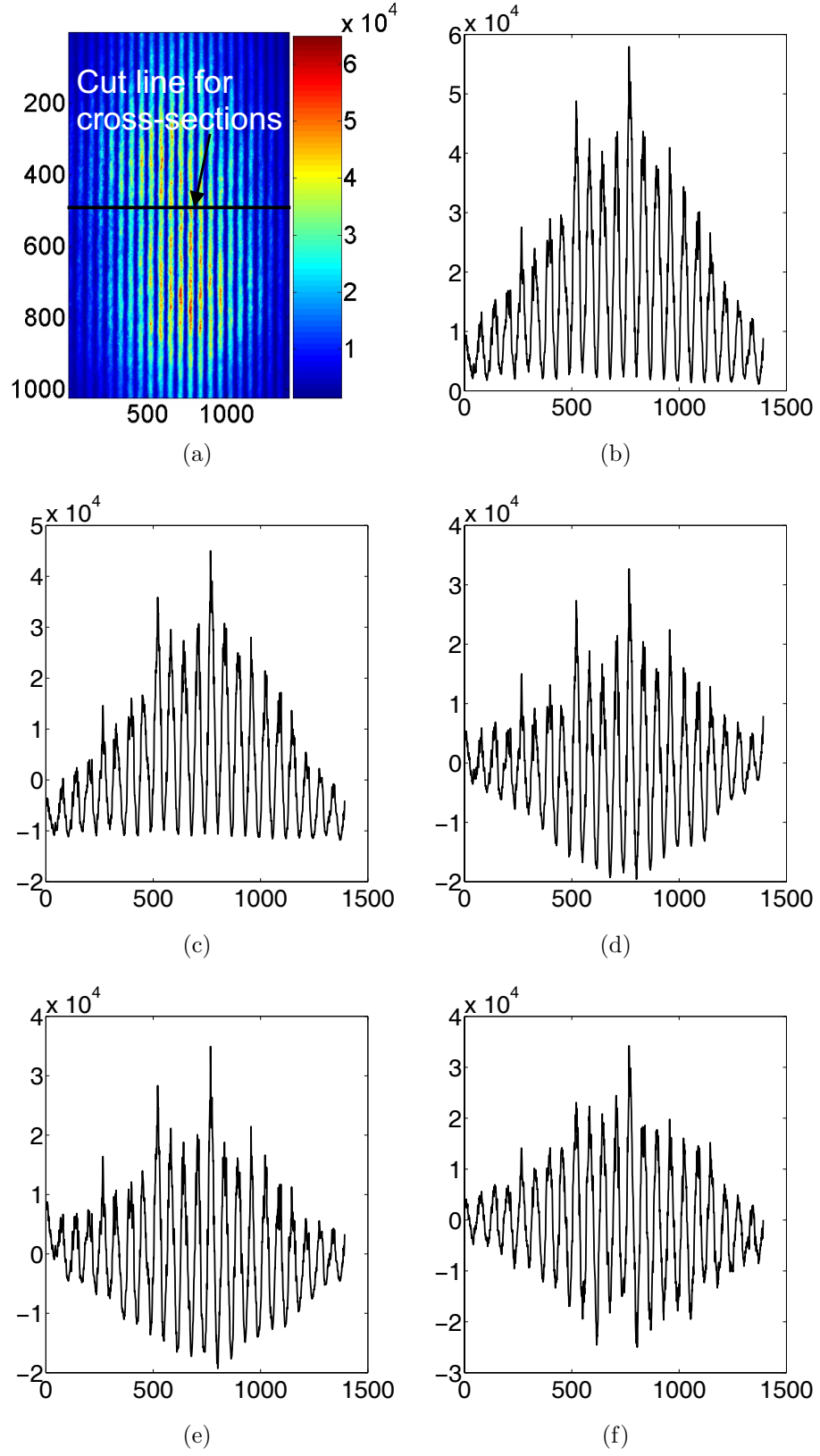
Figure 3.9: (a) Initial interference pattern, cross-sections: (b) without DC-term suppression, (c) average intensity subtraction, (d) inverted median filter, (e) sliding window operation, (f) subtraction of reference and object-beam
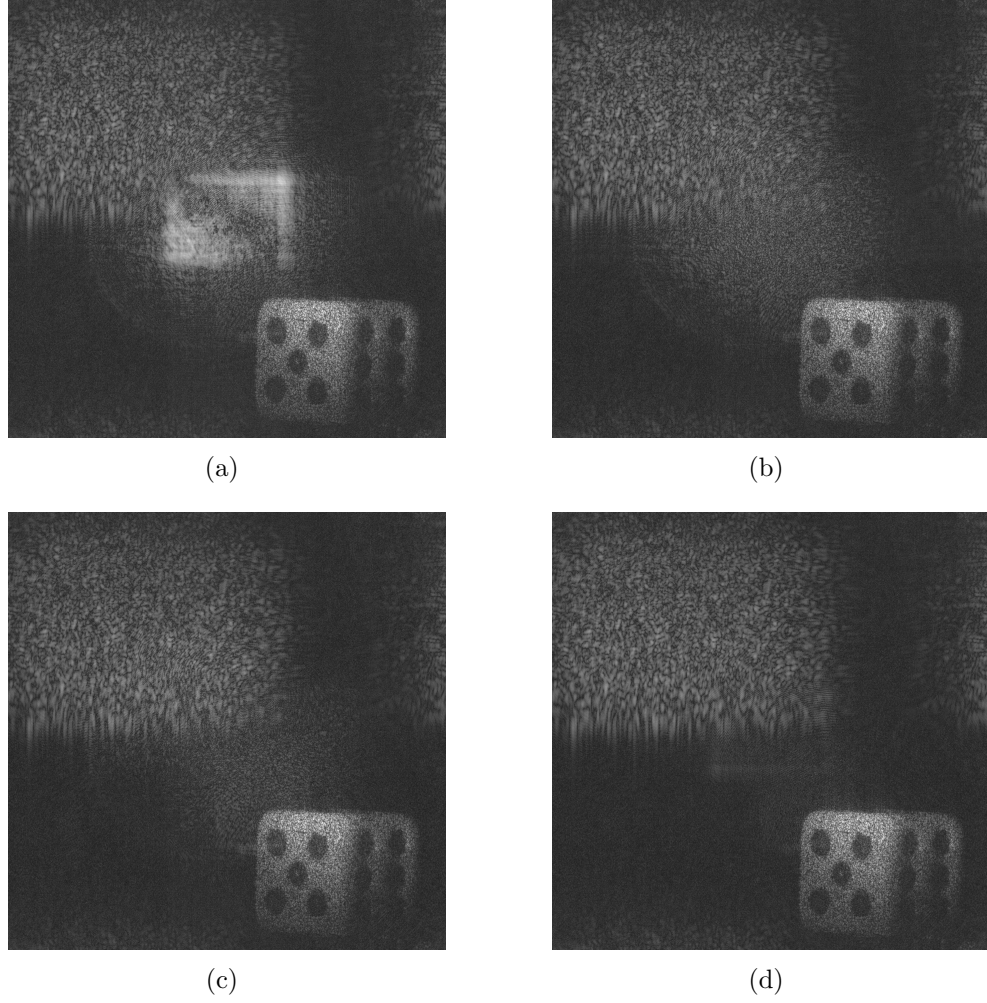
Figure 3.10: (a) Numerical reconstruction after average-value subtraction, (b) Numerical reconstruction with the inverted median filtered image, (c) Numerical reconstruction with sliding window operation,(d) Reconstruction by subtraction of reference and object-wave

3.3.3 Filtering in the Fourier Domain

Another approach to suppress the DC-term is based on a two dimensional *Fourier transformation* of a recorded off-line hologram. Due to the off-line arrangement the image, twin image and DC-term are spatially separated in the Fourier domain, as shown in Fig. 3.12(a). The DC-term and twin image can be filtered by blocking them in the Fourier-domain, see Fig. 3.12(b). Afterwards the inverse
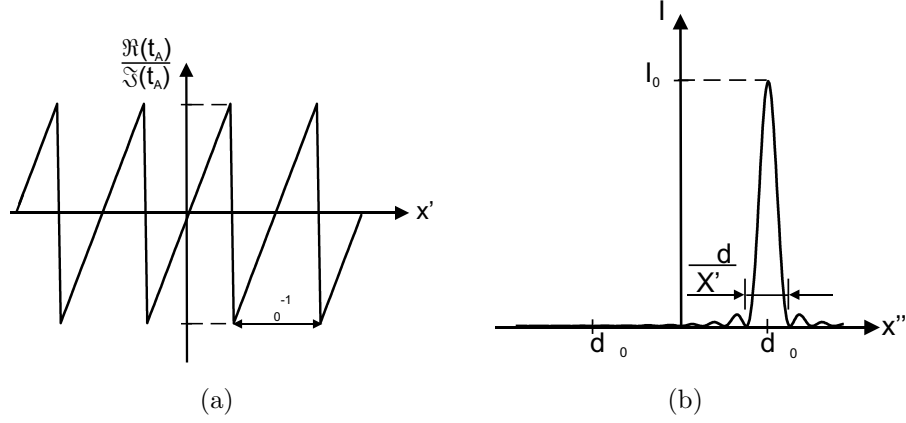
Figure 3.11: (a) Amplitude transmission-function for saw tooth phase, (b) corresponding Fraunhofer diffraction pattern

two dimensional Fourier transformation is applied to obtain the filtered hologram which possesses an unambiguous phase. The reconstruction of an unambiguous phase hologram can be modeled by its amplitude transmission-function, shown in Fig. 3.11(a).

$$t_A = \exp\left(\pm i 2\pi \nu_0\right) \tag{3.22}$$

Its Fourier-transform results in the plus first or minus first order only, see Fig. 3.11(b).

$$\mathcal{F}\left\{t_A\right\} = \delta(\nu_x \mp \nu_0) \tag{3.23}$$

The diffraction efficiency obtained is:

$$\eta_{\pm 1} = 1$$

The hologram of the previously used dice shown in Fig. 3.3(a) has been Fourier-filtered and the phase map of the filtered hologram and its numerical intensity reconstruction are represented in Figs. 3.12(c) and (d), respectively. The Fourier-filtering algorithm is superior to the 'averaged value subtraction' method and the 'subtraction of reference-wave and objective-wave intensity' in terms of its
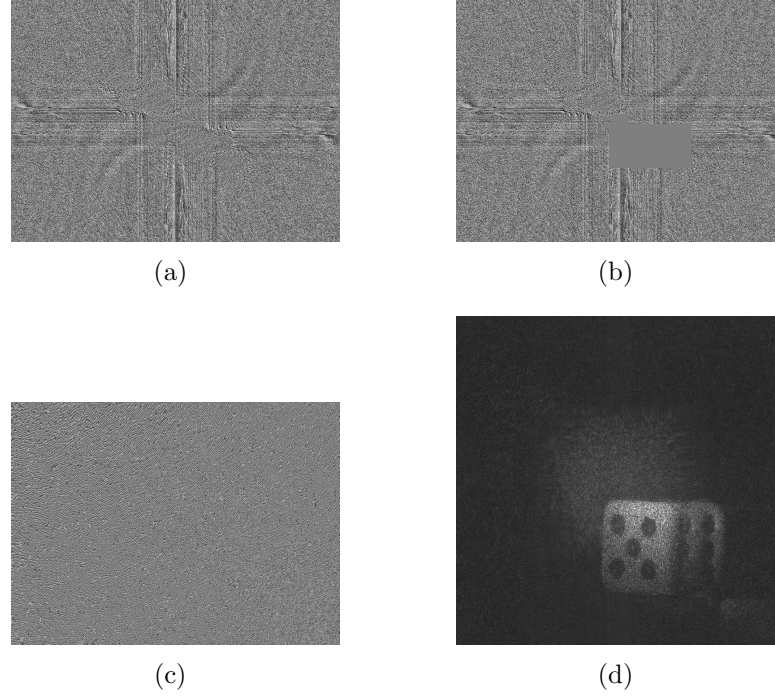
Figure 3.12: (a) Hologram in Fourier-domain, (b) blocked DC-term and twin-image in Fourier-domain, (c) phase of resulting Fourier filtered hologram, (d) numerical reconstruction

diffraction efficiency. Moreover, it additionally enables the suppression of the twin-image.

3.3.4 Phase stepping

A further method for the suppression of the DC-term and twin-image is *Phase Stepping*. This is an important tool used in interferometry and has some advantages in holography such as:

i. High measurement accuracy (>1/1000 fringe) can be obtained.

ii. Good results can be obtained for low contrast fringes.

iii. Reduced impact of temporally stationary fringes caused by double reflections when light passes through an optical element.

iv. Recording distance can be reduced which results in an improved resolution.

Phase stepping could also be listed as a separate reconstruction method. It enables one to obtain phase information for image-holograms which are commonly applied to digital holographic microscopy [Schnars (2005)]. Phase stepping is performed by recording three or more phase stepped holograms. The corresponding phase hologram is calculated by numerical means. The additional phase step is generally applied in the reference arm. A detailed discussion of possible phase stepping devices is presented in Wyant (2009). The phase stepping device introduces an additional optical path length which corresponds to a change of phase between reference and object-wave. Phase stepping utilizing wave retarder plates (shown in Fig. 3.13(a)) and a piezo mounted mirror (Fig. 3.13(b)) have been carried out in the scope of this thesis. A series of temporally separated holograms have been recorded. Thus environmental influences such as air disturbances had to be minimized.
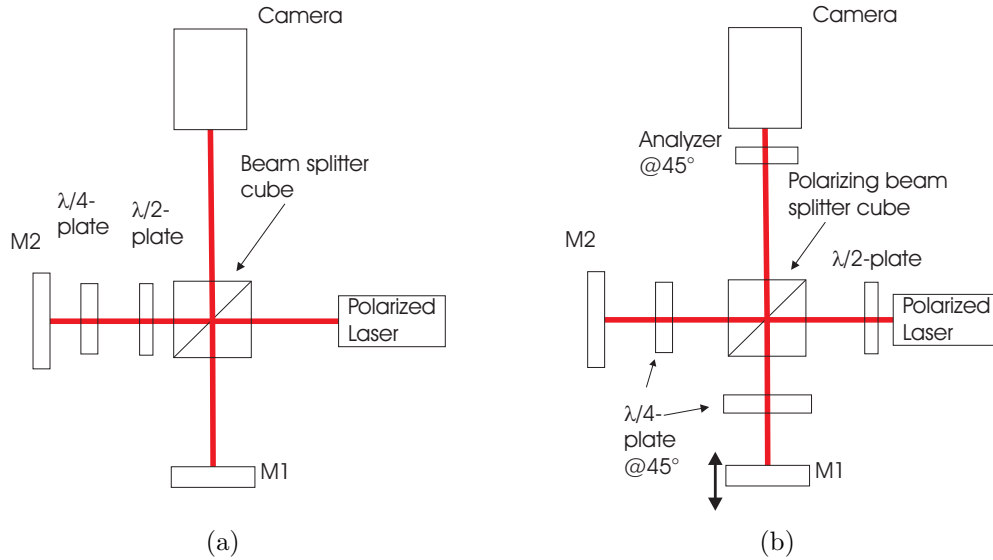
Figure 3.13: (a) Setup with wave retarder plates, (b) setup with piezo-driven mirror M1

Reliability Of Piezo And Polarization Optics

Two independent methods have been implemented which calculate the magnitude of phase step applied. In this manner the impact of disturbing environmental influences or inaccuracies caused by the phase stepping device are minimized, by which the reliability of the results achieved can be improved. The first method, which was proposed by Cai et al. (2004) calculates each phase step *individually.* It requires a minimum number of *three phase stepped holograms* possessing the following intensity distribution:

$$I_1(x', y') = A_r^2(x', y') + A_o^2(x', y') + 2A_r(x', y')A_o(x', y')\cos[\varphi(x', y')] \qquad (3.24)$$

$$I_2(x', y') = A_r^2(x', y') + A_o^2(x', y') + 2A_r(x', y')A_o(x', y')\cos[\varphi(x', y') \\ -\Delta\varphi_1] \qquad (3.25)$$

$$I_3(x', y') = A_r^2(x', y') + A_o^2(x', y') + 2A_r(x', y')A_o(x', y')\cos[\varphi(x', y') \\ -\Delta\varphi_1 - \Delta\varphi_2] \qquad (3.26)$$

Where A_r and A_o are the amplitude of reference- and object-wave, and $\Delta\varphi_1$ and $\Delta\varphi_2$ $(0 < \Delta\varphi_i < \pi, i = 1, 2)$ are the two phase steps. Three new variables, which result from the subtraction of the three intensity distributions, are introduced, as follows.

$$o_{21} = \langle|I_2(x', y') - I_1(x', y')\rangle| = \langle|4A_r(x', y')A_o(x', y') \\ \sin(\varphi - \Delta\varphi_1/2|\rangle\sin(\Delta\varphi_1/2) \qquad (3.27)$$

$$o_{32} = \langle|I_3(x', y') - I_2(x', y')\rangle| = \langle|4A_r(x', y')A_o(x', y') \\ \sin(\varphi - \Delta\varphi_1 - \Delta\varphi_2/2|\rangle\sin(\Delta\varphi_2/2) \qquad (3.28)$$

$$o_{31} = \langle |I_3(x', y') - I_1(x', y')| \rangle = \langle |4A_r(x', y')A_o(x', y')$$

$$\sin(\varphi - (\Delta\varphi_1 + \Delta\varphi_2)/2|\rangle \sin[(\Delta\varphi_1 + \Delta\varphi_2)/2]$$

$$(3.29)$$

$\langle\rangle$ is the average intensity value of the recorded hologram. Assuming that $A_o(x', y')$ and $\varphi(x', y')$ are mutually independent and $\varphi(x', y')$ is spatially randomly distributed one can conclude all terms $\langle |...| \rangle$ on the right hand side of Eqs. 3.27-3.29 to be the same.

$$o_{21} = v\sin(\Delta\varphi_1/2) \tag{3.30}$$

$$o_{32} = v\sin(\Delta\varphi_2/2) \tag{3.31}$$

$$o_{31} = v\sin[(\Delta\varphi_1 + \Delta\varphi_2)/2] \tag{3.32}$$

v can be obtained by the following equation.

$$v = 2o_{21}o_{32}o_{31}[2(o_{21}^2 o_{32}^2 + o_{21}^2 o_{31}^2 + o_{32}^2 o_{31}^2) - (o_{21}^4 + o_{32}^4 + o_{31}^4)]^{-1/2} \tag{3.33}$$

The phase steps $\Delta\varphi_1$ and $\Delta\varphi_2$ can be calculated by using trigonometrical relations.

$$\Delta\varphi_1 = 2\arcsin(o_{21}/v), \quad \Delta\varphi_2 = 2\arcsin(o_{32}/v) \tag{3.34}$$

The complex amplitude of the object-wave is given by:

$$A_o \exp(i\varphi) = \frac{1}{4A_r \sin\left(\frac{\Delta\varphi_2}{2}\right)} \left[\frac{\exp\left(\frac{i\Delta\varphi_1}{2}\right)}{\sin\left\{\frac{\Delta\varphi_1 + \Delta\varphi_2}{2}\right\}} \right.$$
$$(I_1 - I_3) - \frac{\exp\left\{i\left(\Delta\varphi_1 + \Delta\varphi_2\right)/2\right\}}{\sin\left(\Delta\varphi_1/2\right)}$$
$$\left. (I_1 - I_2) \right] \tag{3.35}$$

Another method, which enables one to obtain the unknown phase step is based on Carré-formula, which requires *four equally phase stepped holograms*. The highest

phase step accuracy is achieved by a pointwise calculation. One then needs to average the phase step value for each single pixel since the overall phase step should be constant. In this manner uncertainties and fluctuations, which may have been caused by speckle or environmental influences, are *averaged* out.

$$\Delta\varphi = \frac{1}{NM} \sum_{l=1}^{N} \sum_{m=1}^{M} \arccos \frac{I_1(x', y') - I_2(x', y') + I_3(x', y') - I_4(x', y')}{2[I_2(x', y') - I_3(x', y')]} \quad (3.36)$$

The hologram's phase map can then be calculated taking into account the constant phase step $\Delta\varphi$ of either the first three phase stepped intensity holograms or the last three phase stepped intensity holograms.

$$\begin{aligned}
\varphi = \arctan\Bigg[&\frac{I_3 - I_2 + (I_1 - I_3)\cos\Delta\varphi}{(I_1 - I_3)\sin\Delta\varphi + (I_2 - I_1)\sin 2\Delta\varphi} \\
+ &\frac{[I_2 - I_1]\cos 2\Delta\varphi}{(I_1 - I_3)\sin\Delta\varphi + (I_2 - I_1)\sin 2\Delta\varphi} \\
+ &\frac{3\Delta\varphi}{2} \Bigg]
\end{aligned} \quad (3.37)$$

A series of numerically generated fringe patterns with a phase step between 10 ° and 120 °, in increments of 10 °, have been generated and tested on both methods. Cai's Method, despite representing an approximation and its reduced requirement of three phase stepped holograms rather than four equally phase stepped holograms, performed better than Carré's-formula, see Fig. 3.14. Both methods have a maximum error of less than one percent, which makes both of them reliable approaches for obtaining the desired phase step information. Both methods were then experimentally applied to a Michelson interferometer (see Fig. 3.13) in order to evaluate the phase step accuracy of a piezo-driven mirror and wave-retarder plates. The piezo has an overall positioning range of 37.48 μm with a measurement uncertainty of 0.3 nm, as shown in Appendix D.2. The wave retarder plates had been ordered from the United Crystals company, see
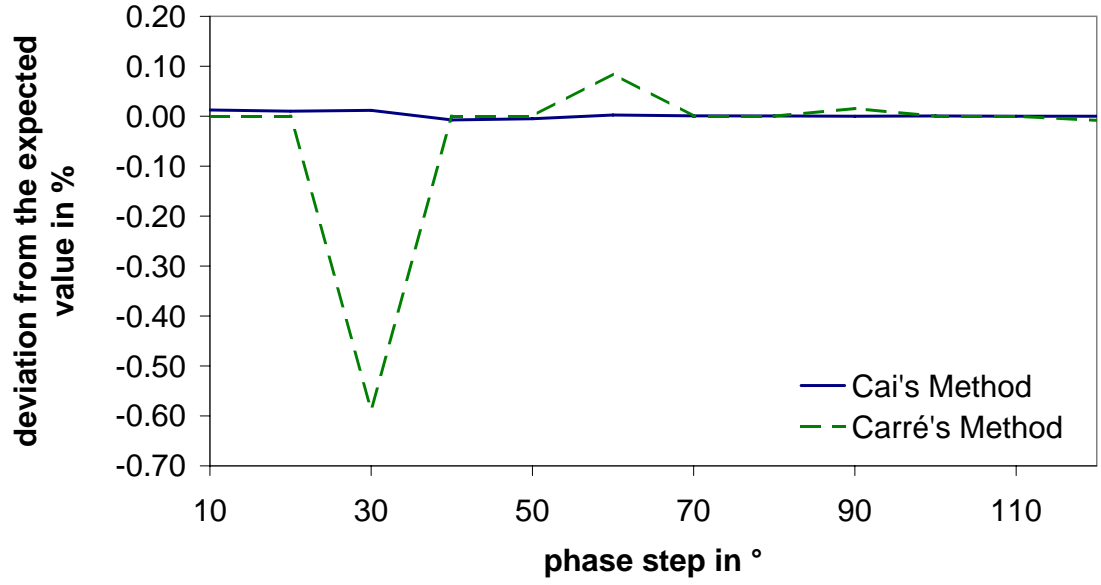
Figure 3.14: Accuracy performance of Cai's and Carré's Methods

Appendix D.3. They have a maximum retardation tolerance of less than three percent, which corresponds to a maximum retardation error of 4.7 nm and 9.5 nm for a quarter-wave-plate and half-wave-plate, respectively. A fundamental requirement for phase stepping with polarization optics is polarized laser light as a light source. The polarized laser light is split into two arms by a beam splitter cube, see Fig. 3.13(a). The light in one arm passes through a quarter- and a half-wave-plate. Four phase steps were generated by rotating the quarter and half-wave-plate between 0° and 90° as shown in Table 3.3.

Table 3.3: Combination of $\lambda/4$- and $\lambda/2$-plate and the resulting phase step

Case	Rotation angle of $\lambda/4$-plate in °	Rotation angle of $\lambda/2$-plate in °	Obtained phase step in °
1	0	0	0
2	90	0	-90
3	0	90	-180
4	90	90	-270

The values shown in Table 3.3 are based on the fact that the optically slow axis of the retarder plates was horizontally orientated and the laser light was vertically polarized. The phase step between two subsequently recorded interference pattern is 90 °. The same phase steps were applied to the piezo-driven mirror. Taking into account that the light is traveling twice the path-length between the polarizing beam splitter and the piezo-driven mirror results in a required piezo-displacement $\lambda/8$. The wavelength of the laser was 632.8 nm, thus the displacement applied to the piezo was 79.1 nm. An analyzer rotated by 45 ° was then required in order to combine both cross-polarized light beams and to record the interference, see Fig. 3.13(a). The setup for both phase stepping approaches are shown in Fig. 3.13. The data represented in the graphs of Fig. 3.15 have been analyzed by statistical methods Stockes (2007) and the results are represented in Table 3.4.

Table 3.4: Evaluation of the phase step data

Statistical properties	polarization optics		piezo-driven mirror	
	Carré	Cai	Carré	Cai
Maximum deviation from expected value in °	30.98	23.35	14.51	17.37
Mean value in °	82.86	84.14	93.26	92.83
Standard deviation from expected value in °	12.22	10.53	5.35	7.71
Standard deviation of the mean in °	82.86±1.46	84.14±1.29	93.26±0.56	92.83±0.95
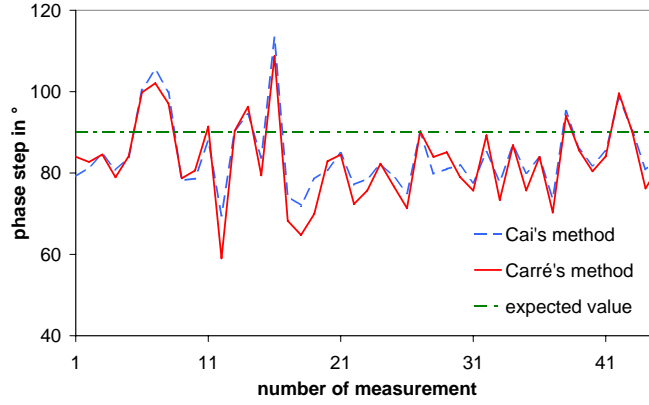
(a)
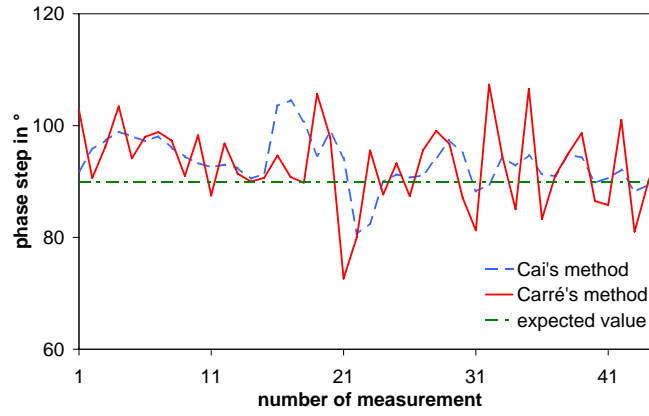
(b)

Figure 3.15: Phase step accuracy obtained by (a) a wave-retarder plates and (b) a piezo-driven mirror

In conclusion, phase stepping performed with a piezo-driven mirror gives a more accurate phase step than when applying polarization optics. A cause of the lower phase stepping accuracy of polarization optical devices might be due to the larger retardation error of both combined wave-plates, as previously mentioned. Moreover, angular alignment errors when mounting the wave retarder plates into its holder results in a further decreased accuracy. Furthermore, reflection is not as strongly affected by disturbances as transmission is. Light passing through the retarder device could be affected by reflection effects, dust and scratches at both sides of the wave-retarder. Another error could have been arisen from the

inclination of the wave-vector $\vec{k}$ of the incident light, which needs to be normal on the retarder plates in order to maintain an optimum performance of the phase step.

At a next stage, a holographic experiment was performed using phase stepping by means of a piezo-driven mirror. An in-line setup was used as shown in Fig. 3.16(a). The object has been a five pence coin. The distance to the camera was 345 mm and the camera used is the pco-pixelfly qe. The obtained result for the reconstruction utilizing an intensity hologram and an unambiguous phase hologram are shown in Figs. 3.16(b) and (c), respectively.

(a)

(b)   (c)
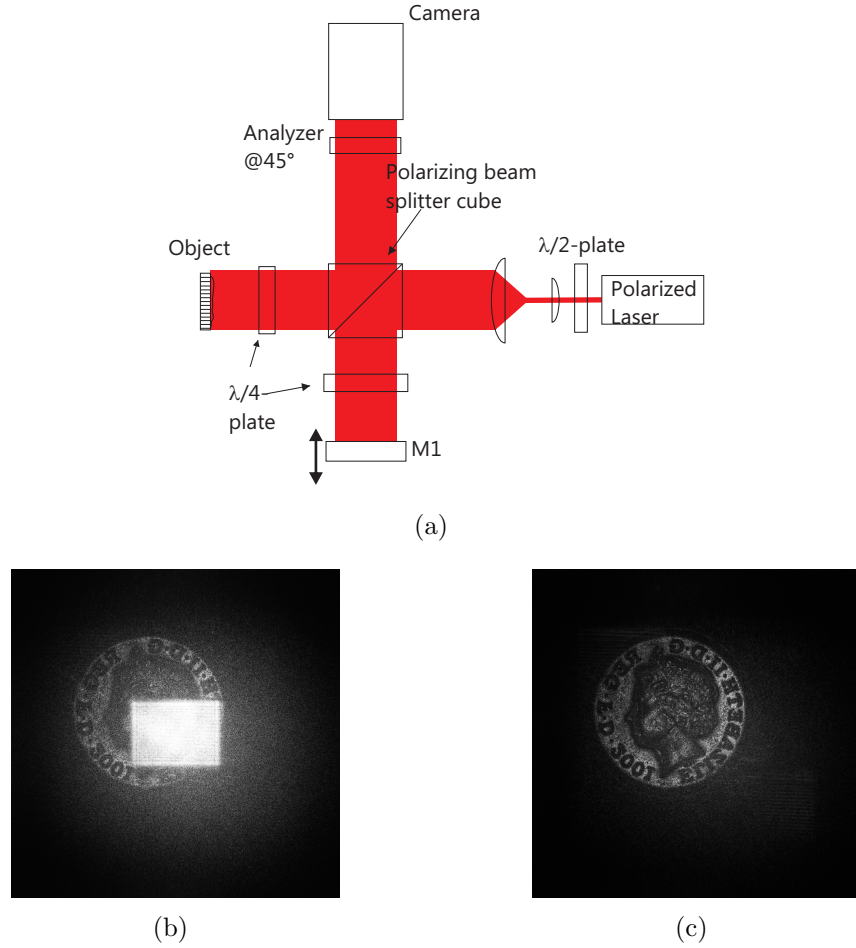
Figure 3.16: (a) Setup, (b) numerical reconstruction of the intensity hologram, (c) numerical reconstruction of the phase hologram

3.4 Fresnel-Method
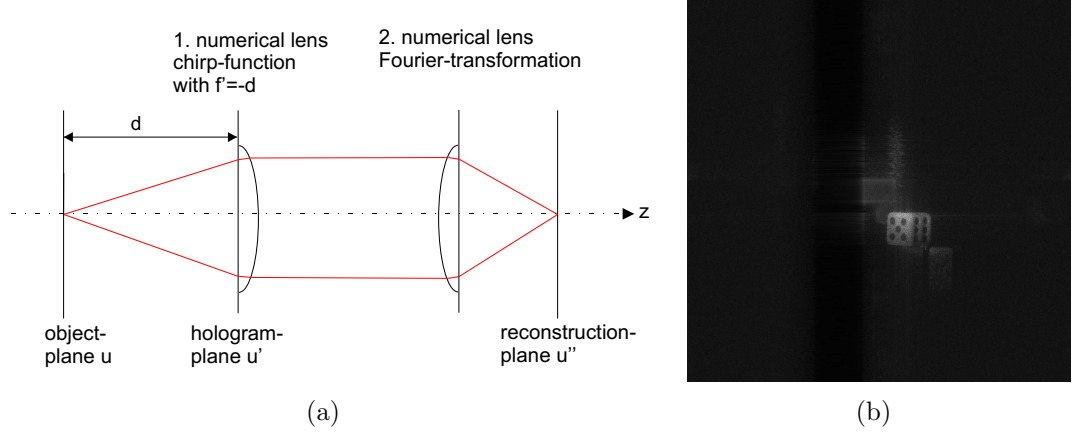
Figure 3.17: (a) Optical model for Fresnel method, (b) numerical reconstruction utilizing Fresnel-method

The Fresnel-propagation model including its validity region has been discussed in Section 2.7.2. The Fresnel reconstruction is performed utilizing the formula:

$$
u(x'', y'') = \frac{\exp(ikd)}{i\lambda\,d} \exp\left[\frac{i\pi}{\lambda\,d}\left(x''^2 + y''^2\right)\right] \int\limits_{-\infty}^{\infty}\int\limits_{-\infty}^{\infty} u(x', y') \cdot u_r^* \exp\left[\frac{i\pi}{\lambda\,d}\left(x'^2 + y'^2\right)\right]
$$
$$
\cdot \exp\left[\frac{-i2\pi}{\lambda\,d}\left(x''x' + y''y'\right)\right] \mathrm{d}x'\,\mathrm{d}y'
$$

(3.38)

For further considerations the term $\frac{\exp(ikd)}{i\lambda d}$ in Eq. 3.38 is neglected since it only introduces a constant phase. The last complex exponential term within the double integral $\left(\exp\left[\frac{-i2\pi}{\lambda d}\left(x''x' + y''y'\right)\right]\right)$ describes a Fourier-transformation and is treated as such. The Fresnel-method in digitized notation is:

$$
u''(l, m) = \exp\left[\frac{i\pi}{d'\lambda}\Delta x'' \left\{(l - N/2 - 1)^2 + (m - M/2 - 1)^2\right\}\right]
$$
$$
\cdot \mathcal{F}\left[u'(l, m) \cdot u_r^*(l, m)\right.
$$
$$
\left. \cdot \exp\left\{\frac{i\pi}{\lambda d}\left((l - N/2 - 1)^2 (m - M/2 - 1)^2\right)\right\}\right]
$$

(3.39)

The complex exponential term in front of the Fourier-transformation can be neglected if just the intensity is of interest or double exposure holography (which will be discussed in Section 4.7.3) is performed. The Fresnel-method is optically modeled in Fig. 3.17(a). The chirp-function within the Fourier-transformation corresponds to a numerical lens, see Eq. 3.10, of $d' = -f$. The reconstruction utilizing the Fresnel method is shown in Fig. 3.17(b). The pixel-size in the reconstruction-plane $\Delta x''$ can be estimated by using the Fourier transform relation:

$$\Delta x'' = \frac{\lambda d'}{N \Delta x'} \qquad (3.40)$$

The reconstructed hologram possesses a width of:

$$N \Delta x'' = \frac{\lambda d'}{\Delta x'} \qquad (3.41)$$

In order to display this width a certain amount of pixels with the initial pixel-size $\Delta x'$ are combined to form a single pixel of width $\Delta x''$ in the reconstruction-plane. The number of pixels displaying the numerical reconstruction decreases with increasing reconstruction distance d' by the ratio:

$$\frac{N \Delta x'^2}{\lambda d'} \qquad (3.42)$$

This does not impose a serious problem, since the reconstructed pixel-size matches the resolution obtained according to Abbe's criterion. In that way the Fresnel-method is more economical in terms of displaying the image than the Rayleigh-Sommerfeld's convolution integral is. If one was interested in displaying the image by a larger amount of pixels zero-padding needs to be applied to the hologram prior to its numerical reconstruction. A certain degree of zero-padding also increases the resolution obtained in the reconstruction, which is demonstrated

at a later stage in Fig. 6.10. Displaying the reconstruction on a larger number of pixels than is needed to display the smallest resolvable object detail results in empty magnification and is therefore not recommended. A factor of two is an adequate choice to perform zero-padding, as shown in the following Chapter 4.7.4:

$$N_{Zero} = 2N \tag{3.43}$$

3.5 Fourier-Method
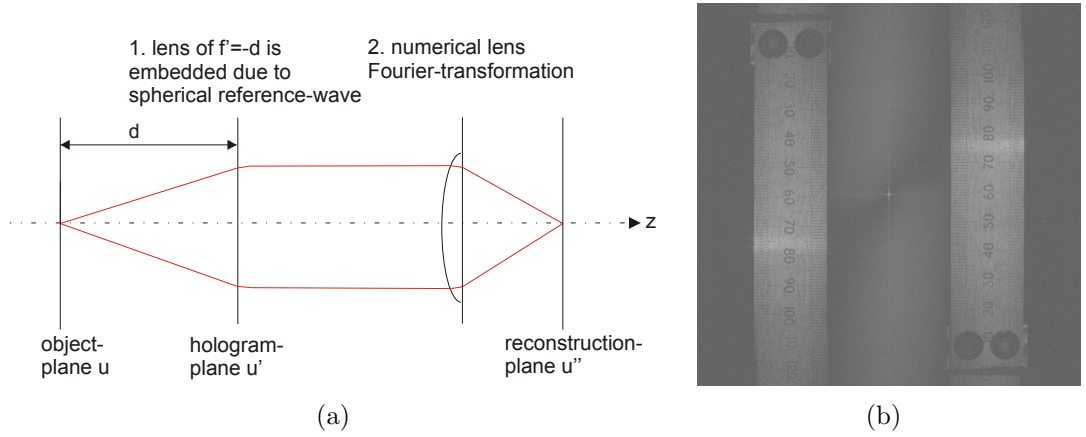
Figure 3.18: (a) Optical model for Fourier method, (b) numerically reconstructed Fourier-hologram

The numerical reconstruction utilizing the Fourier-method is similar to the reconstruction procedure described by the Fresnel-method as shown in Eq. 3.44.

$$
\begin{aligned}
u''(x'', y'') = \exp\left[\frac{i\pi}{\lambda d'}\left(x''^2 - y''^2\right)\right] \cdot \mathcal{F}\Big\{ u'(x', y') u_r^*(x', y') \\
\cdot \exp\left[i\frac{\pi}{\lambda d'}\left(x'^2 + y'^2\right)\right]\Big\}
\end{aligned}
\tag{3.44}
$$

The chirp-function used in the Fresnel-method, which acts like a lens of focal length $f = -d'$, is already embedded in the hologram due to the spherical reference-wave u_r, see Fig. 3.18(a). The spherical reference-wave in the hologram-

plane $(d_r = d')$ can be described by:

$$u_r(x', y') \approx \exp\left[i\frac{\pi}{\lambda d'}\left(x'^2 + y'^2\right)\right] \tag{3.45}$$

Substituting Eq. 3.45 in Eq. 3.44 permits the elimination of the parabolic chirp-function, dependent on x' and y'. Hence the reconstruction algorithm for the Fourier-method becomes:

$$u''(x'', y'') = \exp\left[\frac{i\pi}{\lambda d'}\left(x''^2 - y''^2\right)\right] \cdot \mathcal{F}\left\{u(x', y')\right\} \tag{3.46}$$

The digitized notation for the reconstruction is:

$$\begin{aligned} u''(l, m) = \exp\Bigg[\frac{i\pi}{\lambda d'}\Delta x''\bigg\{&(l - N/2 - 1)^2 \\ &- (m - M/2 - 1)^2\bigg\}\Bigg] \cdot \mathcal{F}\left\{u(x', y')\right\} \end{aligned} \tag{3.47}$$

The numerical reconstruction requires only a two dimensional Fourier-transformation of the hologram u(x',y') multiplied with a phase factor, see Eq. 3.47. Therefore, these kind of holograms, whose optical setup is characterized by an equidistant object and reference point source distance, are coined lens-less Fourier-holograms. By analogy with the Fresnel-reconstruction (discussed in Section 3.4) the complex exponential phase term

$$\left(\exp\left[\frac{i\pi}{\lambda d'}\Delta x''\bigg\{(l - N/2 - 1)^2 - (m - M/2 - 1)^2\bigg\}\right]\right)$$

is only of concern for phase measurement and can be neglected for intensity and double-exposure holography. The reconstructed hologram obtained is focused at the reference-plane distance. Both image and twin-image are in focus in the numerical reconstruction due to focusing at the Fourier-plane, see Fig. 3.18(b).

In the Fourier-plane image and twin-image are in focus. Both represent a complex conjugated pair, which explains the upside down orientation of the twin-image. The computationally inexpensive algorithm to reconstruct a Fourier-hologram is offset by the inability to focus at different axial sections within the object volume, since Eq. 3.46 is not a function of the reconstruction distance d', as discussed in Schnars and Jueptner (2005). One possible way to focus at different axial object sections is to apply Eq. 3.39. The disadvantage of this approach is that the numerical chirp-function possesses high frequencies at its edges, which might not be resolved when applying the synthetic aperture method. In order to avoid numerical under-sampling the camera-object distance needs to be increased the larger the synthetic aperture becomes. Moreover, a chirp-function needs to be calculated twice, once for the object-wave and again for the reference-wave. A more elegant approach is to combine both chirp-functions to a numerical lens as proposed by Goodman (1996) and Haddad et al. (1991). The numerical lens in digitized notation is:

$$
\begin{aligned}
L(l, m, d_{ref}, d_o) = \exp\Bigg[& \frac{i\pi}{\lambda} \frac{d_{ref} - d_o}{d_{ref} d_o} \Delta x' \Big\{ (l - N/2 - 1)^2 \\
& + (m - M/2 - 1)^2 \Big\} \Bigg]
\end{aligned}
\tag{3.48}
$$

The numerical lens presented in Eq. 3.48 is a function of the reference source point distance d_{ref} and the object distance d_o. It is convex for $d_o < d_{ref}$ and concave for $d_o > d_{ref}$. It possesses a very low frequency chirp-function since d_{ref} and d_o are almost matched. It can therefore be applied at any distance without the risk of under-sampling or exceeding the validity of the Fresnel approximation. The parameters in the reconstruction-plane such as pixel-size $\Delta x''$, the reconstructed width $N\Delta x''$ and the pixel-size ratio are calculated by the same method as in the Fresnel-reconstruction, see Eqs. 3.40, 3.41 and 3.42.

3.6 Conclusion

The three most commonly applied reconstruction methods in digital hologra-phy have been presented in their digitized notation. A comparison of the three reconstruction methods is shown in Table 3.5.

In addition to the digitized reconstruction formula found in Schnars and Jueptner (2005) and Kreis (2005) some supplementary numerical methods were developed to either increase the accuracy or to reduce the numerical effort. This in particular refers to the introduction of a spherical numerical lens presented in Eq. 3.9 to increase the accuracy for a focal length smaller than the Fresnel-region allows for. Moreover, the DC-term suppression performance by *Average Inten-sity Subtraction* could be improved by the *inverted median filter* method and the *sliding window* method, which have been developed in the context of this thesis. Furthermore, the numerical effort to center the image in the reconstruction utiliz-ing the convolution integral, which corresponds to the numerical implementation of the Rayleigh-Sommerfeld-method, could be reduced. The shift was initially applied to the impulse-response as shown in Schnars and Jueptner (2005). The numerical method reported in this thesis applies the shift to the transfer-function, see Eq. 3.7. In that manner a two dimensional Fourier-transformation could be saved.

Moreover, it was found that the phase stepping error is smaller using a piezo shifted mirror than when using polarization optics.

This knowledge and the numerical tools developed could then be applied to record, reconstruct and process digital holograms.

Table 3.5: Summary: Comparison reconstruction methods

Parameter	Rayleigh-Sommerfeld-Diffraction-Integral	Fresnel-method	Fourier-method
Calculation time	long, at least two FFT + loop	moderate, one FFT + loop	little, one FFT
Reference-wavefront	generally plane	generally plane	spherical
Pixel size in the reconstruction plane	$\Delta x'' = \Delta x'$	$\Delta x'' = \frac{\lambda d}{N \Delta x'}$	$\Delta x'' = \frac{\lambda d}{N \Delta x'}$
Minimum recording distance d	$0 < d < \infty$	$d_{min} < d < \infty$	$0 < d < \infty$ (for intensity reconstruction)
Application	independent from d and λ; well suited for microscopic objects, e.g. particle detection	large distances macroscopic objects, otherwise undersampling of the chirp-function	d independent from pixel-number N, well suited for synthetic aperture method
Fringe distribution	spherically shaped distribution, high density at corners	spherically shaped distribution, high density at corners	almost homogenous, reference-wave adapted to object-wave

CHAPTER 4

Optical Parameters and Properties of Digital Holography

4.1 Introduction

The main optical parameters such as lateral and axial resolution, field of view and setup dependent recording distance are partly derived and discussed in this chapter. These parameters are influenced by the camera's specification, the light source employed, the object's extension and the setup arrangement as shown in Table 4.1. Furthermore, benefits of digital holography in comparison with photography and optical holography are demonstrated.

Table 4.1: Source and corresponding parameters

Source	Parameter
Recording device	pixel size $\Delta x'$
	number of pixels N
	quantization l_{grey}
Light source	wavelength λ
Object	dimension X
Setup geometry	distance d between recording device and object

4.2 Parameters for Optical Setup

The parameters discussed in this section are closely related to the resolution of the camera sensor and the Nyquist-criterion. The Nyquist-criterion says that in order to recover a band-limited signal the sampling frequency ν_{sa} needs to be at least twice as large as the highest signal frequency ν_x. In our case the signal is represented by the sinusoidal intensity pattern which results from the interference of reference-wave and object-wave.

$$\nu'_x = \frac{1}{g} = \frac{\nu_{sa}}{2} = \frac{1}{2\Delta x'} \tag{4.1}$$

Where ν'_x is the highest frequency of the sinusoidal interference pattern and ν_{sa} is the sampling frequency, which corresponds to the reciprocal of the pixel-size $\Delta x'$.

4.2.1 Minimum Distance Plane Reference-wave

A hologram recorded with a plane reference-wave is often refereed to as a *Fresnel-hologram*. It is assumed that the spherical object-wave can be treated as a plane-wave over an area of a few pixels. From Fig. 4.1 it follows that:

$$g = a + b = \lambda \left(\tan \frac{\alpha}{2} + \frac{1}{\tan \alpha} \right) \tag{4.2}$$

Using the trigonometric relations:

$$\tan \frac{\alpha}{2} = \frac{1 - \cos \alpha}{\sin \alpha} \tag{4.3}$$

$$\tan \alpha = \frac{\sin \alpha}{\cos \alpha} \tag{4.4}$$
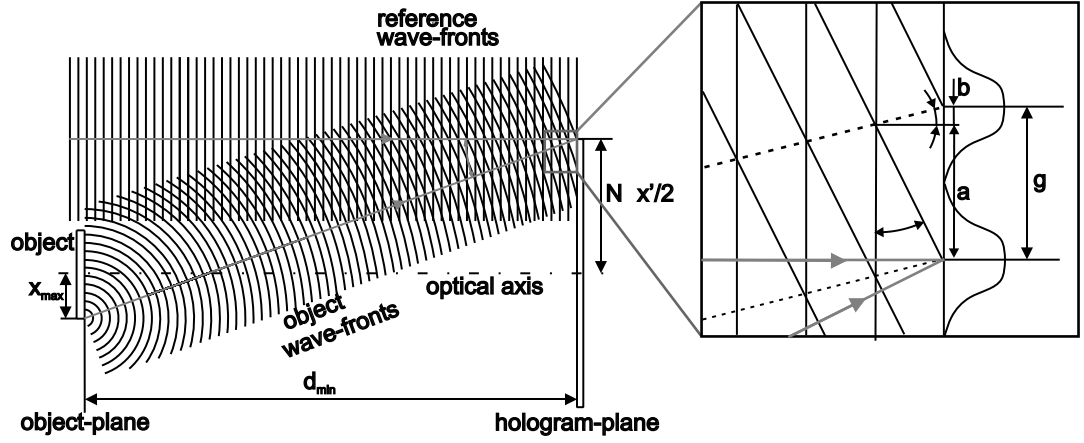
Figure 4.1: Geometry of interfering object and reference-wave when recording a Fresnel-hologram

it follows that:

$$g = \frac{\lambda}{\sin \alpha} \tag{4.5}$$

Taking into account the sampling frequency ν_{sa} results in the largest acceptable angle α:

$$\alpha \leq \arcsin \frac{\lambda \nu_{sa}}{2} = \arcsin \frac{\lambda}{2\Delta x'} \tag{4.6}$$

The object-size X and the recording distance d are mutually dependent on α. The minimum distance between camera and object shown in Fig. 4.1 is:

$$d_{min} = \frac{x_{max} + \frac{N\Delta x'}{2}}{\tan \alpha} \tag{4.7}$$

The angle α in digital holography is small, typically less than five degrees. It can therefore be assumed that $\sin \alpha = \tan \alpha$. Combining Eq. 4.6 and Eq. 4.7 results in:

$$d_{min} = \frac{(X + N\Delta x')\,\Delta x'}{\lambda} \tag{4.8}$$

Eq. 4.8 is valid for an in-line setup. An off-line setup is aimed towards a recon-

struction with spatially separated zero-order, image and twin-image. Therefore the object needs to be displaced from the optical axis by half the sensor width. The minimum distance in that case is:

$$d_{min} = \frac{2 \left(X + N \Delta x' \right) \Delta x'}{\lambda} \tag{4.9}$$

The minimum recording distance for an in-line and off-line Fresnel hologram recorded at a wavelength of 632.8 nm on a camera with 1392 pixels of 6.45 μm pixel-size and 12 mm object-size is 213.83 mm and 427.66 mm, respectively.

4.2.2   Minimum Distance Spherical Reference-wave
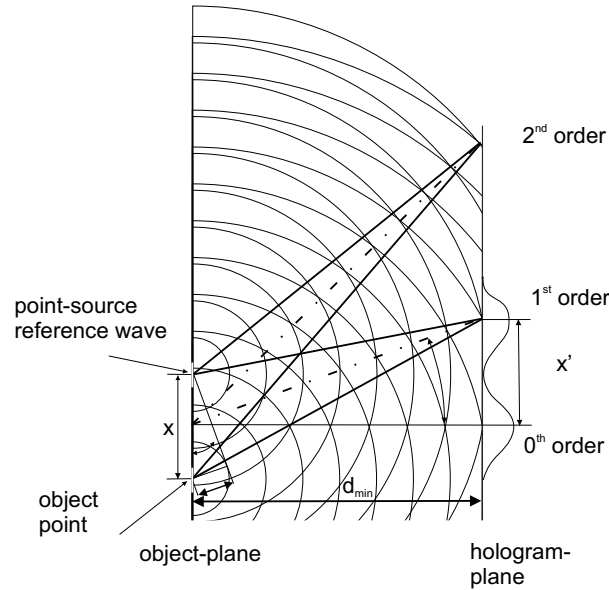
Figure 4.2: Resulting intensity pattern due to interference of spherical reference- and object-wave

From the trigonometric relations shown in Fig. 4.2 the minimum allowable recording distance can be obtained. The highest fringe density is obtained between the 1st and 0th diffraction order. Thus the path-length difference between the two propagating spherical waves, separated by the distance x, needs to be

one wavelength λ.

$$\sin \alpha = \frac{\lambda}{x} \tag{4.10}$$

$$\tan \alpha = \frac{2\Delta x'}{d_{min}} \tag{4.11}$$

Eq. 4.10 and Eq. 4.11 can be combined and solved for d_{min} assuming again that α is relatively small.

$$d_{min} \geq \frac{2\Delta x' x}{\lambda} \tag{4.12}$$

With x the distance between reference-wave source point and furthest distant object point. A hologram recorded with this kind of arrangement is refereed to as a **Fourier-hologram**. The minimum recording distance for an in-line and off-line Fourier hologram recorded at a wavelength of 632.8 nm on a camera with 1392 pixels of 6.45 μm pixel-size and 12 mm object-size is 244.63 mm and 122.31 mm, respectively.

4.2.3   Minimum Distance for Reconstruction Validity Region

The approximated reconstruction methods such as Fresnel-method and Fraunhofer-method, represented in 2.7.2 and 2.7.3, impose a certain reconstruction distance at which the phase errors introduced become negligible. In most cases recording distance d and reconstruction distance d' are matched. Therefore we have to take into account the validity condition:

$$d_{Fresnel} >> \sqrt[3]{\frac{\pi}{4\lambda} \left[(x'-x)^2 + (y'-y)^2 \right]^2} \qquad \text{for Fresnel} \tag{4.13}$$

$$d_{Fraunhofer} >> \frac{2\pi}{\lambda} \frac{x^2 + y^2}{2} \qquad \text{for Fraunhofer} \tag{4.14}$$

The optical resolution of the reconstructed hologram recorded at such far distance as $d_{Fraunhofer}$ is of rather poor quality and hence hardly used in digital holography.

Therefore, if one would like to reconstruct the hologram utilizing the Fresnel-method the smaller distance among $d_{Fresnel}$ and d_{min} needs to be taken into account when setting up the experiment. The minimum distance for the validity of the Fresnel-region and Fraunhofer region, utilizing the same parameters as applied in previous examples of Fresnel and Fourier-hologram, is 363.30 mm and 357.45 m.

4.3   Field of View (FOV)

The minimum distance d_{min} determines the object-size and hence the FOV. The FOV is an important parameter for the performance evaluation of an optical system, which will be discussed at a later stage in conjunction with the lateral resolution in 5. It is assumed that the object is positioned at d_{min} to the camera. Moreover, only the x-dimension is considered in this case. The y-dimension can be obtained in an analogue manner by taking into account the corresponding parameters. The FOV for a *Fresnel-hologram* for in-line and off-line arrangements is given by:

$$X_{in-line} = \frac{d\lambda}{\Delta x'} - N\Delta x' \qquad (4.15)$$

$$X_{off-line} = \frac{d\lambda}{2\Delta x'} - N\Delta x' \qquad (4.16)$$

The FOV for a *Fourier-hologram* for in-line and off-line arrangement is:

$$X_{in-line} = \frac{d\lambda}{\Delta x'} \qquad (4.17)$$

$$X_{off-line} = \frac{d\lambda}{2\Delta x'} \qquad (4.18)$$

The FOV for an image-hologram (image recorded in focus on camera utilizing a lens-system) depends on the sensor size $N\Delta x'$, the focal length f of the lens system* and the distance between sensor and lens system d_2. Fig. 4.3 shows a schematic sketch of the imaging process by a lens; where HH' denotes the principal-planes of the lens. The FOV obtained is thus:
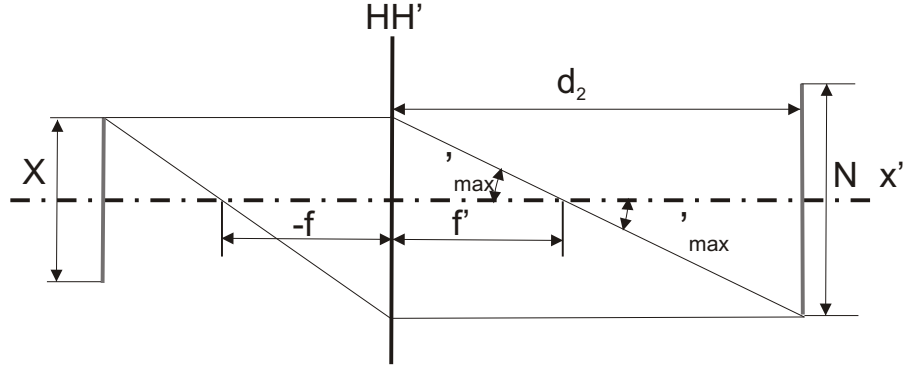
Figure 4.3: Lens field of view

$$X = \frac{N\Delta x'f}{d_2 - f} \tag{4.19}$$

4.4   Resolution

This section is devoted to the axial and lateral resolution obtained by diffraction limited optical systems. The lateral resolution is the one observed in the image or reconstruction plane, whereas the axial resolution refers to the longitudinal region for which an in-focus image can be observed. The axial resolution is also known as Depth Of Field (DOF). The axial resolution can be derived from the lateral resolution.

---

*assuming equal length of back and front-focal length

4.4.1 Lateral Resolution

The lateral resolution describes the smallest resolvable object detail in the lateral dimension. It is defined by the optical parameters of the system such as NA and the wavelength employed. Two coexisting criteria namely Abbe's criterion and Rayleigh's criterion have been developed to determine the lateral resolution with respect to the optical system employed. Abbe investigated the diffracted light as it travels from the object to the optical system as discussed in Lummer and Reiche (1910) and Rayleigh the diffraction effects caused by the spatially limited aperture in the imaging process, which is discussed in Hecht (1998).

Abbe criterion

Abbe investigated the resolution in conjunction with microscopy and realized that the resolution is determined by diffraction and the numerical aperture (NA) of the optical system. The first and zeroth diffraction order of the smallest object detail need to pass through the optical system's aperture. The two grey right-angle triangles shown in Fig. 4.4 are similar, which enables one to obtain an equation for the smallest resolvable object detail δ:

$$\delta = \frac{\lambda}{2\mathrm{NA}} = \frac{\lambda r}{nX'} = \frac{\lambda}{2n\sin\left[\mathrm{atan}\left(\frac{X'}{2d}\right)\right]} \approx \frac{\lambda d}{nX'} \tag{4.20}$$

With the refractive index $n = 1$ the following equations for rectangular and circular aperture, respectively are obtained.

$$\begin{aligned}
\delta &= \frac{\lambda r}{D} && \text{for circular aperture} \\
\delta &= \frac{\lambda r}{X'} && \text{for rectangular aperture}
\end{aligned} \tag{4.21}$$
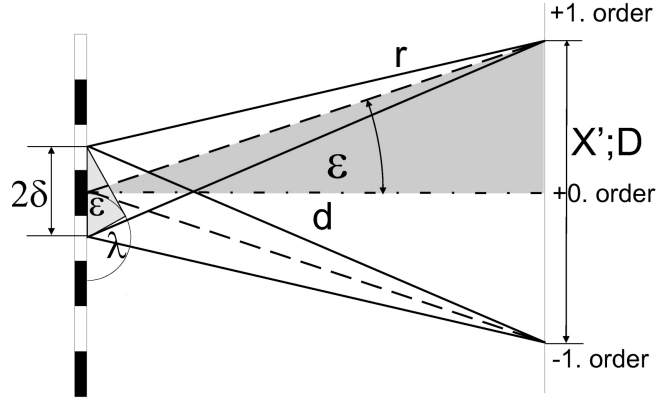
Figure 4.4: Geometry of plus first, minus first and zeroth diffraction order caused by a binary grating

Rayleigh criterion

Lord Rayleigh investigated the minimum lateral distance at which two point sources can still be resolved. He discovered that the maximum of the diffraction pattern related to the first point source needs to match with the minimum of the diffraction pattern caused by the second point source. The observed diffraction pattern can be described by a convolution of the aperture-function with the ideally sharply imaged point Goodman (1996). The angular dependent normalized intensity of the diffracted light is described mathematically by a first order Bessel-function J_1 [†]:

$$\frac{I(\varepsilon)}{I_0} = \left[\frac{2 J_1 \left(\frac{\pi D}{\lambda} \sin \varepsilon \right)}{\sin \varepsilon} \right]^2 \tag{4.22}$$

Where $\sin \varepsilon$ can be described by the axial radius r and the lateral radius in Far-field distance r_l, shown in Fig. 4.5(a):

$$\sin \varepsilon = \frac{r_l}{r}$$

The normalized intensity $\frac{I(\varepsilon)}{I_0}$ first drops to zero at 3.83, see Fig. 4.5(b). The minimum lateral radius r_l, which corresponds to the smallest resolvable object

[†]taken from Hecht (1998)

detail δ is hence described by:

$$\delta = \frac{1.22\lambda r}{D} \approx \frac{1.22\lambda d}{D} \tag{4.23}$$

In case a rectangular aperture is used, which is more appropriate for lens-less digital holography where the interference pattern is directly recorded on a rectangular sensor matrix, the diffraction pattern can be simulated by a sinc-function.

(a)   (b)
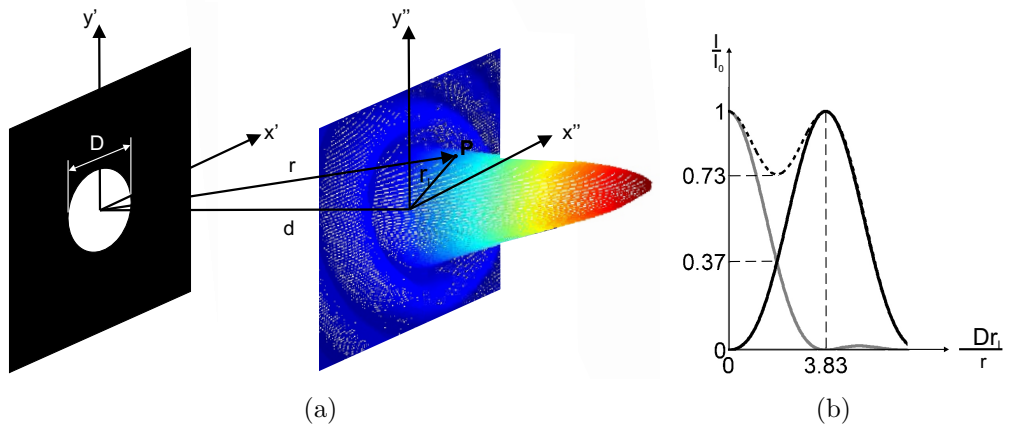
Figure 4.5: Geometry circular aperture, (b) cross-section for resulting diffraction pattern

The mathematical formulation of the sinc-function is:

$$\frac{I(\alpha', \beta')}{I_0} = \left(\frac{\sin \alpha'}{\alpha'}\right)^2 \left(\frac{\sin \beta'}{\beta'}\right)^2 \tag{4.24}$$

α' and β' can be calculated by:

$$\alpha' = \frac{\pi X' x''}{\lambda r}$$
$$\beta' = \frac{\pi Y' y''}{\lambda r}$$

Where X' and Y' are the aperture dimensions in x' and y'-direction as shown in Fig. 4.6(a). The sinc-function's first minimum occurs at ($\alpha' = \pi$), which results

in a smallest resolvable object detail δ:

$$\delta = \frac{\lambda r}{X'} \tag{4.25}$$

For a rectangular aperture Abbe's and Rayleigh's resolution criteria match. The minimum contrast obtained for a circular aperture is 0.27 whereas the minimum contrast for a rectangular aperture is 0.19, shown in Figs. 4.5(b) and 4.6(b), respectively.
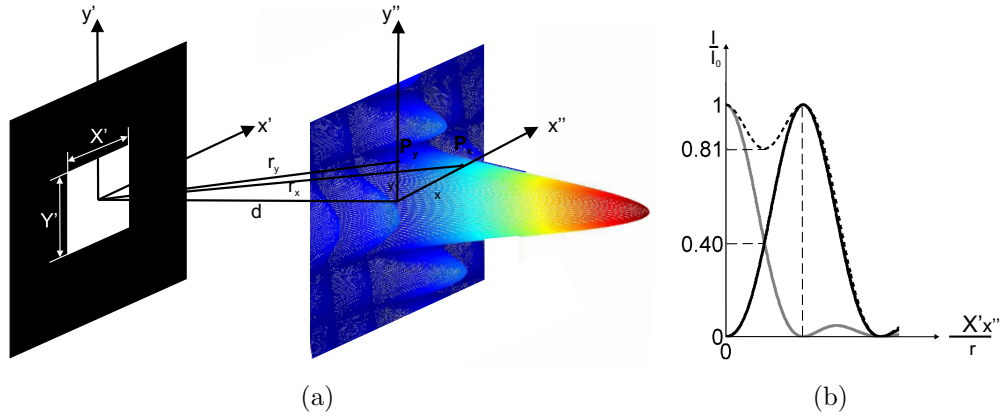
Figure 4.6: (a) Geometry rectangular aperture, (b) cross-section in x"-direction for resulting diffraction pattern

Both resolution criteria were established for incoherent illumination. In case of coherent illumination the resolution depends on the phase relationship between both point sources. The intensity cross section of two coherently superimposing point sources with respect to a rectangular aperture can be calculated as:

$$\frac{I}{I_0} = \left| \frac{\sin(\alpha' - \pi/2)}{\alpha' - \pi/2} + \exp(i\phi)\frac{\sin(\alpha' + \pi/2)}{\alpha' + \pi/2} \right|^2 \tag{4.26}$$

Where I is the obtained intensity of both superimposing point sources and I_0 is the intensity of each individual point source The resolution for two point sources of equal brightness and changing phase difference has been calculated and its

intensity cross section been plotted, shown in Fig. 4.7(a). A worse resolution is obtained if both point sources are in phase. For a phase difference $\phi = \pi/2$ the lateral resolution for coherent and incoherent illumination matches and for a phase difference of π an increased resolution is obtained. Fig. 4.7(b) shows the normalized intensity at the center of both superimposing sources points as a function of the phase difference. Generally diffuse scattering objects are investigated in digital holography. The height and hence the phase between adjacent object points changes randomly. In that manner the statistical mean of the resolution obtained can be described by the resolution obtained for the incoherent case. The validity of this assumption is experimentally confirmed at a later stage in Chapter 6.

(a)

(b)
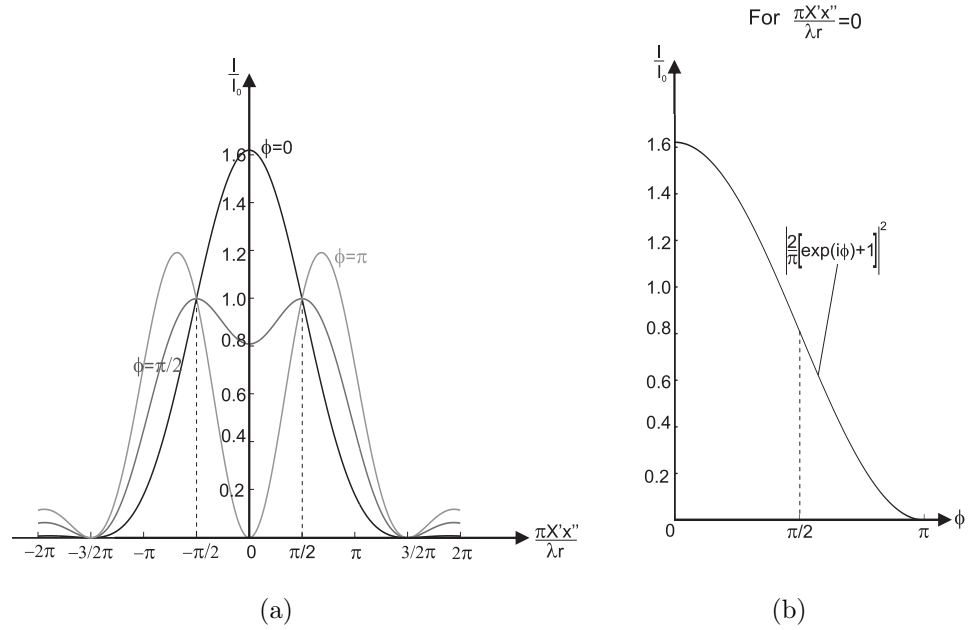
Figure 4.7: (a) Normalized image intensity for two point sources of same brightness and changing phase difference, which are separated by the Rayleigh distance with respect to a rectangular aperture, (b) normalized intensity in dependence of the phase difference

4.4.2 Axial Resolution or Depth of Field
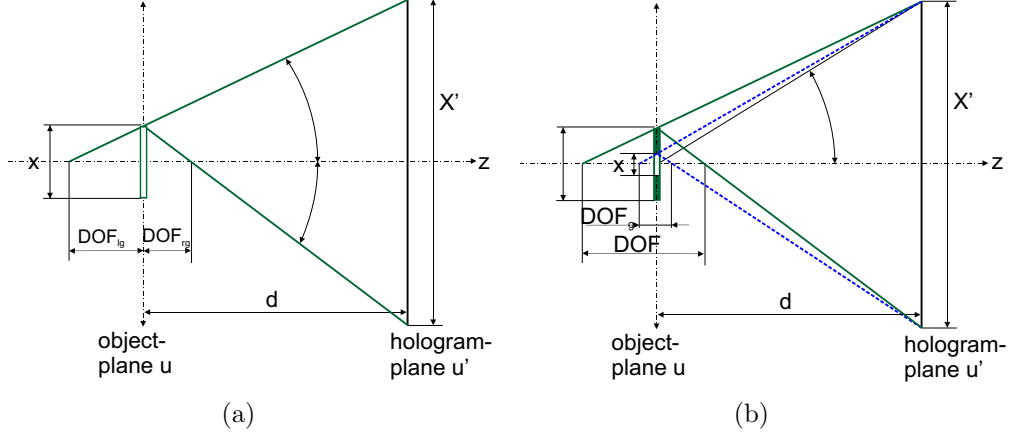
Figure 4.8: (a) Geometric-optical DOF, (b) Geometric optical DOF and wave-optical DOF

The axial resolution or Depth of Field (DOF) for the geometric optical model is defined by the circle of confusion in conjunction with the pixel-size in the reconstruction-plane $\Delta x''$. The ideal infinitesimal small image point is for the observer in-focus until the circle of confusion reaches the size of a pixel $\Delta x''$. In order to obtain the DOF $\Delta x''$ needs to be projected into the object plane. The depth of field for the geometric optical model could be derived with the help of the trigonometric relationships shown in Fig. 4.8(a).

$$\text{DOF}_g = \text{DOF}_{lg} + \text{DOF}_{rg} = \Delta x d \left(\frac{1}{X' + \Delta x} + \frac{1}{X' - \Delta x} \right) = \frac{2\Delta x d X'}{X'^2 - \Delta x^2} \quad (4.27)$$

If a lens-system with a magnification Γ' was employed between object and sensor the pixel-size in the object-plane is obtained by taking into account $\left(\Delta x = \frac{\Delta x''}{\Gamma} \right)$:

$$\text{DOF}_g = \frac{2\Delta x'' d X'}{\Gamma' \left(X'^2 - \frac{\Delta x''^2}{\Gamma'^2} \right)} \approx \frac{2\Delta x'' d}{\Gamma' X'} = \frac{\Delta x''}{\Gamma' \text{NA}} \quad (4.28)$$

For an optical system with a larger NA, such as a microscope-objective, diffraction effects have a stronger impact. The imaging process from a point in the object-

plane to a point in the reconstruction plan is subjected to the laws of diffraction (Rayleigh-criterion, Abbe-criterion). The wave-optical DOF_λ can be obtained from the diameter of the circle of confusion, which in this case is defined by the smallest resolvable object detail δ. According to Haferkorn (2003), both, the wave-optical DOF_λ and the geometric-optical model DOF_g, have to be added when an objective with a large NA is used.

$$\mathrm{DOF}_{NA} = \mathrm{DOF}_\lambda + \mathrm{DOF}_g \tag{4.29}$$

Where DOF_{NA} denotes the DOF of a large NA. A rectangular aperture, which corresponds to the shape of a digital sensor, is assumed for further considerations. Both models and their corresponding DOF are represented in Fig. 4.8(b), in which it is assumed that the projected pixel-size in the object-plane Δx is smaller than the smallest resolvable lateral object detail δ. This on the other hand imposes a condition, which needs to be fulfilled in order to display δ.

$$\Delta x \leq \delta \tag{4.30}$$

In the same manner as applied for the derivation of Eq. 4.27 the wave-optical DOF_λ can be obtained.

$$\mathrm{DOF}_\lambda = \frac{2\delta dX'}{X'^2 - \delta^2} \tag{4.31}$$

Taking into account Eq. 4.20 with the refractive index $n = 1$ results in:

$$\mathrm{DOF}_\lambda = \frac{\lambda X' \mathrm{NA} d}{X'^2 \mathrm{NA}^2 - 0.25\lambda^2} \approx \frac{\lambda}{2\mathrm{NA}^2} \tag{4.32}$$

The wave-optical DOF_λ, the lateral resolution δ in dependence of the wavelength λ and the NA used are shown in Fig. 4.9(a). The DOF_λ has slightly larger values

than δ. The difference between both decreases the larger the NA becomes.

The geometric-optical DOF_g for Fresnel-method and Fourier-method matches with the wave-optical DOF_λ. The geometric-optical DOF_g for Rayleigh-Sommerfeld method is:

$$\text{DOF}_g \approx \frac{\Delta x'}{\Gamma' \text{NA}} \tag{4.33}$$

Fig. 4.9(b) shows a plot of the DOF obtained by the geometric-optical model and wave-optical model in dependence of the NA. The NA value at which both curves meet can be considered to be the critical point $(\text{NA}_{critical})$ at which the wave-optical model needs to be taken into account as well. $\text{NA}_{critical}$ can be calculated by:

$$\text{NA}_{critical} = \frac{\lambda}{2\Delta x'} \tag{4.34}$$

In case the NA is smaller than the $\text{NA}_{critical}$ only the geometric optical field is applicable. In this case the DOF_g obtained by the Rayleigh-Sommerfeld method is smaller than the DOF_g by the Fresnel-method due to the different pixel-sizes $\Delta x''$ for both methods in the reconstruction-plane, see Table 3.5.
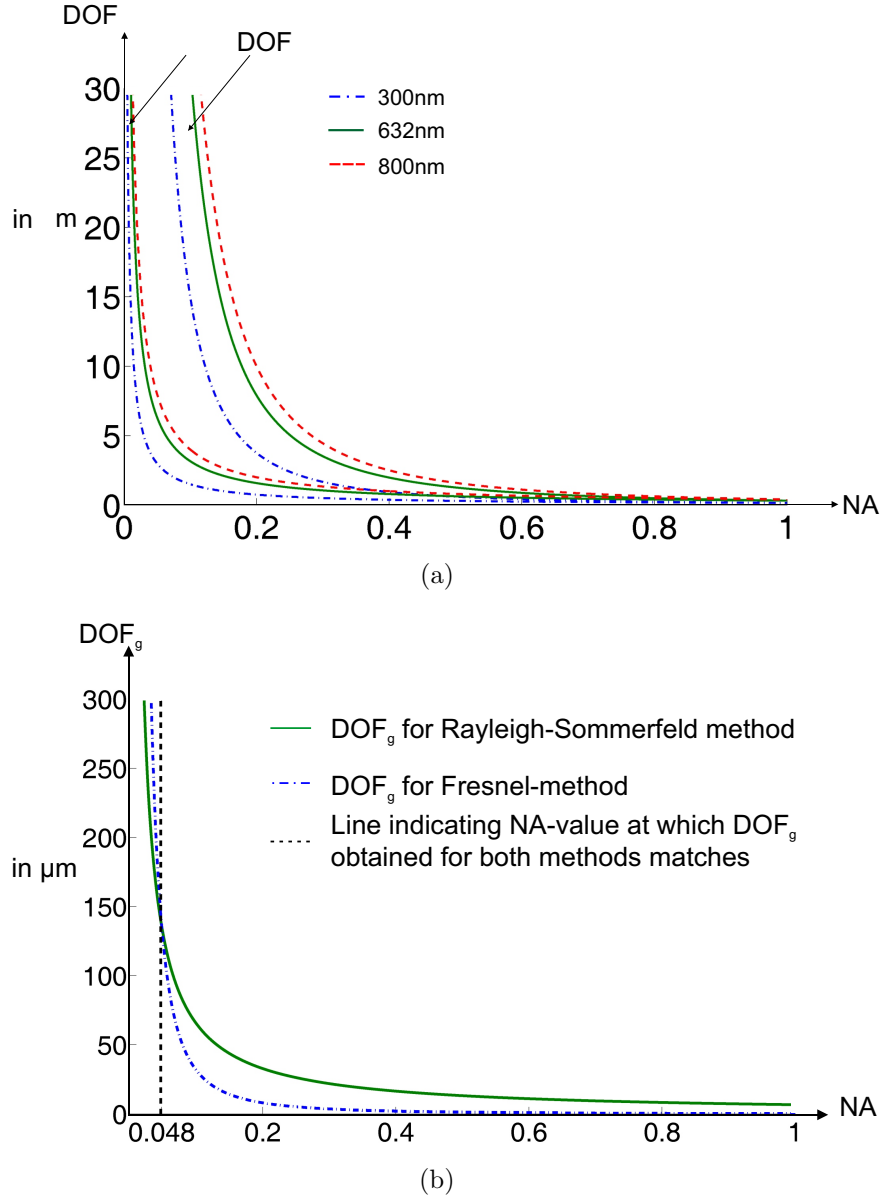
Figure 4.9: (a) DOF_λ and resolution for different wavelengths and NA, (b) DOF_g versus NA for $\Delta x' = 6.54\mu m$ and $\lambda = 632.8nm$

4.4.3 Phase Resolution

The resolution with respect to the phase is examined for the recording and reconstruction process. The phase resolution is strongly related to the number of available quantization levels of the sensor.

Resolution of recorded phase

The phase in the recording process is encoded in the sinusoidal intensity pattern. The resolution of the phase in the recording process depends on the pixel size and the grey scale quantization l_{grey}. The pixelfly camera has a dynamic range of 12 bit. That means 4096 grey levels can be applied when recording the intensity pattern. The recorded intensity pattern can be described by:

$$I(x') = 2I_0(x')\left(1 + \cos\Delta\varphi\right) \tag{4.35}$$

Eq. 4.35 assumes that the amplitudes of the object-wave and reference-wave are matched. The phase can then be calculated by:

$$\varphi = \arccos\left(\frac{I(x')}{2I_0(x')} - 1\right) \tag{4.36}$$

The averaged recordable phase difference for a 12 bit camera is:

$$\Delta\varphi_{grey} = \frac{2\pi}{l_{grey}} = 0.0015\,\text{rad} \tag{4.37}$$
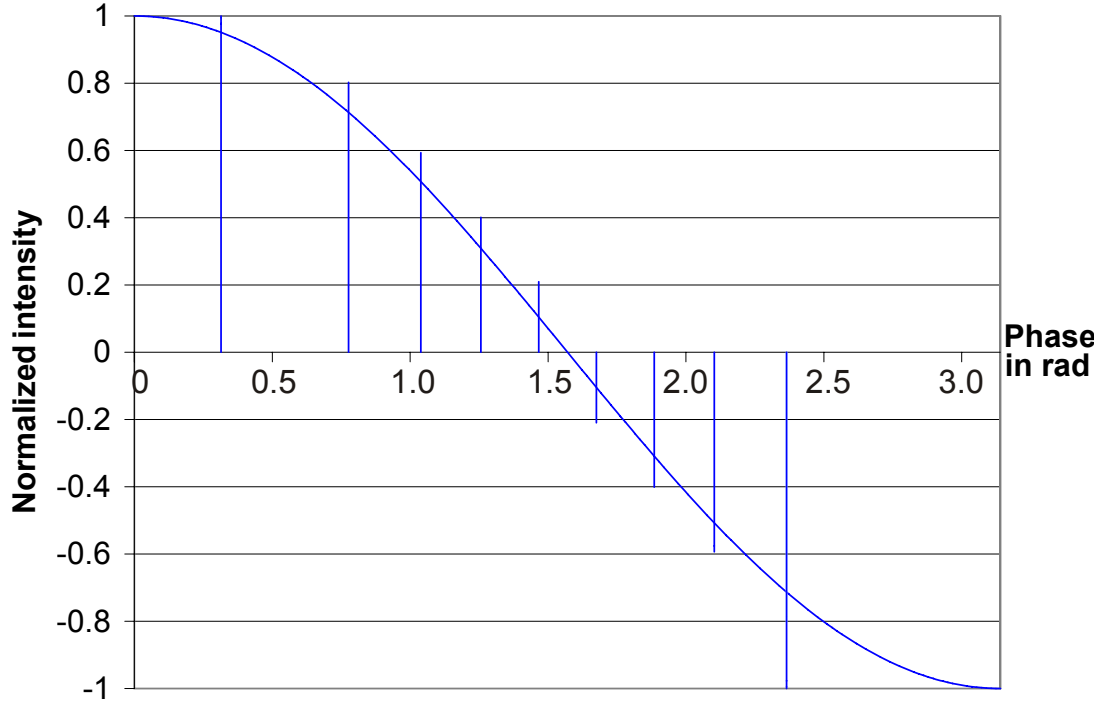
Figure 4.10: Effect of Quantization

Due to the nonlinearity of the cosine function the resolution in respect to the smallest resolvable phase difference increases in areas of stronger intensity gradient. The phase resolution in the recording process is largest near zero where the intensity gradient is largest, shown in Fig. 4.10. On the other hand the phase resolution becomes lowest near maximum and minimum amplitude value since the intensity gradient is lowest at these points. The maximum phase resolution $\Delta\varphi_{max}$ and minimum phase resolution $\Delta\varphi_{min}$ can therefore be calculated by:

$$\Delta\varphi_{max} = \frac{\pi}{2} - \arccos\frac{2}{l_{grey}} = 0.0005\,\text{rad} \tag{4.38}$$

$$\Delta\varphi_{min} = \arccos\left(1 - \frac{2}{l_{grey}}\right) = 0.0313\,\text{rad} \tag{4.39}$$

The recorded phase resolution influences the quality of the reconstructed hologram. In order to obtain a good phase resolution the camera's dynamic range

should be fully covered when recording the fringe intensity. Moreover, the sampling of the interference pattern should be sufficient so that the contrast is not significantly reduced.

4.5 Speckle

If a rough surface is illuminated with coherent light a 'grainy' intensity pattern is observed. The speckle effect is caused by the interference of coherent light scattered from different surface points. The height variation of the surface points needs to be larger than the wavelength of the coherent light source used, otherwise the surface acts like a specular surface for the incident light. The phase of the scattered waves changes randomly according to the surface point height. Hence the interference pattern observed consists of spatially stationary dark and bright points representing interference maxima and minima. The point size d_{sp_lat} increases the further away the observation-plane is located. The speckle has a cigar-like shape with an axial extension larger than the lateral extension, as shown in Fig. 4.11. The mean lateral speckle-size can be derived by the auto-correlation function applied to the observed intensity pattern. The auto-correlation of free space propagated light originating from a uniformly scattering square area of
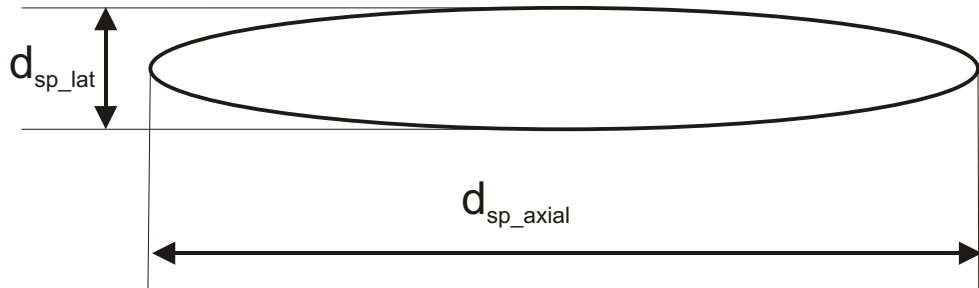
Figure 4.11: Axial and lateral speckle-size

$X \times X$ can be described by [‡]:

$$R'(x', y') = \langle I \rangle^2 \left[1 + \mathrm{sinc}^2 \left(\frac{X \delta x'}{\lambda d} \right) + \mathrm{sinc}^2 \left(\frac{Y \delta y'}{\lambda d} \right) \right] \qquad (4.40)$$

The mean speckle-size is defined between the positions at which $\mathrm{sinc}^2 \left(\frac{X \delta x'}{\lambda d} \right)$ first drops to zero.

$$d_{sp\_lat} = \frac{\lambda d}{X} \qquad (4.41)$$

The same conclusion can be drawn from Young's double slit experiment shown in Fig. 4.12(a). This kind of speckle obtained by unhindered free space propagation is called objective speckle. By analogy, speckle obtained from a setup with imaging optics is called subjective speckle. The in-focus imaged object point at distance d_2 is superimposed with a diffraction pattern caused by the spatially limited lens aperture D.

$$R'(r') = \langle I \rangle^2 \left[1 + 2 \mathrm{J_1}^2 \left(\frac{\pi D r'}{\lambda d_2} \right) \right] \qquad (4.42)$$

The lateral speckle size for a circular aperture is defined by the region between the first two minima of the Bessel-function.

$$d_{sp\_lat} = \frac{0.61 \lambda}{\mathrm{NA}} = \frac{1.22 \lambda d_2}{D} \qquad (4.43)$$

One could see an analogy to the derivation of the smallest resolvable object detail δ. The difference to the derivation of δ exists in the plane at which the features occur. For lens-less holography δ is described in the object-plane and is defined by the size of the sensor's aperture. In contrast the lateral speckle-size (d_{sp_lat}) occurs in the hologram-plane and is determined by the object-size. In case an optical system is applied, such as for the recording of image-holograms, δ and

---

[‡]taken from Goodmann (1975)

d_{sp_lat} depend on the lens-aperture D.
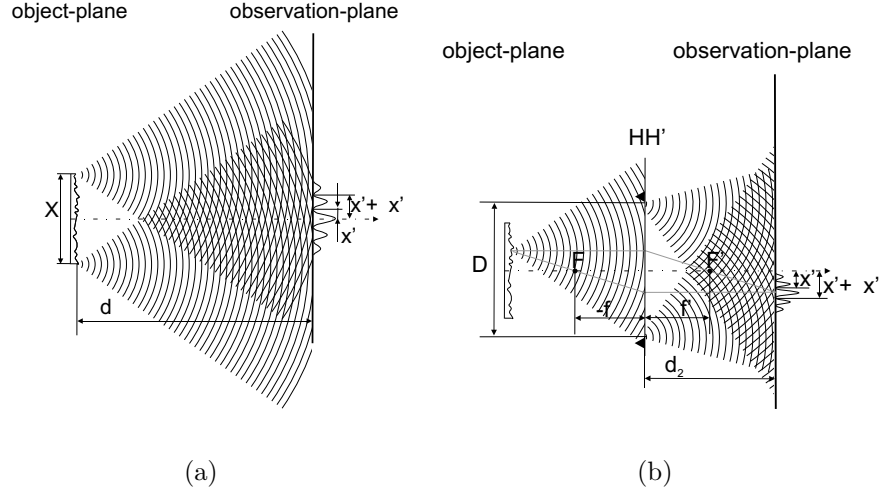
Figure 4.12: Imaging arrangement for (a) objective speckle and (b) subjective speckle

The axial speckle-size according to Ostrovsky et al. (1991) is:

$$d_{sp\_axial} = \frac{\lambda}{\mathrm{NA}^2} = \frac{4d_2^2\lambda}{D^2} \tag{4.44}$$

The speckle effect is not only apparent in the recording process but also in the reconstruction process. The speckle-size in the reconstructed hologram is determined by the hologram-size (X') and the reconstruction distance (d'). The resulting speckle-size in respect to the setup and the recording or reconstruction process is shown in Table 4.2.

4.6 Modulation Transfer Function

This section is devoted to the influence of the pixel-size, the sensor-shape and the sensor-size on the Modulation-transfer-function (MTF).

Table 4.2: Speckle-size

Speckle size d_{sp}	Lateral	Axial
Objective (recorded)	$\dfrac{\lambda d}{X}$	$\dfrac{4\lambda d^2}{X^2}$
Subjective (recorded)	$\dfrac{1.22\lambda d_2}{D}$	$\dfrac{4\lambda d_2^{\,2}}{D^2}$
Reconstructed	$\dfrac{\lambda d'}{X'}$	$\dfrac{4\lambda d'^2}{X'^2}$

4.6.1 MTF of Pixel-size

The camera has a limited capability for recording high **spatial frequencies** (ν_x') due to its pixel-size $(\Delta x')$. A parameter for the camera's frequency response is the *modulation transfer function* (MTF). It is defined as the ratio of output and input contrast (V) at each spatial frequency.

$$MTF = \frac{V_{out}}{V_{in}} \tag{4.45}$$

Where the V can be calculated by:

$$V = \frac{I_{max} - I_{min}}{I_{max} + I_{min}} \tag{4.46}$$

I_{max} and I_{min} represent the maximum and minimum intensity levels. The MTF of a system indicates how the various frequencies are affected by the system.
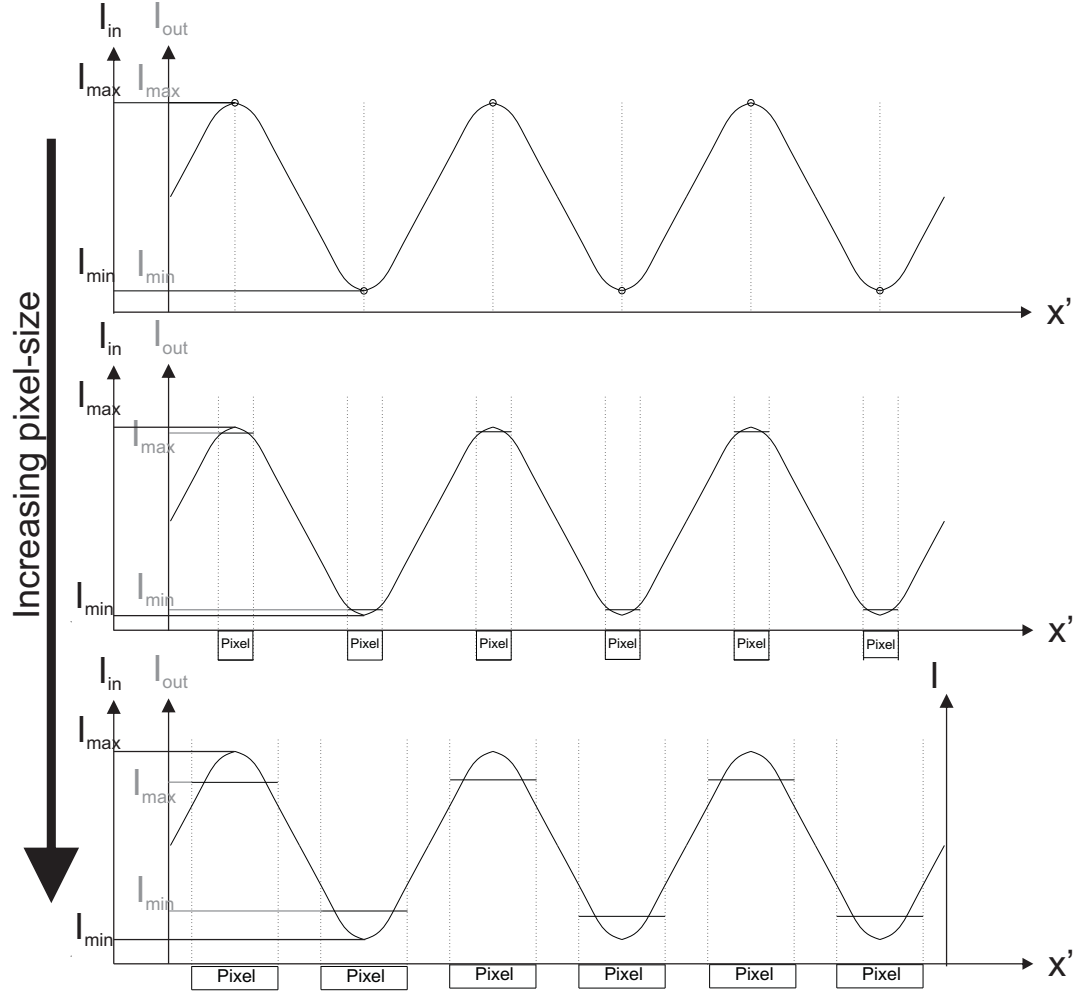
Figure 4.13: Sampling with different pixel-sizes

With increasing pixel-size $\Delta x'$ the bandwidth of the MTF decreases (see Fig. 4.13). According to Boreman (2001) the pixel MTF can be calculated by:

$$MTF_{pixel} = \left| \frac{\sin (\pi \Delta x' \nu_{x'})}{\pi \Delta x' \nu_{x'}} \right| = |\text{sinc} (\Delta x' \nu_x')| \qquad (4.47)$$

Fig. 4.14 shows the pixel MTF including the cutoff frequency $\left(\nu_{cutoff} = \frac{1}{\Delta x'} \right)$ and the Nyquist frequency $(\nu_{Nyquist})$. The Nyquist frequency defines the maximum sampling frequency ν_{sa}. The recording of spatial frequencies ν_x' larger than $\nu_{Nyquist}$ causes aliasing, which results in disturbing imaging features when
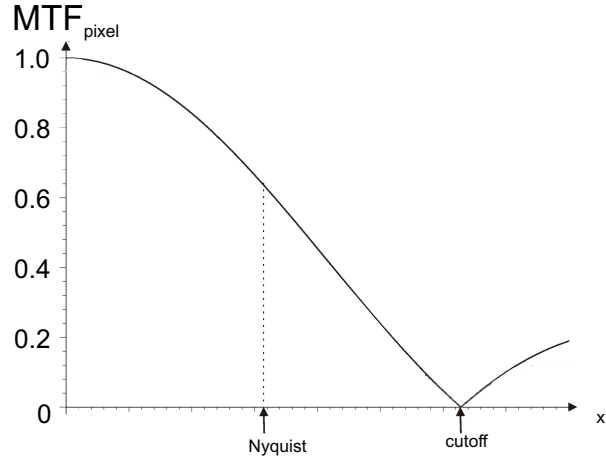
Figure 4.14: Graph pixel MTF

reconstructing the hologram such as ghost images.

4.6.2 MTF for Lens-less and Image-Holography

The sensor's MTF considers how various spatial object frequencies (ν_x) are affected by the sensor's size and shape. The MTF is represented by the auto-correlation of the sensor's aperture-function.

Lens-less Hologram

In the case of lens-less holography the hologram is directly recorded on a rectangular sensor. The auto-correlation function of a rectangle is a triangle, which results in a MTF:

$$MTF\left(\nu_x\right) = 1 - \frac{\nu_x}{\nu_{cutoff}} \tag{4.48}$$

Where the cutoff-frequency represents the reciprocal of the smallest resolvable object detail. In case of lens-less holography the minimum resolvable object detail is determined by Abbe's criterion, see Eq. 4.21.

$$\nu_{cutoff} = \frac{N\Delta x'}{\lambda d} \tag{4.49}$$

Doubling the NA or using a light-source of half the wavelength results in twice the cutoff frequency, which is shown in Fig. 4.15(a).

Image-Hologram

A lens-system is employed between object and hologram. The recorded spatial frequency content is determined by the aperture of the lens-system, which generally has a circular shape. According to Boreman (2001) the autocorrelation function for a circular aperture is defined as:

$$MTF\left(\nu_x\right) = \frac{2}{\pi}\left[\arccos\frac{\nu_x}{\nu_{cutoff}} - \frac{\nu_x}{\nu_{cutoff}}\sqrt{1 - \left(\frac{\nu_x}{\nu_{cutoff}}\right)^2}\right] \tag{4.50}$$

Here the cutoff-frequency is defined by Rayleigh's-criterion applied to a circular aperture, see Eq. 4.23:

$$\nu_{cutoff} = 0.82\frac{D}{\lambda d} \tag{4.51}$$

A comparison between the MTF obtained for a lens-less hologram and an image-hologram is shown in Fig. 4.15(b). It was assumed that the sensor size $N\Delta x'$ matches the diameter of the lens system D. In conclusion, the MTF obtained by lens-less holography possesses a larger spatial frequency bandwidth $(\Delta\nu)$ and a better contrast than the MTF-curve obtained with image-holography. This statement is based on the assumption that both systems have the same NA and the same wavelength λ. Hence the introduction of a lens-system should be avoided unless the object is either too small or too large to be recorded utilizing lens-less holography.
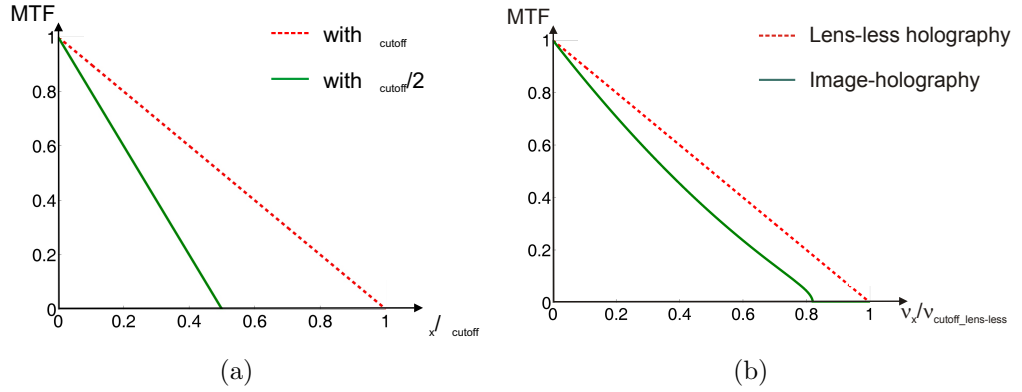
Figure 4.15: (a) Influence of ν_{cutoff} based on a rectangular aperture, (b) Comparison between lens-less holography with rectangular aperture and image-plane holography with circular aperture

The MTFs shown in Fig. 4.15 correspond to incoherent illumination. According to Goodman (1996), the MTF for coherent illumination possesses a uniform maximum value defined over the whole frequency range. At the cutoff-frequency the MTF drops down to a value of zero. The cutoff-frequency for coherent illumination is half the cutoff-frequency for incoherent illumination. It could be concluded that incoherent illumination results in a better image resolution. However, it was pointed out by Goodman (1996) that the cutoff-frequency in the coherent case determines the maximum frequency of the image amplitude, while the cutoff-frequency in the incoherent case refers to the maximum frequency of the image intensity. Therefore, the resolution obtained for both cases is not directly comparable. It depends on the object's phase distribution. Experimental results, presented in Chapter 6, and the cutoff-frequency calculation used by other authors, such as Mico et al. (2006) and Ostrovsky et al. (1991), recommend that the resolution for the reconstructed hologram can best be predicted utilizing the incoherent illumination. Therefore, the resolution for the incoherent case is applied hereafter.
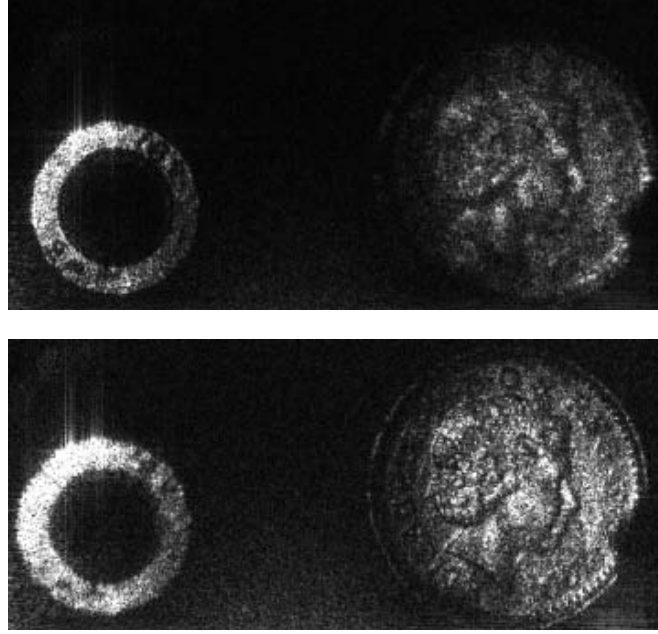
Figure 4.16: Cropped numerical reconstruction, (a) at 1020mm and (b) at 1090mm reconstruction distance

4.7 Properties of Digital Holography

4.7.1 Storage of 3-Dimensional Information

Holographic images are capable of storing **three dimensional information**. This property can be demonstrated by placing two objects at different distances to the camera. An M6 nut (10 mm width across flats) and a five pence coin (18 mm diameter) have been placed at different distances to the camera. A single hologram was recorded. Afterwards the Fresnel-method was used to reconstruct the holograms. The reconstruction distances d' applied ranged from 1000 mm to 1180 mm whereas the reconstruction was performed in 5 mm steps. The nut is in focus at 1020 mm, shown in Fig. 4.16(a). At 1090 mm the coin is sharply focused whereas the nut is now out of focus, see Fig. 4.16(b). The depth of field, which was discussed previously in Section 4.4.2 , determines the sensitivity for the axial range at which the object appears in-focus.

Figs. 4.16(a) and (b) prove the three dimensional storage capability of digital holography.

4.7.2   Homogenous Information Distribution

In the case of lens-less holography, light from each point of an object is distributed over the entire sensor. Therefore, each small region of the recorded hologram holds information of the entire object. Reducing the size of the region used for the reconstruction only affects the resolution of the reconstructed hologram, but not its size or the parts displayed. This property of holography is demonstrated by Fig. 4.17. Some parts of the hologram have been covered by a mask. Nevertheless, the object is still visible in the numerical reconstruction. The shape of the mask can be seen in the DC-term since it represents the zero order, which is build up by the undiffracted transmitted light. To prove that all regions hold information of the object, the hologram was covered with the inverted mask. Pixels which used to hold information are now covered by the inverted mask and vice versa. However, the object's image is still displayed in the reconstruction, see Figs. 4.17(e) and (f). The resolution of the reconstructed image decreased due to a reduction of the available reconstructing pixels. This effect can be interpreted as a decreasing aperture, which results in an increased speckle size and a reduced resolution.

(a)

(b)

(c)

(d)

(e)

(f)
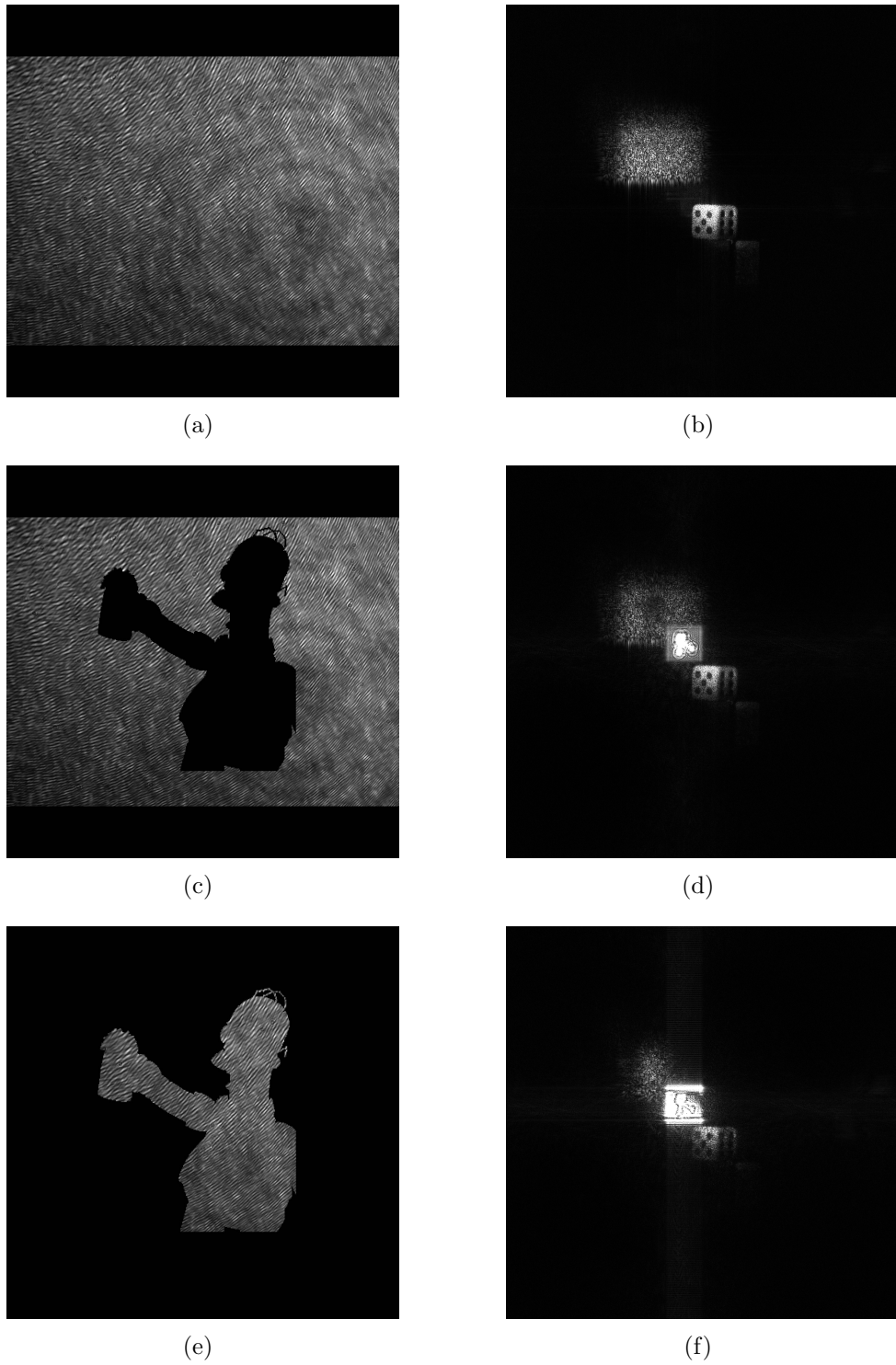
Figure 4.17: (a) Digital hologram (b) Numerical reconstruction suppressing DC-term (c) Masked hologram (d) Reconstruction (e) Negatively masked hologram (f) Reconstruction

In the case of image-holography the light from an object point illuminates a small region of the hologram. Therefore, the reconstruction of a fragment of the hologram displays only the corresponding part of the object.

4.7.3 Direct Phase Accessibility
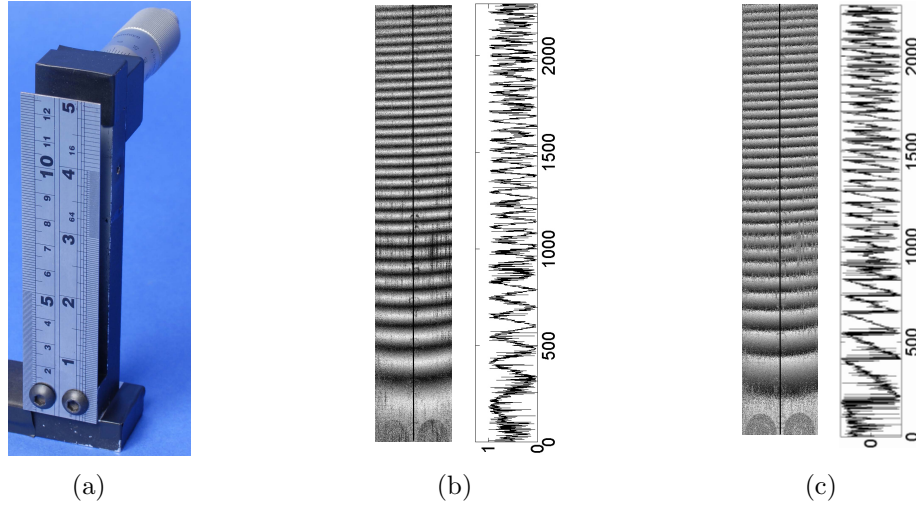
Figure 4.18: (a) Object under investigation, (b) cropped ambiguous double-exposure intensity reconstruction, (c) cropped unambiguous double-exposure phase reconstruction

If a hologram is reconstructed a complex wave field is generated holding amplitude and phase information of the object under investigation. In optical holography the reconstruction is perceived by a receiver which is only intensity sensitive such as the human eye. The phase information in this case is not directly accessible. In digital holography the reconstruction is performed numerically, which directly enables the separation of amplitude and phase information. This is demonstrated by means of double exposure holography. Double exposure holography is an important method when in-plane or out-of-plane deformations need to be investigated with sub-micrometer precision. Fig. 4.18(b) shows the normalized modulus of the double-exposure phase-map as obtained by optical holography including

its cross-section, which is indicated by a black line. A double-exposure phase map is obtained by subtraction of the numerical reconstruction of two holograms recorded at different object states, un-deformed and deformed. In optical holography the reconstruction results in a sinusoidal ambiguous intensity fringes. The direction of deformation is unknown. However, the phase reconstruction of the digital double-exposure hologram shown in Fig. 4.18 is unambiguous. The direction of deformation is known, which is a major advantage of digital holographic interferometry in comparison to optical holographic interferometry.

Sensitivity vector

The double-exposure phase map needs to be evaluated in order to obtain the magnitude of the deformation applied to the object under investigation. The position of the illumination and observation point determines the setup's displacement sensitivity, which can be described by the *sensitivity vector* $\vec{K}$. $\vec{K}$ can be derived with the help of Fig. 4.19, which results in the following vectorial notation:

$$\vec{K} = \vec{k_i} - \vec{k_o} \tag{4.52}$$

The *illumination wave-vector* $\vec{k_i}$ and *observation wave-vector* $\vec{k_o}$ are defined by:

$$\vec{k_i} = \frac{2\pi}{\lambda} \vec{n_i} \qquad \vec{k_o} = \frac{2\pi}{\lambda} \vec{n_o} \tag{4.53}$$
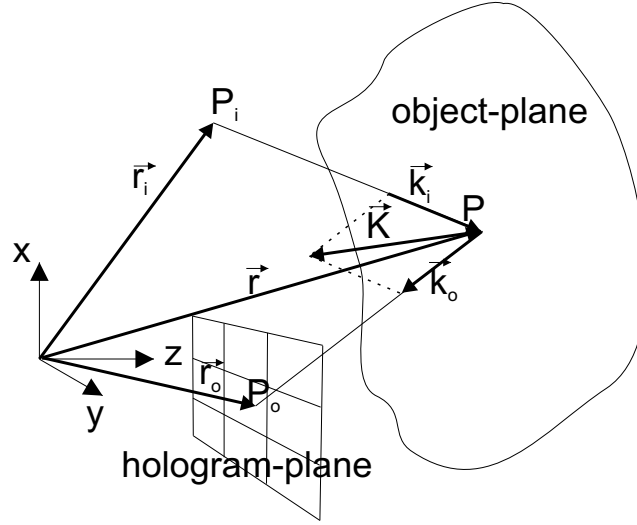
Figure 4.19: Setup geometry with illumination and observation point

Where $\vec{n}_i$ and $\vec{n}_o$ represent the corresponding unit vectors. The unit vector $\vec{n}_i$ can be calculated by the distance between illumination point P_i and object point P.

$$\vec{n}_i = \frac{\vec{r} - \vec{r}_i}{|\vec{r} - \vec{r}_i|} \tag{4.54}$$

$\vec{n}_o$ can be obtained in a similar manner.

$$\vec{n}_o = \frac{\vec{r}_o - \vec{r}}{|\vec{r}_o - \vec{r}|} \tag{4.55}$$

A displacement of the object causes a change of the object-vector $\vec{r}$. The displacement is of small magnitude typically a few microns compared to the magnitude of the vectors $\vec{r}$, $\vec{r}_o$ and $\vec{r}_i$, which are in the meter range. Therefore it can be assumed that $\vec{n}_i$ and $\vec{n}_o$ remain constant for loaded and unloaded object states.

$$\Delta\vec{r} = \vec{r}_2 - \vec{r}_1 \tag{4.56}$$

Where $\vec{r_1}$ indicates the initial object position and $\vec{r_2}$ the object's position after the displacement occurred. The phase change $\Delta\varphi$ obtained utilizing digital holography is related to the displacement $\Delta\vec{r}$ by:

$$\Delta\varphi = \vec{K} \cdot \Delta\vec{r} \tag{4.57}$$

Out-of-plane displacement measurement

The setup geometry for measuring out-of-plane deformation is shown in Fig. 4.20. The sensitivity to detect *out-of plane-displacement* is largest when illumination vector $\vec{k_i}$ and observation vector $\vec{k_o}$ are parallel to each other.
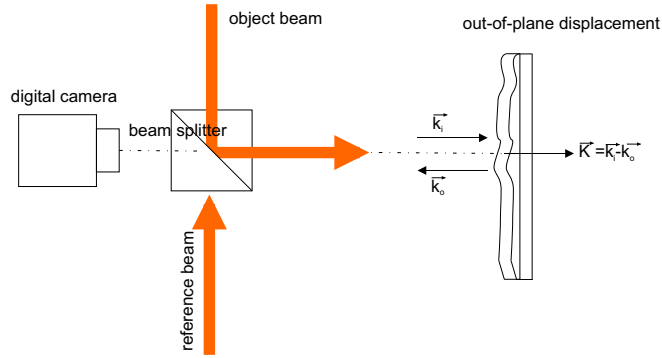
Figure 4.20: Setup geometry for measuring out-of plane displacement

Moreover, both vectors are perpendicularly orientated to the object surface. The resulting sensitivity vector $\vec{K}$ is:

$$\vec{K} = \frac{4\pi}{\lambda}\vec{n_i} \tag{4.58}$$

One can assume that $\vec{K}$ is constant for the entire object if a collimated beam was used to illuminate the object.

In-plane displacement measurement

The measurement of in-plane displacement can be accomplished by illuminating the object with two beams of corresponding illumination vector $\vec{k_{i1}}$ and $\vec{k_{i2}}$. The angle of both beams in respect to the observation vector $\vec{k_o}$ is matched but opposite in sign, as shown in Fig. 4.21. The magnitude of the resulting sensitivity vector is related to the angle α, as discussed in Doval (1999).

$$|\vec{K}| = \frac{4\pi}{\lambda} \sin\alpha \tag{4.59}$$

In that manner the sensitivity can be adjusted to range between zero and $\frac{4\pi}{\lambda}$. A good ratio between recorded scattered light from the object and reasonable sensitivity is obtained by $\alpha = 45°$.
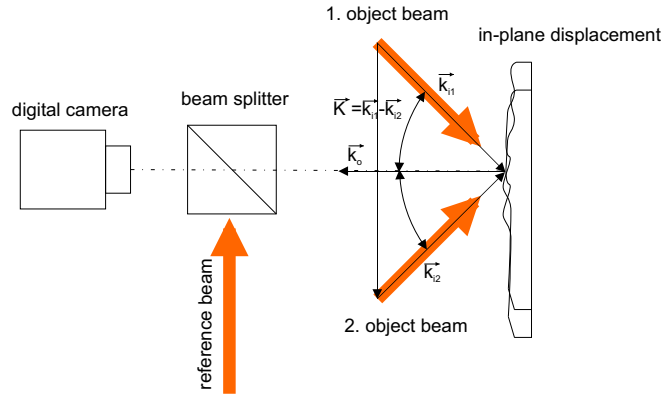
Figure 4.21: Setup geometry for measuring in-plane displacement

Out-of-plane double exposure experiment

An experiment for out-of-plane displacement was performed. The object under investigation was a cantilever shown in Fig. 4.18(a). A micrometer screw was attached to the cantilever, which enabled the application of an adjustable and controllable displacement with micrometer accuracy.
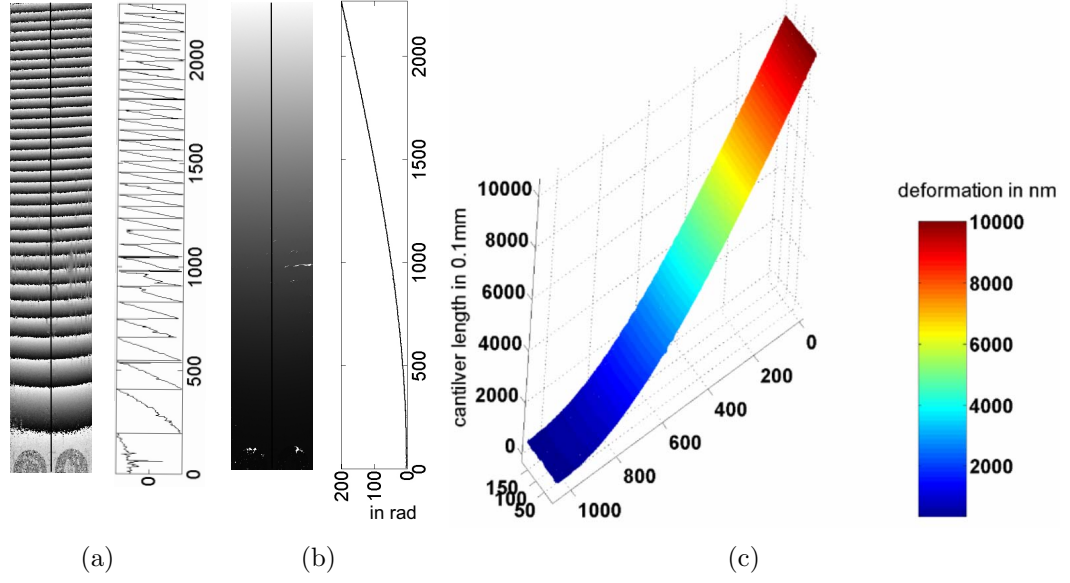
Figure 4.22: (a) 5x5 Median filtered wrapped phase map, (b) Goldstein's cut-line algorithm unwrapped phase map, (c) deformation map

In that manner the results obtained by digital double exposure holography could be validated. Two holograms, one of the initial object state u'_1 and a second one after the deformation was applied to the object u'_2, were recorded. The magnitude of the applied deformation was 10 μm. Both holograms were numerically reconstructed and their reconstructed phase subtracted from each other.

$$\Delta u''(x'', y'') = \frac{u''_2(x'', y'')}{u''_1(x'', y'')} \tag{4.60}$$

The corresponding phase difference in respect to the deformation applied is:

$$\Delta\varphi(x'', y'') = \arctan\frac{\Im\left\{\Delta u''(x'', y'')\right\}}{\Re\left\{\Delta u''(x'', y'')\right\}} \tag{4.61}$$

The subtraction was performed in exponential notation, which results in a better phase contrast compared to subtracting the individually calculated phase maps of each reconstructed hologram. The double-exposure phase map obtained including cross-section is shown in Fig. 4.18(c). Where the x-axis of the cross-section

denotes the cantilever length (L_c) and the y-axis the phase-difference in rad between both object states ($\Delta\varphi$). Afterwards the 2π discontinuities were removed utilizing unwrapping. The unwrapping was performed with the free software HoloVision 2.2 [§] and 'Goldstein's cutline' algorithm, which is implemented in this software. Prior to the unwrapping procedure a median filter was applied to the obtained double exposure phase map to reduce the impact of speckle-noise, which otherwise would result in unwrapping errors. In order to maintain the modulation between π and $-\pi$ the phase is split into its sine and cosine components. The median filter is implemented in Matlab as 'medfilt2' function, which was applied to each individual component. The filtered double exposure phase map, shown in Fig. 4.22(a), was then obtained by applying the atan function.

$$\Delta\varphi_{filtered}(x'', y'') = \arctan\left[\frac{\text{medfilt2}\left(\sin\Delta\varphi(x'', y'')\right)}{\text{medfilt2}\left(\cos\Delta\varphi(x'', y'')\right)}\right] \tag{4.62}$$

The obtained unwrapped phase data, shown in Fig. 4.22(b), was transformed to deformation data by taking into account the sensitivity vector $\vec{K}$, shown in Fig. 4.22(c). The obtained result was then compared with the predicted results. The bending model curve of a cantilever fixed at one end can be derived from Cartwright (2001):

$$z = \frac{z_{max}}{2L_c^3}\left(x^3 - 3L_c^2 x + 2L_c\right) \tag{4.63}$$

Where L_c is the length between the point at which the cantilever is fixed to the point at which the micrometer screw touches the cantilever and z_{max} the displacement applied to the cantilever at L_c. z_{max} applied was 10 μm. Both the obtained and predicted bending curves are shown in Fig. 4.23. The residual to the predicted curve is -0.0128 ± 0.0639 μm. Hence the standard deviation obtained is $\frac{\lambda}{10}$ which matches the expected accuracy claimed by other authors.

[§]developed by Tuft and Øystein (2009) http://www.edge.no/projects/
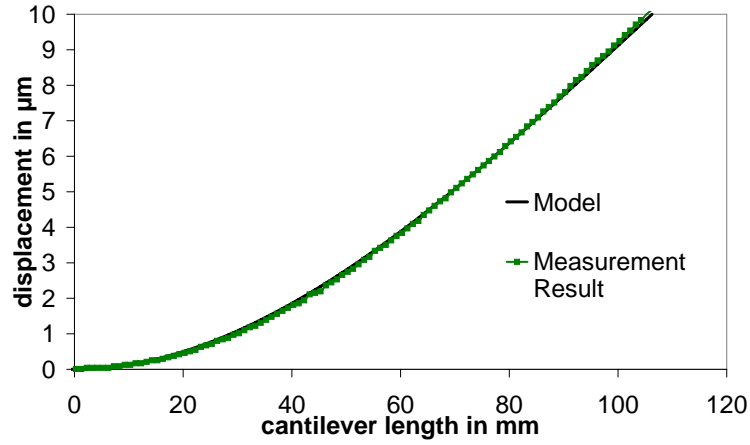
Figure 4.23: Graph experimental data compared to model curve

4.7.4 Resolution Beyond Rayleigh-criterion

The sharply in-focus point arising from the geometric-optical model is convolved with the rectangular aperture-function. In that way the wave-optical model, which represents the diffraction limit due to the aperture is accounted for. The resolution theory describing this effect is known as Rayleigh criterion, see Section 4.4. On the other hand the diffraction limit in the recording process, described by
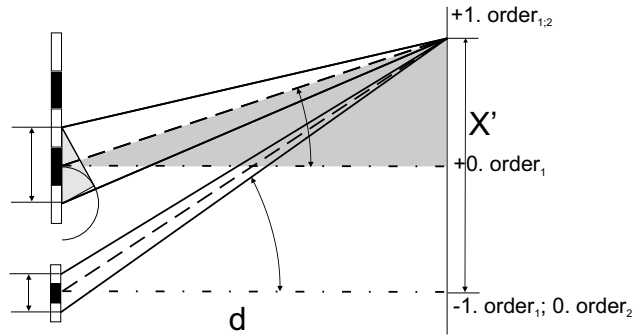
Figure 4.24: Recording of higher spatial frequencies

the Abbe-criterion enables the recording of twice the spatial resolution. According to Abbe, zeroth and first order need to be recorded in order to reconstruct an object detail. This condition is already fulfilled in case zeroth and plus first diffraction order are recorded, shown in Fig. 4.24, because plus and minus first order are conjugated complex pairs and hold identical information. One needs to expand the hologram utilizing zero-padding to at least twice its size in order to be able to reconstruct these spatial frequencies, which otherwise would be lost in the convolution process with the aperture function.

(a)   (b)

(c)   (d)
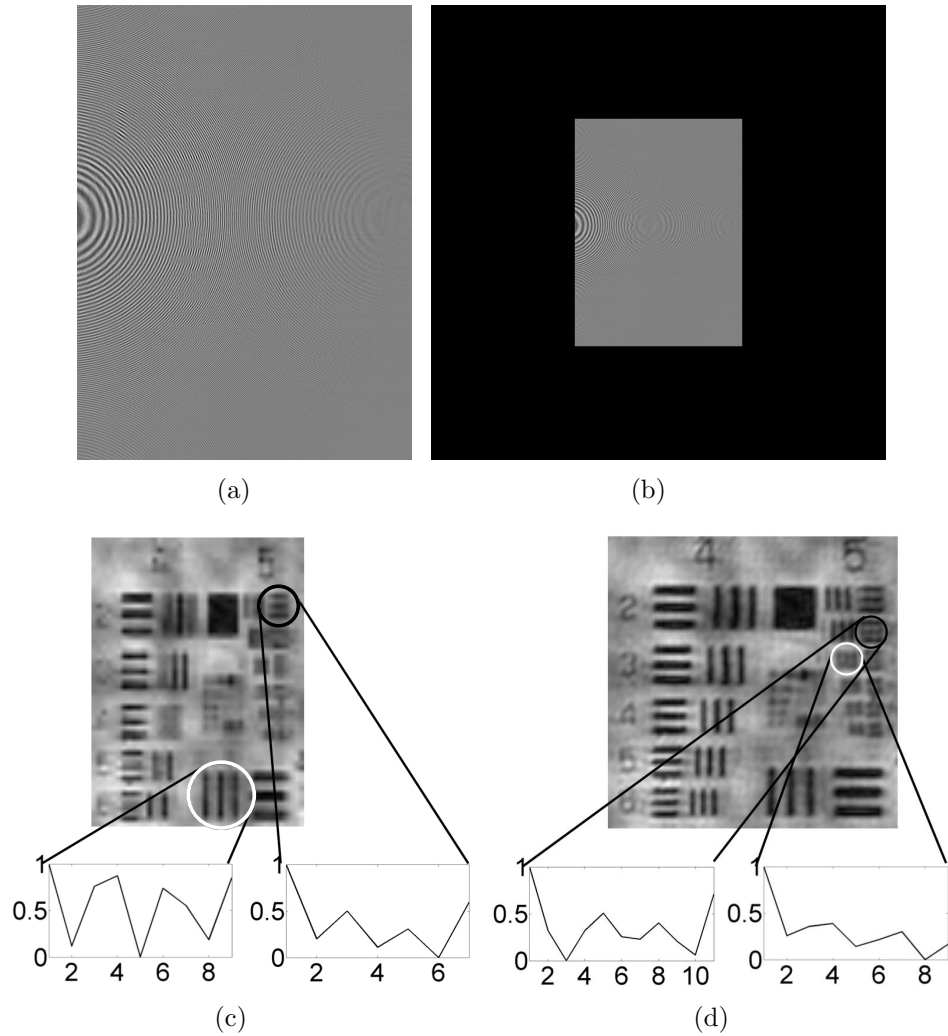
Figure 4.25: (a) Hologram 3000x2208 pixels, (b) zero-padded hologram 6000x6000 pixels, (c) cropped reconstruction of (a), cropped reconstruction of (b)

Table 4.3: Theoretical and practically achieved resolution

Parameters	Vertical resolution in μm	horizontal resolution in μm
Predicted for 3000x2208 pixels	24.2	17.8
Obtained for 3000x2208 pixels	31.3	15.6
Obtained for zero-padded 6000x6000 pixels	13.5	12.4

A hologram of the USAF 1951 resolution test-target was recorded at 295 mm distance. The camera used consists of 3000x2208 pixels and a 25 mW HeNe-Laser with 632.8 nm wavelength was employed. The resolution for vertical and horizontal direction was calculated according to Rayleigh's criterion applied to a rectangular aperture, see Eq. 4.25. The smallest resolvable test target element was determined by calculating an averaged cross section for the investigated element. The cross sections are shown in Fig. 4.25(c) and (d), where the x-axis denotes the pixel-number and the y-axis the normalized intensity. Care was taken so that local minima are visible (black strips) and the ratio of the largest local minima to the smallest local maxima is less than 0.81 according to the resolution criterion for a rectangular aperture shown in Fig. 4.6. In order to view the smallest resolvable object detail a small region has been selected. The black ring in Fig. 4.25 encircles the horizontal resolution and the white ring the vertical one. The same approach to evaluate the resolution obtained is applied in this thesis hereafter. The values for the predicted resolution and the experimentally obtained resolution is presented in Table 4.3. The resolution obtained for the reconstruction of the 3000x2208 pixels hologram matches with the predicted values. Apart from different pixel-numbers, astigmatism could have caused a different resolution in x and y direction due to the recording of an off-line hologram. The resolution utilizing zero-padding could be increased by a factor of 2.3 in vertical direction and 1.3 in horizontal direction. Thus, the

averaged resolution increased by a factor of 1.8, which is close to the expected resolution improvement of factor two. A diffusely scattering object might enhance the resolution obtained. The further enhancement effect can be explained by considering a single point within a small object region enclosing this point. The point has the characteristic that the undiffracted light from the zeroth order holds a certain angle to the optical axis, which enables the recording of one of the first diffraction orders and zeroth order only. This effect can even be enhanced by tilted object illumination, which is discussed in Ishizuka (1994). The process of only recording one of the first diffraction orders and zeroth order was coined *single-side-band holography* by Lohmann (1956).

4.8 Conclusion

Optical Parameters have been derived, which are important to evaluate digital holographic systems presented hereafter. The resolution improvement beyond Rayleigh's criterion needs to be pointed out at this stage. The resolution improvement by zero-padding was realized by other authors such as Gyímesi et al. (2009) and P.Ferraro et al. (2008), but to my knowledge no explanation for the improved resolution was presented.

CHAPTER 5

Space bandwidth product (SBP)

5.1   Introduction

In digital holography the interference pattern produced by the superimposition of reference and object-wave is stored in discrete values by a digital camera e.g. CMOS, CCD. It is assumed that the object under investigation has a finite extent and is centered on the optical axis. Thus the maximum and minimum object extension x, y and $-x$, $-y$ are of same magnitude but opposite sign:

$$
\begin{aligned}
-x \leq X \leq x \quad &\Rightarrow \quad |x| \leq \frac{X}{2} \\
-y \leq Y \leq y \quad &\Rightarrow \quad |y| \leq \frac{Y}{2}
\end{aligned}
\tag{5.1}
$$

Moreover, it is assumed that the continuously defined spatial frequency spectrum $(\Delta\nu = \Delta\nu_x \cdot \Delta\nu_y)$ of the object has significant values only in a finite region. Hence, the object can be considered to be approximately band-limited. The frequency bandwidth $\Delta\nu_x$ and $\Delta\nu_y$ of the object is defined by its highest spatial

object frequency ν_{x_max} and ν_{y_max}, which results in the following relations:

$$
\begin{aligned}
-\nu_{x\_max} \leq \Delta\nu_x \leq +\nu_{x\_max} &\quad \Rightarrow \quad |\nu_{x\_max}| \leq \frac{\Delta\nu_x}{2} \\
-\nu_{y\_max} \leq \Delta\nu_y \leq +\nu_{y\_max} &\quad \Rightarrow \quad |\nu_{y\_max}| \leq \frac{\Delta\nu_y}{2}
\end{aligned}
\tag{5.2}
$$

The total amount of sampling points for the object is given by:

$$
SBP = XY\Delta\nu_x\Delta\nu_y \tag{5.3}
$$

Where X and Y are the object's spatial dimensions. The number of sampling points represents the Space-Bandwidth Product (SBP). The SBP is the physical quantity which describes the information capacity of an optical system. The SBP of the reconstructed hologram is defined as a product of the field of view (FOV) and the highest resolvable spatial frequency ν_{x_max}. The highest spatial frequency is represented by the inverse of the smallest resolvable object detail δ, which was discussed in Section 4.4.1. In order to record a hologram successfully the SBP of the holographic system should be larger than that of the object to ensure no loss of object-information. This section focuses on the required SBP′ of the sensor in the recording process and the obtained SBP″ in the reconstruction process. The nomenclature of the SBP in the recording process SBP′ (hologram-plane) and reconstruction process SBP" (reconstruction-plane) is in accordance with Fig. 3.1. The recording efficiency of different digital holographic setup configurations is analyzed and compared. Furthermore, the performance capacity in terms of the reconstructed FOV and the smallest resolvable object detail are investigated. An in depth study of the SBP in digital holography was conducted by Lohmann (1967) and Xu et al. (2005). Lohmann (1967) studied the most commonly applied holographic setup configurations, the Fresnel-hologram, Fourier(Fraunhofer)-hologram and Image-hologram.

A Fresnel-hologram is recorded when the free space propagated object-wave interferes with a plane reference-wave. A *Fourier-hologram* is recorded when an equidistant spherical reference-wave and an object-wave interfere in the hologram-plane. Lohmann analyzed the holographic setups in an off-line arrangement. Moreover, his investigation of Fourier-holograms were based on a lens, which converted the reference and object point source into plane waves. The Fourier-holograms discussed in this thesis are based on a lens-less setup. Xu et al. (2005) discussed the SBP for Fresnel-holograms in in-line and off-line configurations. In that manner, the next pages desribe an extension of the work conducted by Lohmann (1967) and Xu et al. (2005).

An important property of the SBP is that its size remains constant for the same optical signal, which is defined in one dimension as $X\Delta\nu_x$.

(a) (b) (c)

(d)
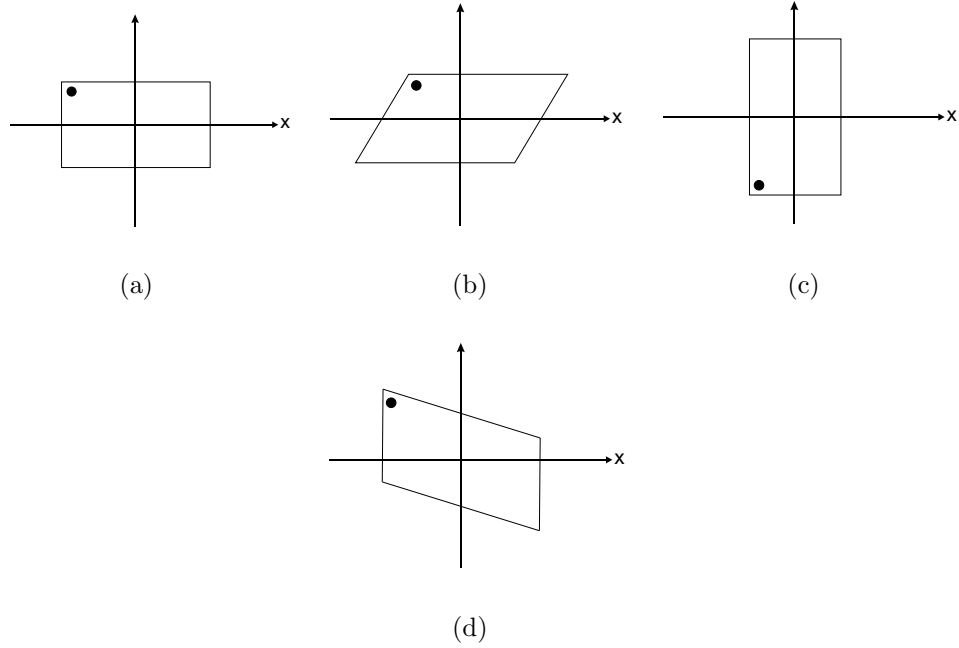
Figure 5.1: Adopted Figs. taken from Lohmann (1996) (a) SBP in the space-frequency domain, (b) SBP of (a) after Fresnel-transformation, (c) SBP of (a) after Fourier-transformation, (d) SBP of (a) after passage through lens

Hence the area of the SBP is independent of the transformation applied to it. The SBP can be described in the space-frequency domain. The impact of an optical transform such as Fresnel-transform or Fourier-transform on the space-coordinates and spatial frequency coordinates representing the SBP can be obtained utilizing the Wigner-distribution function:

$$W(x, \nu_x) = \int u(x + x'/2)u^*(x + x'/2) \exp(2\pi i \nu_x x') \mathrm{d}x' \qquad (5.4)$$

where x denotes the spatial coordinate of the signal and x' the spatial coordinate of the optical system. Further information of the Wigner-distribution function can be found in Lohmann (1967) and Lohmann (1996). It is assumed that the original one dimensional SBP of the object is rectangular as shown in Fig. 5.1. A Fresnel-transformation applied to the original SBP results in a shear of the spatial coordinate in the space-frequency domain (Fig. 5.1(b)). The original SBP is rotated by 90° when a Fourier-transformation is applied to it (Fig. 5.1(c)). A shear in the spatial frequency coordinate is introduced by the passage of light through a lens or lens-system, see Fig. 5.1(d).

5.2 Required SBP′ of The Recording Sensor

This section focuses on how efficiently the sensor's SBP′ is used in respect to the optical arrangement. For simplicity only the one dimensional case is considered. An object with the lateral extension X and a spatial frequency band-width $\Delta\nu$ has a SBP of:

$$SBP = X\Delta\nu \qquad (5.5)$$

Instead of the Wigner-distribution function the impact of optical transforms on the space and spatial frequency coordinate is obtained from the resulting inter-

ference between reference-wave and object-wave. The propagation of light from the object to the hologram was simulated using the Fresnel-method, for which the spherical wavefront is approximated by a parabolic wavefront (Eq. 2.50).

5.2.1 Fresnel-hologram

The object is illuminated with a collimated laser beam. The point x_o in the object-plane is chosen to be located on the optical axis as shown in Fig. 5.2. The object can be modeled as a grating with a grating frequency ν_o. The largest resolvable grating frequency ν_o is determined by the size of the sensor X according to Abbe's criterion, see Section 4.4.1. We can simplify the grating to a double slit, which corresponds to two point sources A_{o1} and A_{o2}, which are located close to x_o. Both point sources are separated by:

$$x_{o2} - x_{o1} = 2\delta = \frac{1}{\nu_o} \tag{5.6}$$

Due to only considering a single point in the object-plane u(x) the integral over dx in Eq. 2.50 can be dropped. Hence, the propagation of light from both points
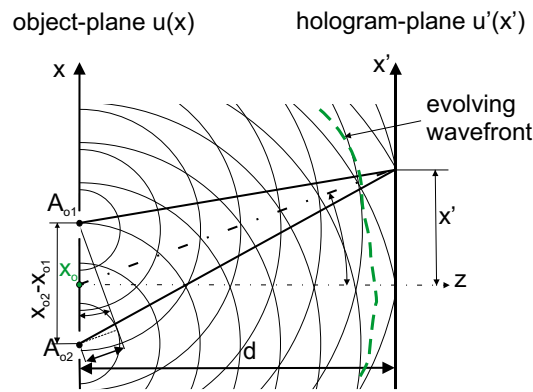
Figure 5.2: Interference pattern caused by smallest resolvable object detail

in the object-plane to the hologram-plane can be described by:

$$u'_{o1}(x') = A_{o1} i\lambda d \exp\left[\frac{i\pi}{\lambda d}(x' - x_{o1})^2\right] \tag{5.7}$$

$$u'_{o2}(x') = A_{o2} i\lambda d \exp\left[\frac{i\pi}{\lambda d}(x' - x_{o2})^2\right] \tag{5.8}$$

The resulting interference pattern from both point sources and its corresponding intensity becomes:

$$I = |u'_{o1}(x') + u'_{o2}(x')|^2 = [u'_{o1}(x', y') + u'_{o2}(x', y')] \cdot [u'_{o1}(x', y')^* + u'_{o2}(x', y')^*]$$

$$= A_{o1}^2 + A_{o2}^2 + 2A_{o1}A_{o2}\cos\left[\frac{\pi}{\lambda d}2x'(x_{o2} - x_{o1})\right]$$

$$\tag{5.9}$$

The phase term $(x_{o1}^2 - x_{o2}^2 \approx 0)$ contributes to a constant phase only and is therefore neglected for further considerations. The interference of both propagating point sources at x_{o1} and x_{o2} results in a linear phase difference (phase tilt) according to Eq. 5.9. Between both propagating waves *no* parabolic phase difference exists, since both possess the same curvature. According to Huygens' principle these two point sources generate a newly evolving propagating distorted parabolical wave, see Fig. 5.2 (dashed green line). The object information is stored in the wavefront distortion. The phase of the parabolic object-wave is visualized when the object-wave interferes with a reference-wave of different curvature. The propagating object-wave can therefore be described as:

$$u'_o(x') = A_o \exp\left[i\frac{2\pi}{\lambda d}x'(x_{o2} - x_{o1})\right]\exp\left[\frac{i\pi}{\lambda d}(x' - x_o)^2\right] \tag{5.10}$$

Eq. 5.10 gives an overview of all phase terms involved in the setup of the object-wave. According to Lohmann (1967) the linear phase term $\left(\frac{2\pi}{\lambda d}x'(x_{o2} - x_{o1})\right)$ can

be replaced by $(2\pi\nu_o x')$. Hence Eq. 5.10 is rewritten as:

$$u'_o(x') = A_o \exp\left(i2\pi\nu_o x'\right)\exp\left[\frac{i\pi}{\lambda d}\left(x' - x_o\right)^2\right].$$ (5.11)

At the hologram-plane u'(x') the spherical object-wave, parabolically represented in Eq. 5.10, interferes with a plane reference-wave, shown in Fig. 5.3. The plane reference-wave can be described as:

$$u'_r(x') = A_r \exp\left(-i2\pi\nu_r x'\right)$$ (5.12)

Where ν_r corresponds to the reference-wave's frequency. The interference pattern obtained can be described by the intensity of the interference between object-wave and reference-wave:

$$
\begin{aligned}
I(x') &= \left| A_o \exp\left(i2\pi\nu_o x'\right)\exp\left[\frac{i\pi}{\lambda d}\left(x' - x_o\right)^2\right] + A_r \exp(-i2\pi\nu_r x'_{max}) \right|^2 \\
&= A_o^2 + A_r^2 + A_o A_r \exp\left[i2\pi x'\left(\nu_o + \nu_r\right)\right]\exp\left[\frac{i\pi}{\lambda d}\left(x' - x_o\right)^2\right] \\
&\quad + A_o A_r \exp\left[-i2\pi x'\left(\nu_o + \nu_r\right)\right]\exp\left[\frac{-i\pi}{\lambda d}\left(x' - x_o\right)^2\right] \\
&= A_o^2 + A_r^2 + 2A_o A_r \cos\left[2\pi x'\left(\nu_o + \nu_r\right) + \left\{\frac{\pi}{\lambda d}\left(x' - x_o\right)^2\right\}\right]
\end{aligned}
$$ (5.13)
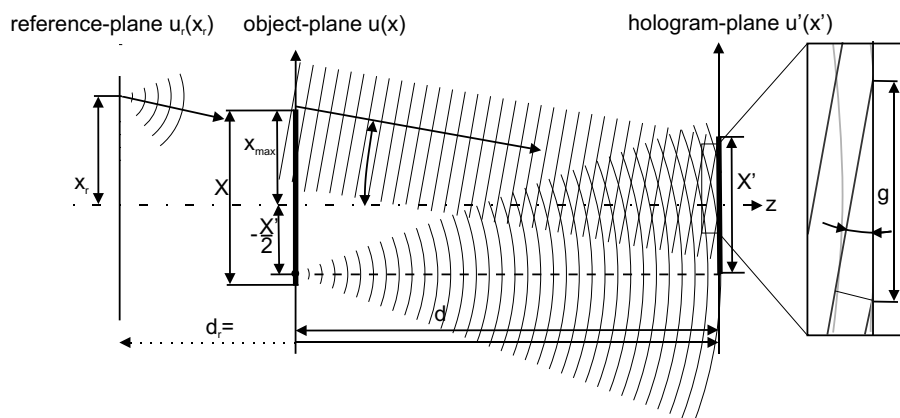
Figure 5.3: Spatial frequency introduced by inclination of plane reference-wave

The recorded intensity pattern arising from both phase terms in Eq. 5.13 can be interpreted as a Fresnel-lens with focal length $f = -d$. This Fresnel-lens is slightly distorted by the spatial frequency of the object point and the reference frequency $(\nu_o + \nu_r)$. From the geometric relations shown in Fig. 5.4 follows:

$$x' = x_o + \lambda d \nu_o \tag{5.14}$$

This means that the recorded data is spatially localized in the hologram-plane, which is caused by the parabolic term $\left\{ \frac{\pi}{\lambda d} (x' - x_o)^2 \right\}$ in Eq. 5.13. The parabolic term needs to be numerically compensated for the correct reconstruction of the object phase. However, it does not hold any additional object information and is therefore not taken into account for the spatial frequency consideration.

In-line Setup

For an in-line setup, $\nu_r = 0$, the spatial frequency recorded is ν_o. Hence the transformation of the spatial and frequency coordinates is:

$$(x_o, \nu_o) \rightarrow (x'_o, \nu'_o) \tag{5.15}$$

$$\rightarrow (x_o + \lambda d \nu_o, \nu_o) \tag{5.16}$$
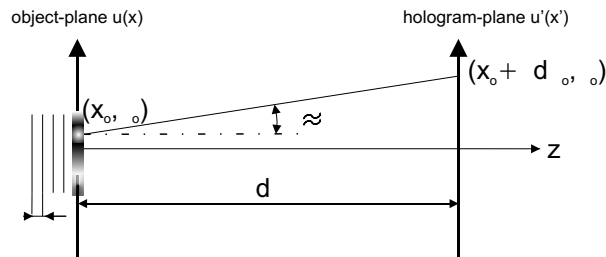
Figure 5.4: Diffracted cone of light from object coordinate x_o to hologram-plane

Where the prime notation ($'$) represents the parameters in the hologram-plane. The SBP$'$ for an in-line Fresnel-hologram is:

$$\begin{aligned} SBP'_{in-line} &= SBP\left(1 + \frac{\lambda d\Delta\nu}{X}\right) \\ &= SBP(1 + \frac{X'-X}{X}) \leq 2SBP \end{aligned}$$

(5.17)

The result shown in Eq. 5.17 represents the optimum case for which $(X' = 2X)$ according to Lohmann (1967).

Off-line Setup

For an off-line Fresnel setup the reference-wave and object-wave interfere at an angle α. Thus a spatial carrier frequency ν_r is superimposed with the object information. The recorded intensity contains three spatial frequency components, and a lateral coordinate shift, as previously discussed. The corresponding space-frequency-coordinate transformation is:

$$(x_o, \nu_o) \to (x_o + \lambda d\nu_o, [-(\nu_o + \nu_r), 0, (\nu_o + \nu_r)])$$

(5.18)

In this case the SBP$'$ is:

$$SBP'_{off-line} = (X + \lambda d\Delta\nu)(\Delta\nu + 2\nu_r)$$

(5.19)

The main advantage of an off-line setup is its ability to suppress twin- image and zero-order term by solely recording a single hologram and filtering those terms in the frequency domain as discussed in Section 3.3.3. In that case ν_r and the corresponding angle α need to be chosen in a way to spatially separate the image, twin-image and zero-order term in the reconstructed hologram. This is especially valid for short reconstruction distances, since the blurred twin-image increases in

sharpness the smaller the reconstruction distance becomes. The zero-order term is caused by the undiffracted light. Hence its size matches with the sensor size (X'). In order to avoid an overlap of zero-order term, image (X")* and twin-image in the reconstructed hologram ν_r needs to be:

$$\nu_r \geq \frac{X + X'}{2\lambda d} \tag{5.20}$$

Rearranging Eq. 5.18 results in:

$$X' - X = \lambda d \Delta \nu \tag{5.21}$$

Both equations, Eq. 5.20 and Eq. 5.21, are combined to:

$$2\nu_r \geq \frac{X' - X + 2X}{\lambda d} = \Delta \nu + \frac{2X}{\lambda d} \tag{5.22}$$

Eq. 5.22 is inserted in Eq. 5.19:

$$\boxed{\begin{aligned} SBP'_{off-line} &= (X + \lambda d \Delta \nu)(2\Delta \nu + \frac{2X}{\lambda d}) \\ &= 2X\Delta\nu + \frac{2X^2}{\lambda d} + 2\lambda d\Delta\nu^2 + 2X\Delta\nu \\ &= 2SBP\left(2 + \frac{X}{\lambda d\Delta\nu} + \frac{\lambda d\Delta\nu}{X}\right) \geq 8SBP \end{aligned}} \tag{5.23}$$

Again the optimum case for which $X' = 2X$ was applied. Hence the term $\frac{X}{\lambda d\Delta\nu}$ in conjunction with Eq. 5.21 could be reduced. In conclusion, the off-line configuration requires the sensor's SBP' to be four times larger than for the in-line configuration. The SBP' for both configurations is shown in Fig. 5.5.

---

*X" matches with the object-size (X) and can hence be replaced by it
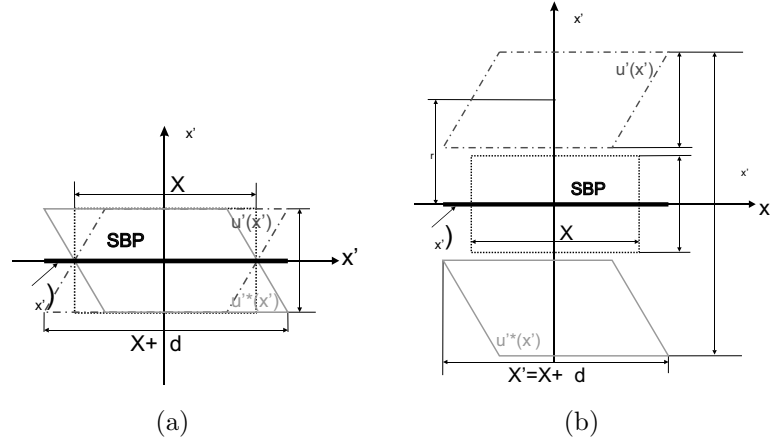
Figure 5.5: SBP of a Fresnel-hologram, (a) in-line arrangement, (b) off-line arrangement

5.2.2 Fourier-hologram

The reference-wave's frequency of a Fourier-hologram depends on the object-size X. The highest spatial reference frequency is obtained from the interference of the emitted light from the reference point-source and the object point-source. The object point-source considered is the one located furthest distant from the reference-wave source point, see Fig. 5.6. The complex object-wave and reference-wave can hence be described by:

$$u'_o(x') = A_o \exp\left(2i\pi x'\nu_o\right) \exp\left[\frac{i\pi}{\lambda d}\left(x' - x_o\right)^2\right] \tag{5.24}$$

$$u'_r(x') = A_r \exp\left[\frac{i\pi}{\lambda d_r}\left(x' - x_r\right)^2\right] \tag{5.25}$$

The assumptions previously made in Section 5.2.1 are equally valid for the investigation of Fourier holograms. Moreover, the distances d_r and d for the point sources of reference and object-wave to the hologram-plane are matched $(d_r = d)$.
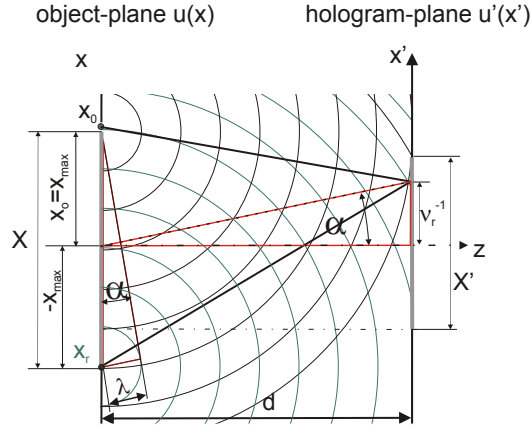
Figure 5.6: Spatial frequency introduced by laterally offsetting the origin of the spherical reference-wave

The intensity pattern recorded can then be described by:

$$I(x') = A_r^2 + A_o^2 + A_oA_r \exp\left[\frac{i\pi}{\lambda d}\left\{2x'\nu_o\lambda d + (x' - x_o)^2 - (x' - x_r)^2\right\}\right]$$

$$+ A_oA_r \exp\left[\frac{-i\pi}{\lambda d}\{...\}\right] \tag{5.26}$$

The focus is now set on solving the complex exponential term in the curly brackets.

$$\{...\} = 2x'\nu_o\lambda d + (x' - x_o)^2 - (x' - x_r)^2 \tag{5.27}$$

The second and third term in $\{...\}$ are responsible for the reference frequency:

$$(x' - x_o)^2 - (x' - x_r) = -2x'x_o + x_o^2 + 2x'x_r - x_r^2 \tag{5.28}$$

From Fig. 5.6 follows that $x_r = -x_{max}$ and $x_o = x_{max}$, which results in:

$$(x' - x_o)^2 - (x' - x_r)^2 = -4x'x_{max} \tag{5.29}$$

The two similar triangles defined by the angle α shown in Fig. 5.6 (highlighted in red) result in the expression:

$$x_r = x_{max} = \frac{\nu_r \lambda d}{2} \tag{5.30}$$

Eq. 5.26 can be rewritten by substituting x_{max} in Eq. 5.29 with Eq. 5.30:

$$I(x') = A_r^2 + A_o^2 + 2A_o A_r \cos\left[2\pi x' \left(\nu_o - \nu_r\right)\right] \tag{5.31}$$

The spherical phase factor inherent to recording of Fresnel-holograms is eliminated by using a spherical reference-wave of equal curvature. This results in a space-coordinate transformation:

$$x' = \lambda d \nu_o \tag{5.32}$$

This means that the object information is *not* localized, on the contrary it is spread over the entire hologram.

In-line Setup

The transformation from the object to the hologram plane for the in-line configuration ($\nu_r = 0$) can be described as:

$$(x_o, \nu_o) \rightarrow (x'_o, \nu'_o) = (\lambda d \nu_o, \nu_o) \tag{5.33}$$

The resulting $SBP'_{in-line}$ is:

$$\boxed{SBP'_{in-line} = \lambda d \Delta \nu \cdot \Delta \nu = X \Delta \nu = SBP} \tag{5.34}$$
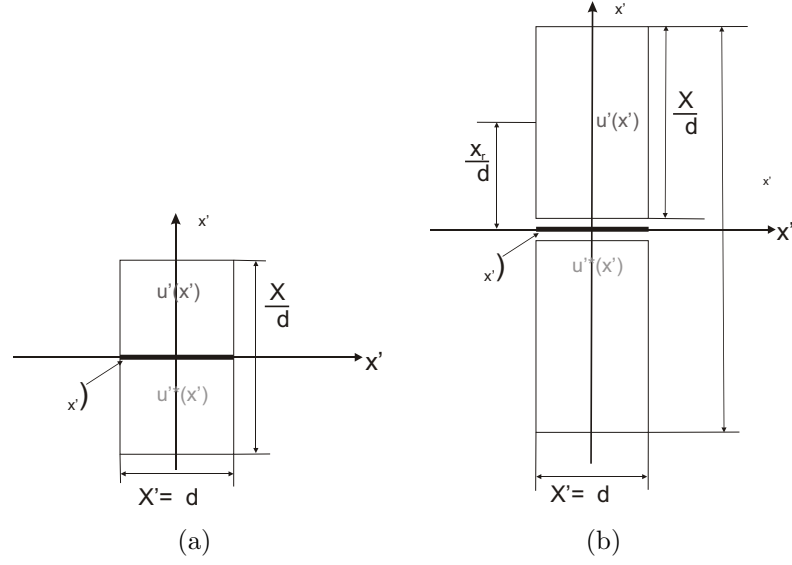
Figure 5.7: SBP of a Frourier-hologram, (a) in-line arrangement, (b) off-line arrangement

Off-line Setup

In the off-line case three different spatial frequency terms (side-bands) arise as previously discussed:

$$(x_o, \nu_o) \rightarrow (x'_o, \nu'_o) = (\lambda d \nu_o, -(\nu_o - \nu_r), 0, (\nu_o - \nu_r)) \qquad (5.35)$$

The $SBP_{off-line}$ is:

$$SBP'_{off-line} = (\nu_r + \nu_o)(\lambda d \Delta \nu)$$
$$\left(\frac{2x_r}{\lambda d} + \frac{x'}{\lambda d} \right) (\lambda d \Delta \nu) \qquad (5.36)$$

With $x_r = \frac{X}{2}$ and $x' = \frac{X'}{2}$ the $SBP'_{off-line}$ obtained is:

$$\boxed{SBP'_{off-line} = \left(X + \frac{X'}{2} \right) \Delta \nu \geq 2SBP} \qquad (5.37)$$

The result presented in Eq. 5.37 does again assume the optimum case ($X' = 2X$) according to Lohmann (1967).

5.2.3 Image-Hologram

The object is imaged onto the sensor with a lens or a lens-system. The recording of the real image of the object instead of the object itself can have some advantages [Hariharan (1984)]. It is possible to position the projected image of the object when recording the hologram. It is often used when the object is three dimensional but not very deep in the third dimension [Goodman (1996)], which is the case in digital holographic microscopy. Moreover, the resolution can be increased for the investigation of lateral object details in the sub-micrometer range. The viewing angle and the highest recordable spatial frequency is restricted by the NA of the imaging lens. In order to analyze the spatial frequency content of both interfering waves the influence of the individual propagation components, shown in Fig. 5.8, need to be investigated. This is again obtained by simulating the propagation of light from the object-plane u(x) to the hologram-plane u'(x') utilizing the Fresnel-approximation. We previously considered only a single point in the object-plane.
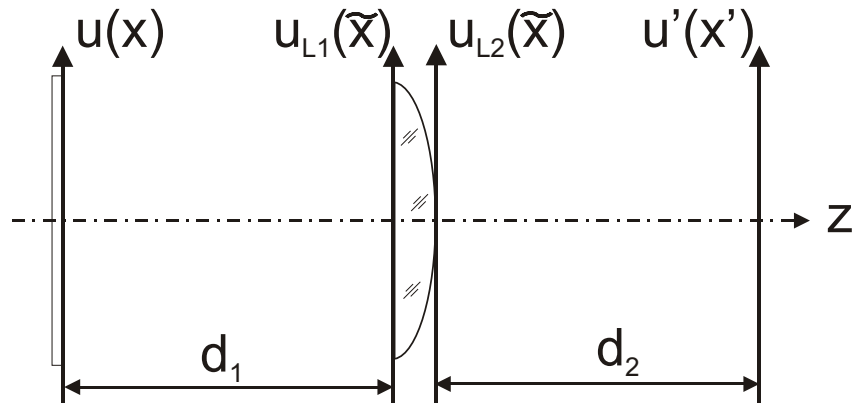
Figure 5.8: Sketch of different planes involved in the image formation

That assumption is not valid any longer, since the result depends on the position of P_o in the object-plane u(x). This is due to the fact that the light path is not retraced in order to obtain the reconstructed object. The recorded hologram holds already the in-focus object information. The recorded object phase information is a quadratic function with respect to the object-coordinate x, which will soon be shown. Thus we need to consider the integral over all object points. The mathematical derivation shown in the following closely corresponds to the imaging equations discussed by Goodman (1996) and Lohmann and Sinzinger (2006). At first, the light performs free space propagation between the object and the first lens surface $u_{L1}(\tilde{x})$. At the first lens plane $u_{L1}(\tilde{x})$ a diverging spherical wave originating from the point P_o can be registered.

$$u_{L1}(\tilde{x}) = \int_{-\infty}^{\infty} u(x) \exp\left[i\pi \frac{(x - \tilde{x})^2}{\lambda d_1}\right] \mathrm{d}x \tag{5.38}$$

From $u_{L1}(\tilde{x})$ light passes through the lens to arrive at the second lens surface $u_{L2}(\tilde{x})$, which can be simulated in the paraxial region by:

$$u_{L2}(\tilde{x}) = u_{L1}(\tilde{x}) \exp\left(\frac{-i\pi\tilde{x}^2}{\lambda f}\right) \tag{5.39}$$

Hence the spatial frequency of the object-wave is subjected to a shear $\left(\nu_{L1}(\tilde{u}) + \frac{\tilde{x}}{\lambda f}\right)$ when passing through the lens from $u_{L1}(\tilde{x})$ to $u_{L2}(\tilde{x})$, see Fig. 5.1(d). From the second lens surface light propagates to the hologram-plane u(x').

$$u'(x') = \int_{-\infty}^{\infty} u_{L2}(\tilde{x}) \exp\left[\frac{i\pi (\tilde{x} - x')^2}{\lambda d_2}\right] \mathrm{d}\tilde{x} \tag{5.40}$$

Substituting Eq. 5.38 and Eq. 5.39 in Eq. 5.40 results in:

$$
\begin{aligned}
u'(x') &= \int\limits_{-\infty}^{\infty} \int\limits_{-\infty}^{\infty} u(x) \exp\left[\frac{i\pi}{\lambda}\left\{\frac{(x-\tilde{x})^2}{d_1} - \frac{\tilde{x}^2}{f} + \frac{(\tilde{x}-x')^2}{d_2}\right\}\right] \mathrm{d}x\mathrm{d}\tilde{x} \\
&= \int\limits_{-\infty}^{\infty} \int\limits_{-\infty}^{\infty} u(x) \exp\left[\frac{i\pi}{\lambda}\left\{\tilde{x}^2\left(\frac{1}{d_2} - \frac{1}{f} + \frac{1}{d_1}\right) - 2\tilde{x}\left(\frac{x}{d_1} + \frac{x'}{d_2}\right)\right.\right. \\
&\quad \left.\left. + \frac{x^2}{d_1} + \frac{x'^2}{d_2}\right\}\right] \mathrm{d}x\mathrm{d}\tilde{x}
\end{aligned}
\tag{5.41}
$$

The in focus image-point should then be represented by a δ-function. Let us therefore consider all exponential terms in $\{...\}$. An in focus image needs to satisfy the lens formula Eq. 5.42.

$$
\frac{1}{f} = \frac{1}{d_1} + \frac{1}{d_2}
\tag{5.42}
$$

The lens-formula is represented in $\{...\}$ by the quadratic phase term in dependence of $\tilde{x}^2$-coordinate. This term should consequently nullify which results in:

$$
\begin{aligned}
u'(x') &= \exp\left(\frac{i\pi x'^2}{\lambda d_2}\right) \int\limits_{-\infty}^{\infty} \int\limits_{-\infty}^{\infty} u(x) \exp\left[\frac{i\pi}{\lambda}\left\{-2\tilde{x}\left(\frac{x}{d_1} + \frac{x'}{d_2}\right)\right.\right. \\
&\quad \left.\left. + \frac{x^2}{d_1} + \frac{x'^2}{d_2}\right\}\right] \mathrm{d}x\mathrm{d}\tilde{x}
\end{aligned}
\tag{5.43}
$$

Assuming that all conditions are met to permit the change of integration order Eq. 5.43 becomes:

$$
\begin{aligned}
u'(x') &= \exp\left(\frac{i\pi x'^2}{\lambda d_2}\right) \int\limits_{-\infty}^{\infty} u(x) \exp\left(\frac{i\pi x^2}{\lambda d_1}\right) \\
&\quad \int\limits_{-\infty}^{\infty} \exp\left[\frac{-2i\pi\tilde{x}}{\lambda}\left(\frac{x}{d_1} + \frac{x'}{d_2}\right)\right] \mathrm{d}\tilde{x}\mathrm{d}x
\end{aligned}
\tag{5.44}
$$

We now substitute the term:

$$\frac{x + \frac{x'd_1}{d_2}}{\lambda d_1} = \hat{\omega} \tag{5.45}$$

Thus we can solve the integral over $\mathrm{d}\tilde{x}$ by applying a Fourier-transformation with frequency $\hat{\omega}$.

$$u'(x') = \exp\left(\frac{i\pi x'^2}{\lambda d_2}\right) \int\limits_{-\infty}^{\infty} u(x) \exp\left(\frac{i\pi x^2}{\lambda d_1}\right) \delta\left(\frac{x + \frac{x'd_1}{d_2}}{\lambda d_1}\right) \mathrm{d}x \tag{5.46}$$

Taking into account the scaling property of the δ-function [†]:

$$\delta(ax) = \frac{\delta(x)}{|a|} \tag{5.47}$$

results in:

$$u'(x') = |\lambda d_1| \exp\left(\frac{i\pi x'^2}{\lambda d_2}\right) \int\limits_{-\infty}^{\infty} u(x) \exp\left(\frac{i\pi x^2}{\lambda d_1}\right) \delta\left(x + x'\frac{d_1}{d_2}\right) \mathrm{d}x \tag{5.48}$$

The integral can be solved by applying the sifting property of the δ-function according to Bracewell (1986):

$$\int\limits_{-\infty}^{\infty} f(x)\delta(x-a)\mathrm{d}x = f(a) \int\limits_{-\infty}^{\infty} \delta(x-a)\mathrm{d}x = f(a) \tag{5.49}$$

The δ-function in an integral shifts the function f(x) outside the integral by replacing the argument with the point at which the δ-function occurs. In our case f(x) is represented by the product $\left[u(x)\exp\left(\frac{i\pi x^2}{\lambda d_1}\right)\right]$. The constant factor $|\lambda d_1|$ in Eq. 5.48 can be neglected and the integral solved as:

$$u'(x') = u\left(-x'\frac{d_1}{d_2}\right) \exp\left[\frac{i\pi x'^2}{\lambda}\left(\frac{1}{d_2} + \frac{d_1}{d_2^2}\right)\right] \tag{5.50}$$

[†]taken from Bracewell (1986)

The factor $\left(-\frac{d1}{d2}\right)$ in the argument of u denotes the magnification Γ' of the optical system. The minus sign indicates an inverted image. Γ' can also be defined by the object and image coordinates.

$$\Gamma' = \frac{d_2}{d_1} = \frac{x'}{x} = -\frac{d_2 - f'}{f} \tag{5.51}$$

Eq. 5.50 can be described by Γ':

$$
\begin{aligned}
u'(x') &= u\left(\frac{x'}{\Gamma'}\right) \exp\left[\frac{i\pi x'^2}{\lambda d_2}\left(1 - \frac{1}{\Gamma'}\right)\right] \\
&= u\left(\frac{x'}{\Gamma'}\right) \exp\left(\frac{i\pi x'^2}{\lambda d_2}\right) \exp\left(\frac{-i\pi x^2}{\lambda d_1}\right)
\end{aligned} \tag{5.52}
$$

If one is only interested in the intensity Eq. 5.52 totally satisfies the condition to obtain an in-focus point in the image-plane. The complex exponential terms only affect the phase. If not only the intensity but also the phase is important the recorded image needs to interfere with a reference-wave. Moreover, in order to record the correct object phase the parabolic exponential terms in Eq. 5.52

$$\exp\left(\frac{i\pi}{\lambda}\frac{x^2}{d_1}\right) \qquad \text{and} \qquad \exp\left(\frac{i\pi}{\lambda}\frac{x'^2}{d_2}\right)$$

need to be eliminated. The quadratic phase factor depending on the x'-coordinate can be eliminated by adapting the curvature of the reference-wave to the curvature of the parabolic phase term. The quadratic phase term depending on the x-coordinate can be neglected according to Goodman (1996) if:

   i. The object is on a spherical surface centered on the optical axis with a radius equals d_1.

   ii. The object is illuminated with a spherical wave which converges towards the point where the optical axis pierces the principle plane of the lens, see

Fig. 5.9.

iii. The phase of the quadratic phase term changes by an amount which is only a fraction of a radian within the object region which contributes significantly to a particular image point. This statement is valid if the object is not greater than a quarter of the size of the lens aperture.

The recorded intensity of the interfering spherical reference-wave, shown in Eq. 5.25, and the object-wave is:

$$
\begin{aligned}
I &= \left| u\left(-\frac{x'}{\Gamma'}\right) \exp\left[\frac{i\pi}{\lambda}\left(\frac{x'^2}{d_2}\right)\right] + A_r \exp\left[\frac{i\pi}{\lambda d_r}(x' - x_r)^2\right] \right|^2 \\
&= u\left(-\frac{x'}{\Gamma'}\right)^2 + A_r^2 + 2u\left(-\frac{x'}{\Gamma'}\right)A_r \cos\left[\frac{\pi}{\lambda}\left(\frac{x'^2}{d_r} - 2\frac{x'x_r}{d_r} + \frac{x_r^2}{d_r} - \frac{x'^2}{d_2}\right)\right]
\end{aligned}
\tag{5.53}
$$

Assuming $(d_r = d_2)$ and neglecting $\left(\frac{\pi x_r^2}{\lambda d_r}\right)$, which only introduces a constant phase offset, results in:

$$
\begin{aligned}
I &= u\left(-\frac{x'}{\Gamma'}\right)^2 + A_r^2 + 2u\left(-\frac{x'}{\Gamma'}\right)A_r \cos\left(\frac{-2\pi x' x_r}{\lambda d_2}\right) \\
I &= u\left(-\frac{x'}{\Gamma'}\right)^2 + A_r^2 + 2u\left(-\frac{x'}{\Gamma'}\right)A_r \cos\left(-2\pi x' \nu_r\right)
\end{aligned}
\tag{5.54}
$$

From Eq. 5.54 can be concluded, that the phase adapted spherical reference-wave
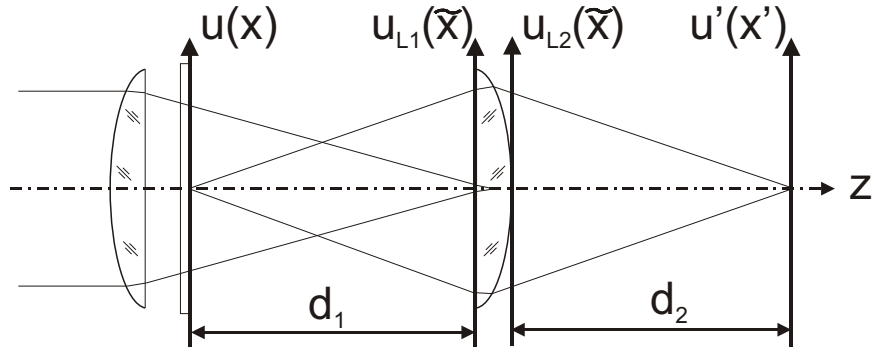
Figure 5.9: Convergent object illumination to suppress quadratic phase term

introduces only a phase-tilt to the recorded image-hologram. The three spatial frequency components encoded in the hologram can be singled out by applying a Fourier-transformation to the recorded intensity.

$$(x_o, \nu_o) \rightarrow (-x_o \cdot \Gamma', [-(\nu_{x'} - \nu_r), 0, (\nu_{x'} - \nu_r)]) \tag{5.55}$$

Although a magnification (Γ') is applied to the image, the SBP$'$ and SBP$''$ must still be kept constant as discussed in Section 5.1. The highest resolvable spatial frequency is determined by the NA of the lens.

$$\nu_{x'} = 2\frac{NA}{\lambda} = \frac{2x'}{\lambda (d_2 - f)} \tag{5.56}$$

Taking into account Eq. 5.51 results in:

$$\nu_{x'} = 2\frac{NA}{\lambda} = \frac{2x'}{\lambda (d_2 - f)} = \frac{2x'}{\lambda \Gamma' f} \tag{5.57}$$

The spatial image frequency $\nu_{x'}$ is inversely proportional to Γ'. Despite taking into account all these conditions to record object intensity and phase the resulting recorded and reconstructed SBP$'$ does not necessarily match the object's SBP. A lens-pupil of infinite extension was assumed to derive the imaging equation. In practice the lens-pupil is spatially limited. The ideal image resulting from $u'(x')$ is convolved with the Fraunhofer diffraction pattern of the lens pupil $P(\tilde{x})$. The lens pupil acts like a low-pass filter and stops the transition of spatial frequency higher than the NA of the pupil allows for, see Eq. 5.58. Hence the recorded SBP$'$ is affected by the spatial frequency bandwidth of the lens or lens-system. Furthermore, the spatial frequency bandwidth $\Delta\nu_{x'}$ decreases the more out-of-field the object point is located. This effect is due to lens abberations, which increase the more laterally displaced from the optical axis the object point is

located, as shown in Fig. 5.10. The spatial frequency bandwidth of the lens $\Delta\nu_L$ can be described by:

$$|\nu(x')| \leq \Delta\nu_L = 2\frac{\text{NA}}{\lambda} = 2\frac{n\sin\left[\arctan(\frac{D}{2f})\right]}{\lambda} \approx \frac{D}{\lambda f} \qquad (5.58)$$

The SBP$'$ of the image is therefore defined by the lens parameters:

$$SBP_L = D\Delta\nu_L = X_L\Delta\nu_L \qquad (5.59)$$

In-line Setup

SBP$'$ for an in-line configuration is:

$$\boxed{SBP'_{in-line} = X_L\Delta\nu_L = SBP_L} \qquad (5.60)$$
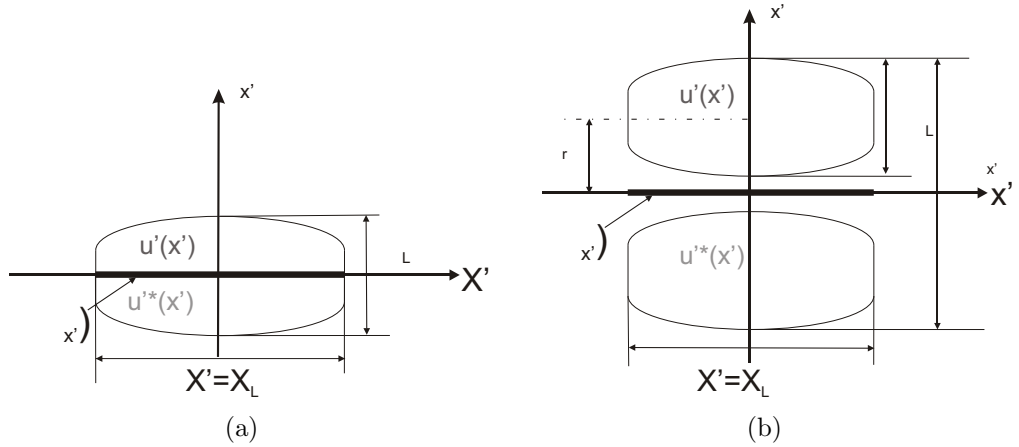
Figure 5.10: SBP of an Image-hologram, (a) in-line arrangement, (b) off-line arrangement

Off-line Setup

The separation of image, twin-image and zero order term is obtained by choosing the inclination of the reference-wave to be larger than the largest light inclination introduced by any imaging components. This statement results in the condition:

$$\nu_r \geq \Delta\nu_L/2 \tag{5.61}$$

The required SBP′ for the off-line configuration needs to have the same spatial width as the recorded image.

$$X \geq X_L \tag{5.62}$$

The spatial frequency bandwidth in the hologram-plane is defined as:

$$\Delta\nu(x') = 2\nu_r + \Delta\nu_L \geq 2\Delta\nu_L \tag{5.63}$$

Thus the $SBP(x')$ in the hologram-plane is:

$$\boxed{SBP_{off-line} \geq 2X_L\Delta\nu_L = 2SBP_L} \tag{5.64}$$

Both, in-line and off-line SBP for an image-hologram are shown in Fig. 5.10.

5.3 SBP″ or Performance Capacity

The SBP″ of the reconstructed hologram is described by the product of the reconstructed field of view (FOV), which is one-dimensionally represented by X'' and the spatial frequency arising from the smallest resolvable object detail $\delta_{x''}$.

$$SBP'' = X'' \cdot \frac{1}{\delta_{x''}} \tag{5.65}$$

It describes the performance capacity of the holographic systems and depends on the camera parameters and on the setup geometry.

5.3.1 Fresnel-hologram

In the first case the recording of Fresnel-holograms (plane reference-wave) is considered. If one likes to reconstruct a certain FOV a minimum recording distance between object and camera needs to be kept for which the recorded interference pattern is not under-sampled. This recording distance differs according to in-line or off-line configuration as described in Section 4.2.1.

$$d_{in-line} = \frac{(X + N\Delta x')\Delta x'}{\lambda} \tag{5.66}$$

$$d_{off-line} = \frac{2(X + N\Delta x')\Delta x'}{\lambda} \tag{5.67}$$

The one dimensional FOV for both cases are:

$$X_{in-line} = \frac{d\lambda}{\Delta x'} - N\Delta x' \tag{5.68}$$

$$X_{off-line} = \frac{d\lambda}{2\Delta x'} - N\Delta x' \tag{5.69}$$

Taking into account the recording distances represented in Eqs. 5.66 and 5.67, and the camera parameters enable the calculation of the holographic system's NA, by which the highest recordable spatial object frequency can be calculated.

$$\frac{1}{\nu(x'')} = \delta(x'') = \frac{\lambda d}{N\Delta x'} \tag{5.70}$$

Replacing the distance d of Eq. 5.70 by Eq. 5.66 and Eq. 5.67 results in:

$$\frac{1}{\nu(x'')_{in-line}} = \delta(x'')_{in-line} = \frac{X + N\Delta x'}{N} \tag{5.71}$$

$$\frac{1}{\nu(x'')_{off-line}} = \delta(x'')_{off-line} = \frac{2\left(X + N\Delta x'\right)}{N} \tag{5.72}$$

Thus the SBP'' for both cases maintaining the minimum possible recording distance are:

$$\boxed{\begin{aligned} SBP''_{in-line} &= \frac{X \cdot N}{X + N\Delta x'} \\ SBP''_{off-line} &= \frac{X \cdot N}{2\left(X + N\Delta x'\right)} \end{aligned}} \tag{5.73}$$

5.3.2   Fourier-hologram

The plane reference-wave has been replaced by a divergent *spherical reference-wave*. Both, camera-object distance and camera-spherical wave point source distance are matched. This results in an equal curvature of reference and object-waves. Thus the interference fringes are homogenously distributed across the sensor. The minimum recording distance for in-line and off-line configuration are:

$$d_{in-line} = \frac{X\Delta x'}{\lambda} \tag{5.74}$$

$$d_{off-line} = \frac{2X\Delta x'}{\lambda} \tag{5.75}$$

The corresponding FOV for in-line and off-line arrangement according to Eq. 4.18 are:

$$X_{in-line} = \frac{d\lambda}{\Delta x'} \tag{5.76}$$

$$X_{off-line} = \frac{d\lambda}{2\Delta x'} \tag{5.77}$$

Consequently the SBP''s for in-line and off-line configuration are:

$$\boxed{\begin{aligned} SBP''_{in-line} &= N \\ SBP''_{off-line} &= \frac{N}{2} \end{aligned}} \tag{5.78}$$

5.3.3   Image-hologram

According to Eq. 4.19 the FOV for an image-hologram is:

$$X = \frac{N\Delta x' f}{d_2 - f} \tag{5.79}$$

The highest recordable spatial object frequency depends on the NA of the lens-system with respect to Rayleigh's criterion.

$$|\nu(x'')| = \nu(x') = 0.81\frac{D}{\lambda f}$$

Thus the SBP'' becomes:

$$\boxed{SBP'' = 0.81\frac{N\Delta x' f}{d_2 - f}\left(\frac{D}{\lambda f}\right)} \tag{5.80}$$

5.3.4   Conclusion

The required SBP$'$ in the recording process and SBP$''$ in the reconstruction process for Fresnel-holograms, Fourier-holograms and Image-holograms was derived. The SBP analysis focused upon the spatial frequency content of the recorded and reconstructed hologram. It is also worthwhile to explore the obtained interference phase in respect to the recorded object phase. The complex reference-wave in the reconstruction process needs to be adjusted in order to display the object's phase correctly. These adjustments with respect to different holographic setups are:

- In-line Fresnel-hologram: spherical phase arising in the recording stage needs to be eliminated in the reconstruction stage

- Off-line Fresnel-hologram: reconstructed object-phase is superimposed with

a tilted reference-phase. Hence, the complex conjugated reference-wave in the reconstruction process needs to be adapted in order to eliminated the introduced tilt.

- In-line Fourier-hologram: quadratic phase term of the spherical reference-phase and the object-phase cancel each other out; no adjustment needed

- Off-line Fourier-hologram : need to correct residual phase tilt arising from the different lateral position of both waves' point sources.

- Image-hologram: An in depth discussion has already been conducted in Section 5.2.3

Having investigated the reconstructed object-phase and which precautions need to be taken in order to obtain the correct phase-reconstruction some conclusions are drawn with regards to the SBP performance of different holographic setups. The best SBP performance for the recorded SBP$'$ and reconstructed SBP$''$ is obtained by a lens-less Fourier-hologram. The SBP performance of the image-hologram depends to a high degree on the lens-system employed. In general one should aim to avoid the introduction of a lens system unless the object is either too small or too large to be recorded with a lens-less setup. Main advantages of a lens-less setup are:

i. The spatial cutoff frequency ν_{cutoff} for a rectangular aperture is larger than for a circular aperture, see Section 4.6.2.

ii. The contrast obtained for various spatial frequencies is larger for a rectangular aperture.

iii. The zero-padding approach implemented to improve the resolution of the reconstructed hologram beyond the Rayleigh criterion can not be applied to image-holograms.

iv. Small inhomogeneities in the pixel response have a stronger influence on the image-quality of image-holograms than for Fresnel-holograms and Fourier-holograms. This is due to the fact that the object information is not localized in a single point only.

v. In lens-less holography all object points are recorded with approximately the same dynamic range. An image hologram displays sharp features such as edges with a higher grey level, which decreases the dynamic range for other object information.

Apart from these and aforementioned advantages a lens-less *Fourier-hologram* does furthermore benefit from:

1. Mathematical simplicity which reduces the computational effort for the numerical reconstruction.

2. Reconstruction by means of a two dimensional Fourier-transformation is not restricted to a minimum distance, whereas the reconstruction of a Fresnel-hologram utilizing the Fresnel-method is only valid in the Fresnel regime.

3. Reduced recording distance compared to Fresnel-holograms, which results in an increased optical resolution.

4. Wave-aberration compensating characteristic due to adapted curvature of reference and object-wave.

5. No need to introduce lenses, whereas Fresnel-holograms require lenses for the collimation of the reference beam. In this manner costs, disturbing scattering effects from dust on optical surfaces and wave-aberrations introduced in the collimation process are minimized.

6. Low coherence light sources can be used in conjunction with the investigation of microscopic objects, since matched reference and object-wave curvature requires less temporal coherence. This results in reduced speckle-noise and improved image quality.

Another important difference between the recording of lens-less holograms and image-holograms is that the smallest resolvable object detail δ in lens-less holography is determined by the sensor-size X'. On the contrary, for an image-hologram the smallest resolvable object detail δ is determined by the pixel-size $\Delta x'$ in conjunction with aperture of the lens-system D. On the other hand the size of the recordable object depends on the pixel-size $\Delta x'$ for lens-less holography, whereas in image-holography it depends on the sensor-size X' in conjunction with the lens-system's specifications.

In conclusion, it could be shown that the SBP is an important tool to compare and investigate different holographic systems in terms of their recorded information and reconstruction capacity.

CHAPTER 6

Resolution Improvement in Digital Holography

6.1 Introduction

In holography the sinusoidal interference pattern resulting from the superimposition of the reference and the object-wave is stored on a recording medium. Photographic plates were originally used in optical holography as recording media. For most applications photographic plates have been replaced by digital receivers such as CCD or CMOS cameras. Digital receivers enable fast image acquisition without the tedious process of developing the image. Furthermore, the image can easily be processed since it is already stored in a digital format.The maximum resolution of digital receivers (typically 500 lp/mm) is small compared to the resolution of photographic plates (typically 3000 lp/mm). This limits the maximum angle between reference and object-wave. If one likes to record a digital hologram of a macroscopic object, a large distance between object and camera needs to be kept in order to avoid under-sampling. Due to the long recording distance a numerically reconstructed hologram possesses larger speckle than a hologram recorded on a holographic plate (see Eq. 4.41). Moreover, the small-

147

est resolvable object detail, according to Rayleigh's criterion (see Eq. 4.25), is much larger than for optical holography. Therefore, this thesis is devoted to the implementation and development of resolution improvement methods for digital holography.

Different approaches have been developed to overcome the reduced resolution in digital holography. Very early in the 1990s Wyrowski and Bryngdahl (1989) described a method to reduce speckle noise in the reconstructed hologram. They used a digital diffuser, based on an iterative Fourier transform algorithm (IFTA). Another resolution improvement approach was based on the introduction of imaging phase-gratings. Paturzo et al. (2008) described a resolution improvement method utilizing an electro-optically tuneable two-dimensional phase grating. The grating directed light to the camera, which otherwise would have been lost. Seven spatially multiplexed holograms were simultaneously recorded. A 50% resolution improvement was obtained. Mico et al. (2006) use a two dimensional Vertical Cavity Surface-Emitting Laser (VCSEL) array consisting of nine elements in conjunction with a diffraction grating, producing the same amount of diffraction orders as the VCSEL has elements.

The most commonly applied and most effective resolution improvement methods are based on speckle de-correlation. One way to obtain speckle de-correlation is *tilted object illumination*, which was carried out by Mico et al. (2008), Kang (2008), and Yuan et al. (2008). Mico et al. (2008) obtained an approximately two times resolution improvement utilizing the tilted illumination method. Nomura et al. (2008) reported another speckle de-correlation method based on superimposition of holograms recorded with different wavelengths. The speckle pattern produced by each wavelength differs for each individual object point. In order to enable superimposition the pixel-size of the recorded holograms had to be changed with respect to the recording wavelength. Kaufmann et al. (2003) pro-

posed an alternative multi-wavelength method. Three lasers Nd:YAG (532nm), HeCd (442nm) and HeNe (633nm), were used in conjunction with a three chip RGB colour camera. The signal with the highest amplitude was then chosen for the reconstruction process. A resolution improvement of 60% was obtained by Kaufmann et al. (2003). The most promising and most widely applied speckle de-correlation method is the *synthetic aperture method*. The synthetic aperture method is based on an the generation of an increased sensor area, which results in an increased NA. In this manner the lateral resolution can be improved and the speckle-size be reduced when reconstructing the hologram. The synthetic aperture method can be implemented by either using a camera array or shifting a single camera to different lateral positions in order to generate an increased recording area. The percentage of resolution improvement equals the percentage of additional pixels. The implementation of the synthetic aperture-method in digital holography has been reported by Clerc and Gross (2001); Clerc and Collet (2000); Di et al. (2008); Zhang (2005); Baumbach et al. (2006); Massig (2002); Nakatsuji and Matsushima (2008); Martinez-León and Javidi (2007); Kreis and Schlüter (2007) and Gyímesi et al. (2009). In most cases a spherical reference-wave is chosen [Di et al. (2008); Zhang (2005); Baumbach et al. (2006); Massig (2002); Nakatsuji and Matsushima (2008); Martinez-León and Javidi (2007) and Gyímesi et al. (2009)]. Another method not associated with speckle de-correlation is based on the reduction of the digital receiver's pixel-size. By sampling the incoming wave-field with sub-pixel accuracy the recording distance can be reduced. This results in the recording of higher spatial frequencies and an improved resolution. Kornis and Gombköto (2005) describes three such sub-pixel methods namely the *Fourier Spectrum method*, the *Drizzle Interlace method* and the *Four Quadrant 2x2 Drizzle method*. These methods use a CCD camera with a fill factor approaching 100%, where the light sensitive area matches the pixel-size. In that

manner it is based on interpolation of a larger pixel-size to a reduced pixel-size. In general CCD cameras are used for the recording of holograms due to their larger fill-factor and less noisy readout in comparison to CMOS technology. However, CCD technology is more expensive than CMOS technology. Moreover, the minimum pixel-size, which determines the minimum object-camera distance, is larger for CCD cameras, see Table 2.4. These properties support the idea to introduce CMOS cameras in digital holography. The noisier readout of CMOS cameras can be reduced by hot-pixel elimination and dark field calibration prior to the measurement. Three resolution improvement methods, the *synthetic aperture method*, the *sub-pixel sampling method* and a *combination of both*, in conjunction with CMOS-technology are presented in this chapter.

The novelty of the synthetic aperture method described in this thesis is that it was carried out on CMOS technology in conjunction with the recording of lens-less Fourier-holograms. The synthetic aperture hologram recorded is to the author's knowledge the largest recorded digital hologram resulting in the largest obtained Space-Bandwidth Product (SBP) for digital holograms. In addition, a comparison of the synthetic aperture and the spatial averaging technique developed by Baumbach et al. (2006) with respect to the obtained optical resolution and phase measurement accuracy was conducted. The spatial averaging approach is based on averaging all individual reconstruction of the laterally shifted holograms.

The sub-pixel sampling method was carried out on CMOS technology and in contrast with Kornis and Gombköto (2005) is not based on interpolation, which demonstrates its novelty.

It is the first time to report the combination of synthetic aperture method and sub-pixel sampling method, which represents another novelty.

To demonstrate the resolution improvement the methods applied have been

evaluated using the USAF 1951 test target. A parameter to define the resolution and imaging performance improvement of the reconstructed holograms is the SBP. The SBP of the reconstructed hologram represents the product of the field of view (FOV) and the highest resolvable spatial frequency. The calculation of the SBP was taken from Lohmann and Sinzinger (2006):

$$SBP = \delta_{x''}^{-1} \cdot \delta_{y''}^{-1} \cdot N\Delta x'' \cdot M\Delta y'' \tag{6.1}$$

Where $\delta_{x''}$ and $\delta_{y''}$ are the smallest resolvable object details in horizontal and vertical-direction, $\Delta_{x''}$ and $\Delta_{y''}$ are the pixel-sizes in the reconstruction-plane, and the product $N\Delta x'' \cdot M\Delta y''$ is the FOV of the numerical reconstruction. In this particular case N and M denote the number of pixels which display the reconstructed image. The SBP is a more meaningful parameter for the judgment of optical systems since it is independent of the recording distance and permits the comparison of different optical systems. The SBP for Fourier-holograms can be calculated as explained in Section 5.2.2, for which only the one-dimensional case was considered. The two dimensional SBP for in-line Fourier-holograms is:

$$SBP_{in-line} = N \cdot M \tag{6.2}$$

The SBP obtained for an in-line Fourier-hologram can be considered to be the optimum SBP. In case of an off-line setup the two dimensional SBP is:

$$SBP = \frac{N \cdot M}{4} \tag{6.3}$$

In order to measure the setup performance with respect to its optimum SBP an

efficiency parameter η is introduced.

$$\eta = \frac{SBP}{SBP_{in-line}} \cdot 100\% \tag{6.4}$$

In this manner different optical setups can be compared. The SBP consideration makes sense when holograms recorded from resolution targets such as the USAF 1951 test target are investigated.

The Signal-to-Noise Ratio (SNR) can be applied in case one would like to evaluate the image quality improvement for the reconstruction of an arbitrary object or a double exposure phase map. The SNR can be calculated by:

$$SNR = 20 \log \left(\frac{\bar{X}}{\sigma} \right) \tag{6.5}$$

Where $\bar{X}$ is the mean value of a population and σ the standard deviation. Assuming that the noise is evenly distributed over the entire reconstructed hologram, only a small representative region of interest with ideally constant grey level needs to be considered for the SNR measurement. Grey level changes in that region should then solely be due to noise. The SNR calculation needs to be slightly changed in order to evaluate double exposure phase maps. The values assigned to the pixels in a double exposure phase map lie within a 2π boundary with a certain phase gradient. This phase gradient results in a fluctuation of phase values. Therefore, the SNR is determined by calculating the standard deviation along a minimum phase gradient.

6.2   Synthetic Aperture Method

This section discusses the potential of the synthetic-aperture method in digital holography to increase the resolution, to perform high accuracy deformation measurement and to obtain a three dimensional topology map. The synthetic aperture method and the resolution improvement described hereafter have been carried out with a backlash free motorized x-y traverse from Physik Instrumente (PI-M150.11) with a step width of 8.5 nm, for further details see Appendix D.4. The camera used is a 6.6 Megapixel CMOS camera (C-Cam, BCi4-6600) with 3.5 μm pixel-size and 35% fill-factor (Appendix D.5). The CMOS sensor is not covered with a micro-lens array. Phase stepping, if applied, was performed with a piezo mounted mirror in the reference arm. A Queensgate Instruments AX100 piezo actuator, see Appendix D.2, including a position control unit was used.

The accuracy performance, repeatability and important specifications, such as pixel-size of the camera-sensor employed, was checked prior to the experiments. Once the performance of the motorized x-y stage, the piezo-actuator and the CMOS-camera was checked, the experimental work could start.

6.2.1   Setup and Methodology

The setup used to implement the synthetic aperture method is shown in Fig. 6.1. Vertically polarized laser light from a He-Ne Laser is rotated by a half-wave-plate. The combination with a polarizing beam splitter cube enables the adjustment of reference and object-wave intensity, by which a good contrast of the recorded interference fringes is ensured. However, not only the intensity of reference- and object-wave need to be the same in order to have a maximum contrast but also the polarization of both waves should match.

(a)

(b)
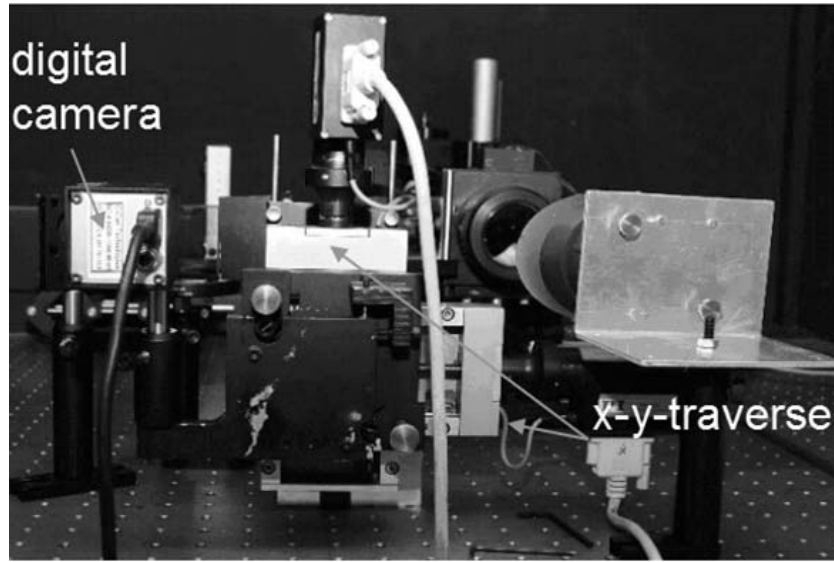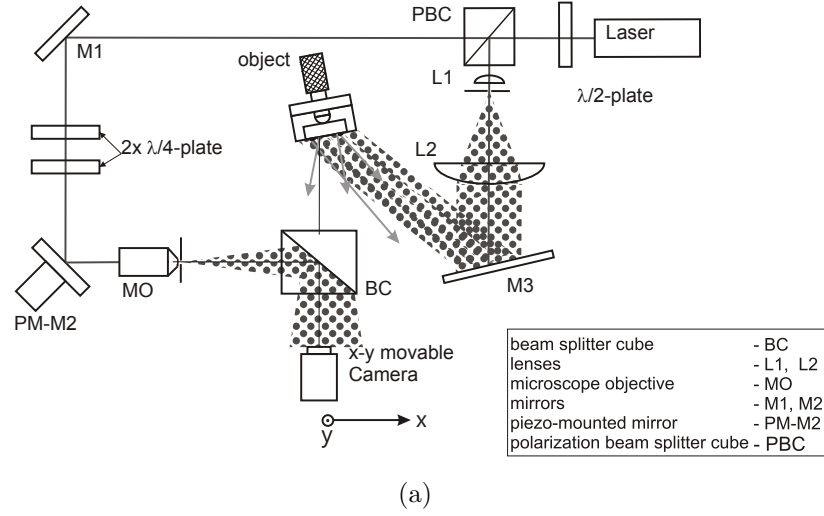
Figure 6.1: (a) Sketch of setup for recording Fourier-holograms, (b) small section of realized setup with camera and motorized x-y traverse

The polarization of the reference-wave can be adapted to the object-wave by two quarter-wave-plates. This configuration allows the adjustment of the incoming linearly polarized light to any arbitrary polarization state. The change of polarization-state using both quarter-wave-plates is described by the Jones-Calculus. The theory of the Jones-Calculus was presented in Section 2.3. Hence the resulting Jones-vector after passage through both rotated quarter-wave re-

tarders can be described by Eq. 6.6.

$$\vec{j_{out}} = \overrightarrow{J_{1QWP}} \cdot \overrightarrow{J_{2QWP}} \cdot \vec{j_{in}}$$

$$= \begin{bmatrix} \cos^2\theta_1 - i\sin^2\theta_1 & \cos\theta_1\sin\theta_1(1+i) \\ \cos\theta_1\sin\theta_1(1+i) & \sin^2\theta_1 - i\cos^2\theta_1 \end{bmatrix}$$

$$\cdot \begin{bmatrix} \cos^2\theta_2 - i\sin^2\theta_2 & \cos\theta_2\sin\theta_2(1+i) \\ \cos\theta_2\sin\theta_2(1+i) & \sin^2\theta_2 - i\cos^2\theta_2 \end{bmatrix} \cdot \vec{j_{in}}$$

(6.6)

Where $\overrightarrow{J_{1QWP}}$ is the Jones-Matrix of the first quarter-wave-plate, $\overrightarrow{J_{2QWP}}$ is the Jones-Matrix of the second quarter-wave-plate, θ_1 is the rotation-angle applied to the first quarter-wave-plate, θ_2 is the rotation-angle applied to the second quarter-wave-plate, $\vec{j_{in}}$ is the Jones-vector of the linearly polarized light before entering the two quarter-wave-plates and $\vec{j_{out}}$ is the resulting Jones-vector once the light has passed through both quarter-wave-plates. After the polarization state of the reference-wave has been adjusted, the focused reference-wave passes through a pin-hole. In this manner a clean single mode reference-beam can be obtained. Moreover, the pin-hole and the object were positioned equidistant to the camera, which enabled the recording of Fourier-holograms. The numerical reconstruction of Fourier-holograms including refocusing was discussed in Section 3.5. The minimum recording distance at which the Fourier-hologram is not under-sampled is:

$$d_{min} \geq \frac{2\Delta x' b}{\lambda}$$

(6.7)

With b the distance between reference-wave source point and furthest distant object point. From Eq. 6.7 it follows that the minimum recording distance d_{min} does not depend on the pixel-number. Hence the recording arrangement of Fourier-holograms is perfectly suited for the synthetic aperture method.

The synthetic aperture method was implemented by laterally displacing the camera with the motorized PI 150.11 x-y-stage. The total amount of shift applied was in the range of the sensor dimension with a small overlap of approximately 200 pixels between adjacent holograms to enable accurate pixel alignment by means of cross-correlation. The setup used is shown in Fig. 6.1. A larger sensor area was generated resulting in a more detailed reconstruction. The more detailed reconstruction is off-set by a smaller DOF. The DOF can be increased by applying the EDOF method described at a later stage of this section Section 6.2.4.

The image quality improvement was demonstrated on a reconstructed intensity and double exposure phase map.

6.2.2   Deformation Measurement

The object under investigation was a cantilever with an attached micrometer screw, which permits the application of an accurately controllable deformation. The setup is shown in Fig. 6.1. The object-camera distance is 780 mm and the mirror illuminating the object is laterally displaced from the object-camera-axis by 260 mm. The camera has been moved in a 4x3 grid to twelve different positions.The generated synthetic aperture hologram occupied a sensor area of 8800x8800 pixels. The results obtained for the intensity reconstruction of the cantilever, shown in Fig. 6.2.(c), demonstrate an increase in SNR from 24.06 dB for a reconstructed hologram of 3000x3000 pixels to 26.66 dB for a reconstructed hologram of 8800x8800 pixels. The synthetic aperture-method was applied to digital double exposure holography by moving the camera to a sequence of positions for the unloaded object state and then moving the camera in reverse sequential direction to exactly the same positions for loaded object state.
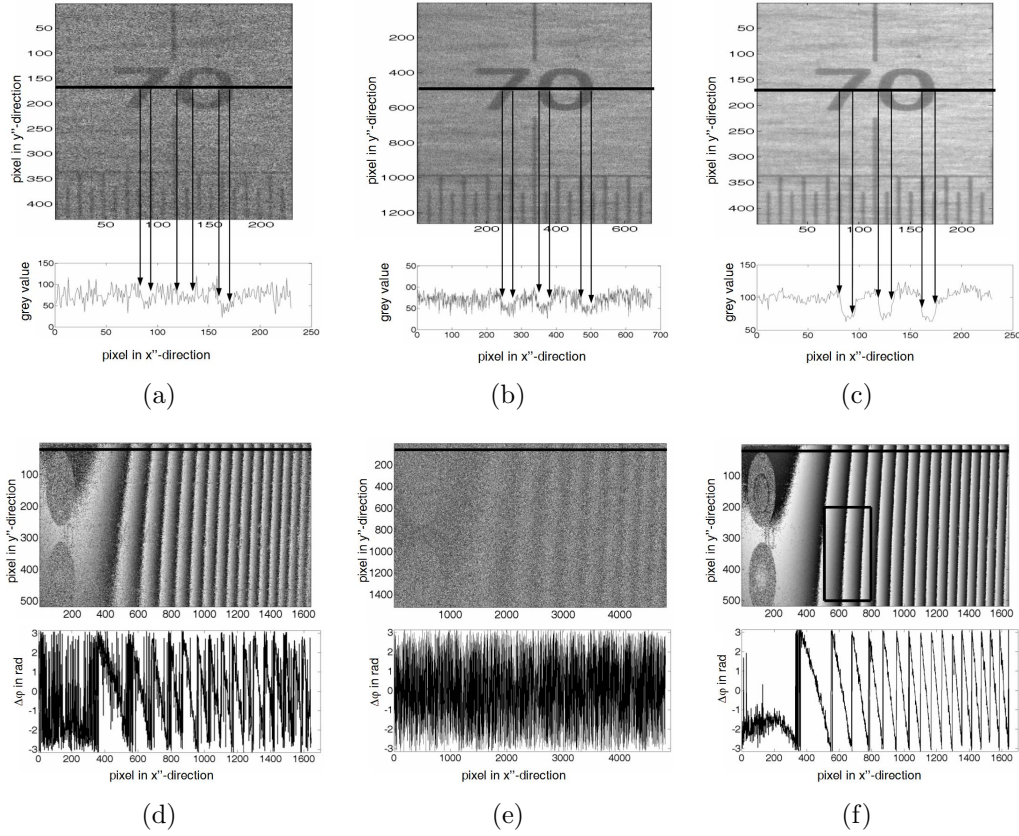
Figure 6.2: Segment of reconstructed hologram and double exposure phase map both with profile line (a), (b) 3000x3000 pixels, (c), (d) 8800x8800 pixels and (e), (f) 3000x3000 pixels averaging approach

A synthetic aperture hologram was obtained for both object states. Both holograms were aligned to each other by means of cross-correlation and then numerically reconstructed. The change of angle between the illumination and observation vector for the centred and most displaced position is 0.2°. Thus its influence on the sensitivity vector and the corresponding phase shift in the double exposure phase map is negligible. The double exposure phase map was calculated by subtracting the reconstructed phase of the loaded φ_2 and unloaded state φ_1 Eq. 6.8.

$$\Delta\varphi(x'', y'') = \varphi_2(x'', y'') - \varphi_1(x'', y'') \tag{6.8}$$

The resulting double exposure phase map is less well defined Fig. 6.2(e). The

phase contrast of the 2π discontinuities is reduced, which might be due to alignment errors. It was noticed when illuminating the sensor with a collimated laser beam that the sensor possesses a slight curvature. Fig. 6.3(a) shows the diffraction pattern obtained from the sensor. The diffraction pattern for an optimum flat sensor should be orientated along straight lines. In our case parabolic lines were obtained which are evidence of a convex sensor curvature. This results in scanning at different axial positions of the incoming speckle field, see Fig. 6.3(b), and hence introduces alignment errors. The reliability of the cross-correlation values obtained have then been examined by calculating its standard deviation. The shift amount in horizontal direction is 1972 ± 1 pixels and in vertical direction 2781 ± 2 pixels.

(a)

(b)

(c)
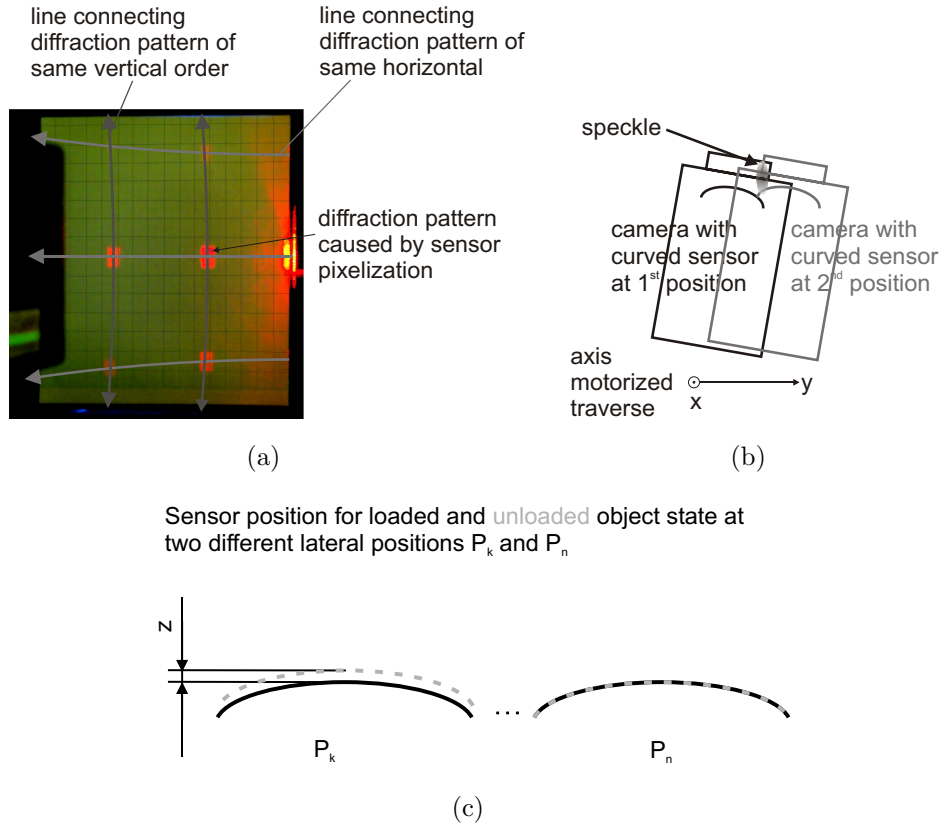
Figure 6.3: (a) Diffraction caused by collimated illumination of the sensor, (b) sketch axial speckle de-correlation due to camera and/or curved sensor, (c) phase offset caused by axial displacement between the two double exposure camera positions

The larger residual in the vertical direction might be due to a larger shift applied, which is combined with an increased axial speckle de-correlation. The error represented in this case is a combination of cross-correlation error and lateral alignment error arising from the x-y-stage. Three additional alignment errors between adjacent holograms and hologram pairs, which represent the two laterally corresponding holograms for the unloaded and loaded object state, could be defined. In conclusion, possible alignment errors might have arisen from:

i cross-correlation error

ii cross-correlation detected lateral misalignment between adjacent holograms and hence laterally corrected

iii axial misalignment between adjacent holograms

iv axial misalignment between corresponding hologram pairs

v lateral misalignment between corresponding hologram pairs

The consequence of these errors on the lateral and axial alignment is shown in Table 6.1, where 0 indicates no alignment error and 1 indicates that an alignment error occurred. This consideration assumes that each error possesses the same degree of impact. A curved sensor is more than twice as sensitive to pick up axial alignment errors than a plane sensor is, according to Table 6.1. Moreover, the impact of axial misalignment is amplified due to the optical setup's sensitivity for out of plane (axial) phase changes. If the two sub-holograms for the loaded and unloaded object state at position P_k differ in their axial position a constant phase offset is introduced in the resulting double exposure phase map, shown in Fig. 6.3(c). Consequently, each of the laterally corresponding hologram pairs might have a different phase offset. Thus combining the information of all hologram pairs to a synthetic aperture hologram results in a double exposure phase map

Table 6.1: Consequences on lateral and axial alignment

Error	Lateral alignment	Axial alignment (curved sensor)	Axial alignment (plane sensor)
i	1	1	0
ii	0	1	0
iii	0	1	1
iv	0	1	1
v	1	1	0
$\sum$	2	5	2

of reduced phase contrast, as shown in Fig. 6.2(e). Possible ways to avoid the introduction of a phase offset between hologram-pairs are:

- to use a plane sensor, which is less sensitive to pick up axial misalignment errors, see Table 6.1

- to record all laterally shifted holograms simultaneously at fixed positions utilizing a camera array

- to apply phase stepping digital holography, which enables the elimination of the phase offset between adjacent holograms prior to the reconstruction process

- to apply *spatial averaging* as described in Baumbach et al. (2006)

The original spatial averaging approach was slightly modified and used in this paper to overcome the problem of reduced phase contrast. Its flow-chart is shown in Fig. 6.4. The loaded object state in Fig. 6.4 is denoted by $\tilde{u}'$ for the recorded hologram and $\tilde{u}''$ for its numerical reconstruction, respectively. Moreover, the functions 'medfilt2' and 'angle' indicate MATLAB functions, which are used to median filter the image and to calculate the phase of the complex exponential reconstruction, respectively. The spatial averaging approach is realized by reconstruction of each individual hologram using Eq. 3.46.
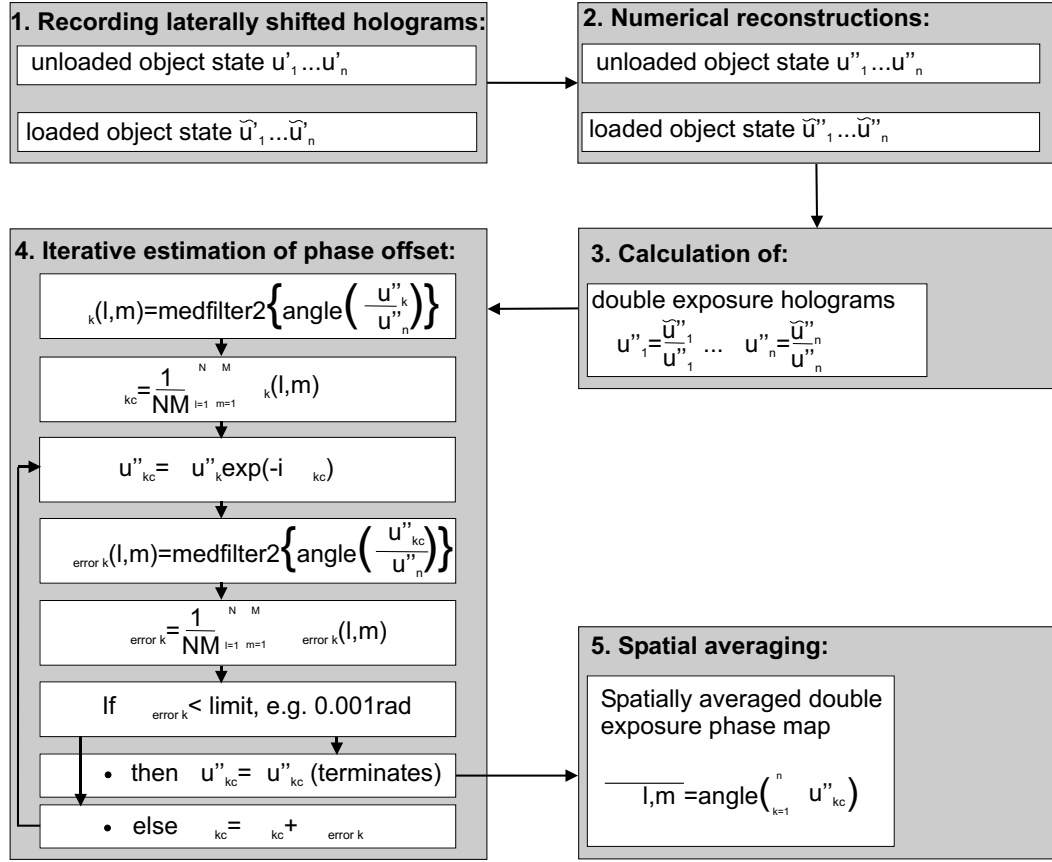
Figure 6.4: Flow-chart of the spatial averaging approach applied to double exposure holography

Due to the shift $\delta x'$ and $\delta y'$ in the hologram-plane the reconstructed hologram needs to be multiplied with an additional complex exponential phase factor Eq. 6.9.

$$\delta\varphi(x'', y'') = \frac{\pi}{\lambda d}\left(2x''\delta x' + 2y''\delta y'\right) \tag{6.9}$$

The additional term only affects the phase and does not need to be applied to average intensity reconstructions. The additional phase term can also be dropped in case a double exposure hologram is recorded. This is due to the same additional phase term for both recorded holograms of loaded and unloaded object state.

The averaged double exposure hologram is obtained by calculating the individual double exposure holograms at each position comparing the loaded and

unloaded state. In that manner a possible phase offset can be removed from each double exposure hologram. The phase offset is determined in an iterative manner by taking the phase map at the last position P_n as the reference phase, see Fig. 6.3(c). At this position the camera has not been translated to another position between recording the unloaded and loaded object state. Hence it should not have any phase offset or phase tilt due to lateral displacement. The phase offset and an eventual phase tilt is then subtracted from the phase map at the corresponding positions. In order to avoid smearing, the phase maps are then added up in complex notation, see Fig. 6.4. The double exposure phase maps obtained for a single position, the synthetic aperture method and the spatial averaging approach are shown in Fig. 6.2(d),(e) and (f). A significant image quality improvement between the synthetic aperture method and the spatial averaging approach is demonstrated. The SNR values were calculated for the region shown in Fig. 6.2(f) at the same corresponding region for all three phase maps. The values obtained are 17.22 dB, 11.47 dB and 25.57 dB. Thus the double exposure phase map obtained by the spatial averaging approach possesses a higher accuracy, which is also shown in both graphs of Fig. 6.5. The standard deviation utilizing the spatial averaging approach is reduced from 0.85 rad with a single double exposure hologram to 0.15 rad by using twelve double exposure holograms. The corresponding object deformation uncertainties are $\frac{\lambda}{14}$ and $\frac{\lambda}{81}$, respectively. The gradient of the trend-line for the standard deviation shown in Fig. 6.5(b) is higher than the one obtained by Baumbach et al. (2006), because the lateral displacement between the consecutive holograms has almost been doubled from 5 mm in Baumbach et al. (2006) to 9.8 mm.
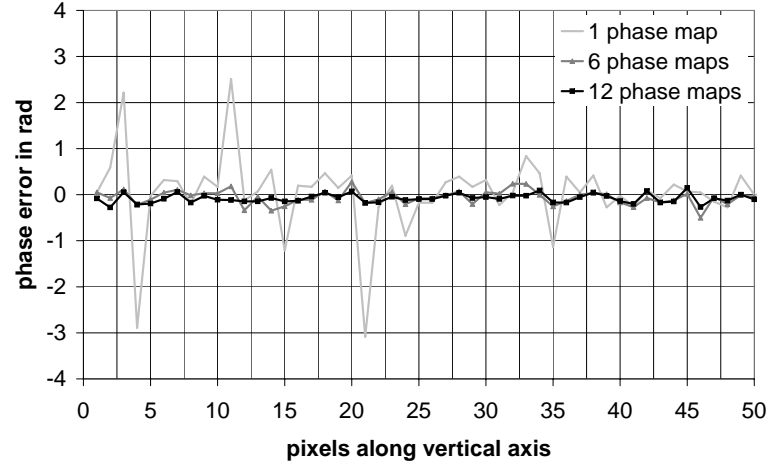
(a)
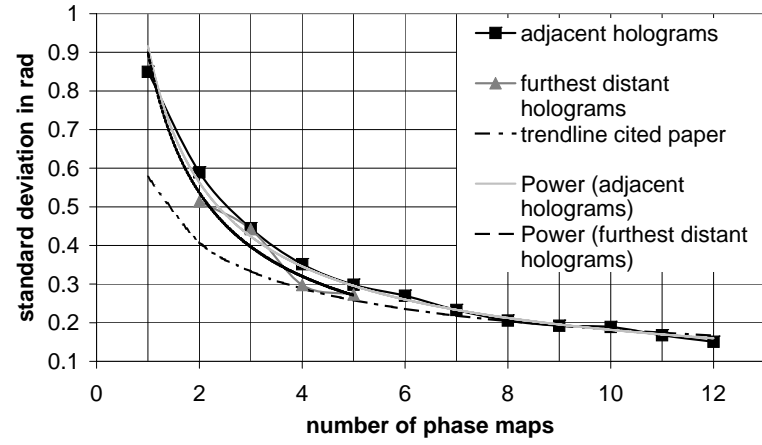
(b)

Figure 6.5: (a) Phase error for vertical cutline of area under investigation, (b) standard deviation of double exposure phase maps for adjacent and furthest distant holograms including trend-line

Although the initial standard deviation for a single reconstruction is higher than in Baumbach et al. (2006) only 12 holograms needed to be recorded instead of 25 to obtain a similar result.

Table 6.2: Trend-line standard deviation of phase

Parameters	Adjacent holograms	Furthest distant holograms	Result obtained by Baumbach et al. (2006)
a	0.9165	0.8987	0.5773
b	-0.70	-0.74	-0.50
R^2	0.994	0.932	—

The standard deviation (σ) could be approximated by a power function.

$$f(\sigma) = a\sigma^b \tag{6.10}$$

The values of a and b are shown in Table 6.2. Fig. 6.5(a) shows the deviation of the phase from the mean value along a cross-section in the region under investigation (boxed area in Fig. 6.2(f)). The area under investigation was rotated by 5.5° in order to scan along the smallest phase gradient. Two statements can be drawn from the standard deviation measurements. Firstly, the phase error decreases the more holograms are used for the spatial averaging approach, see Fig. 6.5(b). Secondly, the further distant the holograms used for the spatial averaging method are the better is the image quality.

The averaging approach has also been applied to intensity reconstructions. Fig. 6.2(c) shows a segment of the reconstructed intensity image. The SNR for the presented segment is 36.61 dB. Contrary to the double exposure phase the influence of a possible phase offset is not too severe for the intensity reconstruction when applying the synthetic aperture method, see Fig. 6.2(b).
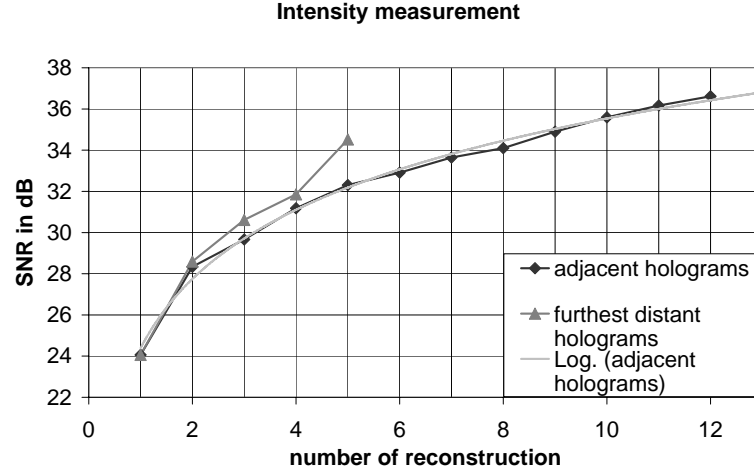
(a)
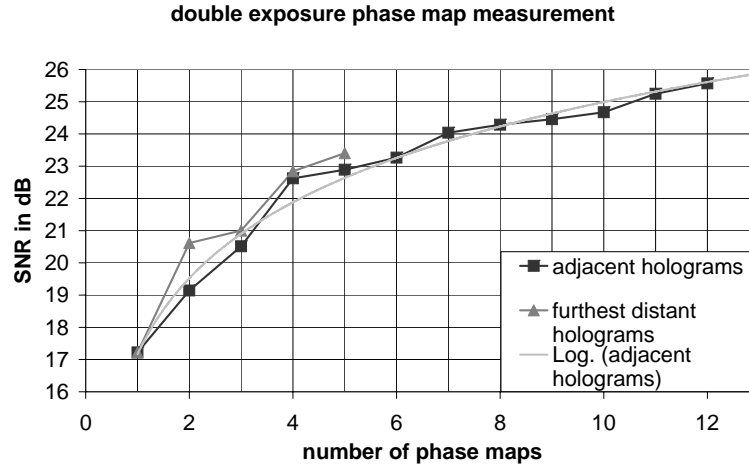
(b)

Figure 6.6: (a) SNR for intensity reconstruction versus number of images and their position, (b) SNR for phase map versus number of images and their position

In Fig. 6.6 the SNR-curves for the intensity reconstructed holograms and double exposure phase maps are shown. The relationship between number of holograms (Nh) used and the SNR follows to a good approximation a logarithmical curve described by:

$$f(Nh) = a \cdot \ln(Nh) + b \qquad (6.11)$$

The logarithmic coefficients and the *squared correlation coefficient R^2* are shown in Table 6.3. In conclusion, the statements previously made for the standard deviation could be confirmed by the SNR-curves.

Table 6.3: SNR spatial averaging method for intensity and double exposure phase map

Parameters	Intensity reconstruction	Double exposure phase map
a	4.842	3.3973
b	24.392	17.169
R^2	0.995	0.985

6.2.3 Resolution Improvement

In order to determine the resolution improvement for the synthetic aperture-method the USAF 1951 test target has been used as the object under investigation. Firstly, a Fourier-hologram without applying the synthetic aperture method was recorded. Zero-padding was applied to generate a hologram of equal dimensions in the x- and y-direction, see Fig. 6.7(a). In this manner the reconstructed hologram does not suffer from different pixel-sizes $\Delta x''$ and $\Delta y''$ (Eq. 6.12), which would otherwise result in a stretched reconstruction and possess different DOF and resolution in vertical and horizontal direction.

$$\Delta x'' = \frac{\lambda d'}{N \Delta x'} \;\; \text{and} \;\; \Delta y'' = \frac{\lambda d'}{M \Delta y'} \tag{6.12}$$

Where N and M are the pixel-numbers in x' and y'-direction.

Table 6.4: Theoretical and practically achieved resolution

Parameters	3000x3000 at 295 mm	8000x8000 at 295 mm
Theoretical resolution in μm	17.8	6.7
Vertical resolution in μm	17.5	6.2
Horizontal resolution in μm	17.5	7.8

Afterwards a hologram was recorded using the synthetic aperture-method. Fig. 6.7 shows the recorded holograms and their reconstructions for 3000x3000 pixels and 8000x8000 pixels, respectively. The smallest resolvable test target element was determined in the same manner as described in Section 4.7.4. According to Rayleigh's-criterion applied to a rectangular aperture (Eq. 4.25) the theoretically possible resolution was calculated and compared with the resolution of the reconstructed holograms, see Table 6.4. Three conclusions can be drawn from this comparison. Firstly, the obtained resolution with the synthetic aperture method is almost three times larger than the resolution obtained with a single hologram. Secondly, the result obtained matches well with the expected value. Last but not least, the vertical and horizontal resolution obtained differ slightly, which might be due to a different vertical and horizontal dimension of the light sensitive pixel area. In a next step the USAF 1951 test-target holograms have been applied to the spatial averaging approach. Each single hologram was zero-padded to create an 8000x8000 pixels hologram in order to have the same pixel-size $\Delta x''$ in the reconstruction-plane. The result is shown in Fig. 6.9(a). The resolution is the

(a)

(b)

(c)

(d)
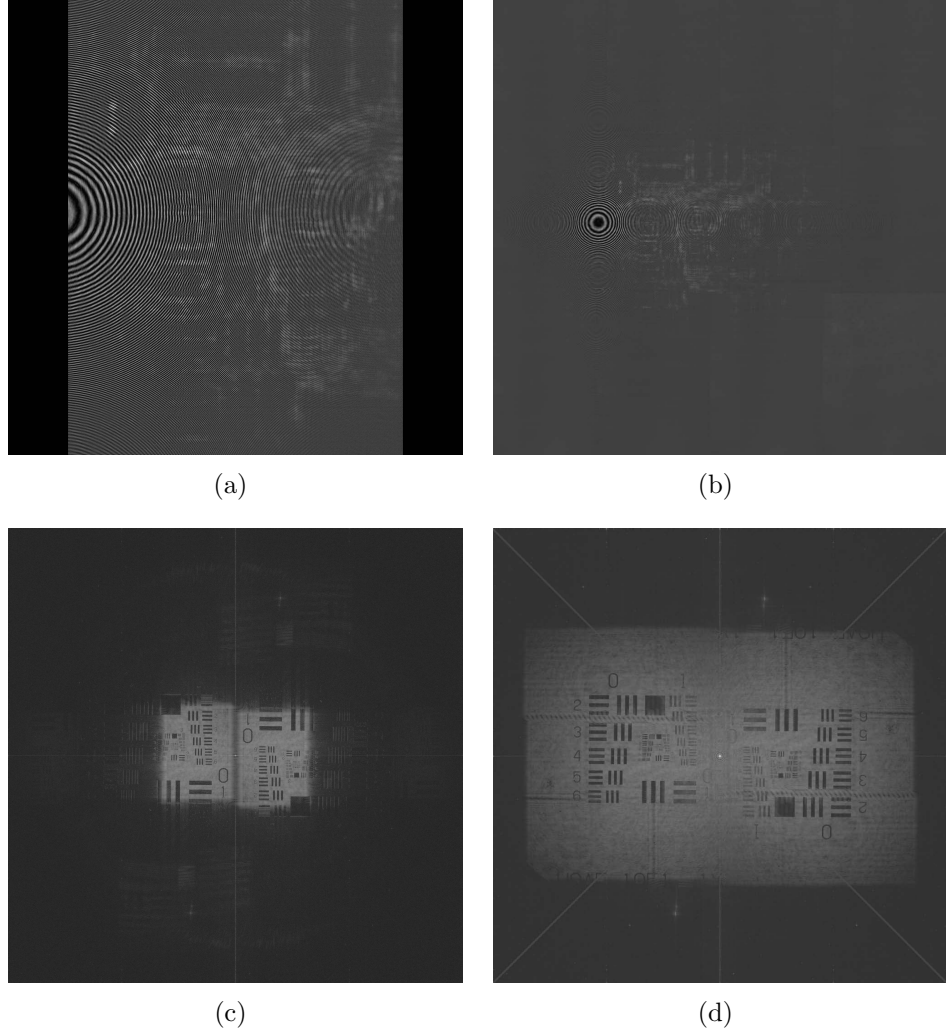
Figure 6.7: Hologram at recording distance of 295 mm for (a) 3000x3000 pixel, (b) 8000x8000 pixel and their reconstructions (c) and (d), respectively

same as in shown in Fig. 6.8(a). Hence no resolution improvement was obtained, which is due to the fact that the experiment was carried out with a transparent object. A large amount of the light used for illuminating the object passes through the object in an undiffracted manner. If the camera is shifted away from the central illuminated object position less light from the object is recorded. The resulting effect can be compared to a high-pass filter, which results in the reconstruction of sharp edges only. The background intensity of the object features is not reconstructed. Therefore, those test target elements, whose size is close
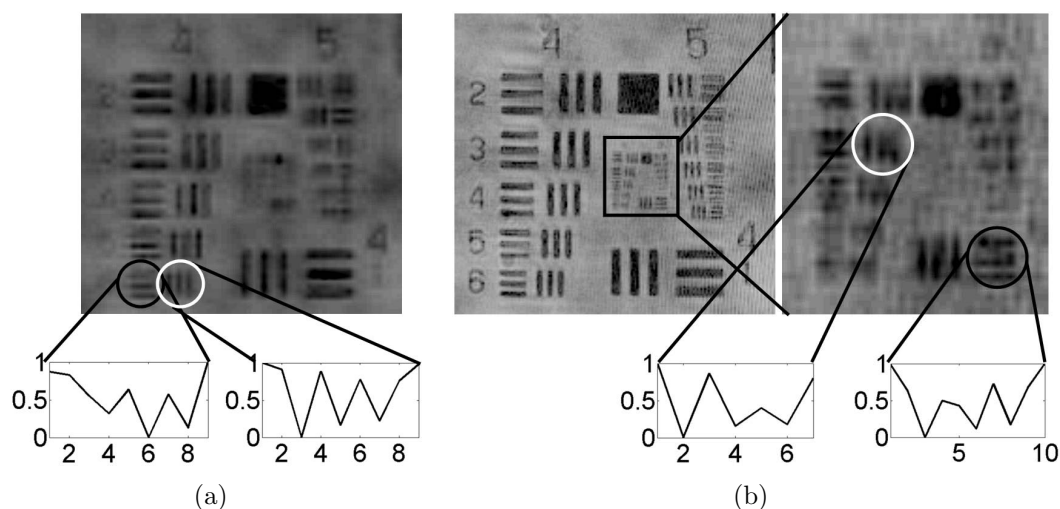
Figure 6.8: Region of interest including cross-section for (a) 3000x3000 pixel hologram, (b) 8000x8000 pixel hologram

to the optical resolution of the holographic system, are reconstructed as bright strips on a dark background. In the spatial averaging process high spatial object frequencies, displayed as a bright pixels for the reconstructed off-centred holograms and as a dark pixel for the reconstructed central hologram, cancel each other out. As a result a reduced resolution is obtained. The central individually reconstructed zero-padded hologram, which holds the major information of the USAF 1951 test-target, has a better resolution than when averaging all reconstructed holograms. This statement is confirmed by comparing Fig. 6.8(a) with Fig. 6.10, which corresponds to the section B2 in Fig. 6.9(b). This proves both statements made in Section 4.7.4. Firstly, zero-padding improves the resolution of the numerically reconstructed hologram. Secondly, increasing the number of zero-padded pixels by more than twice the hologram-size does not result in a significant resolution improvement, which is confirmed by comparing Fig. 4.25(d) with Fig. 6.10. A better resolution with the spatial averaging approach could be obtained using a diffuse reflective object.

(a)

(b)
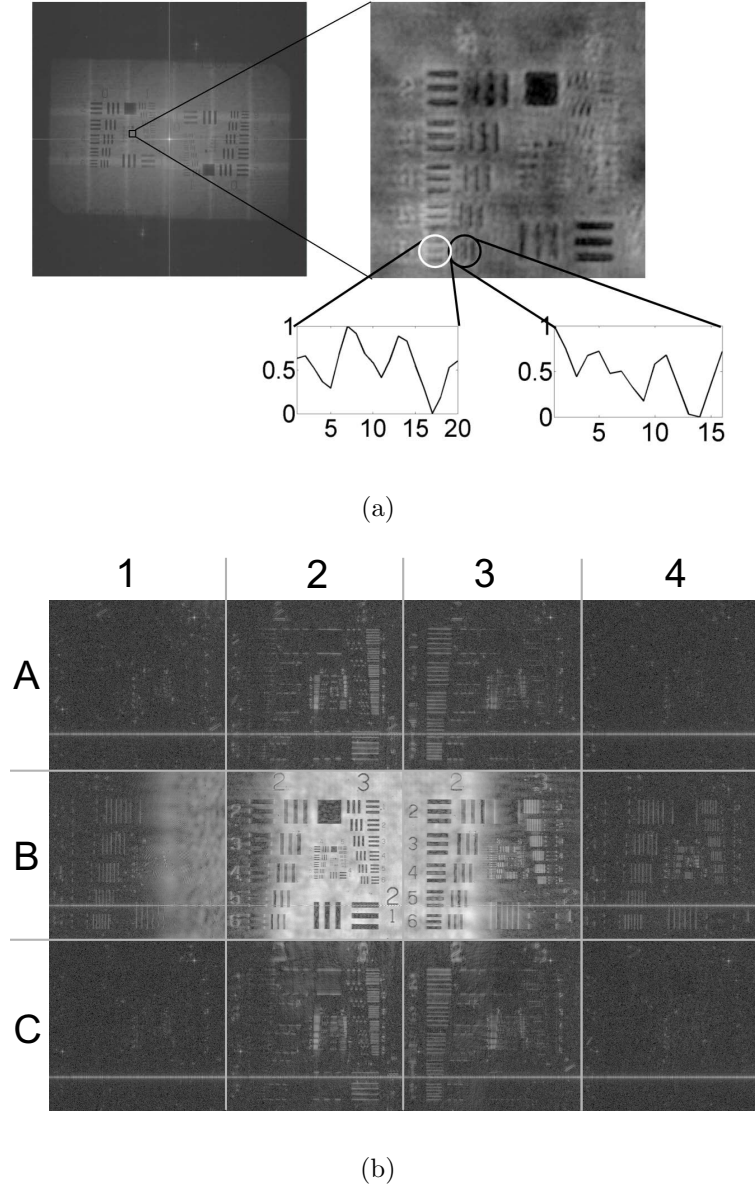
Figure 6.9: (a) USAF 1951 test-target result with the spatial averaging approach, (b) displaying the same section for the twelve reconstructed holograms

6.2.4 Extended Depth of Field (EDOF) Method

The application of large NA optical systems results in a reduced Depth of Field (DOF). Only a small axial region of a three dimensional object is sharply represented in the reconstruction plane as shown in Figs. 6.11(a) and (b). One
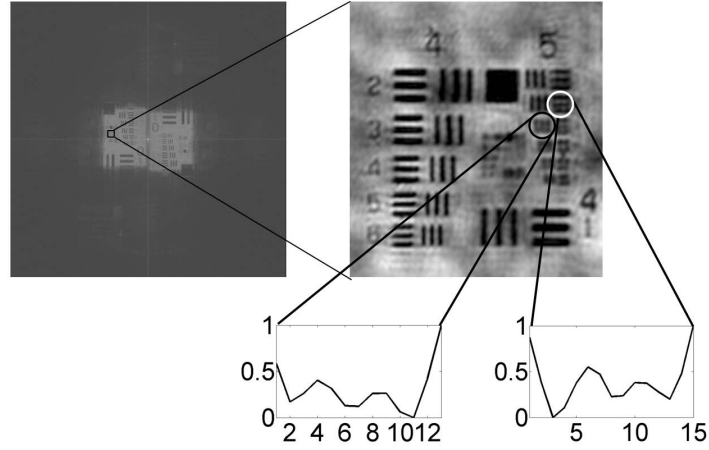
Figure 6.10: Region of interest including cross-section for reconstruction obtained from a 8000x8000 pixels zero-padded single hologram (3000x2208 pixels)

way to overcome this problem is demonstrated in the EDOF method originally applied in confocal microscopy. As a result an image with all parts in focus and a topology map can be obtained. The EDOF method was implemented by generating a stack of reconstructed holograms which are separated by the DOF. The equation to calculate the DOF was derived in Section 4.4.2. The NA obtained is 0.052, which is smaller than the critical ($NA_{critical}$=0.090) obtained by Eq. 4.34. For values smaller than $NA_{critical}$ diffraction effects are negligible for the calculation of the DOF. In this case the DOF calculation is only restricted to the geometric-optical model which results in:

$$DOF = \frac{\Delta x''}{\Gamma' NA} \tag{6.13}$$

With $\Gamma' = 1$ and

$$\Delta x'' = \frac{\lambda d}{N \Delta x}$$

Eq. 6.13 is rewritten as:

$$DOF = \frac{2\lambda d'^2}{(N \Delta x')^2} \tag{6.14}$$
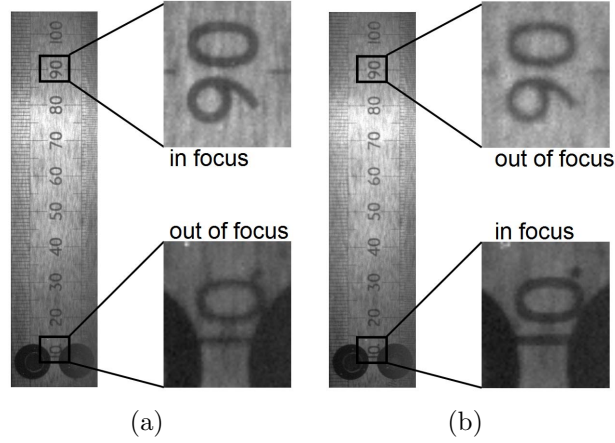
Figure 6.11: (a) Intensity reconstruction for $d' = 728$ mm, (b) intensity reconstruction for $d' = 735$ mm

The DOF obtained with Eq. 6.14 is 0.7 mm for a synthetic aperture hologram of 8800x8800 pixels. The object under investigation is the same cantilever as previously used. The EDOF method had already been applied to digital holography [Do and Javidi (2007); McElhinney et al. (2008) and Tachiki et al. (2008)], but to the authors knowledge it is the first time to report the combination of synthetic aperture-method with the EDOF method. Not all algorithms used in microscopy to define the in-focus object regions can successfully be applied in digital holography due to the speckle effect. The most successful algorithm is based on the variance approach [McElhinney et al. (2008) and Tachiki et al. (2008)], which was also applied in our case. Speckle noise apparent in the numerical reconstruction produces a large change of variance. Therefore before calculating the variance a *speckle-noise reduction filter* [McElhinney et al. (2008)] needs to be applied or the reconstructed *hologram needs be resized*. Furthermore, the variance method requires sufficient object illumination for all parts under investigation. The object illumination ideally needs to be homogenously distributed over the entire object in order to obtain a good contrast of all object parts, which results in large deviation of variance values and reduced impact of noise e.g. speckle noise.

A further requirement is the use the correct Window-Size (WS) for which the variance is calculated. If the WS is too small, fine object details are reproduced in the topology map. A WS which is too large results in a reduced accuracy of the topology map. A last limitation of this method is that the axial resolution of the topology map depends on the numerical aperture and wavelength of the optical system. For macroscopic objects the obtainable axial resolution is only in the mm range. Having discussed the limitations the main advantage of this method needs to be put in focus. Instead of recording images focused at different axial positions of the object, only one hologram is numerically refocused to different axial positions. Thus the experimental effort and disturbing environmental influences are minimized. As a result a high resolution reconstruction of all parts in focus and the topology map of the object under investigation is obtained. Another possible application is the generation of a three dimensional particle field and temporal three dimensional particle tracking, see Kreis (2005).

6.2.5   Variance Approach

The numerical focusing at different axial planes is obtained by reconstructing the Fourier-hologram with help of Eq. 3.46 and a numerical lens described in Eq. 3.10. The refocusing range is defined by the upper and lower limit where the reconstructed object is out of focus.

In our case this was between 726 mm and 743 mm reconstruction distance. Within this region holograms separated by 0.5 mm reconstruction step width were reconstructed. The reconstructed holograms were organized in a stack according to their reconstruction distance, as shown in Fig. 6.12. Some pre-processing is required before applying the EDOF method. The region of interest was cropped and then resized to a quarter of its original size from 3600x832 pixels to 900x208 pixels. This step was necessary in order to minimize the calculation time and

reconstructions from
726 mm to 743 mm in
0.5 mm steps

calculation of variance for all
resized reconstructions

stack of maximum value
for each column

Topology map

Variance
approach

4th order polynomial
approximation

Extended depth of field
reconstruction

A———A'

B———B'

depth
in mm

15

10

5

in focus
in focus
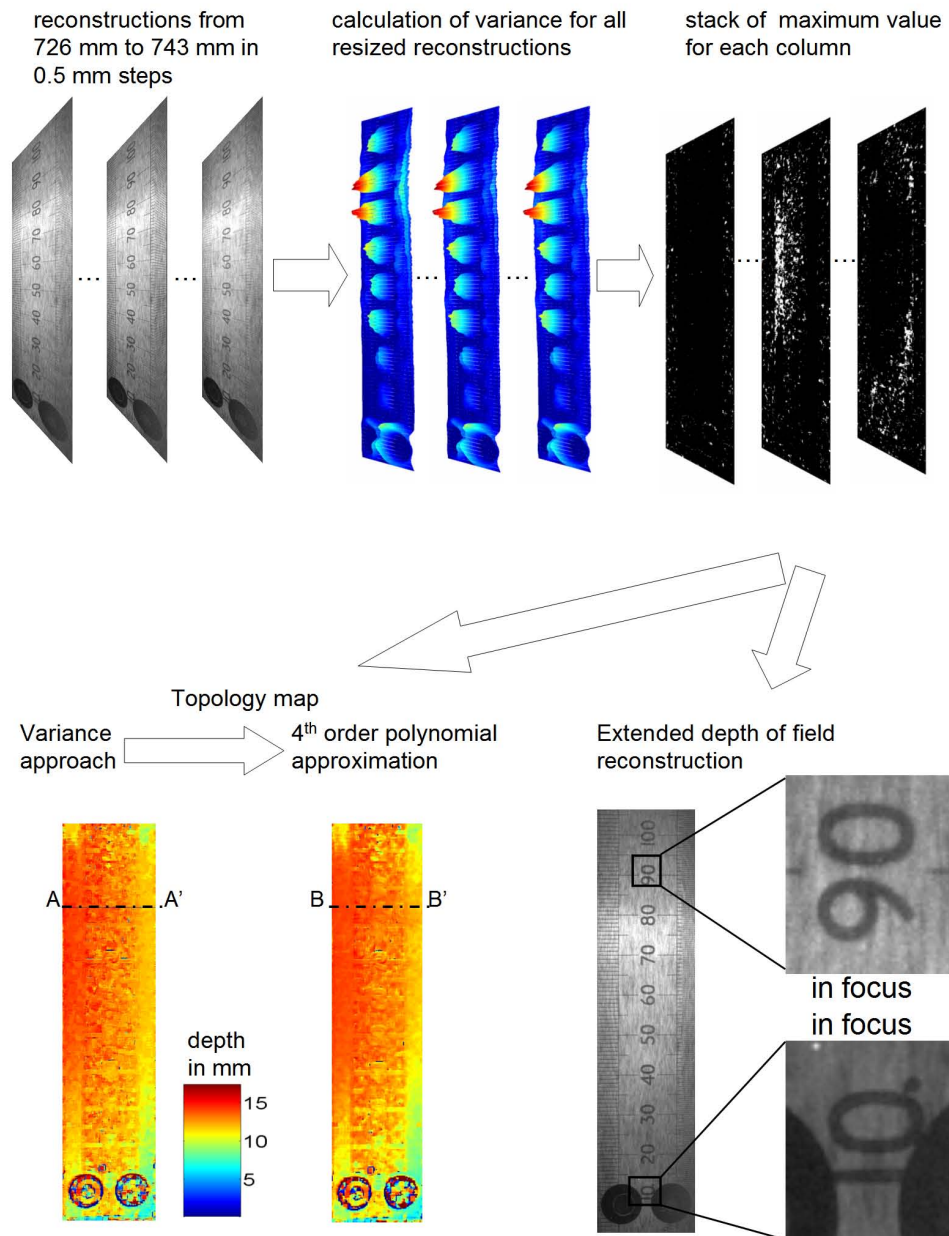
Figure 6.12: Topology map

to reduce the impact of speckle-noise on the variance measurement as previously discussed. The speckle size after resizing is less than the size of a pixel, as a result of which it was not necessary to apply speckle-noise reduction filters, as in McElhinney et al. (2008). The variance of each pixel was calculated with a 10x10 WS. This WS was experimentally found to give the best results. In order to obtain the EDOF reconstruction the stack of the calculated variance maps was binarized on a column by column basis with the threshold set at the maximum variance value in each pixel column. Afterwards, this stack was multiplied in a pixelwise manner with the stack of the reconstructed holograms. A reconstruction with all parts in focus was obtained, shown in Fig. 6.12. The topology map was obtained by recording the position of the maximum variance value for each column in a two dimensional map. The number of quantization levels equals the number of reconstruction planes, see Fig. 6.12.

6.2.6   Gaussian Fitting

Fig. 6.13(a) represents the variance value at each reconstruction distance for both boxed areas shown in Fig. 6.11(a) and (b). It can be concluded that the variance values could be approximated by a Gaussian curve defined by the equation:

$$f(x) = a \exp\left[-\left((x-b)/c\right)^2\right] \tag{6.15}$$

Where a, b and c are the Gaussian coefficients. For both boxed regions shown in Fig. 6.11(a) and (b) the Gaussian coefficients found are shown in Table 6.5. The R^2 values confirm validity of this approximation. This corresponds with the assumption used by other authors to describe the sharpness-distance relationship Chang et al. (2009).

This Gaussian approximation was then applied to obtain interpolated variance values. In practice, instead of a Gaussian approximation a fourth degree
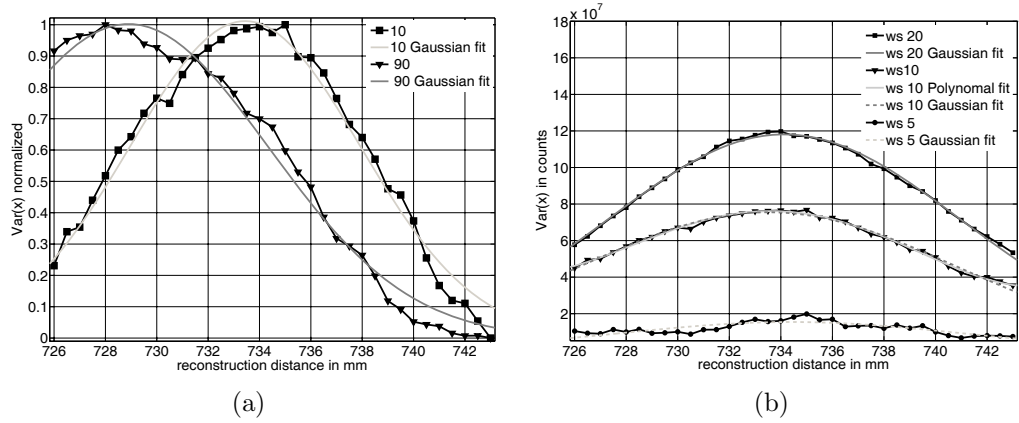
Figure 6.13: (a) Variance plot for both boxed areas shown in Fig. 6.11 including Gaussian curve fitting, (b) Gaussian curve fitting for different WS and comparison polynomial fitting for WS of 10x10 pixels

polynomial approximation was used. In this manner the calculation time could be reduced and the algorithm became more robust towards any calculation errors, which would have caused the program to end abruptly. These errors occurred whenever the maximum variance value was close to the first or last distance value. In this case no Gaussian function could be found to fit the data. The Gaussian and the fourth degree polynomial are shown in Fig. 6.13(b) for a WS of 10x10 pixels. Moreover, from Fig. 6.13(b) can be concluded that the performance of the Gaussian fitting can be used to obtain the correct sliding WS in order to perform the variance calculation. The degree of WS-performance can be described by the R^2 values of 0.667, 0.989 and 0.997 for a WS of 5x5, 10x10 and 20x20, respectively. The quantization levels of the topology map could be increased utilizing the Gaussian fitting method.

Table 6.5: Gaussian coefficients and R-squared values

Parameters	Boxed area 90	Boxed area 10
a	0.9843	0.9834
b	728.1	733.5
c	11.4	10.35
R^2	0.9893	0.9893

(a)

(b)
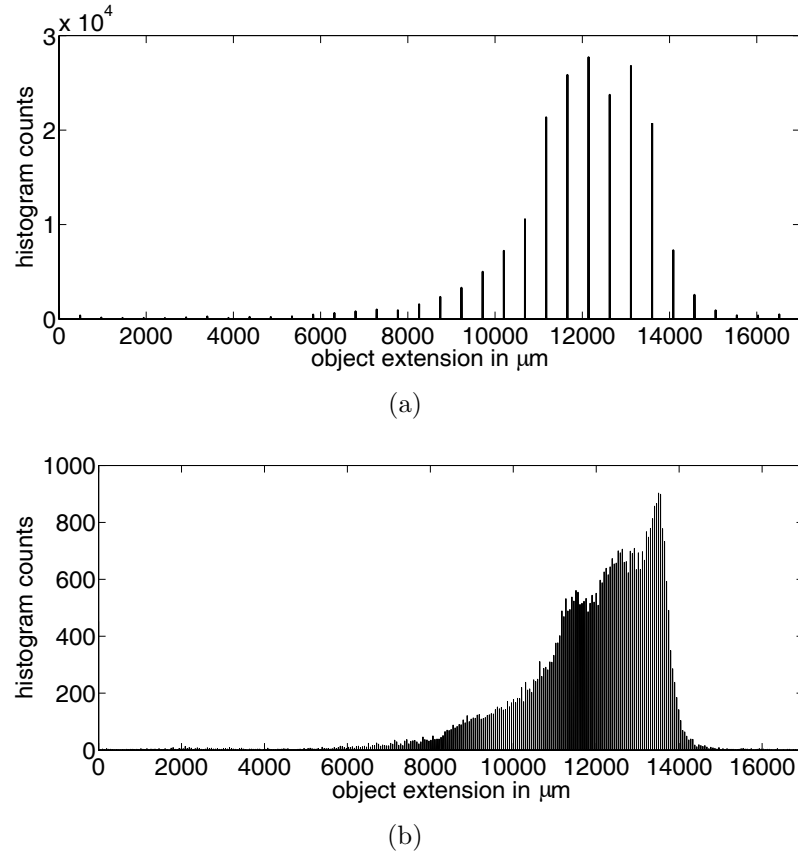
Figure 6.14: Histograms for obtained topology map with, (a) traditional variance approach, (b) polynomial interpolation

The obtained interpolated maximum value is used instead of the original maximum variance value. In this manner the number of quantization levels increased from 35 by solely applying the variance approach to 349 by applying the polynomial fitting. This is shown in Fig. 6.14(a) and Fig. 6.14(b), respectively. Furthermore, location errors for the maximum variance value as shown in Fig. 6.13(a) can be reduced by the interpolated maximum value, which results in an accuracy improvement. This could be demonstrated by a decreased standard deviation, which was calculated for both profile-lines shown in Fig. 6.15 from 0.96 mm to 0.79 mm. The aforementioned advantages are off-set by the long processing time. Despite the reduction of the stack-size from 35x342x1100 pixels to 35x171x550 pixels the calculation time was 40 min with a server using an In-

tel Xeon @2 GHz processor on Matlab at 64 bit. In comparison, the previously described variance approach applied to the original stack-size needed 57 s. The axial extension obtained from the topology map for the cantilever is 7.14 mm. The holographically obtained topology data was validated by tactile manners using a vernier caliper. The axial length differences between the deflected cantilever to its mount was measured at its four corners. The obtained result for the topology map could be confirmed by the measured values with millimeter accuracy. Further calibration work is required in order to validate data in the sub-mm range.

(a)

(b)
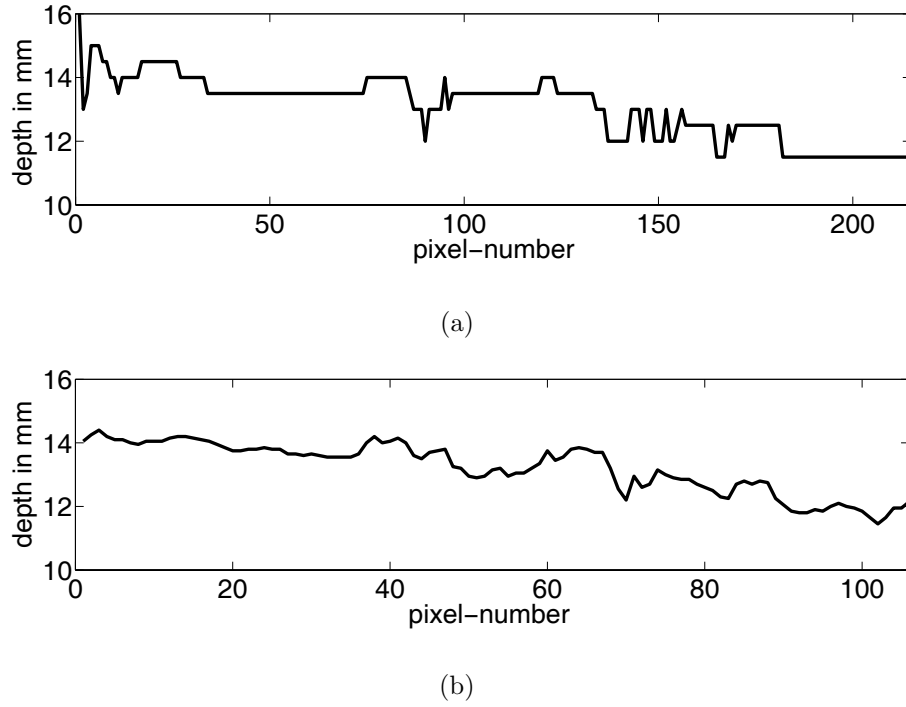
Figure 6.15: Cross-sections for indicated lines shown in Fig. 6.12, (a) A-A', (b) B-B'

6.3 Sub-pixel Sampling Method

The sub-pixel sampling method is focused on resolution improvement by reducing the recording distance. This can be accomplished by recording the hologram with a smaller pixel-size. A smaller pixel-size is obtained by shifting the CMOS camera with sub-pixel accuracy into the light insensitive pixel area. Due to the smaller fill-factor of lens-less CMOS sensors, a more reliable integrated irradiance is obtained in comparison to the application of the sub-pixel sampling method with CCD-technology, described in Kornis and Gombköto (2005). Moreover, the environmental influences have been minimized by applying phase stepping. In that manner, the sub-pixel sampling method described here presents a novel approach to improve the resolution in digital holography.

6.3.1 Setup and Methodology

The setup used is shown in Fig. 6.16. The previously used spherical reference-wave in Section 6.2 was replaced by a plane reference-wave.
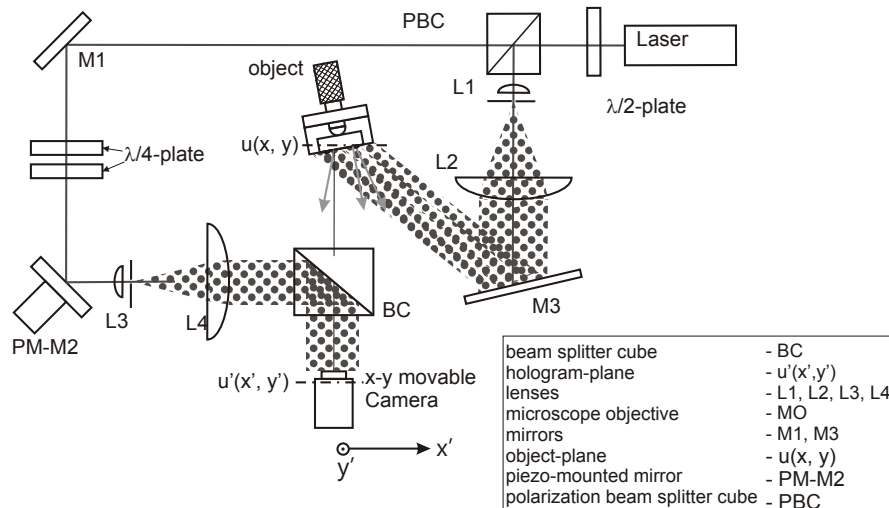
Figure 6.16: Sketch of schematic setup
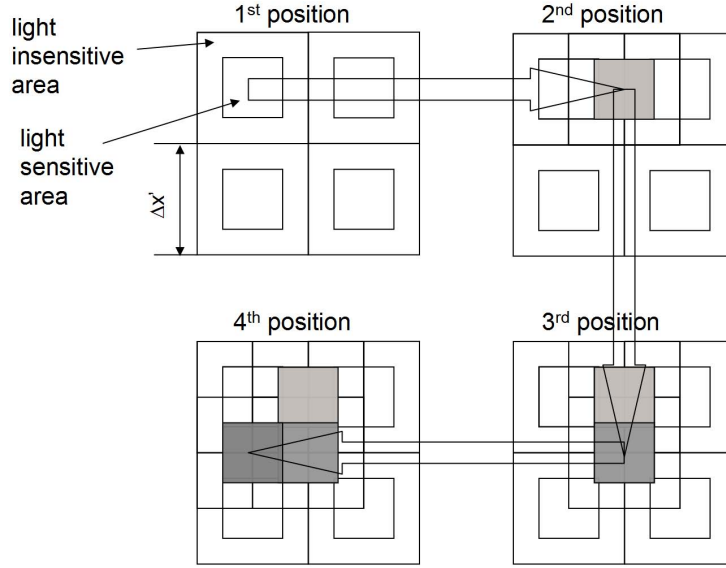
Figure 6.17: Sketch of original camera pixel and schemata of four position movement in order to obtain sub-pixel resolution

The minimum distance for a plane reference-wave according to Eq. 4.8 was taken into account when setting up the experiment. Other setup parameters in order to obtain the best possible contrast, as discussed in Section 2.4, have been taken into account. In order to increase the resolution of the numerically reconstructed hologram, the camera sensor is moved by the PI-150.11 x-y-stage in a 2x2 grid to four positions. The displacement between each consecutive position is half the pixel-size. In that manner one original pixel can be replaced by four sub-pixels of half the pixel-size, see Fig. 6.17. The influence of the pixel-size on the MTF was discussed in Section 4.6.1. The pixel MTF can be described by:

$$\text{MTF}_{\text{pixel}} = |\text{sinc}(\nu_{x'}\Delta x')| \tag{6.16}$$

The pixel MTF contributes to the overall MTF of the opto-electrical system in a multiplicative manner. The benefits of using a smaller pixel-size in conjunction with the recording process and the obtained pixel MTF are:

i. Due to the smaller pixel-size the camera-object distance can be reduced. This results in more light from the object being recorded, which reduces the impact of noise in the recording process.

ii. The reduced camera-object distance enables a more detailed reconstruction.

iii. The cutoff-frequency for the sub-pixel sampling method is higher than when recording with the normal pixel-size, see Fig. 6.18.

iv. Furthermore, spatial frequencies are recorded with a higher contrast using the sub-pixel sampling method.

v. Last but not least, a fill-factor of 100% is obtained by means of the sub-pixel sampling method. Thus the light-sensitivity is larger compared to a CMOS and CCD sensor of equivalent pixel-size.

Temporal phase stepping was applied to each of the four recording positions. In this way environmental disturbances which cause the interference fringes to shift slightly around a centred location were averaged and minimized. Phase stepping was implemented in the setup by a piezo-mounted mirror in the reference-arm.

The additional effort for applying phase stepping is rewarded by enabling an in-line setup with a further reduced object-camera distance. The phase stepping algorithm used was firstly proposed in Cai et al. (2004). It is based on recording at least three phase stepped holograms. This algorithm calculates each phase step by which phase step errors are minimized. The four different phase maps which correspond to each camera position are combined in a common phase map. The combination procedure for a 2x2 pixel sensor is shown in Fig. 6.19. The initial phase among the four phase maps might differ. This would result in sudden phase jump between adjacent pixels in the combined phase map. The numerical reconstruction of a combined phase map without adjusting the initial
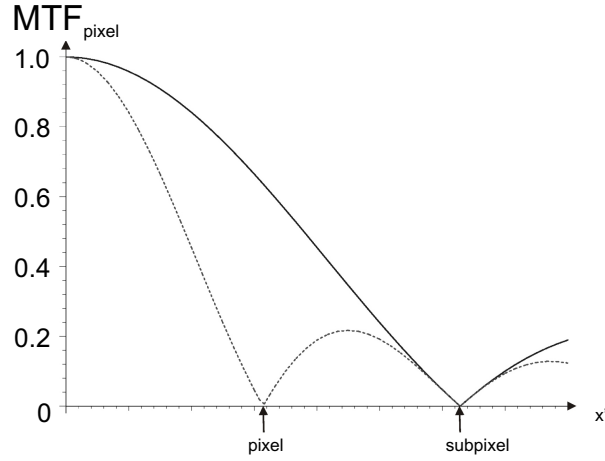
Figure 6.18: Graph comparison of MTF sensor for the normal pixel-size and half the pixel-size employing the sub-pixel sampling method

phase for each of the four individual phase maps leads to the occurrence of higher diffraction orders. These higher diffraction orders cause a splitting of the object information, see Fig. 6.20(b). This problem can be solved by resizing a part of the first phase-hologram A to twice its size. The interpolated phase value of the resized hologram A' are used to calculate the phase difference for the other three phase maps B, C and D. The phase difference is then subtracted from each of the three phase maps B, C and D. A schematic sketch of the phase correction approach is shown in Fig. 6.21. The final combined phase map possesses a smooth phase transition, which to a reasonable extent suppresses higher orders in the reconstructed hologram, see Fig. 6.20(c).
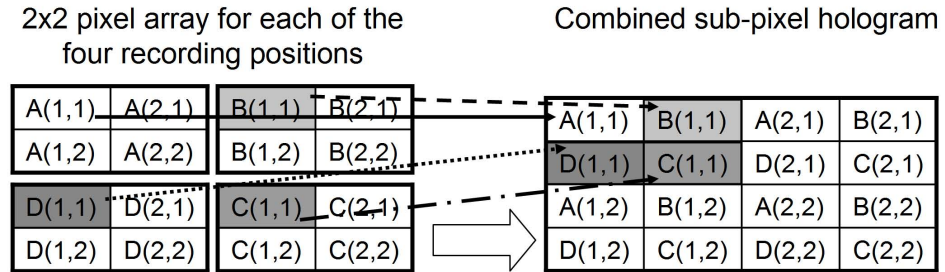
Figure 6.19: Combination procedure to obtain a sub-pixel hologram
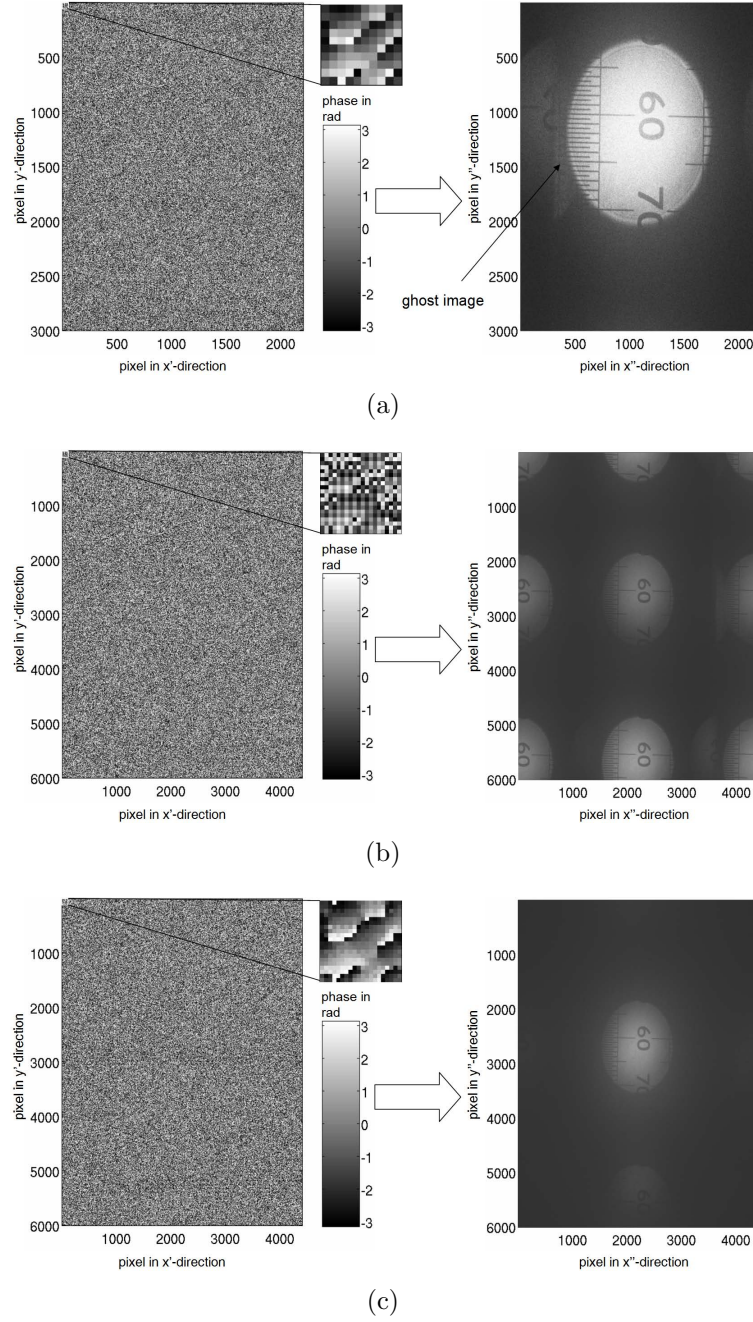
Figure 6.20: Phase-hologram and reconstruction at 191 mm recording distance for (a) normal hologram with 3.5 μm pixel-size, (b) sub-pixel hologram without phase correction and (c) sub-pixel hologram with phase correction

The numerical reconstruction was obtained using the Fresnel method Eq. 3.39. Holograms with and without applying the sub-pixel sampling method have been recorded at a camera-object distance of 191 mm. The centre of the object

is positioned with a 10 mm shift to the optical axis. Applying Eq. 4.8 results in a minimum camera-object distance of 279 mm for 3.5 μm pixel-size and 140 mm for 1.75 μm pixel-size. Thus the Nyquist-criterion is violated for the hologram of 3.5 μm pixel-size recorded at 191 mm distance. In this case, aliasing occurs, which results in the appearance of ghost images, see Fig. 6.20(a) left side. In addition to the recording at a distance of 191 mm, a hologram was recorded at a distance of 300 mm. At this distance the recorded hologram with a 3.5 μm pixel-size is not under-sampled. A small region of interest is selected for the intensity reconstruction without the sub-pixel sampling method at 300 mm, shown in Fig. 6.22(a), and at 191 mm recording distance applying the sub-pixel sampling method, shown in Fig. 6.22(b). The SNR values for these reconstructions are 22.71 dB for Fig. 6.22(a) and 25.18 dB for Fig. 6.22(b).
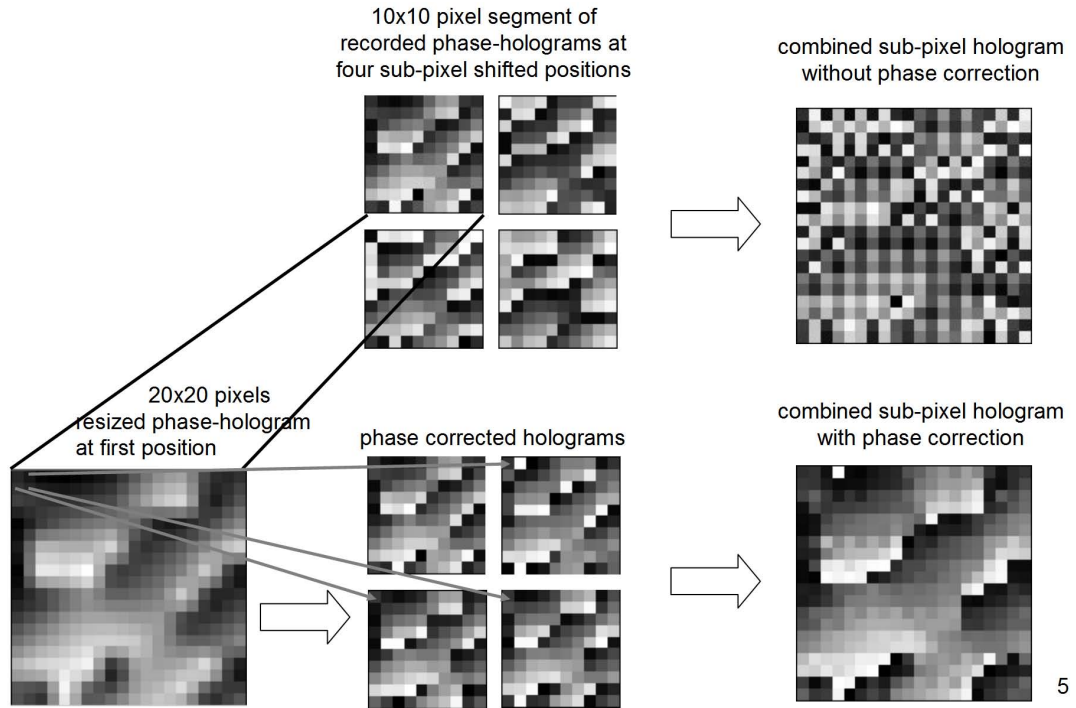
Figure 6.21: Sketch of phase-correction procedure
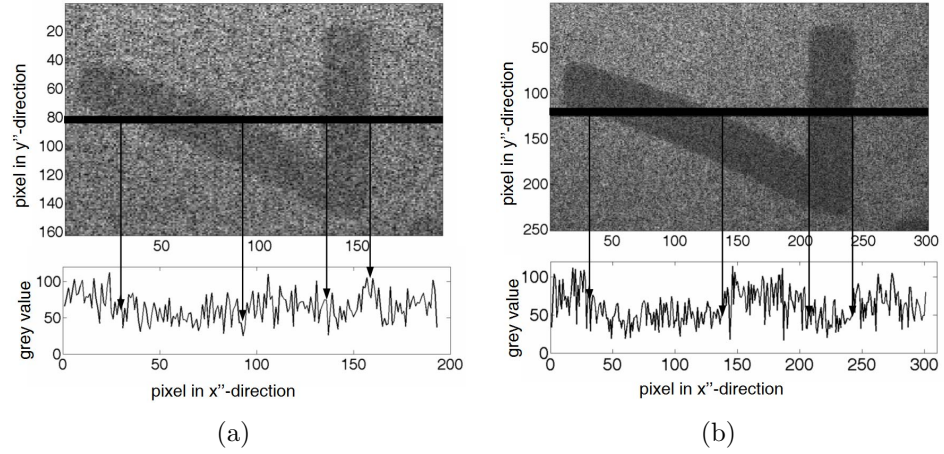
Figure 6.22: Region of interest for intensity reconstruction and their profile lines for (a) 300 mm recording distance with 3.5 μm pixel-size, (b) sub-pixel hologram 191 mm recording distance

Double exposure holograms in conjunction with the sub-pixel sampling method have been recorded to evaluate the visibility of the 2π discontinuities obtained. The recording distance was again chosen to produce an under-sampled hologram for the 3.5 μm pixel-size. The cantilever was deflected by 2 mm in order to produce a high density of fringes in the double-exposure phase map. Due to the high density of fringes only a small segment of both double exposure phase maps are displayed in Fig. 6.23. The fringes are more defined for the sub-pixel sampling method than for the reconstruction with a 3.5 μm pixel-size. This is also represented by the SNR values of 11.07 dB and 10.96 dB, respectively.
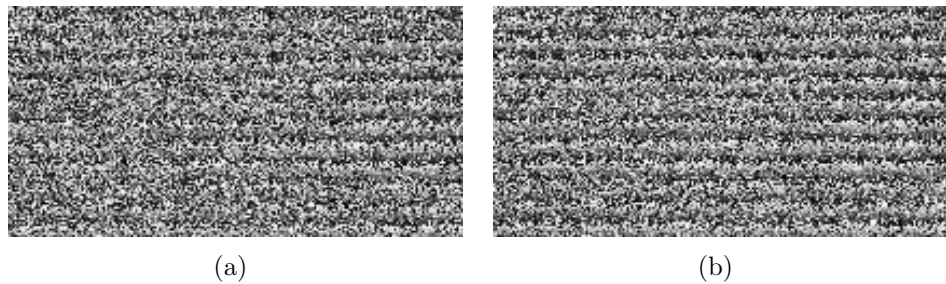
Figure 6.23: Segment of double exposure phase maps for 191 mm recording distance (a) normal hologram with 3.5 μm pixel-size, (b) sub-pixel hologram with 1.75 μm pixel-size

In addition to the SNR the standard deviation and the corresponding relative deformation has been calculated. This parameter is more meaningful to prove the system's accuracy performance. The obtained standard deviation alongside the minimum phase gradient is 1.76 rad and 1.72 rad for double exposure phase maps with 3.5 μm and 1.75 μm pixel-size, respectively. The corresponding relative deformation is $\frac{\lambda}{6.88}$ and $\frac{\lambda}{7.05}$, respectively. Thus the double exposure phase map obtained with the sub-pixel sampling method can resolve to a higher degree of accuracy.

6.3.2 USAF 1951 Test Target

In order to determine the resolution improvement for the sub-pixel sampling method the USAF 1951 test target was used as the object under investigation. The setup used is shown in Fig. 6.24. The previously employed plane reference-wave has been replaced by a spherical one to enable the recording of Fourier-holograms, which possess a more efficient use of the sensor's Space-Bandwidth-Product (SBP), as discussed in Chapter 5. The transparent USAF-1951 test-target was placed between mirror and beam splitter.
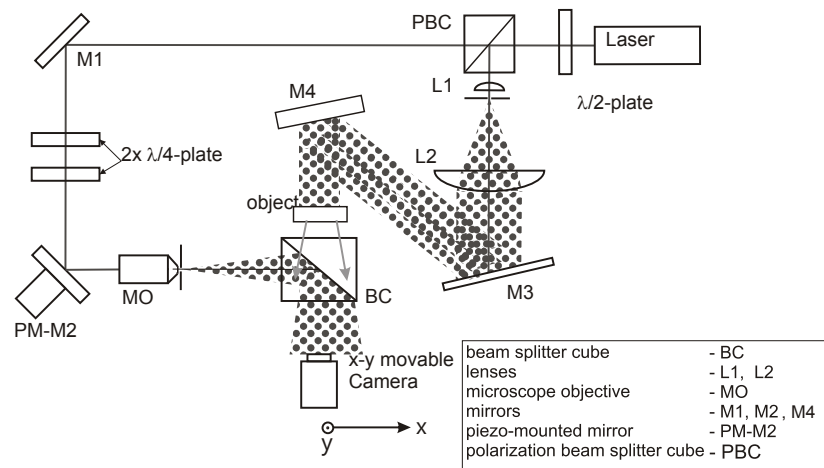
Figure 6.24: Recording setup for determination of optical resolution
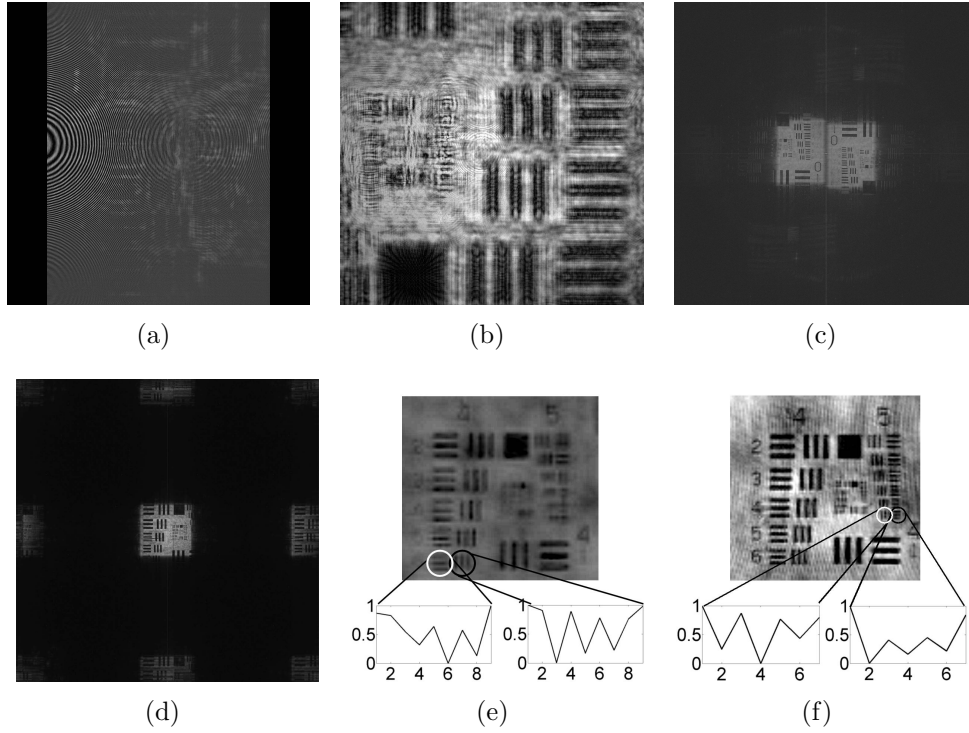
Figure 6.25: (a) Intensity hologram 3000x3000 pixels, (b) modulus of calculated complex object-wave 6000x6000 pixels, numerical reconstructions (c) without sub-pixel sampling method, (d) with sub-pixel sampling method, (e) and (f) corresponding areas of interest to determine smallest resolvable element

An intensity hologram was then recorded without applying the sub-pixel sampling method at 295 mm recording distance. Zero-padding was applied to generate a hologram of equal dimension in x'- and y'-direction. In this manner the reconstructed hologram does not suffer from different pixel-sizes $\Delta x''$ and $\Delta y''$, which otherwise would result in a stretched reconstruction and might produce different horizontal and vertical resolution and DOF. Afterwards, three phase shifted intensity holograms at each sub-pixel position were recorded at 185 mm recording distance. The complex object-wave was then calculated employing Cai's algorithm, see Cai et al. (2004). The intensity hologram recorded at a distance of 295 mm, the modulus of the complex object-wave for the sub-pixel hologram and their corresponding numerical reconstructions are shown in Fig. 6.25. In order to observe the smallest resolvable test target element a small re-

gion has been selected, shown in Fig. 6.25(e) and(f). The theoretically possible resolution according to Eq. 4.25 and the achieved resolution for both holograms shown in Fig. 6.25(a), (b) are presented in Table 6.6. In conclusion, it was found that the resolution obtained could be doubled and the obtained resolution matched well with the expected value.

Table 6.6: Theoretical and practically achieved resolution

Parameters	3000^2 at 295 mm	6000^2 at 185 mm
Theoretical resolution	17.8 μm	11.2 μm
Vertical resolution	17.5 μm	8.7 μm
Horizontal resolution	17.5 μm	8.7 μm

6.4 Combination of Synthetic Aperture and Sub-pixel Sampling Method

The advantages of both methods were combined and the resolution improvement demonstrated on an USAF 1951 resolution test target.

6.4.1 Setup and Methodology

The setup used is the same as previously used for the synthetic aperture method to explore the resolution improvement. Fourier holograms have been recorded in combination with phase stepping. The in-line arrangement enables the most efficient use of the sensor's SBP, as demonstrated in Chapter 5. The sensor was firstly moved to four different sub-pixel positions, at which phase stepping was applied. This micro-shift, sub-pixel movement, was followed by a macro-shift, which was in the range of the sensor's dimension.
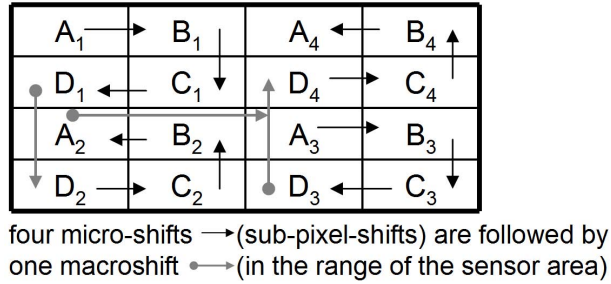
Figure 6.26: Camera movement
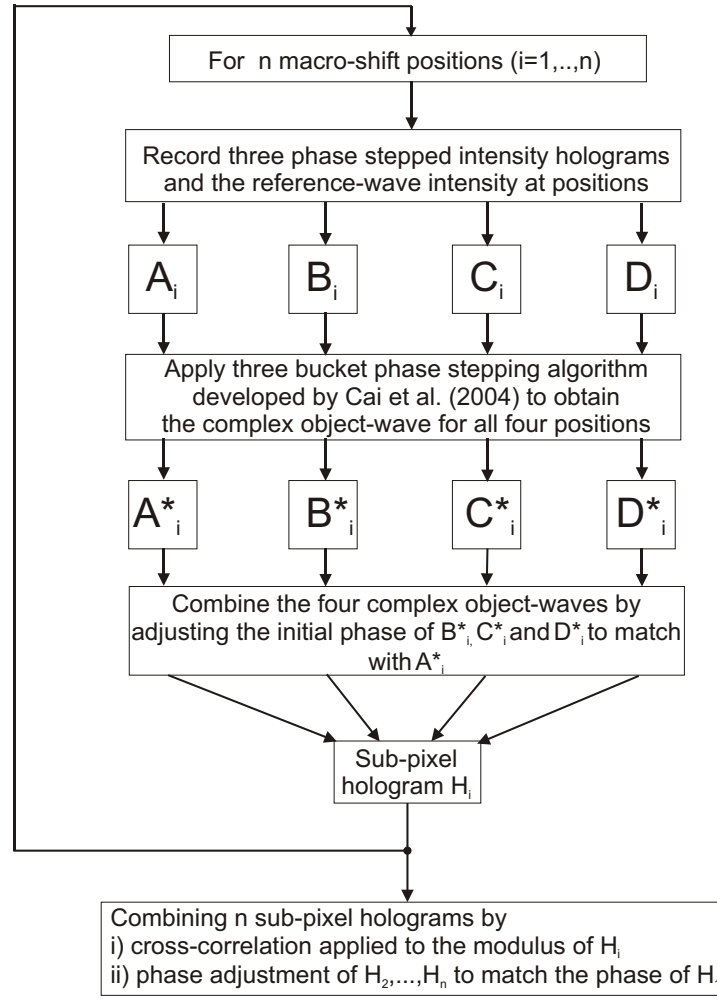
Figure 6.27: Flow chart combination procedure

The procedure was repeated four times to obtain a synthetic aperture of 10,040x10,040 pixels with 1.75 μm pixel-size. The different movement steps are shown in Fig. 6.26. Thus the camera was traversed to a total number of 16 different positions. At each of which phase stepping was applied. Not only the initial phase of each individually combined hologram had to be adjusted to obtain a sub-pixel hologram, shown in Fig. 6.21, but also the initial phase of each sub-pixel

hologram in order to generate the synthetic aperture hologram. Fig. 6.27 represents a more detailed description of the image acquisition and processing steps. The phase and modulus for the hologram obtained by combining both methods is shown in Fig. 6.28 (b) and (c). The resolution obtained was compared to a normal hologram of 3000x3000 pixels with 3.5 μm pixel-size. The reconstruction for both holograms are shown in Fig. 6.29. The resolution obtained is shown in Table 6.7. The results obtained were then compared with those obtained when applying solely the synthetic aperture method and the sub-pixel sampling method. Furthermore, two recent publications on resolution improvement Di et al. (2008) and Gyímesi et al. (2009) have been taken into account for this comparison to serve as a reference for the results obtained. Instead of taking into account only the smallest resolvable object detail the SBP of the reconstructed hologram and the setup efficiency factor η were calculated, as discussed in Section 6.1. From Table 6.8 can be concluded that the SBP and the η obtained can compete with the results published in recent papers.

(a)   (b)   (c)
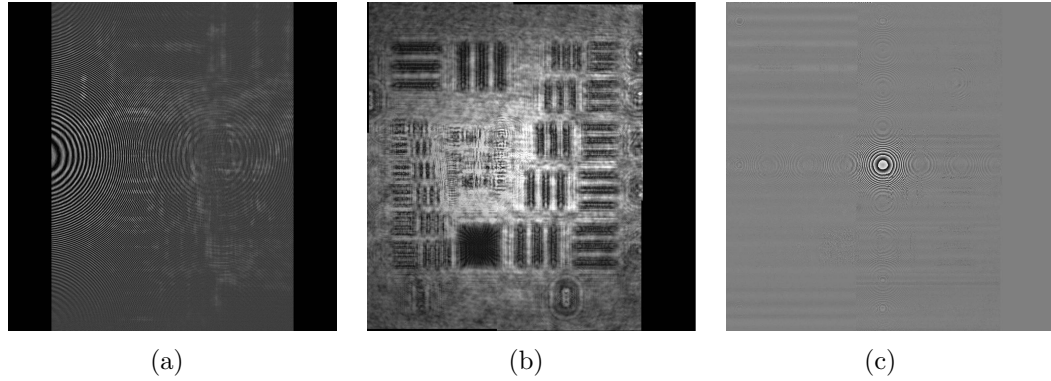
Figure 6.28: (a) Intensity hologram 3000x3000 pixels with 3.5 μm pixel-size at 295 mm, (b) and (c) phase and modulus of hologram 10040x10040 pixels with 1.75 μm pixel-size at 185.25 mm

Table 6.7: Theoretical and practically achieved resolution

Parameters	3000^2 at 295 mm	10040^2 at 185 mm
Theoretical resolution	17.8 μm	6.7 μm
Vertical resolution	17.5 μm	7 μm
Horizontal resolution	17.5 μm	5.5 μm

A larger FOV and consequently a larger SBP and η was expected for the sub-pixel hologram and the hologram obtained combining both methods. Only a small part of the reconstructed hologram displays the image, shown in Fig. 6.25(d) and 6.29(b). The reduced FOV is due to the use of a transparent object. Diffraction only occurs at the edges of the target bar elements. The major part of the recorded light is undiffracted. A collimated laser beam was used to illuminate the USAF test target. Thus the size of the undiffracted recorded light corresponds with the projection of the sensor on the object.
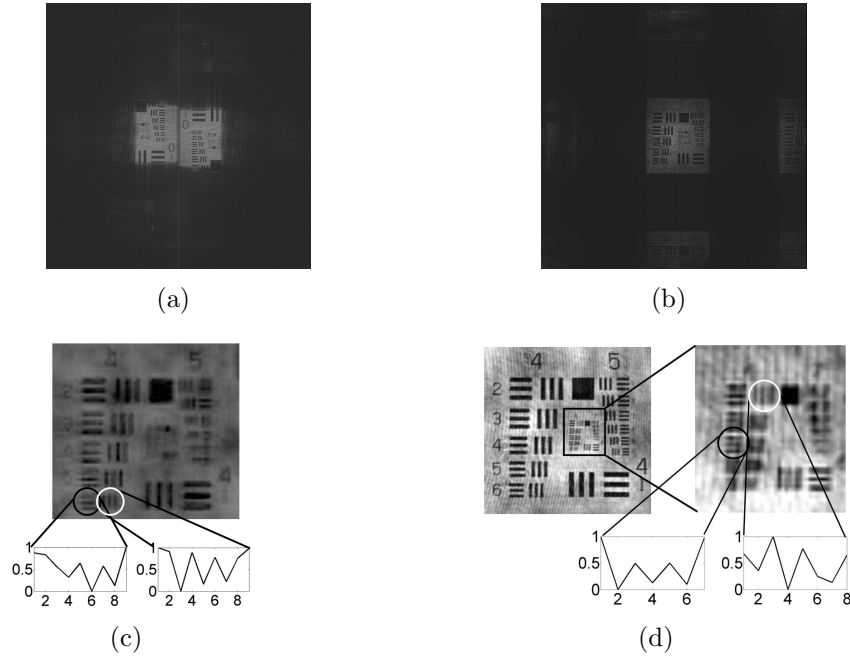
Figure 6.29: (a), (b) Numerical reconstruction for holograms shown in Fig. 6.28, (c), (d) region of interest to evaluate the resolution obtained for both reconstructions, respectively

Table 6.8: SBP comparison

Parameters	Normal holo-gram	Synthetic aperture holo-gram	Sub-pixel holo-gram	Combin-ation	Results refer-ence Di et al. (2008)	Results ref-erence Gyímesi et al. (2009)
Pixel-number in 10^3	3^2	8^2	6^2	10.04^2	5^2	5.12^2
Pixel-size in μm	3.5	3.5	1.75	1.75	7	7.5
FOV in mm^2	9.0x12.1	30x23	11.7^2	16.7x19.5	4x4	330^2
$\delta_{x''}$ in μm	17.5	6.2	8.7	7.0	2.6	446.4
$\delta_{y''}$ in μm	17.5	7.8	8.7	5.5	2.6	446.4
SBP in 10^6	0.36	14.27	1.79	8.44	2.37	0.55
η_{SBP} in %	3.9	22.3	4.9	9.5	8.4	2.1

In that manner, diffracted light which originates from object points outside the projected sensor area is recorded with almost no background intensity. This results in a reduction of visibility for the corresponding object region. In case of the synthetic aperture hologram a larger sensor area was obtained, which results in a larger FOV. The FOV obtained with the synthetic aperture method matches well with the maximum possible recordable object size. The SBP obtained for the reconstructed synthetic aperture hologram is more than six times larger than to the authors knowledge up to date published SBPs in digital holography. The value of η_{SBP} is close to the theoretical value of 25% according to Eq. 6.3 and is largest of the compared results shown in Table 6.8. It needs to be pointed out that the experiments in the two cited papers were performed with a CCD camera of larger pixel-size. Furthermore, in both papers optical imaging elements were used between object and camera, which might explain a reduced η_{SBP}. The result could prove that CMOS cameras can perform at least equally well as

CCD cameras under sufficient lighting conditions. The main advantage of CMOS cameras is their availability with smaller pixel-size. Thus the recording distance can be reduced, which results in a further resolution improvement, see Table 6.8.

6.4.2 Conclusion

Two resolution improvement methods and their combination have been discussed in detail. The resolution improvement could be proven by numerical reconstructions of the commonly used USAF 1951 test target. The potential of these methods in combination with the recording of Fourier-holograms has been demonstrated. It was shown that these methods offer new applications for the investigation of microscopic, such as the finest elements of the resolution target shown in Fig. 6.8, and macroscopic objects, such as the cantilever shown in Fig. 6.2. In case of the *synthetic aperture method*, good results were obtained for the intensity reconstruction and the double exposure phase map, which was proven by an increase of the SNR value. The reduced phase contrast in double exposure phase maps due to axial misalignment could be overcome by applying the spatial averaging approach. It was found that the more laterally displaced the holograms used for spatial averaging approach the better is the image quality. Furthermore, it was found that the image quality increases in a logarithmic manner with the number of adjacent holograms used. The resolution improvement experiment was carried out on the USAF 1951 test target. Here the synthetic aperture method performed better than the spatial averaging technique. The reduced resolution with the spatial averaging approach is most likely due to the usage of a transparent object as previously explained in Section 6.2.3. Moreover, it was demonstrated that the SBP obtained with the synthetic aperture method is the largest reported SBP utilizing digital holography. The highly detailed resolution was combined with a long DOF by using the EDOF method. It is to

the author's knowledge the first time that the synthetic aperture method and the EDOF method have been combined in digital holography to produce firstly a reconstruction with all parts of the axial extended object in focus, and secondly a three dimensional topology map. Furthermore, Gaussian interpolation of the variance values was applied to increase the precision and accuracy of the topology data. A further improvement of the result may be obtained by a more homogeneous illumination (flat-top profile) and reflectivity of the object. All object points would then have the same impact on the recorded hologram, which results in an improvement of measurement accuracy.

The *sub-pixel sampling method* presented is based on a novel approach to improve the resolution. The camera was moved by half the pixel-size to four consecutive lateral positions. In addition phase stepping was applied to increase the environmental stability. The low fill-factor inherent in the application of CMOS technology could be maximized to 100%. The sub-pixel sampling method is not based on interpolation, which increases the reliability of the results obtained. Assuming that the light sensitivity per unit area is constant, this method results in a less noisy read out than a CMOS camera with equivalent pixel-size would produce. The successful implementation of the sub-pixel sampling method was shown for an intensity reconstructed hologram and double-exposure hologram of a cantilever. The image quality improvement for these reconstructions was demonstrated by the SNR obtained. In order to prove the resolution improvement holograms with normal pixel-size and with the sub-pixel sampling method were recorded and reconstructed. A resolution improvement and an increase of the SBP could be demonstrated. The system as it stands at the moment is limited to static measurements due to shifting the camera to four positions at each of which phase stepping is applied. The sub-pixel sampling method could also enable the analysis of real-time events. Three conditions need to be set to allow

this. Firstly, the environmental influences need to be minimized to enable the recording of a single hologram. This could be accomplished by the implementation of a pulsed laser. Secondly, the camera needs to be moved to the four positions with sufficient velocity. Thirdly, at each position a hologram needs to be recorded, which requires a certain frame rate of the camera used. Both x-y stage velocity and camera frame rate need to be temporally aligned. Care needs to be taken that the speckle de-correlation caused by the moving object needs is less than half the speckle size according to Kreis (2005) whilst recording the four laterally sub-pixel shifted holograms. The real-time measurement could be a potential future work and improvement of this method.

The *combination* of both methods, synthetic aperture and sub-pixel sampling method, proves an increased SBP compared to the sub-pixel sampling method alone. The resolution obtained matched well with the one obtained by the synthetic aperture method, although a smaller sensor area was used. This is due to the reduced recording distance, which results in the same NA (NA=0.0474) for both methods.

The presented methods can be applied to improve the optical resolution of intensity and phase reconstructions and the accuracy for phase measurements. It can be carried out on microscopic and macroscopic objects. Thus it offers a large range of possible future applications in the field of e.g. bio-medicine, study of microsystems and in auto-motive industry.

CHAPTER 7

Digital Holographic Microscope

7.1 Introduction

In previous chapters macroscopic amplitude objects have been investigated. However, this chapter is devoted to a new field of applications for digital holography, the investigation of *microscopic phase* objects. In order to record the diffraction pattern of microscopic objects with sufficient spatial resolution a microscope objective is placed between camera and object. Therefore this type of holography was coined *Digital Holographic Microscopy* (DHM). The image of the object is recorded slightly out-of-focus on the camera with respect to the microscope objectives depth of field. A BCi4-6600 CMOS camera with 3000x2208 pixels and $\Delta x' = 3.5 \mu m$ is utilized for the recording. The advantages of an out of focus recording are:

- Bright in-focus object details are avoided by the out of focus recording. Consequently, a more evenly grey level distribution within the camera's dynamic range is realized.

- The sensor's space-bandwidth product (SBP) is used more effectively by distributing the object information over the entire sensor.

197

- Recording the out-of-focus image in front of the image plane reduces the dispersion effect of high spatial frequencies, which increases with the recording distance (Goodman (1996)).

- The field-of-view and resolution can be increased when recording in front of the image-plane.

- Out-of-focus recording enables the application of zero-padding to improve the resolution, which was demonstrated by Gyímesi et al. (2009) and P.Ferraro et al. (2008).

- Furthermore, a visual control of the object position in the recording process is enabled.

Care needs to be taken that the image is not too much out of focus otherwise the spatial frequencies are subjected to a shear, which results in an increase of the hologram's required SBP, see 5.2.3. The in-focus image is then obtained by a numerical reconstruction process, which was presented in section 3. The resolution of DHM is not as strongly constrained by the pixel-size as in lens-less holography. Moreover, it enables the introduction of low coherent light sources such as Light Emitting Diodes (LED) as demonstrated by Repetto et al. (2004), which results in a reduction of speckle noise. DHM could, with reasonable optical resolution, be applied to many different fields such as shape measurement, phase visualization, living cell analysis Rappaz et al. (2005) and refractive index measurement Charriére et al. (2006) and Rappaz et al. (2008). The main advantages of a DHM compared to conventional microscopy are:

i. It permits to obtain object amplitude and phase by recording a single hologram, see Fig. 7.1.

ii. It enables the recording of dynamic events such as living cell monitoring.

iii. It permits numerical focusing to different axial object regions.

iv. The axial resolution obtained is in the sub-nanometer region, which was demonstrated by Kuehn et al. (2008).

v. Wave-aberrations, such as spherical aberrations, can be corrected numerically.

The images in Fig. 7.1 show the same specimen, namely a human cheek-cell, using different microscopes. The reduced resolution of the images obtained with the DHM are likely to be due to the reduced NA employed. However, the contrast obtained is superior to the Zernike phase contrast microscope, which is commonly applied for the analysis of phase objects. This statement is confirmed by the contrast values calculated for each image.

(a)   (b)

(c)   (d)
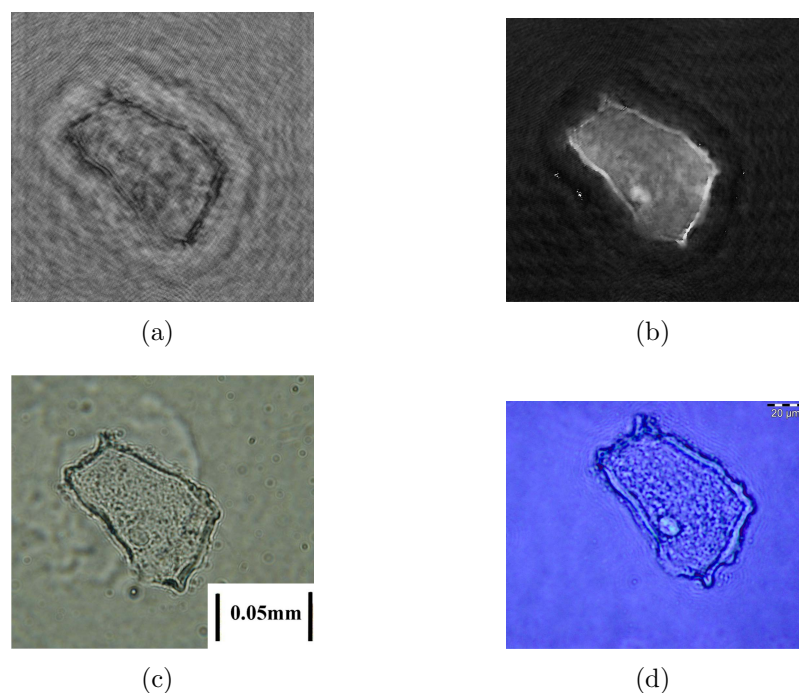
Figure 7.1: Comparison of, (a) DHM results with 20xMO (NA=0.40) intensity reconstruction and (b) phase reconstruction, (c) conventional microscope Polyvar 50xMO (NA=0.85) , (d) Zernike phase contrast microscope Olympus IX51 40xMO (NA=0.60)

The contrast definition used is based on the Weber-contrast V_{Weber}, which is well suited for small features of intensity I_o on a large uniform background of intensity I_b.

$$V_{Weber} = \frac{I_o - I_b}{I_b} \tag{7.1}$$

The values obtained for Fig. 7.1 from left to right and top to bottom are:

$$0.137, \quad 6.127 \quad \text{and}$$

$$0.037, \quad 0.098, \quad \text{respectively}$$

The work described in this chapter was focused on the analysis of a transparent phase object (human cheek-cell), which benefits from the advantages previously mentioned. The resolution improvement algorithms presented in 6.4 have been applied to the DHM to prove its validity in the microscopic domain in conjunction with imaging optics. Moreover, a three dimensional topology map of the cheek-cell could be obtained, which was derived by the algorithm described in 6.2.4. The topology map in combination with the two dimensional phase map enabled the generation of a two dimensional refractive index distribution of the cheek-cell.

7.2   Setup

A schematic sketch of the setup and the practically realized setup are shown in Fig. 7.2. A large amount of the mechanical parts used have been designed by the author and manufactured in the engineering workshops, see Appendix C.1. The setup has been realized in an in-line fashion. Hence phase stepping was applied in order to suppress DC-term and twin-image, which was discussed in 3.3.4. In an analogue manner as explained in 6.2.1 the combination of linearly polarized laser light, half-wave retarder and polarizing beam splitter are used to

adjust the intensity of reference and object-beam. Single mode fibres have been used, which permit a matched length adjustment of both optical arms without the introduction of further optical elements such as mirrors. Consequently, the setup is more compact. Moreover, a clear Gaussian beam profile in reference and object arm was obtained, which reduced the impact of background noise in the recorded hologram. Furthermore, the setup became more environmentally stable. In addition, the polarization state of the reference and object-wave could be aligned by rotating the reference single mode fibre by 90°. A short fibre length and large radii were applied in order to minimize polarization dispersion effects due to the birefringent properties of the fibre. These dispersion effects would otherwise result in a reduced linear polarization state at the fibre output. The polarization dispersion can be described as a function of the square root of the fibre length, which is discussed in Gong and Jian (1999).

Furthermore, the setup permits the possibility to illuminate the object with circularly polarized light by the introduction of 45° rotated quarter-wave retarders. In that manner the contrast of a birefringent object can be increased independently of the object's birefringent axis orientation [Whittaker et al. (1994)]. When setting up the experiment a convergent object illumination was used in order to record the correct object phase, as discussed in 5.2.3. In addition, convergent object illumination enables one to obtain the highest resolution for transparent objects compared to other illumination arrangements (Pawley (2006)). The quadratic phase term arising from the 20 x DIN achromatic microscope objective could be minimized by adjusting the axial position of a convex lens placed in front of the fibre output in the reference arm. This is an analogue principle as used in Linnik interferometers, where the optical components in the reference arm duplicate the optics used in the object-arm, see Malacara (2006). Moreover, a matched wave-front curvature for reference-beam and object-beam offers

the advantage that the sensor is less occupied with fringes, which do not arise from the object-diffracted light. The suppression of an eventually arising residual phase term is discussed at a later stage of this Chapter in 7.4.
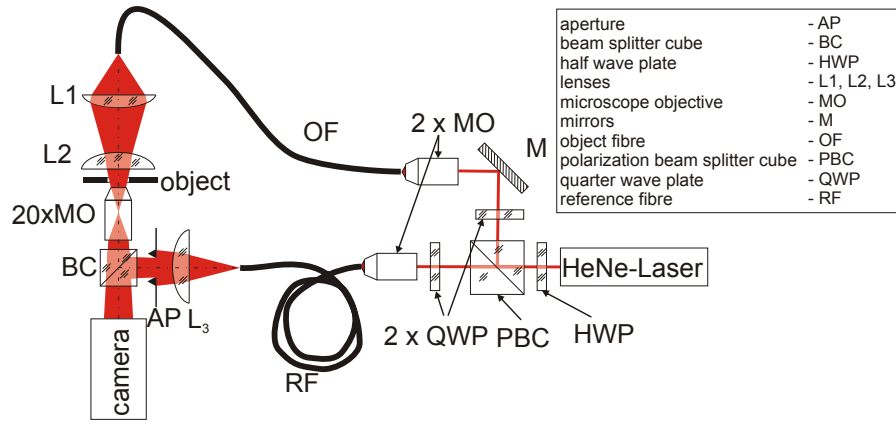
(a)
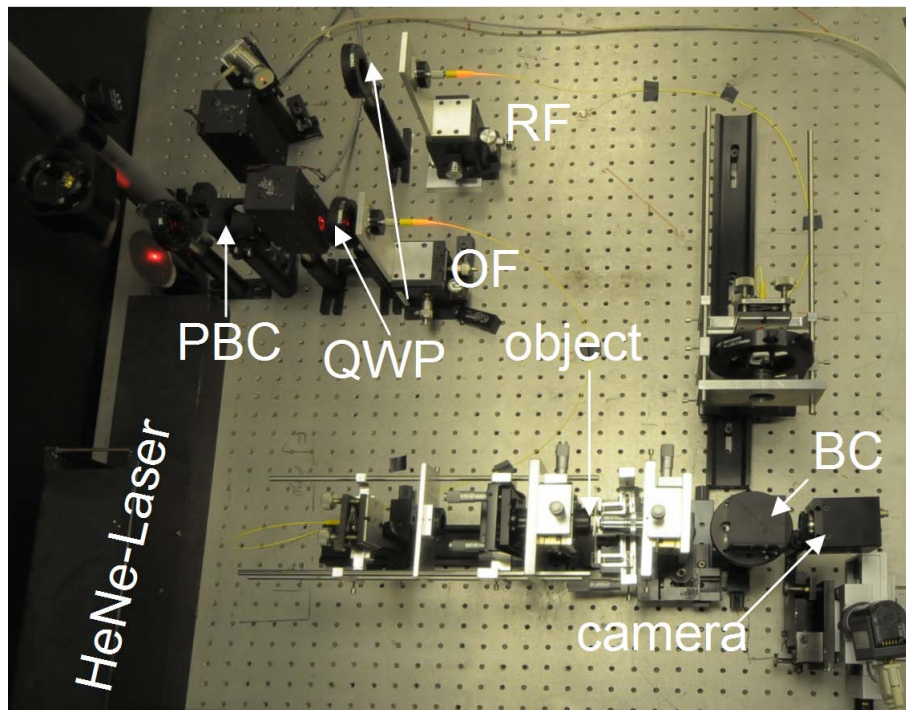
(b)

Figure 7.2: (a) Schematic sketch of DHM setup, (b) practically realized setup

7.3 Optical Parameters of DHM

This section focuses on the derivation of optical parameters for an out-of-focus recorded hologram. The optical parameters supplied by the manufacturer and obtained by the normalized measures taken from ISO 9345-1 are shown in Fig. 7.3.
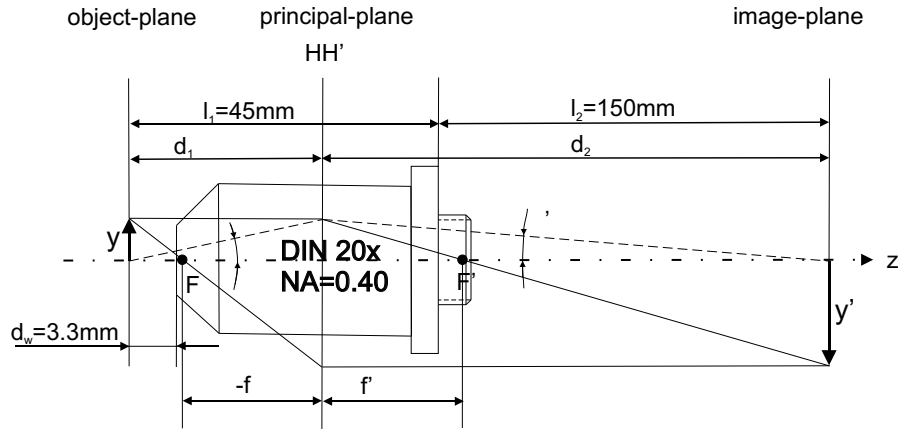
Figure 7.3: Specified and normalized dimensions for microscope objective

7.3.1 Thin Lens Model

The microscope objective consisting of a range of lens elements is simplified to a single *thin lens model.* In addition to the given measures the common focal length f and f', the distances d_1 between object-plane and the common principal-plane and d_2 between common principal-plane and image-plane is calculated. The sum of d_1 and d_2 when maintaining the microscope objective's working distance d_w is 195 mm according to ISO 9345-1. The common focal length f can be calculated by taking into account the geometric relations shown in Fig. 7.3

$$
\begin{aligned}
\frac{y + y'}{d_1} = \frac{y'}{f} &\quad \Rightarrow \quad d_1 = \frac{(y + y')f}{y'} = \frac{(1 + \Gamma')f}{\Gamma'} \\
\frac{y + y'}{d_2} = \frac{y}{f'} &\quad \Rightarrow \quad d_2 = \frac{(y + y')f'}{y} = (1 + \Gamma')f'
\end{aligned}
\tag{7.2}
$$

Presuming that the front and rear focal length are matched results in:

$$f = f' = \frac{\Gamma'(d_1 + d_2)}{(1 + \Gamma')^2} = \frac{20 \cdot 195 \text{ mm}}{21^2} = 8.844 \text{ mm} \tag{7.3}$$

From Fig. 7.3 it follows that:

$$d_1 = \frac{y + y'}{y'} f' = \frac{1 + \Gamma'}{\Gamma'} f' = 9.286 \text{ mm} \tag{7.4}$$

and d_2:

$$d_2 = (1 + \Gamma') f' = 185.710 \text{ mm} \tag{7.5}$$

Ideally the object should be recorded at the manufacturer's specified working distance, for which the optical system is optimized and at which Abbe's sine-condition, shown in Eq. 7.6, is fulfilled. Abbe's sine condition implies that the ratio between sine of the angular aperture on the object side ε and on the image side ε', see Fig. 7.3, equals the magnification.

$$\Gamma' = \frac{\sin \varepsilon}{\sin \varepsilon'} \tag{7.6}$$

Recording the object at a different distance than specified by the working distance results in aberration effects such as coma caused by different lateral magnifications. Therefore, the position of the object, the microscope objective and the camera should be arranged in the following manner:

    i. Setup the object and the camera by taking into account the object-sensor distance of 195 mm specified in ISO-9345-1 and shown in Fig. 7.3.

    ii. Adjust the microscope objective's position until an in-focus image appears on the camera sensor.

    iii. Move the camera slightly closer to the microscope objective as shown in

Fig. 7.4 in order to increase the recorded field of view and the optical resolution.

The optical resolution obtained can be calculated as shown in Eq. 4.23. For microscope objectives it can generally be assumed that the object-distance d almost matches with the focal length f. Therefore, the resolution can be calculated by:

$$\delta = 0.61\frac{\lambda}{\text{NA}} \approx 1.22\frac{\lambda f}{D} \tag{7.7}$$

Recording the hologram in front of the image-plane as shown in Fig. 7.4 results in reduced phase dispersion with respect to high spatial object frequencies, as discussed in Goodman (1996), by which an increased optical resolution is obtained.

Figure 7.4: Imaging and reconstruction process

7.3.2   Reconstruction Distance (d')

The numerical reconstruction can either be performed by applying the conjugated complex reference beam in conjunction with the physical recording distance ($d' = d_{image}$) or by calculating the corresponding reconstruction distance d', which would have arisen if a plane reference-wave was employed for the reconstruction. The latter was used for the reconstruction discussed in this chapter. It offers the advantage to be computationally less time consuming. An estimate for the in-focus reconstruction distance d' is obtained by subtraction of the distances $\left(\tilde{d}_2 - d_2 \right)$. $\tilde{d}_2$ stretches from the principal-planes HH' of the microscope objective to the hologram-plane, and d_2 stretches from the principal-planes HH' to the image-plane, as shown in Fig. 7.4. The subtraction corresponds to the hologram-image-plane distance d_{image}. The spherical reference-wave in the recording process acts like an additional lens which needs to be accounted for in the reconstruction process. The reconstruction distance d' with respect to the source point distance of the spherical reference-wave d_{ref} can be calculated according to Eq. 3.48 as:

$$d' = \frac{d_{image} d_{ref}}{d_{ref} - d_{image}} \tag{7.8}$$

In case of a large object-wave curvature, the compactness of the setup can benefit from the introduction of a lens in the reference beam, which projects the reference-wave point-source further distant. The lens projected reference-wave's source point distance (d_r) depends on the distance of the lens L3 as shown in Fig. 7.2(a) in the reference arm to the fibre (d_{fb}) and the focal length of the lens. The distance between fibre and lens in order to obtain the desired distance (d_r) can be calculated according to Appendix A by:

$$d_{fb} = f \left(1 - \frac{d_r \tan \vartheta}{y_1} \right) \tag{7.9}$$

Where ϑ indicates the angle under which the light is emitted from the fibre and y_1 denotes the height at which the light strikes the lens. ϑ can be calculated by the manufacturer's specified NA of the fibre. The fibre used in the experiment is a 630HP Thorlabs fibre, which possesses a NA of 0.13 ($\vartheta = 7.41$ °). In order to obtain the whole reference distance d_{ref}, the distance from the lens to the hologram-plane needs to be added to d_r. Due to the relatively short reconstruction distance d' the reconstruction can not be performed using the Fresnel approximation [*], which would otherwise introduces errors in the reconstructed phase. In this case the *Rayleigh-Sommerfeld diffraction integral*, see Section 3.2, needs to be applied.

7.3.3 Magnification, Image-Size, and Field of View (FOV)

- **Magnification Γ''**

The recorded lens due to the spherical reference-wave introduces a change of magnification. The magnification of the reconstructed hologram (Γ'') can be calculated by:

$$\Gamma'' = \Gamma' \cdot \frac{d'}{d_{image}} = \Gamma' \cdot \frac{d_{ref}}{d_{ref} - d_{image}} \tag{7.10}$$

Where Γ' indicates the manufacturer's specified magnification.

- **Calculation of Image-Size y''**

The image-size in the reconstruction plane y" can be calculated taking into account the geometric relations as shown in Fig. 7.4 and the magnification with respect to the reference-wave distance.

$$y'' = \frac{d_{ref}}{d_{ref} - d_{image}} \left(y' + \Delta y' \right) = \frac{d_{ref}}{d_{ref} - d_{image}} M \Delta x' \left(1 - \frac{d_{image}}{d_2 - f'} \right) \tag{7.11}$$

---

[*]see Eq. 2.52 for validity-region of Fresnel-method

Where M is the number of pixels in the y-direction. Recording the hologram in front of the image-plane results in a reconstructed image which is larger than the camera sensor-size. In the reconstruction process utilizing the convolution integral, see Section 3.2 the hologram either needs to be zero-padded by $\left(M' = M + \frac{y'' - M\Delta x'}{\Delta x'} \right)$ or a numerical lens of magnification $\left(\Gamma' = \frac{M\Delta x'}{y''} \right)$ needs to be introduced to display whole the object information.

- **Calculation of FOV**

The object-size in y-direction can be calculated as:

$$y = \frac{y''}{\Gamma''} = \frac{M\Delta x'}{\Gamma'} \cdot \left(1 - \frac{d_{image}}{d_2 - f} \right) \tag{7.12}$$

The object-size in the x-direction can be calculated in the same manner by replacing M with the number of pixels in the x-direction (N).

$$FOV = x \times y = N \times M \left[\frac{\Delta x'}{\Gamma'} \cdot \left(1 - \frac{d_{image}}{d_2 - f} \right) \right]^2 \tag{7.13}$$

7.3.4 Depth of Field (DOF)

The DOF in conjunction with a lens-system of a certain magnification (Γ') has been discussed in Section 4.4.2. Due to the large NA the wave-optical DOF and the geometric-optical DOF need to be taken into account. Due to the numerical reconstruction with the Rayleigh-Sommerfeld diffraction integral Eq. 4.33 was applied in order to calculate the geometric-optical DOF_g. The wave-optical DOF_λ is calculated according to Eq. 4.32. Combining both equations results in:

$$\text{DOF} = \text{DOF}_g + \text{DOF}_\lambda = \frac{\Delta x'}{\Gamma'' (\text{NA})} + \frac{\lambda}{2 (\text{NA})^2} \tag{7.14}$$

7.3.5 Experimental Validation

The obtained parameters have been validated by employing the USAF-test target as the object under investigation. The camera was moved to different axial positions in close proximity to the image-plane (maximum axial camera displacement $\pm$ 40 mm). A spherical reference-wave was employed which was positioned at 325 mm distance to the in-focus image of the object. The camera used has 3000x2208 pixels with 3.5 μm pixel-size. Fig. 7.5 shows graphs in which the experimental data and the calculated data have been compared. It was experimentally found that obtained magnification for an in-focus recorded image (19.32 x) is slightly smaller than the manufactures specified magnification (20 x), which has been taken into account when calculating the theoretical values.
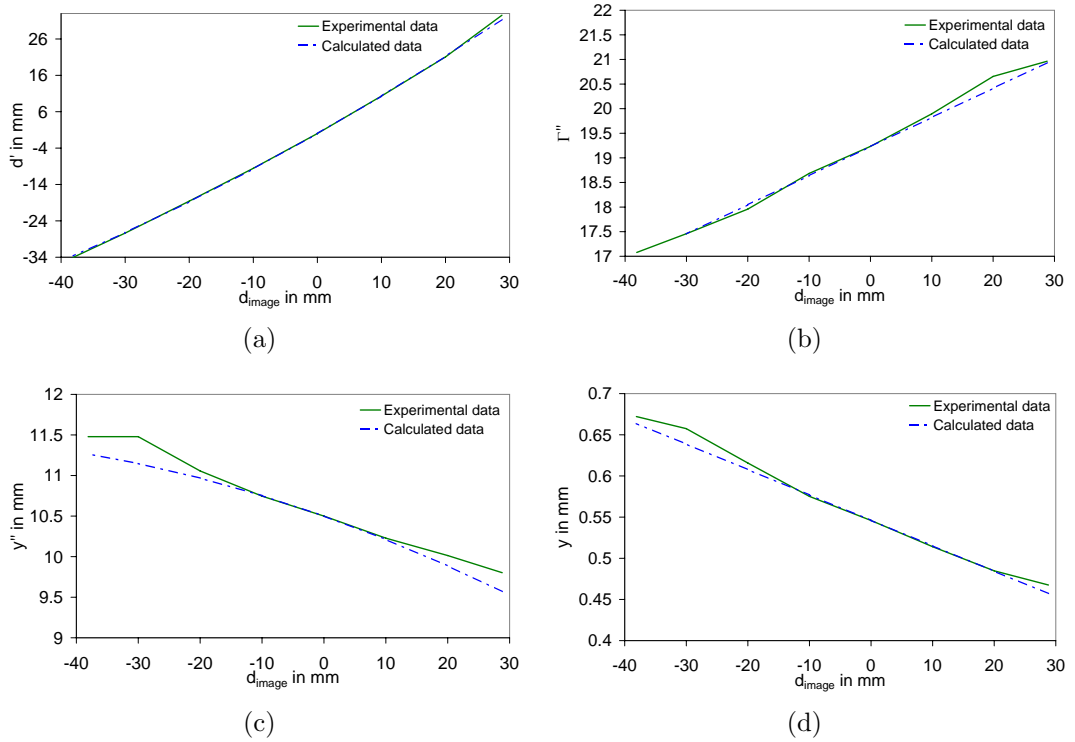
Figure 7.5: Comparison of experimentally obtained data and calculated data for, (a) reconstruction distance (d'), (b) magnification obtained for the numerically reconstructed hologram (Γ''), (c) image-size in the reconstruction-plane (y"), (d) object-size (y)

Table 7.1: Evaluation of the experimentally obtained data

Statistical properties	d$'$ in mm	Γ''	y$''$ in mm	y in μm
Maximum deviation from expected value	1.171	0.242	0.332	18.84
Mean value	0.102	0.073	0.126	5.43
Standard deviation	0.469	0.110	0.124	7.25
Standard deviation of the mean	0.162	0.039	0.044	2.57

The statistical data which indicates how well the calculation matches the experimental data is shown in Table 7.1. In conclusion, the mathematical model created to describe the optical parameters matches well with the experimental data. A fundamental derivation of optical parameters in conjunction with DHM has already been conducted by Carl et al. (2004). Their mathematical description was based on a plane-reference beam and a numerical reconstruction utilizing the Fresnel-method, which is not the most suitable method for the reconstruction of phase information in DHM. The correct choice of reconstruction method was discussed in Section 7.3.2. The derivation described in this section takes into account the shape of the reference-wave and the reconstruction by means of the Rayleigh-Sommerfeld diffraction integral. In that respect it represents a novel approach.

7.4   Subtraction of Additional Spherical Phase Term

The application of the microscope objective introduces an additional spherical phase term, as discussed in Section 5.2.3. The spherical phase term can be suppressed in three different ways as discussed in Osten (2006b).

i. **Phase stepping** is applied to record the phase of the interference pattern.

A region of well defined fringes of the obtained phase map which does not hold object information is selected. This area is then used to obtain the curvature of the spherical phase term. Afterwards a non-linear fit is applied to generate the corresponding phase for the hologram regions which do hold object information.

ii. In analogy to the principle of **double exposure holography** a hologram with the object and then without the object is recorded. The hologram without the object should then only carry information of the spherical phase arising from the microscope objective.

iii. The corresponding spherical wavefront is obtained **numerically**. The numerical wavefront is obtained in the hologram plane and then reconstructed with exactly the same parameters as applied to the hologram. An estimate of the wavefront's curvature according to Osten (2006b) can be obtained by counting the number of circular fringes originating from the center.

It was empirically found that the subtraction of the spherical phase term can best be accomplished in the off-line arrangement by the double exposure technique. However, for the in-line arrangement described in this chapter numerical phase correction was applied. This holds the benefit of not having to displace the object under investigation. The digital hologram and the numerical reconstruction of the phase is shown in Fig. 7.6(a) and (b), respectively.

In order to obtain an estimate of the magnitude of the spherical phase map, it was presumed that an in-focus image is recorded and the microscope objective is illuminated with a convergent light beam. Hence the spherical phase term caused by the lens and the free space propagation from the object to the microscope objective can be neglected as discussed in Section 5.2.3. The phase term, which corresponds to the free space propagation from the microscope objective

(a)

(b)

(c)

(d)
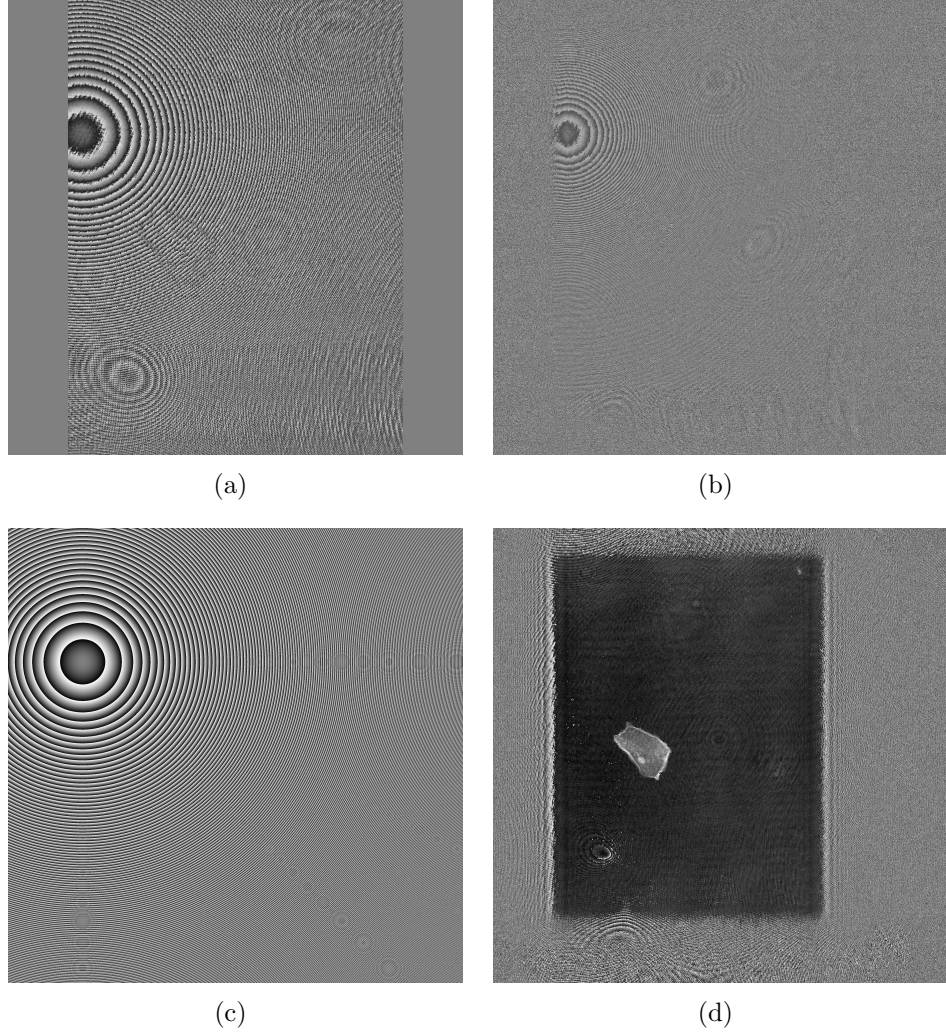
Figure 7.6: (a) Hologram of human cheek-cell, (b) reconstructed phase without suppression of spherical phase term , (c) numerically calculated spherical correcting wavefront, (d) reconstructed phase with suppression of spherical phase term

to the hologram-plane (d_2) and the reference-wave source point distance (d_{ref}), results in a combined spherical phase term that in parabolic approximation can be described by:

$$\varphi(x', y') = \frac{\pi \left(x'^2 + y'^2 \right)}{\lambda} \frac{d_{ref} - d_2}{d_{ref} d_2} \tag{7.15}$$

For the investigation of the cheek-cell the hologram was recorded at a distance of 197 mm from the microscope-objective and the reference-wave source point distance was 408 mm, which results in a curvature radius of 381 mm for the

combined phase map. An accurate magnitude of the curvature radius can then be obtained in an iterative manner by subtracting the hologram from the correcting phase-map until the spherical phase term disappears. The final numerical phase map obtained possessed a curvature radius of 430 mm and a shift of 618 pixels in x-direction and of 1008 pixels in y direction, which is shown in Fig. 7.6(c). The correcting phase map was then reconstructed utilizing the same parameters as applied for the reconstruction of the hologram. Afterwards both were subtracted from each other to reveal the object's phase. The obtained corrected phase-reconstruction is shown in Fig. 7.6(d).

7.5   Resolution Improvement

The resolution improvement algorithm presented in Section 6.4 was applied to DHM to prove its validity for microscopic objects in conjunction with imaging optics. The main difference to the preceding work is that the resolution improvement obtained is additionally limited by the NA of the microscope objective used. Phase holograms were recorded in order to overcome previously experienced problems encountered with the application of resolution improvement methods as discussed in Section 6.2.2. In that manner the phase of each individual hologram could be adjusted prior to the reconstruction. The results obtained for intensity in phase reconstruction are shown in Fig. 7.7 for a reconstruction with 3000 x 3000 pixels and 8805 x 8805 pixels, respectively. The SNR obtained for the boxed area shown in Fig. 7.7(d) and for the corresponding area in Fig. 7.7(b) is 13.82 and 12.42, which proves an image quality improvement. Moreover, the object details shown are less noisy and possess an increased contrast, which is shown in Figs. 7.7(c) and 7.7(a) for 8805 and 3000 pixels, respectively.

(a)   (b)

(c)   (d)
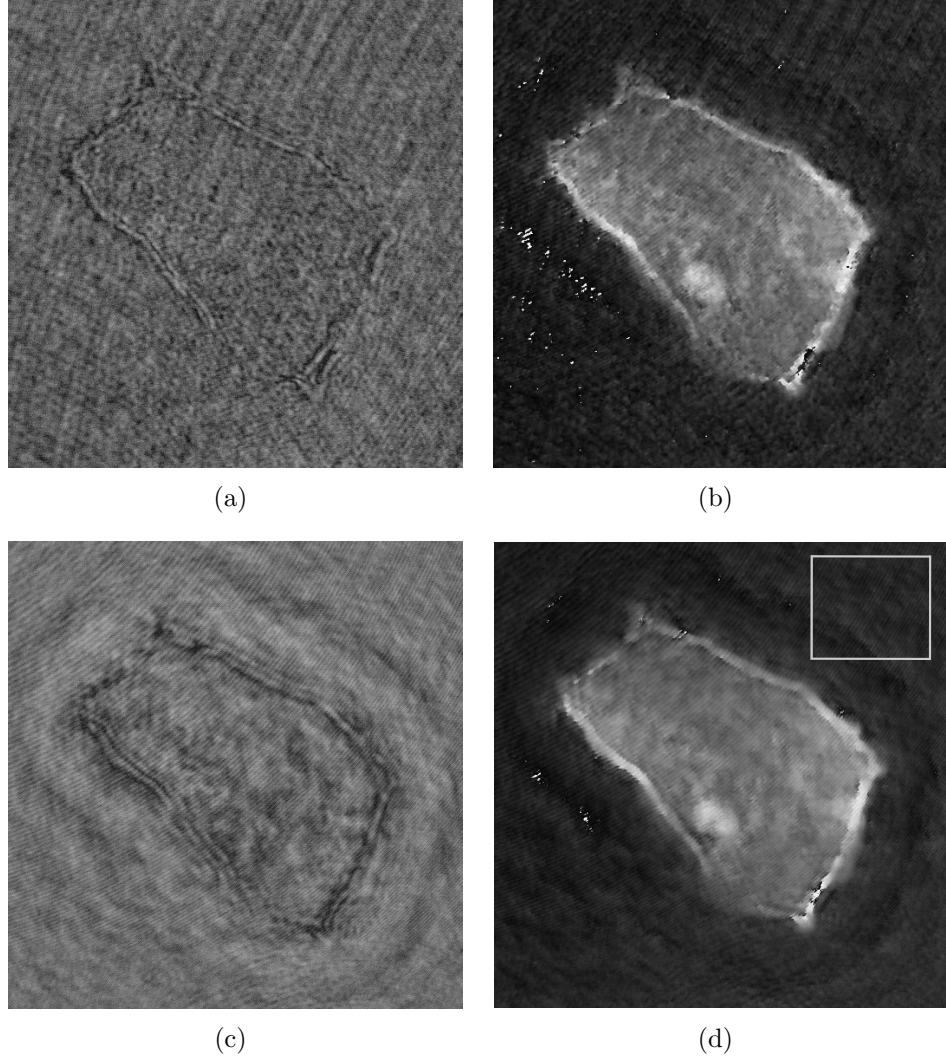
Figure 7.7: Intensity and phase reconstruction at d' =91 mm for (a) and (b) 3000x3000 pixels with $\Delta x' = 3.5$ μm , (c) and (d) 8805x8805 pixels with $\Delta x' = 1.75$ μm

7.6 Extended Depth of Field (EDOF) and 2D Refractive Index Distribution

Due to the large NA of the microscope objective employed, only a finite region of the image is in focus. In-focus reconstructions of the object were obtained within a reconstruction region of 91 mm to 101 mm in 0.5 mm steps, see Fig. 7.8. An in-focus reconstruction of the entire axial object extension can be obtained utilizing the extended depth of field method, which was discussed in Section 6.2.4. In

addition to the in-focus image the topology map of the image is obtained. In order to obtain the object topology map the image coordinates need to be converted to the object coordinates. Firstly, the reconstruction distance d' was converted to the physical distance d_{image}. The reconstruction distance (d') represents a combination of recording distance (d_{image}) and the point source distance of the spherical reference-wave (d_{ref}), as described in Eq. 7.8. The camera image distance d_{image} can be calculated by rearranging Eq. 7.8

$$d_{image} = \frac{d' d_{ref}}{d_{ref} + d'} \qquad (7.16)$$

The reference source point distance used was 408 mm. The corresponding image distances range from 74.4 mm to 81 mm. Secondly, the axial image extension needs to be related to the axial object extension by taking into account the magnification Γ''. The axial object extension can then be calculated according to Haferkorn (2003) by:

$$\Delta z_{obj} = -\frac{f}{f'} \frac{\Delta z_{image}}{\Gamma''^2} \qquad (7.17)$$

(a) (b)
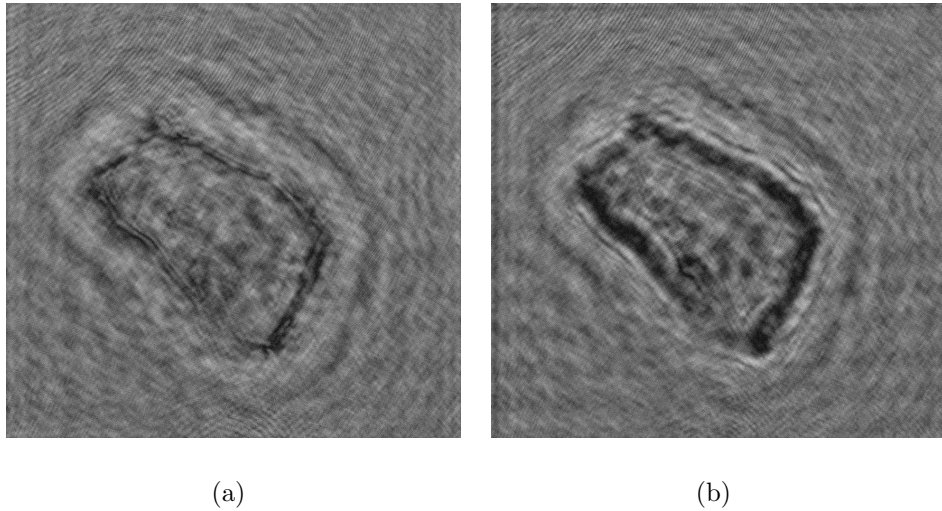
Figure 7.8: Reconstruction at (a) 91 mm and (b) 101 mm

The minus sign indicates an inverted axial orientation of the image compared to the object and is therefore neglected in succeeding explanations. Assuming that back focal length f and front focal length f' are matched results in:

$$\Delta z_{obj} = \frac{\Delta z_{image}}{\Gamma''^2} = \frac{6.6 \text{ mm}}{14.4^2} = 31.8 \ \mu\text{m} \tag{7.18}$$

This experiment with a cheek-cell was sequentially performed before the consideration of the optical parameters was conducted. The camera could not be located at 195 mm distance to the object due to using a 50x50 mm beam splitter to combine reference and object-beam. This beam-splitter was needed in order to carry out the resolution improvement methods. The distance between the microscope objective and the microscope slide was adjusted by a vernier caliper to the specified working distance. The increased working distance due to the physical thickness of the microscope cover-slide and the additional optical path length due to the cover-slide's refractive index ≈ 1.5 was not taken into account. Therefore, the image-plane was located further in front of the hologram-plane than initially intended. Later calculation revealed that the object was positioned at 3.4 mm working distance rather 3.3 mm. In order to obtain an exact estimate of the magnification the object-size in the reconstructed image was compared with those images obtained with a conventional microscope and a phase contrast microscope as shown in Fig. 7.1. The magnification obtained was 14.4. This magnification was then used to calculate the axial object-extension ($\Delta z_{obj} = 31.8 \ \mu$m).

In conjunction with the extended depth of field (EDOF) method, described in Section 6.2.4, and the phase information obtained a refractive index map can be calculated. Prior to the application of the EDOF method the reconstructed images were filtered in order to suppress disturbing fringe features as shown in Figs. 7.9(a) and (b), which otherwise would result in errors when calculating

the variance value. Then the EDOF method based on the calculation of a three dimensional variance map followed by the Gaussian fitting method was applied. A 5x5 pixels window size was employed for the EDOF method. The obtained in-focus image is shown in Fig. 7.9 (c). The obtained topology map was filtered utilizing a 5x5 median filter in order to suppress noise.
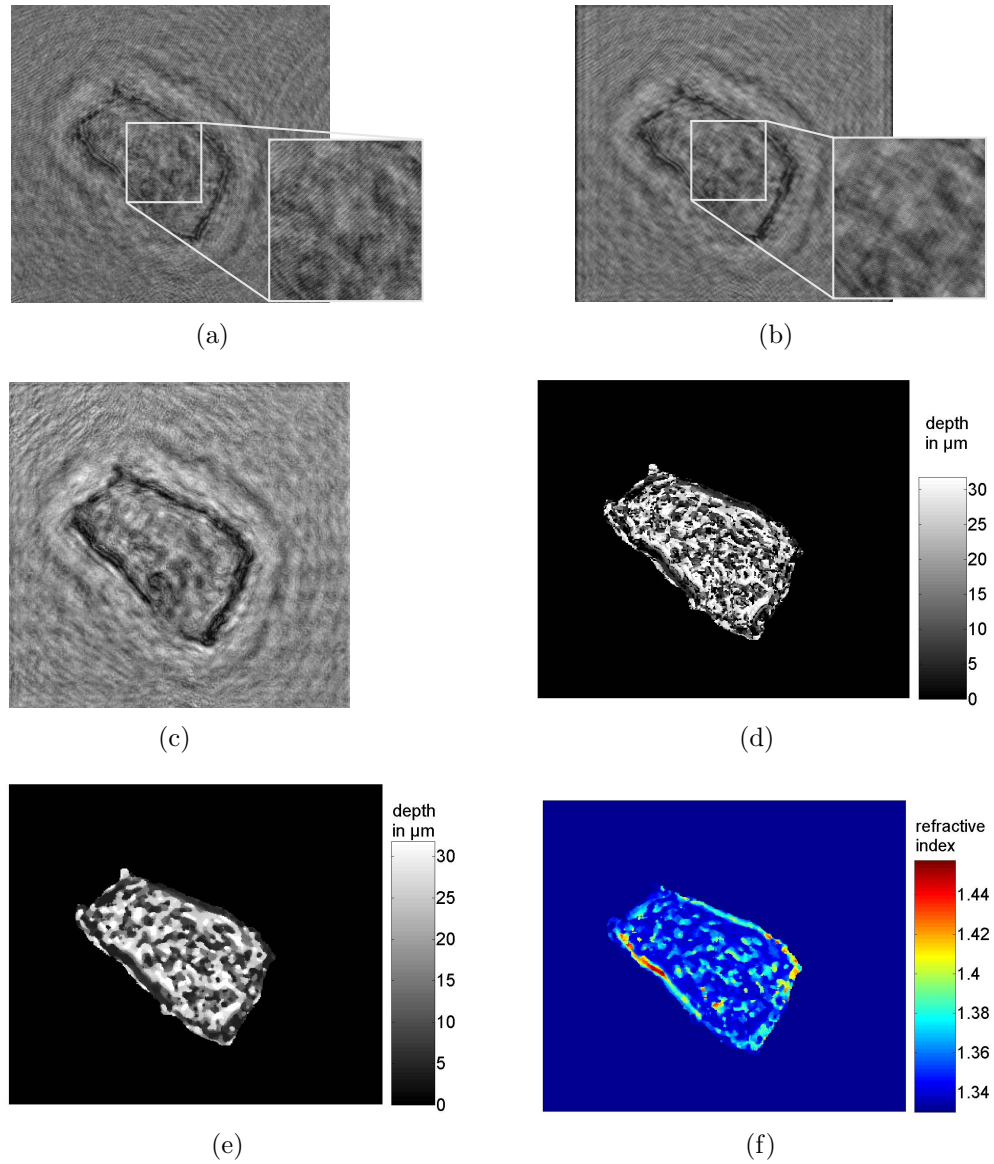
Figure 7.9: (a) Intensity reconstruction, (b) frequency filtered intensity reconstruction, (c) EDOF map, (d) topology map unfiltered, (e) topology map median filtered, (f) 2D refractive index distribution

The unfiltered and filtered topology map are shown in Figs. 7.9 (d) and (e), respectively. The object's two dimensional refractive index distribution $n_{object}(l, m)$ can be calculated by:

$$n_{object}(l, m) = n_{solution} + \Delta n(l, m) \tag{7.19}$$

Where $n_{solution}$ denotes the refractive index of the solution and $\Delta n(l, m)$ the difference in refractive index between object and solution. $\Delta n(l, m)$ can be determined by:

$$\Delta n(l, m) = \frac{\lambda \cdot \Delta \varphi(l, m)}{2\pi \Delta z_{obj}(l, m)} \tag{7.20}$$

 The solution used is saline, which has a refractive index of $n_{solution} = 1.33$. The two-dimensional refractive index map is shown in Fig. 7.9 (f) and the averaged refractive index obtained is 1.355 which matches with the averaged refractive index of cheek-cells reported by Moh et al. (2008). Furthermore, the refractive index map obtained shows a higher refractive index for the cell-wall which matches with the result presented by Moh et al. (2008).

7.7 Conclusion

This chapter dealt with the DHM and its potential for the investigation of phase objects. The optical parameters for a DHM were derived, which to the authors knowledge have not been described so far in such a comprehensive manner. The resolution improvement methods, which were discussed in Chapter 6, have been applied to DHM. Although the whole frequency bandwidth transmitted through the microscope objective is already recorded by the camera sensor without applying the resolution improvement methods, the contrast and the SNR could

further be increased. The image quality improvement might be due to the improved MTF as shown in Fig. 6.18. Furthermore, the topology map obtained by the EDOF method in conjunction with the two dimensional phase map were used to generate a two dimensional refractive index map of the object. The result obtained are in correspondence with the refractive index map obtained by Moh et al. (2008).

The result presented by Moh et al. (2008) was obtained utilizing surface plasmon resonance sensing. It is based on collecting object localized data in conjunction with scanning microscopy. In Moh et al. (2008) a set of images needed to be recorded in order to obtain the two-dimensional refractive index distribution. In that manner, the method described in this chapter is superior with respect to the experimental effort. The obtained two dimensional refractive index distribution represents a proof of principle. A further improvement could be obtained by combining digital holography with tomography. Furthermore, the EDOF image as such might already reveal the object depths due to features such as the black edge which hems the cell wall, see Fig. 7.9(c). The appearance of the black edge is due to total internal reflection and hence corresponds to a physical ramp. These are points to be addressed for in future research.

CHAPTER 8

Conclusions and Future Work

8.1 Conclusion

This Ph.D. thesis was focused on the development and implementation of resolution and image quality improvement methods applied to digital holography. The lateral resolution improvement was demonstrated by experiments carried out on a USAF 1951 resolution test target and the phase resolution improvement by the standard deviation obtained from double exposure phase maps. The smaller the standard deviation, the smaller the measurement uncertainty. The image quality improvement was demonstrated by the obtained Signal to Noise Ratio (SNR) as defined in Eq. 6.5. It needs to be emphasized that the SNR is defined in a logarithmic manner. Therefore, an SNR improvement by the magnitude smaller than one already proves a significant image quality improvement. In the following paragraphs the conclusions drawn from the resolution improvement methods are as follows.

- The sub-pixel sampling method, in conjunction with CMOS technology, was developed by the author. A three bucket phase stepping algorithm developed by Cai et al. (2004) was implemented to minimize environmental influences. The original pixel-size was decreased by a factor of two whilst

maintaining the light-sensitivity. The lateral resolution obtained was doubled from 17.5 μm to 8.7 μm, which compares well with other resolution improvement methods mentioned in Section 6.1. The measurement uncertainty for the interpreted double exposure phase map was reduced from $\frac{\lambda}{6.9}$ to $\frac{\lambda}{7.1}$. Moreover, the fringe visibility was enhanced, which enables more accurate deformation analysis. The SNR for the intensity reconstruction for an investigated cantilever was increased from 10.96 dB to 11.07 dB. Moreover, the small fill-factor inherent to CMOS-technology, 35% in our case, was increased to 100% utilizing the sub-pixel sampling method.

- The successful combination of the synthetic-aperture method and the sub-pixel sampling method to improve the optical resolution and image quality was demonstrated. The lateral resolution obtained in comparison to the sub-pixel sampling method could further be improved by a factor of three from 17.5 μm to 5.5 μm.

- The well established synthetic-aperture method, in conjunction with the recording of Fourier-holograms, was applied to improve the resolution of the reconstructed hologram. The lateral resolution could be improved by a factor of three. The product of lateral resolution and field of view obtained, namely the Space-Bandwidth Product (SBP), was 14.27^{10}, which represents the largest SBP obtained in comparison to recent publications in the field of digital holography. The problem encountered with the curved sensor area when performing double exposure holography could be overcome by the spatial averaging method developed by Baumbach et al. (2006). The measurement uncertainty obtained with the spatial averaging method was decreased from $\frac{\lambda}{14}$ to $\frac{\lambda}{81}$.

- The extended depth of field method was improved by the Gaussian fitting

method developed by the author to result in a quantization increase by a factor of ten and an improved accuracy utilized by more precise scanning. The Gaussian fitting method takes into account all variance values rather than only the maximum variance value. In that manner, dislocations of the maximum variance value, as shown in Fig. 6.13(a), can be correct, which further increases the accuracy.

In the following paragraphs the conclusions obtained from the Digital Holographic Microscope (DHM) are summarized.

- A two dimensional refractive index distribution of a microscopic phase object (check-cell) was obtained by solely recording a single hologram. This was enabled by combining the information obtained from the topology map with the numerically reconstructed two dimensional phase map of the object. The topology map was obtained by the extended depth of field method combined with Gaussian fitting. This, to the author's knowledge, has not been reported before.

- A detailed derivation of the optical parameters of the digital holographic microscope, in conjunction with a spherical reference-wave and the recording of an out-of-focus image hologram, was conducted. To the authors knowledge this was done for the first time. It was theoretically shown and practically proven that the field of view can be increased when recording the hologram in front of the image-plane.

- Image quality improvement based on the combination of synthetic aperture and sub-pixel sampling method could successfully be demonstrated on the DHM. The pixel-number was increased from 3000^2 pixels to 8805^2 pixels and the sampling frequency doubled. This resulted in an increase of the

SNR from 12.42 to 13.82, which proves that the speckle-noise could be reduced significantly.

In the following paragraphs the conclusion derived from the computer aided implementation of the *numerical reconstruction methods* are given. This in particular refers to the accuracy and performance improvement developed by the author.

- The performance of the *averaged-intensity subtraction method* to suppress the DC-term in the numerical reconstruction could be improved by two methods developed by the author, namely the *inverted median filter method* and the *sliding window method*, as demonstrated in Fig. 3.10.

- The numerical effort to center the image of the reconstructed hologram could be reduced by shifting the transfer-function rather than shifting the impulse response. In this manner the two dimensional Fourier-transformation in order to obtain the transfer-function from the impulse-response was not needed.

- A numerical lens, which is valid in the Rayleigh-Sommerfeld region, was obtained, by which the accuracy of the reconstructed phase for short recording distances is increased.

- Cai's three bucket phase stepping method [Cai et al. (2004)] was compared with the well established four bucket phase stepping Carré method. Cai's method requires the recording of three phase stepped holograms, whereas the magnitude of phase step is unknown and can differ among the three holograms. Carré's method requires the recording of four phase stepped holograms, whereas the magnitude of phase step is unknown and has to be the same for the four recorded holograms. A series of computer generated

sinusoidal interference pattern was used for the analysis. The measurement uncertainty for Cai's method was 0.0001 rad and for Carré's method 0.003. This proves that Cai's method can perform at least equally as well as Carré's method does. Moreover, the implementation of Cai's method enables the reduction of the experimental effort and the impact of disturbing environmental influences by calculating the magnitude of each individual phase step.

- It was found that phase stepping utilizing a piezo-mounted mirror results in an increased phase step accuracy than when using wave-retarder plates. The measurement uncertainty for the generated phase step utilizing a piezo-mounted mirror was 0.0748 rad and 0.1543 rad utilizing polarization optics.

The final list of conclusions refers to the Space-bandwidth product (SBP) consideration.

- The SBP considerations for the required SBP' in the recording process and obtained SBP" in the reconstruction process conducted by Lohmann (1967) and Xu et al. (2005) has been extended to lens-less Fourier-holograms in in-line and off-line configurations and image-plane holograms in in-line configuration.

- The Fresnel-approximation has been employed to obtain the amplitude and phase information for the interference pattern produced by different holographic setups. In that manner, conclusions for the SBP' analysis in the recording process could be drawn.

- Moreover, the obtained interference phase was analyzed in respect to the reconstruction of the correct object phase. To enable a correct phase reconstruction conditions upon the shape of the optical or numerical reference-

wave have been imposed.

- Advantages of Fourier holograms, other than the largest SBP' and SBP" in comparison to the other holographic setups, have been listed such as reduced impact of wave-aberrations and shortest recording distance. This confirms the choice of Fourier holographic setups used throughout most of the experiments performed during my PhD.

8.2 Future Work

Future research work could be split in two fields, the improvement of hardware and the improvement of software, as detailed below.

8.2.1 Software

A Graphical User Interface (GUI) could be created based on a low level programming language, such as C, C++ or Delphi. The most common digitized numerical tools developed in the scope of this PhD thesis would be implemented in this GUI. Future research projects and the calculation speed would benefit from this. The GUI would include:

- The three numerical reconstruction techniques including DC-term suppression, Fourier-filtering and numerical lens as discussed in Chapter 3.

- An optimization tool to obtain the best in-focus reconstruction based on the variance value.

- Implementation of numerical resolution improvement algorithm such as speckle noise reduction filter or Inverse-Fourier-Transform-algorithm (IFTA) to obtain the best possible impulse response with respect to the resolution in the reconstructed hologram.

- An optimization tool to remove the spherical wavefront of the reconstructed phase in conjunction with digital holographic microscopy by tip, tilt and de-focus removal.

- The implementation of phase stepping algorithms such as Cai's and Carré's method.

- The implementation of phase unwrapping algorithms such as Goldstein's cut-line or Least-square unwrap.

- The creation of a topology map based on the variance method in conjunction with Gaussian fitting.

- A calculator to obtain parameters such as the minimum distance in respect to the setup and the reconstruction model used, statistical values (maximum, minimum, mean, standard-deviation) of a two dimensional image or a cross-section line.

8.2.2   Hardware

A more compact, easily transportable and measurement task adaptable holographic system should be aimed for, which would benefit from being more environmentally stable and would enable a less time consuming implementation for industrial inspection. The introduction of optical fibres has already proven to enable the design of a more compact system. Moreover, fibres enable common path interferometry, by which environmental influences are minimized. The setup could further benefit from the introduction of laser diodes or in microscopy also Light Emitting Diodes (LED). The coherence length of laser diodes and LEDs is shorter than the one obtained for corresponding gas and solid state laser, see Table 2.3. The setup becomes less bulky and more easily transportable. Fur-

thermore, laser-diodes and LEDs can be pulsed down to the level of picoseconds, which enables high speed measurements and further increases the environmental stability of the setup. Moreover, the recording process is less strongly subjected to the speckle effect, which would result in an improved image quality. However, in order to perform accurate phase measurements care needs to be taken that either the wavelength is kept stable or that a possible wavelength shift is monitored and taken into account for the data interpretation. A shift to longer wavelengths is common among semi-conductors due to a stronger impact of temperature, which causes a narrowing of the gap between conduction and valence-band.

The flexibility of the holographic system could be increased by simultaneous application of different wavelengths and object illumination geometries. In this manner real time shape measurement and in and out-of-plane deformation measurement would be enabled. This could be accomplished by interference of multiple beams separated in the Fourier domain by different inclination angles of the reference beam. Multiple light sources of different wavelength could be employed to ensure that only corresponding object and reference beam interfere. In case a single light source was used, unwanted interference could be prevented by destroying temporal coherence using fibres of different optical path-lengths separated by the coherence length.

A resolution improvement of the aforementioned holographic system could be obtained by implementing the resolution improvement methods developed in this thesis. In order to maintain the realtime measurement capability of the proposed holographic system the resolution improvement methods developed need to be adapted. A camera array, rather than shifting a single camera in x and y direction could be used, to implement the synthetic aperture method. The following requirements need to be fulfilled in order to enable realtime measurement by means of the sub-pixel sampling method. Firstly, the shift to the four recording

positions and the camera frame rate need to be aligned and automated. Secondly, both camera frame rate and shift-speed should be large enough in order not to record speckle de-correlation caused by the object movement. Speckle de-correlation needs to be less than half the speckle size according to Kreis (2005) whilst recording the four laterally sub-pixel shifted holograms. The synthetic aperture method has a larger potential to be applied in lens-less systems, whereas the sub-pixel method is more likely to be useful in digital holographic microscopy (DHM). In DHM the pixel-size of the sensor employed correlates more strongly to the recordable and observable smallest object detail. The sub-pixel sampling method would enable the application of a high NA system of relatively small magnification such as Nikon CFI Apo LWD 25XW (25x,NA=1.1). The application of such a microscope objective would result in an increased FOV and hence an increased SBP. Moreover, a high resolution image is combined with a large depth of field when applying a smaller magnification, see Eq. 4.28.

A high resolution compact holographic system including software for lens-less holography and DHM can then be applied to analyze dynamic events, which result in a change of phase, such as different temperature gradients of a jet stream or the monitoring of living cells, which generally are transparent. The developed software would allow any user to carry out the measurement without the need to understand the programming language and the installation of the programming language. The proposed system could then be applied to solve many problems, among others in biology, chemistry, medicine, engineering design and monitoring of manufacturing process.

Bibliography

T. Baumbach, E. Kolenovic, V. Kebbel, and W. Jüptner. Improvement of accuracy in digital holography by use of multiple holograms. *Appl. Opt.*, 45(24): 6077–6085, 2006. 149, 150, 160, 162, 163, 164, 221

G. D. Boreman. *Modulation Transfer Function in Optical and Electro-Optical Systems*, volume TT52. SPIE Press, Bellingham, 2001. 100, 102

R. Bracewell. *The Fourier Transform and Its Applications*, chapter The Impulse Symbol, pages 69–97. McGraw-Hill, 1986. 135

B. Braunecker, R. Hentschel, and H. J. Tiziani. *Advanced optics using apherical elements*, chapter Metrology, page 64. SPIE Press, 2008. xiv, 6

L. Z. Cai, Q. Liu, and X. L. Yang. Generalized phase-shifting interferometry with arbitrary unknown phase steps for diffraction objects. *Opt. Lett.*, 29(2): 183–185, 2004. 64, 181, 187, 220, 223

D. Carl, B. Kemper, G. Wernike, and G. v. Bally. Parameter-optimized digital holographic microscope for high-resolution living-cell analyis. *Appl. Opt.*, 43 (36):6536–6544, 2004. 210

A. J. Cartwright, editor. *Engineering Data Book*. University of Warwick, 2001. 113

H. Chang, T. Shih, N. Chen, and N. WenPu. A microscope system based on bevel-axial method auto-focus. *Optics and Lasers in Engineering*, 47(5):547–551, 2009. 175

F. Charriére, A. Marian, F. Montfort, J. Kuehn, and T. Colomb. Cell refractive index tomography by digital holographic microscopy. *Opt. Lett.*, 31(2):178–180, 2006. 198

F. Le Clerc and L. Collet. Numerical heterodyne holography with two-dimensional photodetector array. *Opt. Lett.*, 25(10):716–718, 2000. 149

F. Le Clerc and M. Gross. Synthetic-aperture experiment in the visible with on-axis digital heterodyne holography. *Optics Letters*, 26(20):1550–1552, 2001. 149

R. J. Collier, E. T. Doherty, and K. S. Pennington. New method for generating depth contours holographically. *Appl. Phys. Lett.*, 7(8):223–225, 1965. 3

T. Colomb, F. Montfort, J. Kühn, N. Aspert, E. Cuche, A. Marian, F. Charrire, S. Bourquin, P. Marquet, and C. Depeursinge. Numerical parametric lens for shifting, magnification and complete aberration compensation in digital holographic microscopy. *J. Opt. Soc. Am. A*, 23(12):3177–3190, 2006. 6

K. Creath. Phase shifting speckle interferometry. *Appl. Opt.*, 24(18):3053–3058, 1985. 4

K. Dholakia and W.M. Lee. Optical trapping takes shape: The use of structured light fields. *Adv. At. Mol. Opt. Phy.*, 56:261–337, 2008. 31

J. Di, J. Zhao, H. Jiang, P. Zhang, Q. Fan, and W. Sun. High resolution digital holographic microscopy with a wide field of view based on a synthetic aperature

technique and use of linear ccd scanning. *Appl. Opt.*, 47(30):5654–5659, 2008. 149, 191, 193

C. Manh Do and B. Javidi. Multi-focus holographic 3d image fusion independent component analysis. In Jung-Young Son Bahram Javidi, Fumio Okano, editor, *Three-Dimensional TV, Video, and Display VI*, volume 6778, pages 67789P1– 67789P8, Boston, Massachusetts, USA, 2007. SPIE. 172

A. F. Doval. A systematic approach to tv holography. *Meas. Sci. Technol.*, 11 (1):R1–R36, 1999. 111

H. M. A. El-Sum and P. Kirkpatrick. Microscopy by reconstructed wavefronts. *Phys. Rev.*, 85:763, 1952. 3

D. Gabor. A new microscopic principle. *Nature*, 161:777–778, 1948. 1

D. Gabor. Microscopy by reconstructed wavefronts. *Proc. R. Soc. Lond., Ser. A*, 197:454–487, 1949. 1

Y. Gong and S. Jian. Measurement of polarization-mode dispersion in single mode fibre. *Czech. J. Phys.*, 49(8):1169–1175, 1999. 201

J. W. Goodman. *Introduction to Fourier Optics*. McGraw-Hill, second edition edition, 1996. 10, 11, 36, 52, 75, 86, 103, 132, 133, 136, 198, 205

J. W. Goodman and R. W. Lawrence. Digital image formation from electronically detected holograms. *Appl. Phys. Lett.*, 11:77–79, 1967. 5

J. W. Goodmann. *Laser Speckle and Related Phenomena*, volume 9, chapter Statistical properties of laser speckle patterns, pages 9–75. 1975. 97

F. Gyímesi, Z. Füzessy, V. Borbély, B. Ráczkevi, G. Molnár A. Czitrovszky A. Tibor Nagy G. Molnárka A. Lotfi, A. Nagy, I. Harmati, and D. Szigethy. Half-

magnitude extensions of resolution and field of view in digital holography by scanning and magnification. *Appl. Opt.*, 48(31):6026–6034, 2009. 117, 149, 191, 193, 198

W.S. Haddad, D. Cullen, J. C. Solem, J. W. Longworth, A. McPherson, K. Boyer, and C. K. Rhodes. Fourier-transform holographic microscope. *Appl. Opt.*, 31 (24):4973–4978, 1991. 75

H. Haferkorn. *Optik, Physikalisch-technische Grunlagen und Anwendungen.* Willey-VCH, 2003. 15, 16, 91, 215

K. A. Haines and B. P. Hildebrand. Surface-deformation measurement using the wavefront reconstruction technique. *Appl. Opt.*, 5(4):595–602, 1966. 3

P. Hariharan. *Optical holography.* Cambridge University Press, 1984. 3, 132

Eugene Hecht. *Optics.* Addison Wesley, 1998. 85, 86

S. Hecht. student experiment: Faseroptischer sensor, 2005. 29

M. H. Horman. An application of wavefront reconstruction to interferometry. *Appl. Opt.*, 4(3):333–336, 1965. 3

K. Ishizuka. Resolution improvement by titled single-sideband holography: preliminary experiments. *Ultramicroscopy*, 53(1):9–14, 1994. 117

X. Kang. An effective method for reducing speckle noise in digital holography. *Chin. Opt. Lett.*, 6(2):100–103, 2008. 148

J. Kaufmann, M. Gahr, and H. J. Tiziani. Noise reduction in speckle pattern interferometry. In K. Gastinger, O. J. Lokberg, and S. Winther, editors, *Speckle Metrology 2003*, volume 4993, pages 9–14, Trondheim, Norway, 2003. SPIE. 148, 149

J. Kornis and B. Gombköto. Application of super image methods in digital holography. In W. Osten, editor, *Optical Measurement Systems for Industrial Inspection IV*, volume 5856, pages 245 – 253, Munich, 2005. SPIE. 149, 150, 179

T. Kreis. *Handbook of holographic interferometry: optical and digital methods.* Wiley-VCH, 2005. 10, 47, 49, 50, 52, 76, 173, 196, 228

T. Kreis and K. Schlüter. Resolution enhancement by aperture synthesis in digital holography. *Opt Engineering*, 46(5):0558031–0558037, 2007. 149

T. Kreis, B. Fischer, W. Jüptner, and G. Sepold. Automatisierte auswertung holografischer interferenzmuster mit dem zeilen-scan-verfahren. In W. Waidelich, editor, *Laser 81 - Optoelektronik in der Technik*, volume 863, pages 105–110. Springer, 1981. 4

J. Kuehn, F. Charriére, T. Colomb, E. Cuche, F. Montfort, Y Emery, P. Marquet, and C. Depeursinge. Axial sub-nanometer accuracy in digital holographic microscopy. *Meas. Sci. Technol.*, 19(7), 2008. 6, 199

E. N. Leith and J. Upatnieks. Reconstructed wavefronts and communication theory. *J. Opt. Soc. Am.*, 52(10):1123–1128, 1962. 3

D. Litwiller. Ccd vs. cmos: Facts and fiction. *Photonics Spectra*, 2001. 33

A. Lohmann. Optische einseitenbanduumlbertragung angewandt auf das gabor-mikroskop. *J. Mod. Optic*, 3(2):97–99, 1956. 3, 117

A. W. Lohmann. The space-bandwidth product, applied to spatial filtering and to holography. *IBM Research Paper*, RJ-438, 1967. 8, 119, 120, 121, 123, 126, 132, 224

A. W. Lohmann. Space-bandwidth product of optical signals ans systems. *J. Opt. Soc. Am. A*, 13(3):470–473, 1996. xx, 120, 121

A. W. Lohmann and S. Sinzinger. *Optical Information Processing.* Universitätsverlag Ilmenau, 2006. 15, 133, 151

O. Lummer and F. Reiche, editors. *Die Lehre von der Bildentstehung im Mikroskop, von Ernst Abbe.* F. Vieweg, 1910. 85

T. H. Maiman. Stimulated optical radiation in ruby. *Nature*, 187(4736):493–494, 1960. 3

D. Malacara, editor. *Optical Shop Testing.* Wiley-VCH, 2006. 201

L. Martinez-León and B. Javidi. Improved resolution synthetic aperture holographic imaging. In J. Y. Son B. Javidi, F. Okano, editor, *Three-Dimensional TV, Video and Display VI*, volume 6778, page 7, Boston, Massachusetts, USA, 2007. SPIE. 58, 149

J. H. Massig. Digital off-axis holography with a synthetic aperture. *Opt. Lett.*, 27(24):2179–2181, 2002. 149

Apollo Instrument Inc. http://www.apolloinstruments.com/product_colmodule.html, 2010. [Online; accessed 3-March-2010]. 31

Charles Day Ltd.. http://www.daysteel.co.uk/laser.php?id=1, 2010. [Online; accessed 1-July-2010]. 31

Nobel − prize. http://nobelprize.org/nobel_prizes/physics/laureates/1971/gabor.html, 2010. [Online; accessed 28-June-2010]. xvi, 1

Ondax Inc. http://www.ondaxinc.com/PDFs/to_658_ds, 2010. [Online; accessed 1-March-2010]. 31

SIOS GmbH. http://www.sios.de, 2010. [Online; accessed 3-March-2010]. 30

Stanford University. http://engineering.stanford.edu/research/layout.php?sunetid=goodman, 2010. [Online; accessed 28-June-2010]. xvi, 1

TWI Ltd.. http://www.twi.co.uk/content/laser_welding.html, 2010. [Online; accessed 1-July-2010]. 31

C. P. McElhinney, B. M. Hennely, and T. J. Naughton. Extended focused imaging for digital holograms of macroscopic three-dimensional objects. *Appl. Opt.*, 47 (19):D71–D78, 2008. 172, 175

V. Mico, Z. Zalevsky, and J. Garcia. Superresolution optical system by common-path interferometry. *Opt. Express*, 14(12):5168–5176, 2006. 103, 148

V. Mico, Z. Zalevsky, C. Ferreira, and J. Garcia. Superresolution digital holographic microscopy for three-dimensional samples. *Opt. Express*, 16(23):19260–19270, 2008. 148

K.J. Moh, X.-C. Yuan, J. Bu, S. W. Zhu, and Bruce Z. Gao. Surface plasmon resonance imaging of cellsubstrate contacts with radially polarized beams. *Opt. Express*, 16(25):20734–20741, 2008. 218, 219

T. Nakatsuji and K. Matsushima. Free-viewpoint images captured using phase-shifting synthetic aperture digital holography. *Appl. Opt.*, 47(19):D136–D143, 2008. 149

T. Nomura, M. Okamura, E. Nitanai, and T. Numata. Image quality improvement of digital holography by superposition of reconstructed images obtained by multiple wavelengths. *Appl. Opt.*, 47(19):D38–43, 2008. 148

W. Osten, editor. *Fringe 2005*, chapter Digital Holographic Microscopy (DHM) applied to Optical Metrology: A resolution enhanced imaging technology applied to inspection of microscopic devices with subwavelength resolution, pages 308–314. Springer, 2006a. 6

W. Osten, editor. *Optical Inspection of Microsystems*. Taylor and Francis, 2006b. 210, 211

W. Osten, R. Höfling, and J. Saedler. Two computer-aided methods for data reduction from interferograms. In W. F. Fagan, editor, *Industrial optoelectronic measurement systems using coherent light*, volume 863, pages 105–113. SPIE, 1987. 3

Y. I. Ostrovsky, V. P. Shchepinov, and V. V. Yakovlev. *Holographic interferometry in experimental mechanics*. Springer, 1991. 3, 98, 103

M. Paturzo, S. Grilli F. Merola, S. De Nicola, A. Finizio, and P. Ferraro. Super-resolution in digital holography by a two-dimensional dynamic phase grating. *Optics Express*, 16(21):17107–17118, 2008. 148

J. Pawley, editor. *Handbook of Biological Confocal Microscopy*. Springer, 2006. 201

P.Ferraro, L. Miccio, S. Grilli, R. Meucci, S. De Nicola, and Paul Buah-Bassuah. Infrared digital holographic imaging. *SPIE newsroom*, 2008. 117, 198

R. L. Powell and K. A. Stetson. Interferometric vibration analysis by wavefront reconstruction. *J. Opt. Soc. Am.*, 55(12):1593–1597, 1965. 3

B. Rappaz, P. Marquet, E. Cuche, Y. Emery, C. Depeursinge, and P. J. Magistretti. Measurement of the integral refractive index and dynamic cell mor-

phometry of living cells with digital holographic microscopy. *Opt. Lett.*, 13 (23):9361–9373, 2005. 198

B. Rappaz, F. Charriére, C. Depeursinge, P. J. Magistretti, and P. Marquet. Simulataneous cell morphometry and refractive index measurement with dual-wavelength digital holographic microscopy and dye-enhanced dispersion of per-fusion medium. *Opt. Lett.*, 33(7):744–746, 2008. 198

L. Repetto, E. Piano, and C. Pontiggia. Lensless digital holographic microscope with light-emitting diode illumination. *Opt. Lett.*, 29(10):1132–1134, 2004. 198

G. L. Rogers. Experiments in diffraction microscopy. *Proc. R. Soc. Edinb., Ser. A*, 63:193–221, 1952. 3

B. E. A Saleh and M.C. Teich. *Fundamentals of photonics*. Wiley-VCH, 1991. 10, 28, 30, 240

U. Schnars. Direct phase determination in hologram interferometry with use of digitally recorded holograms. *J. Opt. Soc. Am.*, 11(7):2011–2015, 1994. 5

U. Schnars. *Digtal Holography*. Springer, 2005. 63

U. Schnars and W. Jueptner. *Digital Holography*. Springer, 2005. 47, 52, 75, 76

G. Schröder and H. Treiber. *Technische Optik*. Vogel, 2007. 30

K. A. Stetson and W. R. Brohinsky. Electrooptic holography and its application to hologram interferometry. *Appl. Opt.*, 24(21):3631–3637, 1985. 4

N. Stockes. lecturenotes: Research methods; error analyis and experimental engineering, 2007. 68

D. W. Sweeney and C. M. Vest. Reconstruction of three-dimensional refractive index fields from multidirectional interferometric data. *Appl. Opt.*, 12(11): 2649–2664, 1973. 3

M. L. Tachiki, M. Itoh, and T. Yatagai. Simulataneous depth determination of multiple objects by focus analysis in digital holography. *Appl. Opt.*, 47(19): D144–D153, 2008. 172

B. J. Thompson. Applications of holography. *Prog. Phys.*, 41:633–669, 1978. 3

J. D. Trolinger, R. A. Belz, and W. M. Farmer. Holographic techniques for the study of dynamic particle fields. *Appl. Opt.*, 8(5):957–961, 1969. 3

V.L. Tuft and S. Øystein. http://www2.edge.no/projects/index.php, 2009. [Online; accessed 17-July-2009]. 113

C. Wagner, W. Osten, and S. Seebacher. Direct shape measurement by digital wavefront reconstruction and multiwavelength contouring. *Opt. Eng.*, 39(1): 79–85, 2000. 6

P. Whittaker, R. A. Kloner, D. R. Boughner, and J. G. Pickering. Quantitative assessment of myocardial collagen with picrosirius red staining and circularly polarized light. *Basic Res Cardiol*, 89(5):397–410, 1994. 18, 201

J. C. Wyant. lecturenotes: Modern optical testing, 2009. 63

F. Wyrowski and O. Bryngdahl. Speckle-free reconstruction in digital holography. *J. Opt. Soc. Am. A*, 6(8):1171–1174, 1989. 148

L. Xu, Z. Guo X. Peng, J. Miao, and A. Asundi. Imaging analysis of digital holography. *Opt. Express*, 13(7):2444–2552, 2005. 8, 119, 120, 224

C. Yuan, H. Zhai, and H. Liu. Angular multiplexing in pulsed digital holography for aperture synthesis. *Opt. Lett.*, 33(20):2356–2358, 2008. 148

S. Zhang. Application of super-resolution image reconstruction to digital holography. *EURASIP*, 2006:1–7, 2005. 149

APPENDIX A

Lens Equation

A.1 Derivation of Fibre Point Source Distance d_{fb} and Projected Fibre Point Source Distance d_r

Light going through a lens experiences a change of propagation angle according to Snell's law of refraction Saleh and Teich (1991). This change is influenced by the refractive indexes of lens n_{Lens} and the surrounding medium n_{Sur}. Furthermore, the thickness-function combined with the position where the light beam stricks the lens and the incident light angle ϑ influences the angle of light β_2, see Fig. A.1. The lens maker equation, shown in Eq. A.1, describes how light is affected by the lens. This equation does not take into account diffraction effects. It describes the impact of the radius of both planes R_1 and R_2, the refractive index n_{Lens} and the thickness z_{Lens} on the focal length.

$$\frac{1}{f} = (n_{Lens} - 1) \left[\frac{1}{R_1} - \frac{1}{R_2} + \frac{(n_{Lens} - 1)z_{Lens}}{nR_1R_2} \right] \tag{A.1}$$
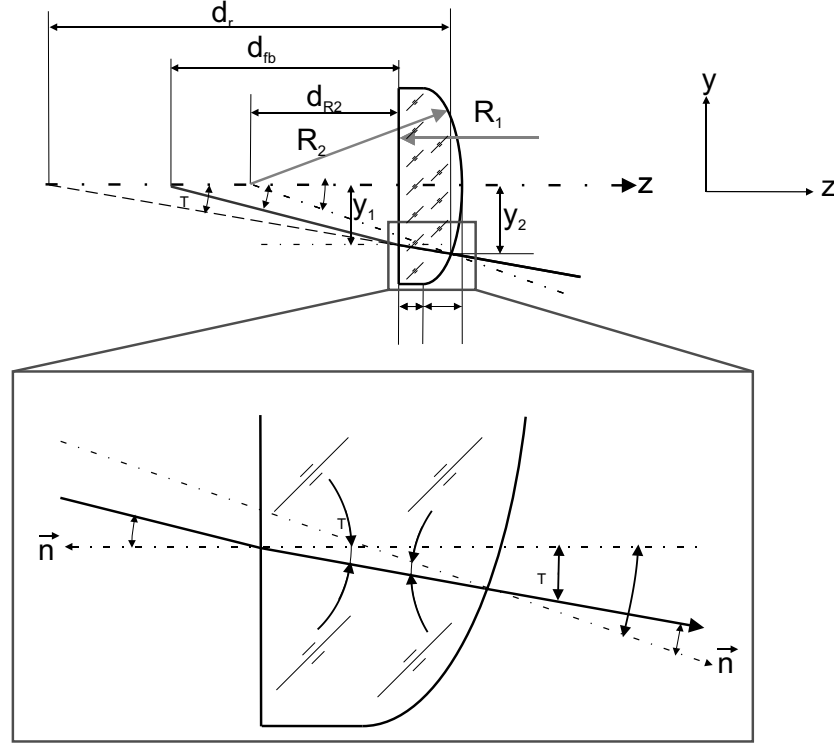
Figure A.1: Passage of light through a plano-convex lens

For a plano-convex lens ($R_1 = \infty$) Eq. A.1 can be simplified. Furthermore, it is assumed that back and front focal length are the same.

$$\frac{1}{f} = \frac{n_{Lens} - 1}{R_2} \tag{A.2}$$

In our case, the thickness-function z_{Lens} describes a plano-convex lens:

$$z_{Lens} = \Delta_1 + \Delta_2 - \left[R_2 - \sqrt{R_2^2 - y_2^2} \right] \tag{A.3}$$

The focus is set upon the derivation of two parameters, the distance d_{fb}, and the distance d_r which represents the distance from which the light would have originated under the angle κ_T without any lens. The knowledge of these parameters is important if the spherical wavefronts of a reference beam need to be adapted to the object beam's curvature. It is assumed that the focal length

f, the refractive indexes n_{Lens} and n_{Sur}, the angle ϑ, and the thickness of the plane lens part Δ_1 and the spherical lens part Δ_2 are known. Furthermore, n_{Sur} is assumed to be one. In order to obtain an equation with both terms d_{fb} and κ_T the light path is retraced as it traveled through the lens. Thus we are starting with an equation to obtain κ_T. The derivation of the equations shown in the following are partially based on the geometric relationships shown in Fig.A.1. From Fig. A.1 follows for κ_T:

$$\kappa_T = \beta_1 - \beta_2 \tag{A.4}$$

Where β_1 is the angle between the normal $\vec{n}_1$ on the lens surface for the coordinates (y_2, d_{R2}) and the optical axis. β_2 is the angle between the normal $\vec{n}_2$ on the lens surface and the light leaving the lens. β_2 can be described by Snell's law:

$$
\begin{aligned}
\sin \beta_2 &= n_{Lens} \sin \kappa \\
&= n_{Lens} \sin (\beta_1 - \vartheta_T)
\end{aligned} \tag{A.5}
$$

With $\vartheta_T = \operatorname{asin}\left(\frac{\sin \vartheta}{n_{Lens}}\right)$ Combing Eq. A.4 and Eq. A.5 results in a new equation in which κ_T can solely described as a function of ϑ and β_1.

$$\kappa_T = \beta_1 - \operatorname{asin}\left[n_{Lens} \sin (\beta_1 - \vartheta_T)\right] \tag{A.6}$$

Now we face the difficult task of solving this equation for β_1. This could be solved with the help of Matlab.

$$\beta_1 = \vartheta_T + \operatorname{atan}\left[\frac{\sin(\kappa_T - \vartheta_T)}{\cos(\kappa_T - \vartheta_T) - n_{Lens}}\right] \tag{A.7}$$

Having obtained an equation to describe β_1 as a function of κ_T we now need to

find an equation which combines β_1 and d_{fb}. This can be done by describing β_1 as a function of the coordinates y_2 and d_{R2}:

$$\tan \beta_1 = \frac{y_2}{d_{R2}} = \frac{y_2}{\sqrt{R_2^2 - y_2^2}} \tag{A.8}$$

Assuming that the light is only traveling in the paraxial region, a finite region close to the optical axis, the denominator in Eq. A.8 can be simplified by replacing the spherical thickness-function with a parabolic one.

$$\sqrt{R_2^2 - y_2^2} = R_2 - \frac{y_2^2}{2R_2} \tag{A.9}$$

Thus Eq. A.8 becomes:

$$\tan \beta_1 = \left(\frac{R_2}{y_2} - \frac{y_2}{2R_2} \right)^{-1} = \left(\frac{f(n-1)}{y_2} - \frac{y_2}{2f(n-1)} \right)^{-1} \tag{A.10}$$

All parameters apart from y_2 are known in order to solve Eq. A.10. y_2 can be calculated from the two distances d_{fb} and z_{Lens} and their corresponding angles ϑ and γ, respectively.

$$y_2 = \tan \vartheta_T \left[\Delta_1 + \Delta_2 - \left(R_2 - \sqrt{R_2^2 - y_2^2} \right) \right] + d_{fb} \tan \vartheta \tag{A.11}$$

ϑ_T is the angle of light after refraction in the lens. It can be calculated by:

$$\tan \vartheta_T = \tan \left[\mathrm{asin} \left(\frac{\sin \vartheta}{n_{Lens}} \right) \right] \tag{A.12}$$

To keep the equations relatively simple and easy to follow $\tan \gamma$ instead of its solutions is used in the following.

Assuming again the paraxial region, the term $\left(R_2 - \sqrt{R_2^2 - y_2^2} \right)$ in Eq. A.11

can be simplified as:

$$R_2 \left(1 - \sqrt{1 - \frac{y_2^2}{R_2^2}}\right) \approx R_2 \left[1 - \left(1 - \frac{y_2^2}{2R_2^2}\right)\right] = \frac{y_2^2}{2R_2} \tag{A.13}$$

Thus Eq. A.11 becomes a quadratic equation which can be solved for y_2:

$$y_2^2 + \frac{2R_2 y_2}{\tan \vartheta_T} - 2R_2 (\Delta_1 + \Delta_2) - \frac{2R_2 d_{fb} \tan \vartheta}{\tan \vartheta_T} = 0 \tag{A.14}$$

Only the positive result of the quadratic equation for y_2 makes physically sense. Thus y_2 becomes:

$$\begin{aligned} y_2 &= -\frac{R_2}{\tan \vartheta_T} + \sqrt{\left(\frac{R_2}{\tan \vartheta_T}\right)^2 + 2R_2 \left(\Delta_1 + \Delta_2 + \frac{\tan \vartheta d_{fb}}{\tan \vartheta_T}\right)} \\ &= -\frac{f(n_{Lens} - 1)}{\tan \vartheta_T} + \sqrt{\left(\frac{f(n_{Lens} - 1)}{\tan \vartheta_T}\right)^2 + 2f(n_{Lens} - 1)\left(\Delta_1 + \Delta_2 + \frac{\tan \vartheta d_{fb}}{\tan \vartheta_T}\right)} \end{aligned} \tag{A.15}$$

The angle $\kappa_T(d_{fb})$ as a function of the distance d_{fb} can now be calculated by combing Eq. A.10, Eq. A.15 and Eq. A.5.

In a next step these equations need to be solved for d_{fb}. To reduce the length of the equations some substitutions are made.

$$\begin{aligned} a &= \frac{f(n_{Lens} - 1)}{\tan \vartheta_T} \\ b &= \sqrt{\left(\frac{f(n - 1)}{\tan \vartheta_T}\right)^2 + 2f(n_{Lens} - 1)\left(\Delta_1 + \Delta_2 + \frac{\tan \vartheta d_{fb}}{\tan \vartheta_T}\right)} \\ c &= f(n_{Lens} - 1) \\ d &= \tan(\kappa_T + \beta_2) = \tan \beta_1 \end{aligned} \tag{A.16}$$

Combining Eq. A.4 and Eq. A.15 with the substitutions results in:

$$d = \frac{-a+b}{c - \frac{a^2-2ab+b^2}{2c}} \tag{A.17}$$

Solving Eq. A.17 for b by only allowing the positive answer is:

$$
\begin{aligned}
b &= -\left(\frac{c}{d} - a\right) + \sqrt{\left(\frac{c}{d} - a\right)^2 - \left(a^2 - 2c^2 - \frac{2ac}{d}\right)} \\
&\approx f(n_{Lens} - 1)\left[\frac{1}{\tan\vartheta_T} + \tan\left(\kappa_T + \beta_2\right)\right]
\end{aligned}
\tag{A.18}
$$

We can now calculate d_{fb} by inserting all the parameters, which were previously substituted. d or $\tan\beta_1$ can be obtained by Eq. A.7 and the result used for calculating d_{fb}.

$$
\begin{aligned}
d_{fb} &= \left[\frac{b^2 - a^2}{2c} - (\Delta_1 + \Delta_2)\right]\frac{\tan\vartheta_T}{\tan\vartheta} \\
&\approx \left[\frac{f(n_{Lens} - 1)\tan\beta_1}{2}\left(\tan\beta_1 + \frac{2}{\tan\vartheta_T}\right) - (\Delta_1 + \Delta_2)\right]\frac{\tan\vartheta_T}{\tan\vartheta}
\end{aligned}
\tag{A.19}
$$

The second task is to obtain an equation to calculate d_r. From our previous calculations κ_T and y_2 are known. These are the parameters needed to calculate d_r.

$$d_r = \frac{y_2}{\tan\kappa_T} \tag{A.20}$$

An easier but less accurate approach is based on the thin lens model, see Fig. A.2. Thus the curvature and the thickness-function of the lens in not taken into account. With the geometrical relationships shown in Fig. A.2 d_{fb} and d_r can be calculated. Both parameters can solely be described by a function of the known parameters f, κ_T and ϑ by substituting y_1 with:

$$y_1 = f\left(\tan\vartheta - \tan\kappa_T\right) \tag{A.21}$$
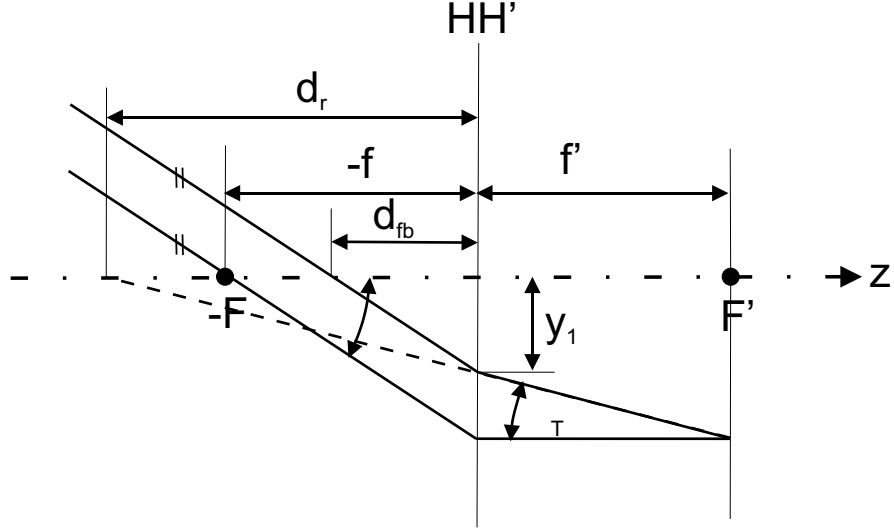
Figure A.2: Parallel incident beams on a thin lens with ϑ the angle of incidence

Hence d_{fb} becomes:

$$d_{fb} = \frac{y_1}{\tan\vartheta} = f(1 - \frac{\tan\kappa_T}{\tan\vartheta}) = f\left(1 - \frac{d_r\tan\vartheta}{y_1}\right) \tag{A.22}$$

The distance d_r is:

$$d_r = \frac{y_1}{\tan\kappa_T} = f\left(\frac{\tan\vartheta}{\tan\kappa_T} - 1\right) = f\frac{y_1}{f\tan\vartheta - y_1} \tag{A.23}$$

A comparison of the more accurate paraxial method and the thin-lens model is graphically shown in Fig. A.3. The parameters chosen for both calculations are $f = 57$ mm, $\vartheta = 7°$, $\Delta_1 = 1.5$ mm, $\Delta_2 = 0.7$ mm and $n_{Lens} = 1.515$. The maximum deviation is 1.63 mm for $\kappa_T = 5.2°$, which would result in a change $\Delta\kappa_T = 0.2°$. Which of both models to chose does thus depend on how accurate the angle κ_T needs to be adjusted for, see Fig. A.3.
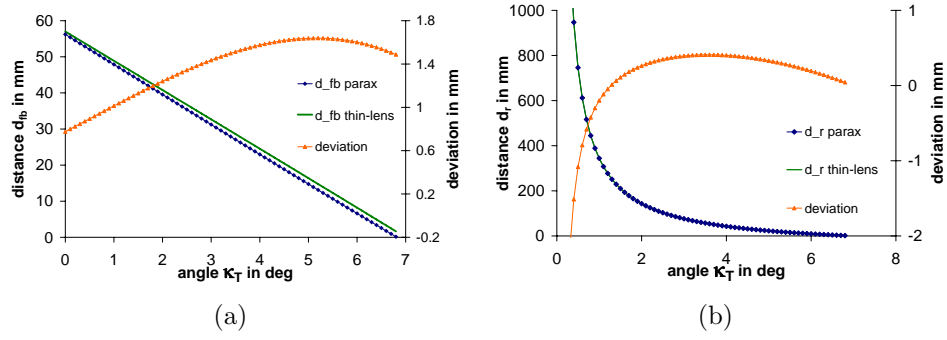
Figure A.3: Graphs dependence and accurracy of (a) d_{fb} and (b) d_r on the angle κ_T and the chosen calculation model

A.2 Numerical Phase-Function of a Lens

When light passes through the lens it is delayed due its refractive index n_{Lens} compared to the surrounding medium n_s. We assume air to be the surrounding medium, which has a refractive index of one. The total phase delay of incident plane waves compared to plane-waves, which have not been subjected to the passage through the lens is:

$$\varphi(x, y) = k\left(n_{Lens} - 1\right) z_{Lens}(x, y) \tag{A.24}$$

A plano-convex lens (see Fig. A.1) is once again considered which is characterized by a two-dimensional thickness function:

$$z_{Lens}(x, y) = \Delta_1 + \Delta_2 - \left[R_2 - \sqrt{R_2^2 - (x^2 + y^2)}\right] \tag{A.25}$$

and by the lens maker equation, shown in Eq. A.2. $\Delta_1 + \Delta_2$ are combined to Δ_0. Inserting Eq. A.2 in Eq. A.25 results in:

$$\begin{aligned} z_{Lens}(x, y) =& \Delta_0 - \left[f\left(n_{Lens} - 1\right) - \sqrt{\left\{f^2\left(n_{Lens} - 1\right)^2 - (x^2 + y^2)\right\}}\right] \\ & \Delta_0 - \left[f\left(n_{Lens} - 1\right)\left\{1 - \sqrt{\left(1 - \frac{x^2 + y^2}{f\left(n_{Lens} - 1\right)}\right)}\right\}\right] \end{aligned} \tag{A.26}$$

The corresponding phase delay can be described in complex exponential notation by:

$$L(x,y) = \exp\left[ik\left(n_{Lens} - 1\right)\Delta_0\right]\exp\left[-ik\left(n_{Lens} - 1\right)\right.$$
$$\left. \cdot f\left(n - 1\right)\left\{1 - \sqrt{\left(1 - \frac{x^2 + y^2}{f^2\left(n_{Lens} - 1\right)^2}\right)}\right\}\right] \tag{A.27}$$

The complex exponential terms Eq. A.27 which do not depend on $(x^2 + y^2)$ represent a constant phase and can be dropped hereafter. Hence Eq. A.27 can be rewritten as:

$$L(x,y) = \exp\left[-ik\left(n_{Lens} - 1\right)^2 f\sqrt{1 - \frac{x^2 + y^2}{f^2\left(n_{Lens} - 1\right)^2}}\right] \tag{A.28}$$

Eq. A.28 represents a complex Lens-formula, which is valid for the Rayleigh-Sommerfeld region, see Fig. 2.12. A suitable refractive index is the 1.5 which matches with the commonly applied BK7-Glass for lenses. The lens-formula can be simplified for the Fresnel-region at which a parabolic wave-front approximation is valid. The term under the square root can be expressed by:

$$\sqrt{1 - \frac{x^2 + y^2}{f^2\left(n_{Lens} - 1\right)^2}} \approx 1 - \frac{x^2 + y^2}{2f^2\left(n_{Lens} - 1\right)^2} \tag{A.29}$$

Thus Eq. A.28 is simplified to:

$$L(x,y) = \exp\left[-ik\frac{x^2 + y^2}{2f}\right] \tag{A.30}$$

Matlab Functions

There is little to be gained by providing a printout of all Matlab-functions used in the frame of this thesis. Therefore, only a few but important subroutines are included merely as an example.

```
function out = fresnel(d,p,image1)
%function for calculating the reconstruction results obtained by the
%Fresnel integral.
%----------------------------------------------------------------------
%----------------------------------------------------------------------
tic image1=single(image1);
d=d*10^-3; % conversion of distance from mm to m
w = 632.8e-9;% conversion of the wavelength from nm to m
pz=p*10^-6; % conversion pixel-size microns to m
 c=i*pi*pz^2/(w*d);
[N M] = size(image1);
% In order to obtain same aspect ratio, same resolution and DOF in
%x- and y direction of reconstructed hologram.
if N>M
    b=(N-M)/2;
   image1=padarray(image1,[0 b]);
 else
    b=(M-N)/2;
    image1=padarray(image1,[b 0]);
end [N M] = size(image1);
ch=single(zeros([N,M]));%pre-assign chirp-function to calculate
                        %the reconstruction
for k = 1:N
     for l=1:M
            ch(k,l) = (k-N/2-1)^2+(l-M/2-1)^2;
     end
end
out=fftshift(fft2(image1.*exp(ch*c)));%result numerical reconstruction
toc t=toc %calculation time
figure(1); imagesc(abs(out));
```

Figure B.1: Matlab function: `fresnel`.

```
function [finres,y] = convolution(dist,p,m,s,t,image1)
% This function represents the digitized implementation of the
%Rayleigh Sommerfeld diffraction integral.
%In addition a numerical lens is employed, which offers the possibility to
%change the magnification of the reconstructed hologram. In that way one does
%not need to apply zero-padding to the hologram in
%order to reconstruct a hologram of an object larger than the camera sensor.
%This would be very time consuming and requires lots of memory resources.
%Moreover, a shift can be introduced in x and y direction in order to
%center the reconstruction.
%--------------------------------------------------------------------------
%--------------------------------------------------------------------------
tic image1=single(image1);
[nR nC]=size(image1);
w=632.8*10^(-9);%wavelength conversion from nm to m
di1=dist*10^-3;%distance to the object converted from mm to m
pz=p*10^(-6); %normal pixel size
nR % number of rows y-values;
nC %number of columns x-values
c1=(nR*pz)^2/(di1*w); c2=(w/(nR*pz))^2; di2=di1*m;
f=(1/di1+1/di2)^(-1); di1=di2; [N M] = size(image1)
h=waitbar(0,'Wait, still busy calculating...');
G=single(zeros(nR,nC)); L=G; for n=1: N
    waitbar(n/N)
     for m=1: M
        %calculates term of the transfer-function which changes for each pixel
        %enables one to apply a shift s and t in x and y direction, respectively
        G(n,m)=1-(w*(n-N/2-1+s*N*pz^2/(di2*w))/(N*pz))^2-(w*(m-1-M/2+t*M*pz^2/(di2*w))/(M*pz))^2;
        %calculates term of the numerical lens which changes for each pixel
        L(n,m)=(n-1-N/2)^2+(m-1-M/2)^2;
     end
end close(h);
%One can decide to use either a parabolic or a spherical lens for the reconstruction.
%parabolical wave front for lens
y=exp(-1i*pi/(w*f)*pz^2*L);
%spherical wave front for lens
%y=exp(1i*2*pi*f*0.5^2/(w)*sqrt(1-pz^2*L/(f^2*0.5^2)));
G=exp(1i*2*pi*di1/w*sqrt(G)); a=fftshift(fft2((image1.*y)));
finres=ifftshift(ifft2(a.*G)); figure(1) imagesc(abs(finres));
figure(2),imagesc(angle(y));
toc t=toc;
end
```

Figure B.2: Matlab function: `convolution`.

```
function out =fourierfocus(d_obj1,d_obj2,d_ref,p,image1,x1,x2,y1,y2)
%Function which calculates the best in-focus reconstruction distance d_obj
%for certain image region defined by x1,x2,y1,y2 with a Fourier setup;
%-------------------------------------------------------------------------
%-------------------------------------------------------------------------
tic image1=single(image1);
% conversion of distance from mm to m of lower and upper limit for
% the in-focus estimate
d1obj=d_obj1*10^-3;       %estimate for lower limit of in-focus position
d2obj=d_obj2*10^-3;       %estimate for upper limit of in-focus position
d2=d_ref*10^-3;
w = 632.8e-9;             %conversion of the wavelength from nm to m
pz=p*10^-6;               %conversion pixel-size microns in m
[N M] = size(image1)      %pixel-numbers in x and y direction
%optimization function fminbnd which results in best in-focus object-distance
%for specified region d_obj1<=d_obj<=dobj2
[x,fval,exitflag,output]=fminbnd(@(x)geterror(x,image1,pz,d2,w,x1,x2,y1,y2),d1obj,d2obj);
x                         %best in-focus d_obj
f=d2*x/(d2-x);            %calculation of focal length for numerical lens
h=waitbar(0,'Wait, still busy...');
lens=single(zeros(N, M)); %pre-assign lens-matrix
for
k=1:N
    waitbar(k/N)
        for l= 1:M
              lens(k,l) = (k-1-N/2)^2+(l-1-M/2)^2;
        end
end close(h)
y=exp(1i*pi/(w*f)*pz^2*lens);    %numerical lens
out=ifftshift(ifft2(image1.*y)); %changed
toc t=toc figure(1);
imagesc(abs(out));% phase of chirpfunction
%out = fftshift(fft2(ch.*image4));
end
%Optimization function
function er = geterror(x,image1,pz,d2,w,x1,x2,y1,y2)
[N,M]=size(image1);
w=632.8*10^(-9);
f=d2*x/(d2-x);
h=waitbar(0,'Wait, still busy...');
lens=single(zeros(N, M)); for k
= 1:N
    waitbar(k/N)
        for l= 1:M
              lens(k,l) = (k-1-N/2)^2+(l-1-M/2)^2;
      end
end close(h) y=exp(1i*pi/(w*f)*pz^2*lens);
res=ifftshift(ifft2(image1.*y)); %reconstruction
res=abs(res);                    %calculates modulus of reconstruction
res=res(x1:x2,y1:y2);            %image region under investigation
[N M]=size(res);
er=imresize(res,0.5);            %resize image in order to reduce impact of
                                 %speckle effect
er=nlfilter(res,[20 20],'var2'); %sliding window function to calculate the
                                 %variance value of each pixel
er=1/sum(sum(er));               %optimization for error-function 'er' to
                                 %be smallest (largest sum of variance) end
```

Figure B.3: Matlab function: `fourierfocus`.

```
function [res] = phasemap_cai(image1,image2,image3,reference)
%function in order to obtain the wrapped phase map of unknown phase step
%by an iterative approach and use of the reference and object beam
%based on a method developed by Cai
%--------------------------------------------------------------------------
%--------------------------------------------------------------------------
tic
%convert three phase stepped holograms and intensity of reference-wave to single
%precision
image1=single(image1);
image2=single(image2);
image3=single(image3);
reference=single(reference);
%auxiliary variables according to Cai's paper
ar1=sqrt(reference);
p=abs(image2-image1);
q=abs(image3-image2);
r=abs(image3-image1);
pa=mean2(p);
qa=mean2(q);
ra=mean2(r);
c=2*pa*qa*ra/(sqrt(2*(pa^2*qa^2+pa^2*ra^2+qa^2*ra^2)-(pa^4+qa^4+ra^4)));
a1=(2*asin(pa/c))              %indicates first phase step
a2=(2*asin(qa/c))              %indicates second phase step
%result of complex object-wave
ans1=1./(4*ar1*sin(a2/2)).*(exp(1i*a1/2)/sin((a1+a2)/2).*(image1-image3)-
     exp(1i*(a1+a2)/2)/sin(a1/2).*(image1-image2));
%need to check for NaN (not assigned number) or Inf (infinity)
%which otherwise might result into errors or cause problems when
%calculation the reconstructed hologram
image=ans1;
a=image;
b1=isinf(a);
b2=isnan(a);
b=b1+b2;
before=sum(sum(b))
[N M]=size(a);
if before==0
    image=image;
else
    h=waitbar(0,'Wait, still busy...');
  for k=1:N
    waitbar(k/N)
    for l=1:M
        if b(k,l)==0
            image(k,l)=image(k,l);
        else
            % whenever NaN or Inf appears it will be replaced by the mean
            % of its surrounding pixels
            a(k,l)=(a(k-1,l-1)+a(k-1,l)+a(k-1,l+1)+a(k,l-1)+a(k,l+1)+a(k+1,l-1)
                +a(k+1,l)+a(k+1,l+1))/8;
        end
    end
  end
  close(h)
  c1=isinf(image);
  c2=isnan(image);
  c=c1+c2;
  after=sum(sum(c))
end
res=image;
toc;
t=toc                                  %calculation time for whole process
end
```

Figure B.4: Matlab function: `phasemap_cai`.

```
function [out,t]=gaussfit(stack);
%calculates a fourth polynomial fit of the stack obtained by the variance
%method
%outpot is a two dimensional topology map(out)and the calculation time(t)
[M N O]=size(stack); out=single(zeros([N O])); tic
h=waitbar(0,'Wait, still busy...'); for j=1:N
    waitbar(j/N)
    for k=1:O
        out(j,k)=getcolumn3(stack,j,k);
    end
end close(h); t=toc end function out=getcolumn3(stack,x,y);
%applies fourth degree polynomial fitt to a pixel-column of the stack
%speciefied by x and y
%reads out the maximum the maximum interpolated data and transfers it to
%function gaussfit.m
[M N O]=size(stack); out_y=(zeros([M 1])); out_x=out_y; for j=1:M
    out_y(j)=stack(j,x,y);
    out_x(j)=j;
end gfit=fit(out_x,out_y,'poly4'); out=feval(gfit,0:0.1:M); [a,b]=
max(out); out=(b-1)/10; end
```

Figure B.5: Matlab function: `gaussfit`.

APPENDIX C

Solid-works Drawing

C.1 Solidworks assembly drawing for digital holographic microscope
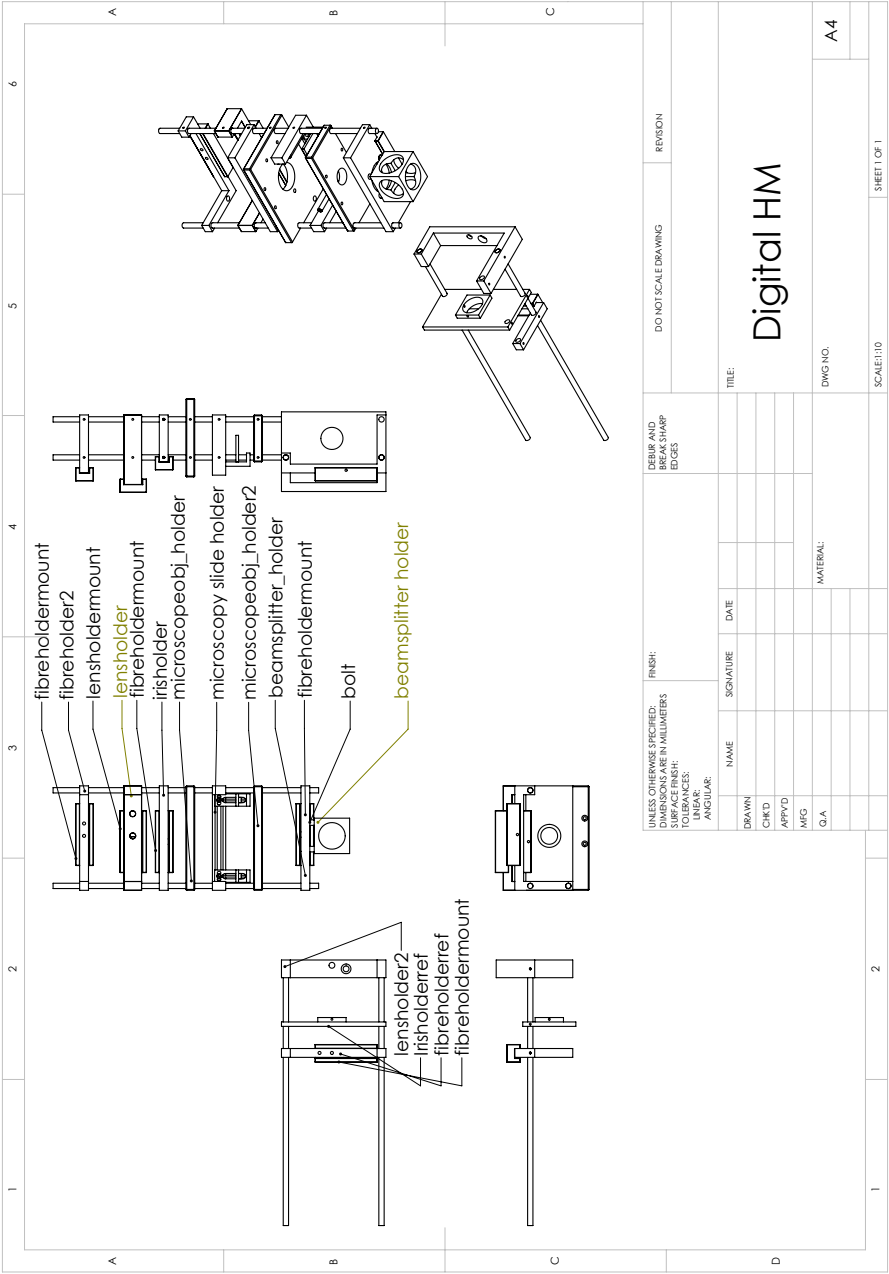
C.2 Solidworks assembly drawing for box covering the optical table

C.3   Solidworks assembly drawing holder for 'Physik Instrumente' x-y traverse

C.4 Solidworks assembly drawing holder for fibre launcher

C.5 Solidworks assembly drawing laser shutter

APPENDIX D

Data-Sheets of Optical Elements and Instruments used

D.1 Data-Sheet Pixelfly qe Camera

System Data

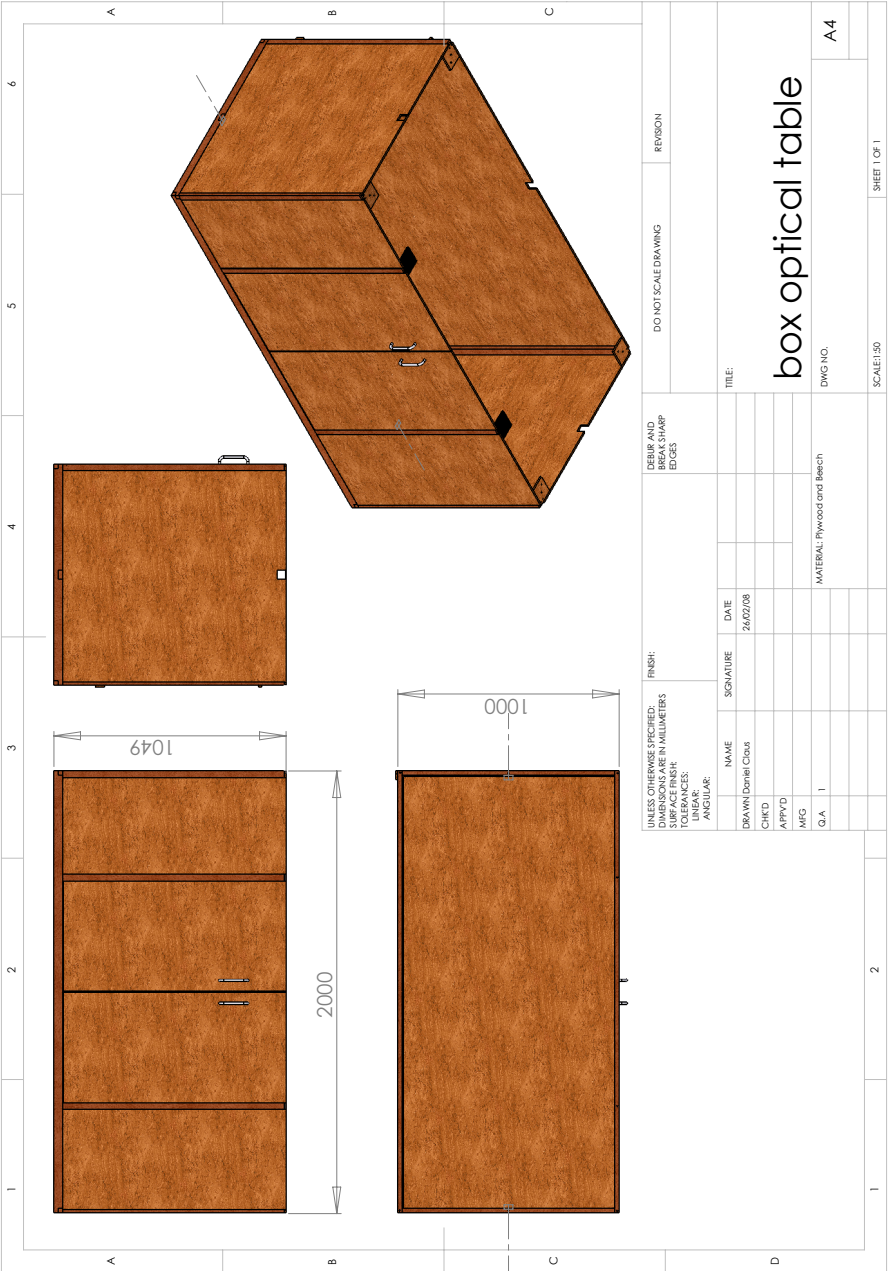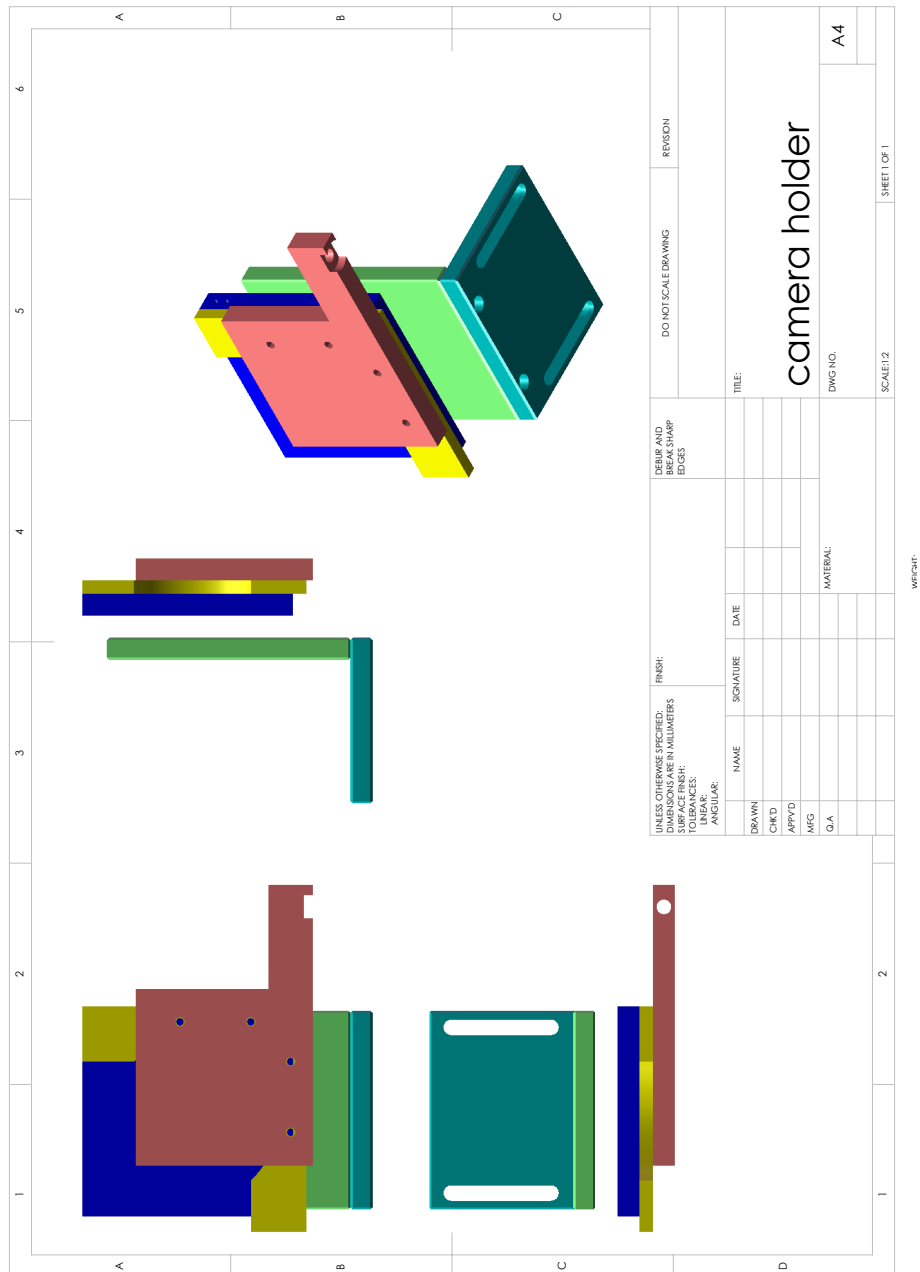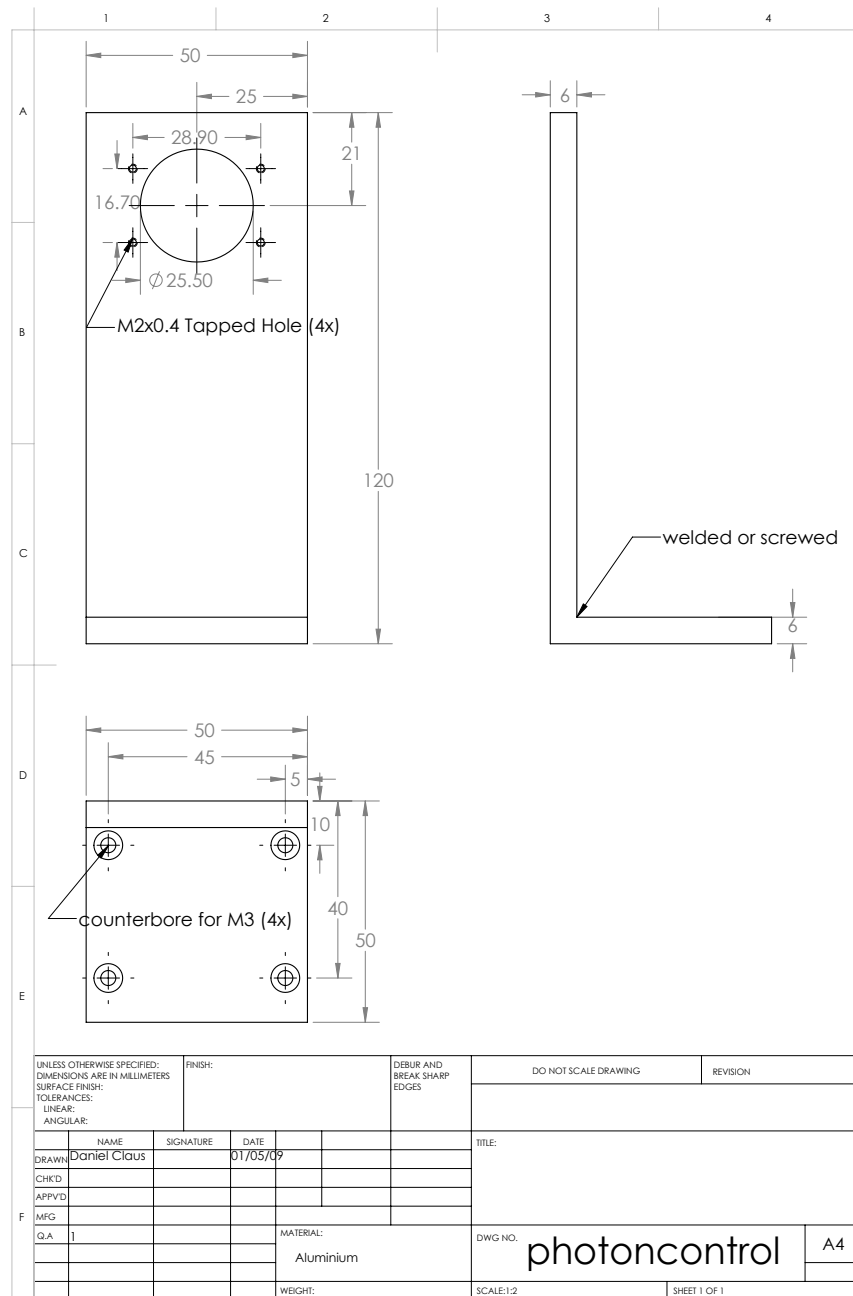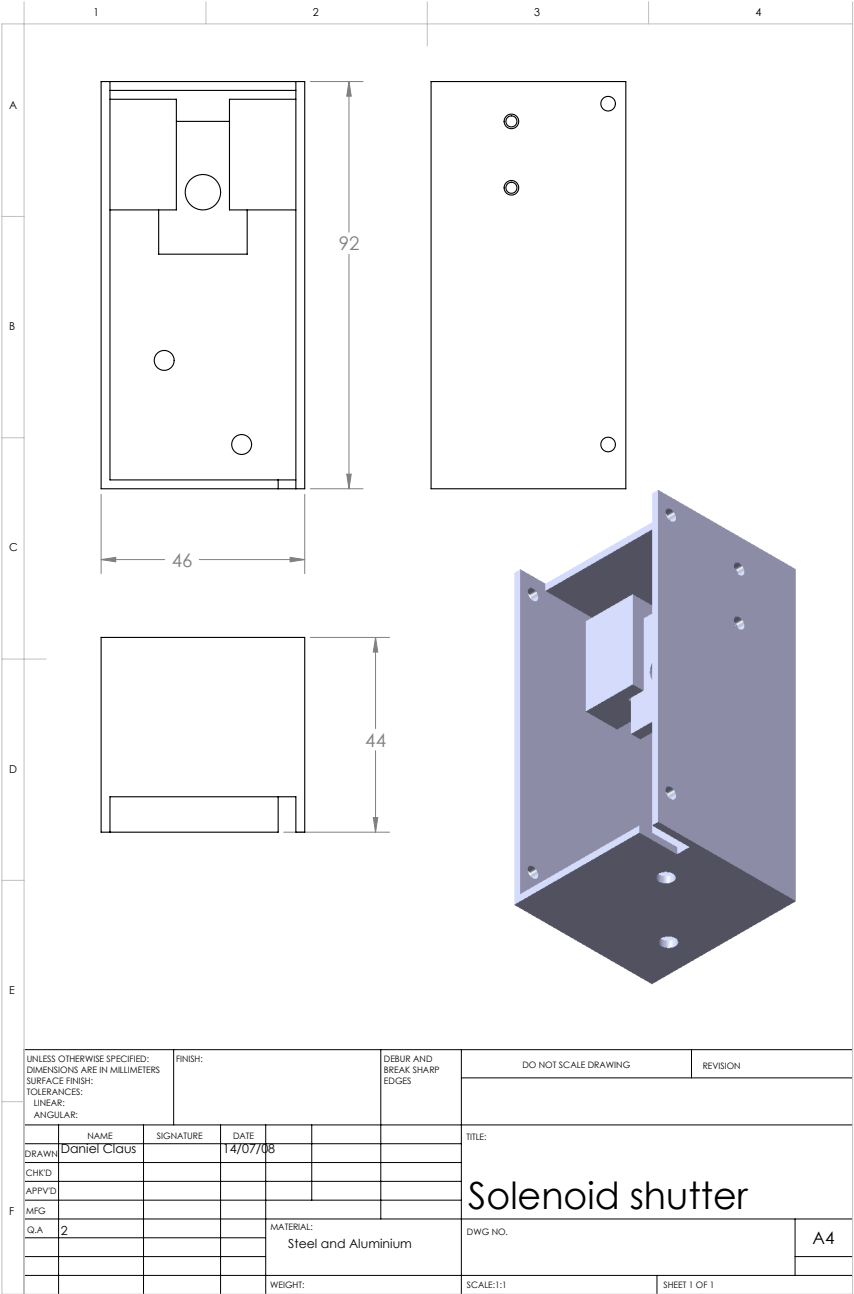| CCD Sensor	VGA (200 / 205)	VGA (210 / 215)	Scientific (230 / 235)
Number of Pixels	640 (H) x 480 (V)	640 (H) x 480 (V)	1280 (H) x 1024 (V)
Pixel Size	9.9µm x 9.9µm	9.9µm x 9.9µm	6.7µm x 6.7µm
Sensor Format	1/2"	1/2"	2/3"
Scan Area	6.3 x 4.8 mm	6.3 x 4.8 mm	8.6 x 6.9 mm
Full Well Capacity	30.000 e⁻	30.000 e⁻	20.000 e⁻
Readout Noise	11…14 e⁻	16 e⁻	12 e⁻
Scan Rate	20 MHz	16 MHz	20 MHz
Imaging Frequency …			
… at binning mode 1	50 fps	40 fps	12,5 fps
… at binning mode 2	95 fps	76 fps	24 fps
… at binning mode 4	177 fps	140 fps	not available
A/D Conversion Factor	6.5 e⁻/count	7 e⁻/count	4,5 e⁻/count
Spectral Range b/w	290 ... 1000 nm	290 ... 1000 nm	290 ... 1000 nm
Spectral Range color	primary color, RGB	primary color, RGB	primary color, RGB
Anti Blooming	> 1000	> 1000	> 1000
CCD Quality	grade 0	grade 0	grade 0
Non-Linearity (Differential)	< 2%	< 2%	< 2%
Binning Vertical	factor 1, 2, 4	factor 1, 2, 4	factor 1, 2
Binning Horizontal	factor 1, 2	factor 1, 2	factor 1, 2

CCD Sensor	HiRes (220 / 225)	QE (270 / 275)
Number of Pixels	1360 (H) x 1024 (V)	1392 (H) x 1024 (V)
Pixel Size	4.65µm x 4.65µm	6.45µm x 6.45µm
Sensor Format	1/2"	2/3"
Scan Area	6.3 x 4.7 mm	9.0 x 6.6 mm
Full Well Capacity	13.000 e⁻	18.000 e⁻
Readout Noise	6…9 e⁻	6…9 e⁻
Scan Rate	16 MHz	20MHz
Imaging Frequency …		
… at binning mode 1	9,5 fps	12 fps
… at binning mode 2	18 fps	23 fps
… at binning mode 4	not available	not available
A/D Conversion Factor	3 e⁻/count	3.8 e⁻/count
Spectral Range b/w	290 ... 1000 nm	290 ... 1000 nm
Spectral Range color	primary color, RGB	primary color, RGB
Anti Blooming	> 1000	> 400
CCD Quality	grade 0	grade 0
Non-Linearity (Differential)	< 2%	< 2%
Binning Vertical	factor 1, 2	factor 1, 2
Binning Horizontal	factor 1, 2	factor 1, 2

Camera Head + PCI-Board	
Power consumption	1 A at 5 V, 400mA at 12 V
PCI-Board	about 10 W
Camera Head	about 2,6 W …3,3 W

D.2 Data-Sheet Piezo-Actuator
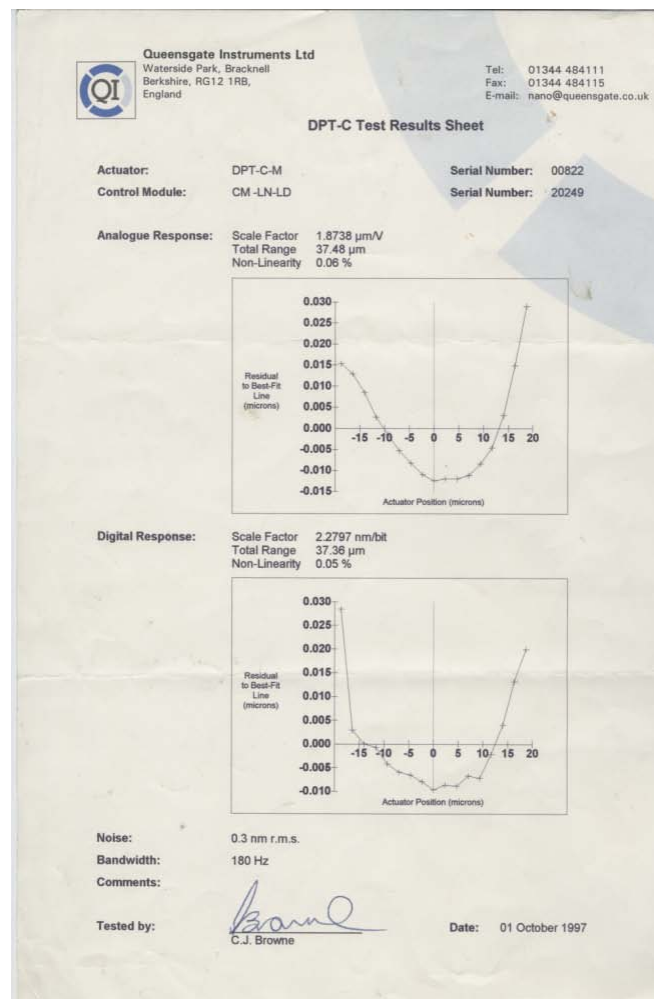
D.3   Data-Sheet Wave-Plates

Quartz 35mm waveplate

Mica λ/4 wave plate
with aperture 10mm

United Crystals' Wave Plate Features:

- Massive Production to support industrial and Commercial Applications
- Fast Delivery – directly from our factory via UPS Express
- Strict Quality Control
- Competitive Price and Huge OEM Discount
- Free Technical Support Always

United Crystals' Warranty on Wave Plates:

- Material: Mica, Quartz
- Type: λ/8, λ/4, λ/2, λ etc
- Dimension tolerance: +0.0mm –0.02mm
- Transmitting wavefront distortion: less than λ/8 @633nm
- Transparent Range: 400–2100 nm
- Surface Quality: 20/10 to MIL-O-13830A
- Parallelism: <1 arc second
- Retardation Tolerance: <3%
- AR Coating: R<0.2%

D.4 Data-Sheet PI M-150.11 Stage

M-100 Series Linear Stages   **Operating Manual MP 32E**

Stage Model :	M-150.10	M-150.11	M-150.20
Drive Type	DC, 2 Watts (DC-Mike drive)	DC, 3 Watts C-136.10 backlash free	Stepping Motor C-545 direct drive
Gear head reduction ratio	140.759183 : 1	29.64197530 : 1	---
Encoder angular resolution	60 c/rev.	2000 c/rev.	---
Linear resolution	0.059202768 µm/c	0.0084339858 µm/c	0.25 µm/step
Linear transmission Ratio [1]	16.891102 c/µm	118.5679012 c/µm	4 steps/µm
Max. count frequency @ 11V (Max. free running speed)	9000 c/s	200 000 c/s	Max. step frequency: 12000 steps/s with C-500 Stepping Motor Controllers
Max. Linear Speed	0.53 mm/s	1.68 mm/s	3 mm/s @ 12 kHz
Limit Switches	installed	installed	installed
QMove drive identifier [2]	DRIVEn=0	DRIVEn=1	---
Cable connection	Flat ribbon cable	DB15(m) connector	12-pin round connector
Cable part number	C-815.62 Flat ribbon cable	C-815.36 Round cable with DB15 connectors at both sides	C-500.32 Cable for 5-phase stepping motors
Controller options	C-842, C-832, C-804, C-812		C-500 Series Stepping Motor Controllers
C-842 : parameters [3]	DP 200...380 DI 0...12 DD 0...1000 DL 0...2000 SV 1...8000 SA 1..20	DP 100...300 DI 0...10 DD 0...800 DL 0...2000 SV 1...200000 SA 1...450	

Table 3

Notes:

[1] This values can be used in the QMove configuration file for RATIOn=... entries to convert count based positioning commands to µm-based.

[2] Use this number in QMove configuration file for DRIVEn= entries.

[3] Motion control parameters can be varied within the given limits. The motors will work within a stable operating range unless significant mechanical load changes may require to modify some parameters.

Release 4.0   **Physik Instrumente (PI)**   **Page 9**

D.5 Data-Sheet 6.6MP-CMOS sensor

IBIS4-A-6600
CYII4SM6600AB

Specifications

General Specifications

Table 2. General Specifications.

Parameter	Specification	Remarks
Pixel architecture	3T-pixel	
Pixel size	3.5 m x 3.5 m	The resolution and pixel size results in a 7.74 mm x 10.51 mm optical active area.
Resolution	2210 x3002	
Pixel rate	40 MHz	Using a 40- MHz system clock and 1 or 2 parallel outputs.
Shutter type	Electronic rolling shutter	
Full frame rate	5 frames/second	Increases with ROI read out and/or sub sampling.

Electro-optical specifications

Overview

Table 3. Electro-optical Specifications

Parameter	Specification	Remarks
FPN (local)	<0.20%	RMS% of saturation signal.
PRNU (local)	<1.5%	RMS of signal level.
Conversion gain	Conversion gain	@ output (measured).
Output signal amplitude	0.6V	At nominal conditions.
Saturation charge	21.500 e-	
Sensitivity (peak)	411V.m2/W.s 4.83 V/lux.s	@ 650 nm (85 lux = 1 W/m2).
Sensitivity (visible)	328 V.m2/W.s 2.01 V/lux.s	400-700 nm (163 lux = 1 W/m2).
Peak QE * FF Peak Spectral Resp.	25% 0.13 A/W	Average QE*FF = 22% (visible range). Average SR*FF = 0.1 A/W (visible range). See spectral response curve.
Fill factor	35%	Light sensitive part of pixel (measured).
Dark current	3.37 mV/s 78 e-/s	Typical value of average dark current of the whole pixel array (@ 21 °C).
Dark Signal Non Uniformity	8.28 mV/s 191 e-/s	Dark current RMS value (@ 21 °C).
Temporal noise	24 RMS e-	Measured at digital output (in the dark).
S/N Ratio	895:1 (59 dB)	Measured at digital output (in the dark).
Spectral sensitivity range	400 - 1000 nm	
Optical cross talk	15% 4%	To the first neighboring pixel. To the second neighboring pixel.
Power dissipation	190 mWatt	Typical (including ADCs).

[+] Feedback